

**Doctoral thesis**

for the doctoral degree

**Doctor rerum naturalium (Dr. rer. nat.)**

Novel Hybrid Hydrogels Based on Poly(2-oxazoline)  
*Neuartige Hybrid Hydrogele auf Basis von Poly(2-oxazolin)*



Submitted by

**M.Sc. Chen Hu**

from

Weinan, China

Würzburg, 2022



Submitted on: .....

Stamp Graduate School

**Members of thesis committee**

Chairperson: .....Prof. Dr. Vladimir Dyakonov.....

1. Reviewer and Examiner: .....Prof. Dr. Robert Luxenhofer.....

2. Reviewer and Examiner: .....Prof. Dr. Paul Dalton.....

3. Examiner: .....Prof. Dr. Jürgen Groll.....

Additional Examiners: .....

.....

Day of thesis defense: .....12 July 2022.....



Die vorliegende Arbeit wurde in der Zeit von Oktober 2018 bis Oktober 2021 am Lehrstuhl für Chemische Technologie der Materialsynthese der Julius-Maximilians-Universität Würzburg unter der Betreuung von Herrn Prof. Dr. Robert Luxenhofer angefertigt.



# |Acknowledgments

At this point, I would like to thank everyone who has contributed to the success of this work.

First and foremost, my special thanks go to my supervisor Prof. Dr. Robert Luxenhofer for the great opportunity to work on this extremely interesting topic, and for his willingness to continue to look after me thereafter his call to Helsinki. I would also like to thank him for the trust he has placed in me regarding the free design of my work, and unlimited support with questions and problems. In addition, I am very grateful that I attended various conferences, although it's only virtually attendance due to the currently special global Covid-19 situation.

I would like to express the deepest appreciation to Prof. Dr. Jürgen Groll and Prof. Dr. Paul Dalton for their willingness to co-supervise my doctorate, and for the always motivating and enriching discussions. In this context, I would also like to thank Dr. Stephan Schröder-Köhne for his kindness help and support in regards to organizational questions.

I would like to thank my laboratory colleagues Michael, Daniel, Solomiia, Christine, Lukas, Haider, Stefan, Jochen, Sebastian, Mengshi and all the others for the always good atmosphere and kindness help. We have experienced many grateful times together at the chair, in Würzburg, while the Christmas parties, ChemCup, Bosseln, numerous meetings, barbecues, and beer party. Many thanks to my bachelor student Phan Tuong Vy Dinh from University of Würzburg and master student Moonika Kinnunen (co-supervised) from University of Helsinki for their good cooperation. It was really a pleasure for me to be able to accompany them on part of their research training.

I would like to thank our technician Christian May, who with his calm, conscientious and friendly manner is indispensable as an aid in everyday laboratory work and is always at my side with advice and action. In this context, I would also like to thank Dr. Guntram Schwarz for his always willingness to help with the computer problems, as well as with the UV-*vis*-NIR and rheological measurement issues. I would like to thank our technicians Sandra Stockmann, Anna Kucharski, Stephanie Maaß, and our secretary Diana Stürmer for the excellent organization and maintenance of all the equipment, and for the always kindness support and help at the chair.

For the introduction to the existing extrusion-based 3D printers in FMZ and the possibility to carry out printing experiments by myself, I would like to thank Alexander Altmann and Ruben G. Scheuring for their kindly help with the G-code writing and continuously support with the 3D printing of the hybrid hydrogel inks. For the (Cryo-) SEM images characterization of the hybrid hydrogels in this work, I would like to thank Philipp Stahlhut and Judith Friedlein from FMZ, without whom, these measurements would not have been possible. I would like to thank Isabell Biermann and Manuel Roesener from FMZ for their kindly introduction to the universal testing machine, and their countless technical support and scientific discussion during the mechanical tests. In this context, also a thank to Johannes Wiest from the Institute of Pharmacy and Food Chemistry for his help in carrying out the XRD tests.

I would like to thank Dr. Taufiq Ahmad from FMZ for the great collaboration in performing the biological experiments, and his professional discussion in scientific issues including experiments design and results evaluation.

I am grateful to China Scholarship Council (CSC) for the award of PhD scholarship to fund my research and living in Germany.

Finally, I would like to thank my family and friends for their support outside of the scientific work. Here, a unique thank goes to my boyfriend Jin-Jiang for his moral support during my doctorate and, for his understanding during the time I was writing my dissertation.



# |Publications

“Improving Printability of a Thermoresponsive Hydrogel Biomaterial Ink by Nanoclay Addition”

**C. Hu**, L. Hahn, M. S. Yang, A. Altmann, P. Stahlhut, J. Groll and R. Luxenhofer  
Journal of Materials Science, 2021, 56, 691-705.

“Development of a 3D Printable and Highly Stretchable Ternary Organic-Inorganic Nanocomposite Hydrogel”

**C. Hu**, M. S. Haider, L. Hahn, M. S. Yang and R. Luxenhofer  
Journal of Materials Chemistry B, 2021, 9, 4535-4545.

“A Thermogelling Organic-Inorganic Hybrid Hydrogel with Excellent Printability, Shape Fidelity and Cytocompatibility for 3D Bioprinting”

**C. Hu**, T. Ahmad, M. S. Haider, L. Hahn, P. Stahlhut, J. Groll and R. Luxenhofer  
Biofabrication, 2022, 14, 025005.

“Tuning the Thermogelation and Rheology of Poly(2-oxazoline)/Poly(2-oxazine)s Based Thermosensitive Hydrogels for 3D Bioprinting”

M. S. Haider, T. Ahmad, M. S. Yang, **C. Hu**, L. Hahn, P. Stahlhut, J. Groll and R. Luxenhofer  
Gels, 2021, 7, 78-98.

"Synthesis and Investigation of Chiral Poly(2,4-disubstituted-2-oxazoline) Based Triblock Copolymers, Their Self-Assembly and Formulation with Chiral and Achiral Drugs"

M. S. Yang, M. S. Haider, S. Forster, **C. Hu** and R. Luxenhofer  
Macromolecules, submitted, DOI: 10.26434/chemrxiv-2022-6rfsb.



---

# |Contents

Abbreviations and Symbols.....	V
1 Introduction.....	1
2 State of Knowledge.....	5
2.1 Additive Manufacturing Technology.....	7
2.1.1 Extrusion-Based Printing.....	9
2.1.2 Inkjet Printing.....	10
2.1.3 Laser-Assisted Printing.....	12
2.1.4 Stereolithography.....	13
2.1.5 Summary - A Comparison of Different Printing Technologies.....	14
2.2 Materials for Extrusion-Based 3D Printing.....	16
2.2.1 Hydrogel Inks Based on Natural Polymers.....	17
2.2.2 Hydrogel Inks Based on Synthetic Polymers.....	22
2.2.3 Naturally Derived <i>versus</i> Synthetic Polymers for 3D Printing.....	24
2.2.4 Development of Ink Materials - Requirements and Challenges.....	25
2.3 Printability Assessment of a Hydrogel (Bio)Ink.....	27
2.3.1 Rheological Factors Affecting Printability and Shape Fidelity.....	28
2.3.1.1 Viscosity.....	29
2.3.1.2 Shear Thinning.....	29
2.3.1.3 Viscoelastic Moduli and Loss Factor.....	30
2.3.1.4 Yield Stress.....	31
2.3.1.5 Viscoelastic Recovery.....	32
2.3.2 Extrudability and Filament Formation.....	33

2.3.3	Filament Fusion and Filament Collapse .....	34
2.3.4	Shape Fidelity in Printed Structures .....	35
2.3.5	Summary .....	37
2.4	Approaches to Improve Printability .....	39
2.5	Poly(2-oxazoline)s and Poly(2-oxazine)s .....	41
2.5.1	Synthesis .....	41
2.5.1.1	Initiation .....	42
2.5.1.2	Propagation .....	43
2.5.1.3	Termination .....	44
2.5.1.4	Summary of the LCROP of 2-oxazolines and 2-oxazines .....	44
2.5.2	Properties .....	45
2.5.2.1	Aqueous Solubility of Poly(2-oxazoline)s and Poly(2-oxazine)s .....	45
2.5.2.2	Thermal Properties of Poly(2-oxazoline)s and Poly(2-oxazine)s .....	47
2.5.2.3	Cytocompatibility of Poly(2-oxazoline)s and Poly(2-oxazine)s .....	47
2.5.3	Poly(2-oxazoline)s and Poly(2-oxazine)s Based Hydrogels .....	47
2.5.3.1	Chemical Hydrogels .....	48
2.5.3.2	Physical Hydrogels .....	49
2.5.3.3	Hydrogels for 3D Printing .....	51
3	Motivation .....	53
4	Results and Discussion .....	57
4.1	Synthesis of Poly(2-oxazoline)- <i>b</i> -Poly(2-oxazine) Copolymers .....	59
4.2	Temperature Dependent Rheological Properties of PMeOx- <i>b</i> -PnPrOzi Copolymer Solutions .....	63
4.3	Development of Novel Hybrid Hydrogels Based on PMeOx- <i>b</i> -PnPrOzi Copolymers .....	68
4.3.1	PMeOx- <i>b</i> -PnPrOzi/clay Hybrid Hydrogels .....	68
4.3.1.1	Preparation and Characterization of PMeOx- <i>b</i> -PnPrOzi/clay Hybrid Hydrogels .....	68

---

4.3.1.2	Rheological Properties of PMeOx- <i>b</i> -PnPrOzi/clay Hydrogels .....	71
4.3.1.3	Printability of PMeOx- <i>b</i> -PnPrOzi/clay Hybrid Hydrogels .....	78
4.3.1.4	Clay Influence on The Printing Window of PMeOx- <i>b</i> -PnPrOzi/clay Hybrid Hydrogels.....	81
4.3.1.5	Conclusion.....	85
4.3.2	PMeOx- <i>b</i> -PnPrOzi/PDMAA/clay Hybrid Hydrogels .....	87
4.3.2.1	POx- <i>b</i> -POzi/PDMAA/clay Hydrogel Preparation .....	87
4.3.2.2	Rheological Properties of POx- <i>b</i> -POzi/DMAA/clay Precursor .....	92
4.3.2.3	Mechanical Properties of POx- <i>b</i> -POzi/PDMAA/clay Hydrogel.....	94
4.3.2.4	Characterizations of POx- <i>b</i> -POzi/PDMAA/clay Hydrogel .....	97
4.3.2.5	3D Printing .....	99
4.3.2.6	Conclusion.....	104
4.3.3	PMeOx- <i>b</i> -PnPrOzi/Alg/clay Hybrid Hydrogels .....	106
4.3.3.1	Preparation of POx- <i>b</i> -POzi/Alg/clay Hybrid Hydrogel .....	106
4.3.3.2	Rheological Properties of POx- <i>b</i> -POzi/Alg/clay Precursor Solution .....	111
4.3.3.3	Mechanical Properties of POx- <i>b</i> -POzi/Alg/clay Hydrogel.....	115
4.3.3.4	3D Printing .....	117
4.3.3.5	Cytocompatibility and 3D Cell-laden Printing .....	122
4.3.3.6	Conclusion.....	127
5	Summary and Outlook.....	129
6	Zusammenfassung und Ausblick .....	139
7	Experimental .....	149
7.1	Equipment and Methods of Measurement .....	151
7.2	Reagents and Solvents .....	161
7.3	Methods .....	162
7.3.1	Polymer Synthesis .....	162
7.3.2	Hybrid Hydrogels Preparation.....	165
	Bibliography .....	169

---



# |Abbreviations and Symbols

## ABBREVIATIONS

AA	acrylic acid
ACN	acetonitrile
AGDV	alanine-glycine-aspartic acid-valine
AM	additive manufacturing
Boc-Pip	Boc-piperazine
CAD	computer-aided design
CAM	computer-aided manufacturing
CMC	carboxymethylcellulose
Cryo-SEM	cryogenic scanning electron microscopy
CT	computed tomography
dECM	decellularized extra cellular matrix
DI	deionized
DLS	dynamic light scattering
DMAA	N, N-dimethylacrylamide
DMEM	dulbecco's modified eagle medium
DP	degree of polymerization
DSC	dynamic scanning calorimetry

ECM	extra cellular matrix
EtOx	2-ethyl-2-oxazoline
F127	Pluronic F127
FDA	Food and Drug Administration
GelMA	gelatin methacrylate
GPC	gel permeation chromatography
HA	hyaluronic acid
HAMA	methacrylated hyaluronic acid
HEMA	2-hydroxyethyl methacrylate
HFIP	hexafluoroisopropanol
HPMC	hydroxypropyl methylcellulose
IPN	interpenetrating network
KPS	potassium persulfate
LCROP	living cationic ring opening polymerization
LCST	lower critical solution temperature
LVE(R)	linear viscoelastic (range)
MBAA	N, N'-methylenebisacrylamide
MC	methylcellulose
MeOTf	methyl trifluoromethylsulfonate
MeOx	2-methyl-2-oxazoline
MRI	magnetic resonance imaging
MWCO	molecular weight cut-off
NMR	nuclear magnetic resonance
<i>n</i> PrOzi	2- <i>n</i> -propyl-2-oxazine



OCT	optical coherence tomography
PBhOzi	poly(2-benzhydryl-2-oxazine)
PBzOx	poly(2-benzyl-2-oxazoline)
PBzOzi	poly(2-benzyl-2-oxazine)
PC	polymer composition
PcPrOx	poly(2- <i>cyclo</i> -propyl-2-oxazoline)
PDMAA	poly(N, N-dimethylacrylamide)
PEG	poly(ethylene glycol)
PEGDA	poly(ethylene glycol diacrylate)
PEtOx	poly(2-ethyl-2-oxazoline)
PEtOzi	poly(2-ethyl-2-oxazine)
PhCN	benzonitrile
PiBuOx	poly(2- <i>iso</i> -butyl-2-oxazoline)
PiPrOx	poly(2- <i>iso</i> -propyl-2-oxazoline)
PMeOx	poly(2-methyl-2-oxazoline)
PMeOzi	poly(2-methyl-2-oxazine)
PMMA	poly(methyl methacrylate)
PnBuOx	poly(2- <i>n</i> -butyl-2-oxazoline)
PnBuOzi	poly(2- <i>n</i> -butyl-2-oxazine)
PNIPAAm	poly(N-isopropylacrylamide)
PnPenOzi	poly(2- <i>n</i> -pentyl-2-oxazine)
PnPrOx	poly(2- <i>n</i> -propyl-2-oxazoline)
PnPrOzi	poly(2- <i>n</i> -propyl-2-oxazine)
POx	poly(2-oxazoline)

POzi	poly(2-oxazine)
PPG	polypropylene glycol
PPhenEtOx	poly(2-phenethyl-2-oxazoline)
PPheOx	poly(2-phenyl-2-oxazoline)
PPheOzi	poly(2-phenyl-2-oxazine)
PVC	polyvinyl chloride
RGD	arginine-glycine-aspartic acid
RM	regenerative medicine
SANS	small angle neutron scattering
SD	standard deviation
SEM	scanning electron microscopy
SFF	solid freeform fabrication
SLS	static light scattering
SR	swelling ratio
TE	tissue engineering
TGA	thermogravimetric analysis
UCST	upper critical solution temperature
UV- <i>vis</i> -NIR	ultraviolet- <i>visible</i> -near infrared
XRD	X-ray diffraction

## SYMBOLS

(k)Pa	(kilo) pascal
°C	degree celsius
2D	two-dimensional
3D	three-dimensional
Đ	dispersity ( $\text{Đ} = M_w/M_n$ )
eq	equivalent
g	gram
G'	storage (or elastic) modulus
G''	loss (or viscous) modulus
h	hour
Hz	hertz
K	kelvin
k	consistency index
kDa	kilo Dalton
L	liter
M	molar
min	minute
mm	millimeter
$M_n$	number-average molar mass
$M_w$	weight-average molar mass
n	flow behavior index or shear-thinning index
ppm	parts per million

## Abbreviations and Symbols

---

s	second
t	time
T	temperature
$\tan \delta$	loss factor
$T_{CP}$	cloud point temperature
$T_g$	glass transition temperature
$T_{gel}$	gelation temperature
wt%	weight percent
$\gamma$	strain
$\eta$	dynamic viscosity
$\tau$	shear stress
$\dot{\gamma}$	shear rate

# 1 | Introduction



Materials science is a highly interdisciplinary field that has a tremendous impact on the development of revolutionary technologies. Transformative technologies - like the steam engine, the light bulb, the microchip and including the “subtractive” manufacturing technology - unalterably changed our world and the way we do things. Since the traditional “subtractive” manufacturing suffers some inherent drawbacks, for instance, complex processes, waste of materials and limited feature design freedom, developing new approaches with high efficiency and economical friendly feature is highly attractive not only for us human beings but also for entire biosphere. Thereupon, additive manufacturing (AM), also known as the three-dimensional (3D) printing, comes to the center of stage as an emerging technology which offers a new paradigm for engineering design and manufacturing with profound economic, environmental and security implications.

Over the past few decades, 3D printing has made significant advancements in many areas including aerospace, consumer products, arts, food industry and manufacturing in general. And recently, it has also intrigued increasing interest of researchers in biomedical engineering field and developed as a novel promising biofabrication approach, called 3D bioprinting, aiming to address the tissues and organs shortage suitable for transplantation, as well as the applications such as explorative *in vitro* models for drug screening and toxicity testing. Here the materials, either natural or synthetic polymers, used in 3D (bio)printing process are called biomaterial inks (without cells) or bioinks (with cells), which is a crucial basis of any printing technologies.

Despite the remarkable progress have been achieved regarding 3D (bio)printing technologies, it has recently become more and more evident that the limited availability of printable material systems has become one of the major drawbacks, significantly hindering the further development of this research field. Therefore, many research groups are currently working on the development of novel printable materials, either by developing new polymers to broaden the available ink platforms or by post modification to continuously advance existing polymers.

In general, compared with non-biological printing, 3D biological printing or bioprinting places higher demands on the printing devices as well as on the ink materials utilized. Poly(2-oxazoline)s (POx) is currently a frequently discussed alternative to poly(ethylene glycol) (PEG), the “gold standard” for synthetic polymers used for biomedical applications at the moment. POx is synthesized by living cationic ring opening polymerization (LCROP) and shows a remarkable high degree of synthetic variability, allowing for a wide range of tunable physicochemical properties. In addition, POx exhibits good cytocompatibility and has been well studied in drug delivery and antifouling systems over the last decades.

Very recently, POx has attracted a great deal of interest as a novel ink material in the field of biofabrication, especially after the first fully POx-based cytocompatible thermogelling bioink described in 2017. Although a family of POx-based thermoresponsive copolymers exhibiting (inverse) reversible thermogelation behavior were subsequently described and claimed to potentially provide a very promising polymer platform for 3D (bio)printing, the printing of real 3-dimensional constructs had not been achieved prior to this work.



## 2 | State of Knowledge



## 2.1 Additive Manufacturing Technology

Additive manufacturing (AM), also referred to as 3D printing, was first described by Charles W. Hull in 1986 when developing the stereolithography technique for converting 3D computer-aided design (CAD) into solid 3D objects.<sup>[1-2]</sup> This development was quickly followed by the emergence of several other 3D fabrication techniques and has long been regarded as a set of revolutionary technologies for materials processing in many areas, ranging from engineering fabrications in automotive and aerospace to customized products in biomedicine and daily life.<sup>[3-8]</sup> Compared to conventional formative and subtractive manufacturing techniques, this advanced manufacturing technology allows the production of customized 3D objects by precisely depositing ink materials such as ceramics, metals and polymers in a layer-by-layer fashion, which supersedes the use of molds or machining and allows for a much greater freedom of design.

Over the past few decades, 3D printing has made significant advancements and has now evolved into a promising biofabrication approach, especially in the tissue engineering (TE) and regenerative medicine (RM) applications, called 3D bioprinting. In this context, the relatively young but rapidly growing technology of biofabrication is therefore defined by the International Society for Biofabrication as:

*“the automated generation of biologically functional products with structural organization from living cells, bioactive molecules, biomaterials, cell aggregates such as micro-tissue, or hybrid cell-material constructs, through Bioprinting or Bioassembly and subsequent tissue maturation process”.*<sup>[9]</sup>

As a novel biofabrication approach besides the bioassembly, 3D bioprinting allows printing of cells, growth factors and scaffold materials together into the customized biological constructs that can either be cultured *in vitro* to generate 3D tissue models or implanted with or without previous *in vitro* maturation (**Fig. 2.1**). The current developments in 3D (bio)printing in the field of biofabrication have very recently been summarized in several excellent reviews.<sup>[10-19]</sup>

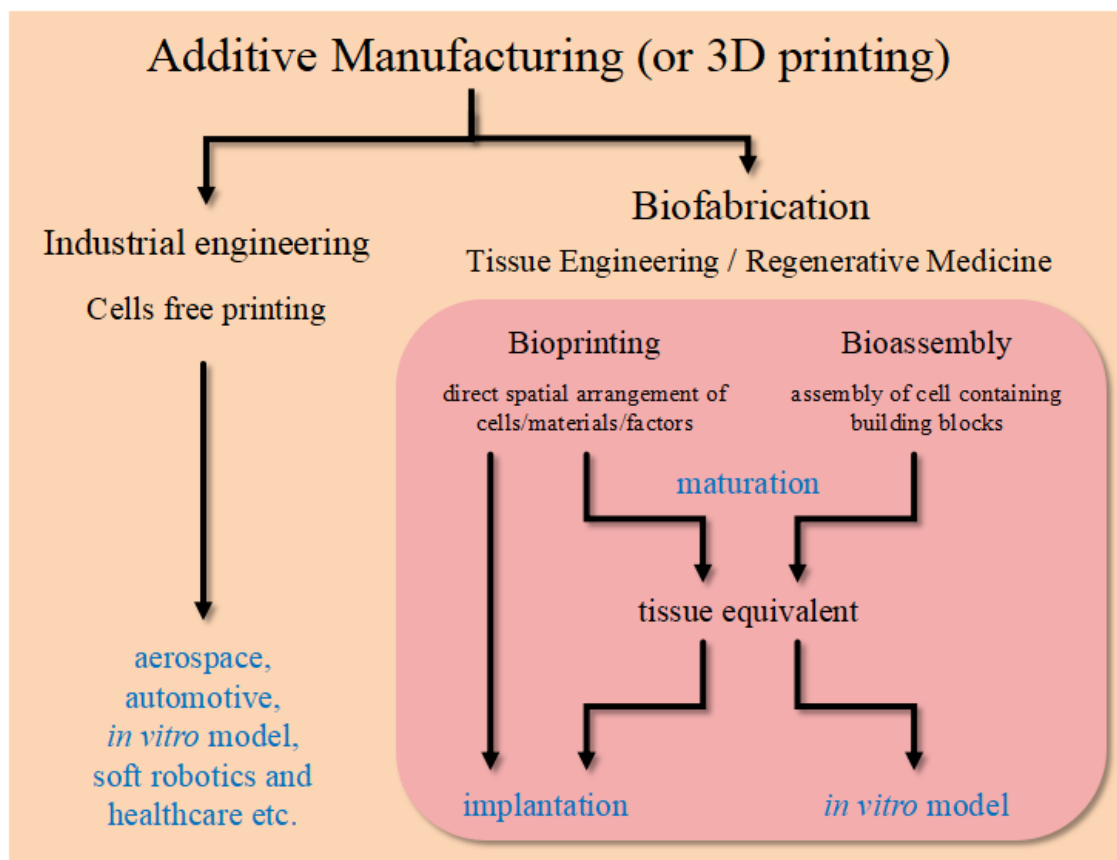


Fig. 2.1| Additive manufacturing technology to directly create customized 3D objects in both industrial engineering and biofabrication fields.

In general, the 3D (bio)printing technology typically involves several steps, including imaging a 3D geometry model of the target object, designing the print approach, selecting the suitable materials (and cells if needed), performing 3D printing, and evaluating the printed constructs for the specific applications (**Fig. 2.2**).<sup>[20]</sup> Model imaging of a 3D object can be created with CAD software or obtained from scanning data of clinical imaging technologies, such as magnetic resonance imaging (MRI) and computed tomography (CT).<sup>[21-24]</sup> The possibility of using clinical scan data makes this manufacturing technology particularly useful for applications in biomedical engineering, as it allows the fabrication of patient-specific models or implants. After creating a 3D model of desired object and importing it to 3D printer in STL file format, the machine's built-in specialized software interprets the CAD data and virtually slices the model into cross-sectional thin layers according to the accuracy requirement. It then instructs the machine's printer head

to follow a specific path to deposit the ink materials layer-by-layer until the entire 3D structure is built.<sup>[25]</sup>



Fig. 2.2| Generalized 3D (bio)printing process.

Currently, the four major 3D (bio)printing techniques are extrusion-based printing, inkjet printing, laser-assisted printing, and stereolithography. Each technique has specific advantages and limitations, as well as very specific requirements for the inks to achieve reliable fabrication of 3D constructs, and have already been summarized and compared in a number of excellent reviews.<sup>[20, 26-30]</sup> For the sake of completeness of this paper, a brief overview and comparison of these technologies is presented below.

### 2.1.1 Extrusion-Based Printing

Extrusion-based printing, also known as direct writing or robotic dispensing, is the most commonly used commercially available 3D printing technology at present due to its high compatibility with the ink fluid properties (acceptable ink viscosities range from 30 to  $6 \times 10^7$  mPa s<sup>[31-32]</sup>) as well as the solidification methods.<sup>[33-35]</sup> This approach allows the fabrication of designed constructs ranging from clinically relevant tissue sizes to micro tissues in a realistic time frame.<sup>[36-38]</sup> Driven by pneumatic<sup>[39-42]</sup> or mechanical (piston or screw)<sup>[43-44]</sup> dispensing systems (**Fig. 2.3**), ink formulation loaded into a cartridge is extruded out through a nozzle or needle to form filament, which is then deposited onto the building platform in a layer-by-layer fashion.<sup>[9, 45]</sup>

Many commercial (bio)printer devices are based on pneumatic dispensing, which is more versatile but tends to provide lower control over the ink deposition due to the delay of the compressed gas volume in pneumatic systems.<sup>[46]</sup> In contrast, mechanical dispensing systems, particularly the screw-driven system, is more suitable for dispensing inks with higher viscosities and may provide greater spatial control over the material flow.<sup>[10, 47]</sup> In addition, in order to allow for controlled dispensing of multiple inks within

a single construct serially without retooling, the printer setups equipped with multiple printheads, cooling and heating systems, and light sources are more often used.<sup>[48-49]</sup>

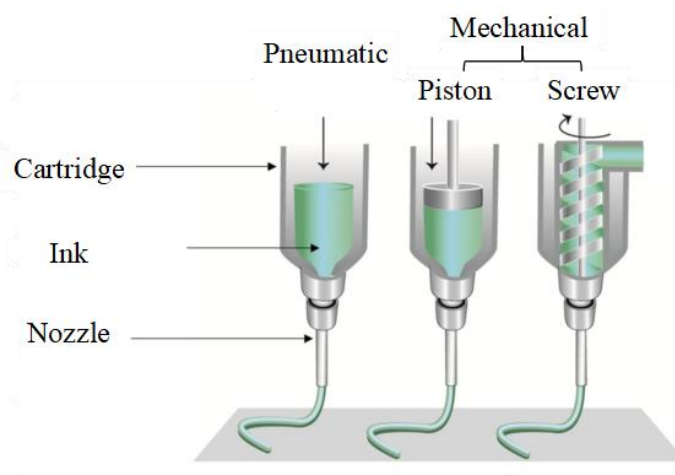


Fig. 2.3| Schematic illustration of extrusion-based printing technique: pneumatic, piston, and screw driven printing, adapted with permission from <sup>[45, 50]</sup>.

Currently, various tissue-like constructs such as bone,<sup>[25, 51]</sup> cartilage,<sup>[52]</sup> aortic valves,<sup>[53-54]</sup> vasculature<sup>[55]</sup> and tumor models<sup>[56]</sup> have been successfully engineered with this method. In the case of printing with cells-embedded bioinks, the resolution is usually limited in the hundred micrometers to millimeters, as shear stresses at the dispenser tip is inversely correlate with the nozzle diameter and should be minimized to prevent damage to the embedded cells. In contrast, cell-free inks have a much higher resolution because they are not subject to this limitation and can be extruded through finer needles with higher pressures.<sup>[57]</sup> Despite the great versatility, improving print resolution and speed remains a challenge for extrusion printing technology compared to other printing technologies, like the inkjet printing.<sup>[45]</sup>

### 2.1.2 Inkjet Printing

Inkjet printing (also known as drop-on-demand printing) is a noncontact printing technique by dispensing low-viscous inks onto a substrate with tiny ink drops.<sup>[31]</sup> The first 3D inkjet printers were realized from commercial 2D inkjet printers modified with an elevator stage as z-axis for printer.<sup>[58-60]</sup> This technology is also available for both the non-biological and biological applications.<sup>[20, 61]</sup> For the advantages of fast fabrication, low-

cost, high resolution and great control on the deposition patterns, inkjet 3D printing technique has been successfully utilized in multiple research areas such as to fabricate bone constructs,<sup>[57]</sup> *in situ* regeneration of functional skin<sup>[62]</sup> and cartilage.<sup>[63]</sup> Currently, the fabrication strategies most adopted for generating ink droplets are thermal inkjet printing,<sup>[64-68]</sup> and piezoelectric inkjet printing (**Fig. 2.4**).<sup>[59, 69-72]</sup>

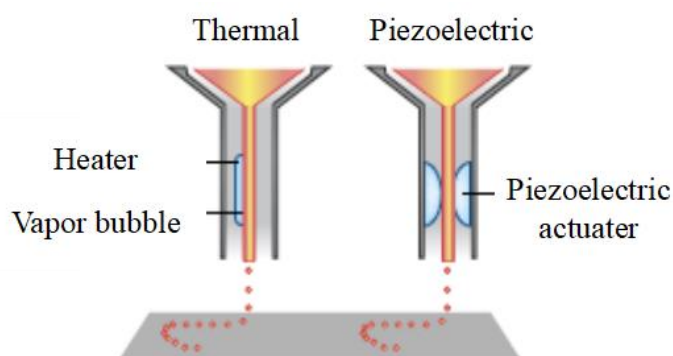


Fig. 2.4| Schematic illustration of the inkjet printing technique, adapted with permission from [45, 50].

Thermal inkjet printer ejects the ink drops from print head due to the high pressure of air bubbles generated by localized high frequent heating up to 300 °C.<sup>[20, 68]</sup> Here, it has demonstrated that only a short duration of heating ( $\sim 2 \mu\text{s}$ ) to 300 °C does not have significant impacts on the stability of biological molecules such as DNA,<sup>[71-72]</sup> and substantial damage on the viability and function of the cells.<sup>[73-75]</sup> In piezoelectric inkjet printing, heating is not used, but a mechanical pulse is applied to the piezoelectric material in the nozzle by a piezoelectric actuator, which generate an pressure inside the print head to break the liquid ink into droplets at regular intervals.<sup>[76-77]</sup> Additionally, to avoid exposure of cells to heat and pressure, alternative inkjet printers that use acoustic radiation force associated with an ultrasound field was introduced.<sup>[78-82]</sup> With this method, the shear stress imposed on cells at the nozzle tip can be avoided by using an open-pool nozzle-less ejection system, which can reduce the potential loss of cell viability and avoid the problem of nozzle clogging.<sup>[79]</sup>

Although inkjet printing is an economic and efficient printing approach, there are still some challenges. One of the main restrictions of this technology is limitation on the

viscosity for the ink formulations, which is not available for the deposition of higher viscous materials.<sup>[69]</sup> It is difficult to translate this technology to more clinically relevant large sizes and high cell densities, for a high cell density can cause clogging of the nozzle and may create unwanted shear stress issues.<sup>[69-70, 75, 81]</sup> Additionally, inkjet printing technology shows a poor droplet directionality, and normally results in mechanical strength inferior printed structures when compared to the target tissue.<sup>[64]</sup>

### 2.1.3 Laser-Assisted Printing

Laser-assisted printing is based on the principles of laser-induced forward transfer technology that refers to the use of a donor slide (usually made from glass) covered with a laser energy absorbing layer (e.g., gold or titanium) and a layer of ink materials (e.g., cells or hydrogel) (**Fig. 2.5**).<sup>[83-84]</sup> During printing, the focused laser pulses cause local evaporation of the absorbing layer, which in turn generates a high gas pressure propelling the ink towards the collector slide. It is reported that the resolution of laser-assisted printing is affected by many factors, including the laser fluence, surface tension, wettability of the substrate, air gap between the ribbon and the substrate, as well as the thickness and viscosity of the ink layer.<sup>[85-86]</sup>

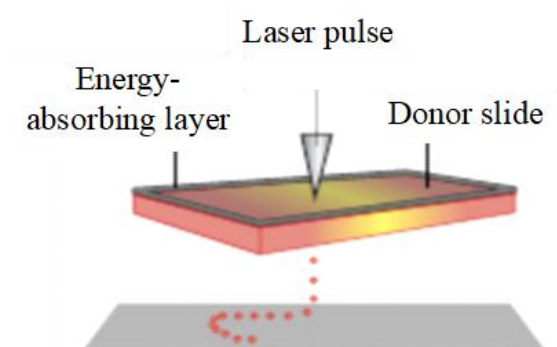


Fig. 2.5| Schematic illustration of laser-assisted printing technique, adapted with permission from <sup>[45, 50]</sup>.

Although less popular than other printing approaches, laser-assisted printing has also been successfully applied for biofabrication fields, such as printing of biological materials peptides,<sup>[87]</sup> DNA,<sup>[88]</sup> and cells.<sup>[89]</sup> Laser-based bioprinting is compatible with a materials viscosities range of 1-300 mPa s<sup>-1</sup>, and allows for the precise deposition of high cells



densities (up to  $10^8$  cells/ml) materials with only a negligible effect on cell viability and functions.<sup>[90-94]</sup> Furthermore, this technology is nozzle-free and, therefore, the problem of clogging with materials or cells that suffered by other printing technologies is avoided.<sup>[26]</sup> Nevertheless, laser-assisted printing has extremely low throughput comparing to other printing techniques, which limits its wide applications in tissue engineering.<sup>[95]</sup> In addition, this procedure is costly and time-consuming, which might hamper the successful translation towards widespread application.<sup>[70]</sup>

### 2.1.4 Stereolithography

Stereolithography introduced in the late 1980s is the first commercially available solid freeform fabrication (SFF) technique.<sup>[96]</sup> The manufacturing of 3D objects with this method is based on the spatially controlled photopolymerization of the photo-sensitive resins, using a bottom-up system (illumination by a computer-controlled laser beam) or a top-down setup (illumination by a computer-driven digital light projector) (**Fig. 2.6**). In both systems 3D objects are built in a layer-by-layer manner by spatially controlled photopolymerization, differences are in the build orientation and the method of illumination.

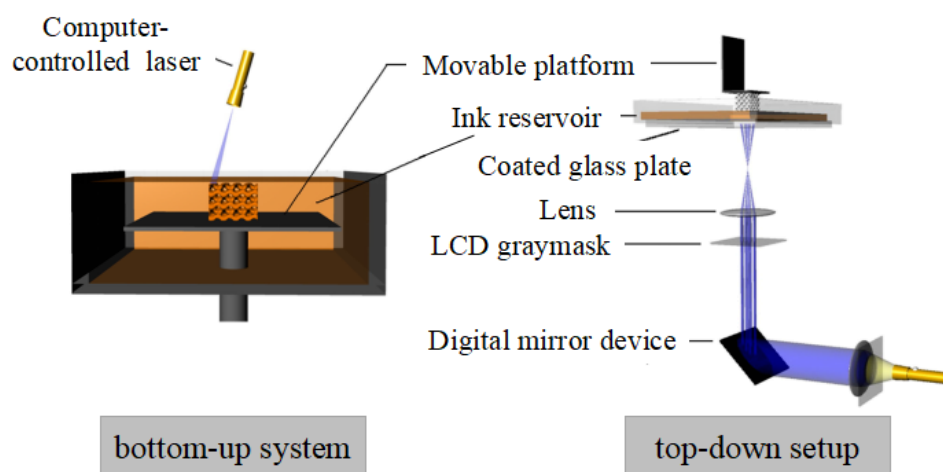


Fig. 2.6| Schemes of two types of stereolithography setups. Left: a bottom-up system with scanning laser. Right: a top-down setup with digital light projection. Adapted with permission from <sup>[96]</sup>.

Although many other techniques have been developed, stereolithography remains one of the most powerful and versatile of all AM techniques.<sup>[96]</sup> Stereolithography has the

highest fabrication accuracy, and is particularly versatile with respect to the design and scales freedom of the structures that can be built. Additionally, with the introduction of hydroxyapatite composites and cell-containing hydrogels as new ink materials, stereolithography has developed into an applicable technique for biomedical engineering purposes and even printing of cell-laden constructs.<sup>[96-97]</sup> However, stereolithography is limited to only photo-crosslinkable materials and, thus the application of live cell printing is highly restricted.<sup>[34]</sup>

### 2.1.5 Summary - A Comparison of Different Printing Technologies

All these printing technologies can be used in biological printing for tissue engineering applications. Although each printing approach has the advantages and limitations, it still reveals a broad range that can be printed by a thoughtful combination of ink with suitable printing methods. An overview and comparison of these different printing techniques is summarized in **Tab. 2.1**. According to the specific requirements form different application scenarios, the printing resolution, deposition accuracy, structure dimension of the printed subjects and the consumed printing time should all be well taken into consideration when selecting a printing approach. Additionally, cell viability should be considered at higher priority, when aiming at the bioprinting of cell-laden scaffolds.

Tab. 2.1| Comparison of four common 3D printing technologies.

Printer type	Extrusion-based	Inkjet	Laser-assisted	Stereolithography
Working principle	contact	noncontact	noncontact	contact
Cell compatible	yes	yes	yes	yes
Fabrication speed	medium	fast	slow	fast
Ink viscosity	30-6×10 <sup>7</sup> mPa·s	3.5-12 mPa·s	1-300 mPa·s	-
Nozzle	yes	yes	nozzle free	nozzle free
Resolution	100 μm	30 μm	20-100 μm	20-50 μm
Cost	low	low	high	high

Among the presented technologies, extrusion-based 3D printing is normally considered the most common printing methodologies, although it cannot keep up with other technologies regarding the printing resolution sometimes. This method benefits from wide adoption, ease of use, precision printing of complex geometries and compatible with multiple solidification methods. Moreover, the force leading to material extrusion can be precisely controlled, and the nozzle diameters can be simply adjusted by interchanging the utilized needle. Commercially available systems of the low-cost open-source extrusion printer significantly contributed to the recently development of novel ink materials and its expansion in biofabrication. Researchers, especially from material chemistry academic disciplines with no engineering background, have now the possibility to develop new ink candidates and investigate their printability directly on user-friendly bench-top (bio)printers. Therefore, we will largely focus on this type of printing, and use the extrusion-based 3D printer to perform all the printing experiments in this study.

## 2.2 Materials for Extrusion-Based 3D Printing

Advances in AM technology strongly relies on the availability of suitable ink materials. Like for other 3D printing technologies, the “classic” ink materials used for extrusion-based 3D printing including metals, ceramics, and polymers. The printing of these materials normally involves the conditions such as toxic chemicals, high temperatures, or a dry environment, which are not compatible with living cells and most of the biomedical applications.<sup>[13, 26]</sup> By contrast, hydrogels are three dimensionally crosslinked hydrophilic polymer networks that swell without dissolution in large amount of water. They are more and more frequently discussed currently as an appealing class of ink materials for 3D printing technologies, particularly for the scaffolds development in TE and RM fields, as they can mimic the natural extra cellular matrix (ECM) and possess similar mechanical properties to soft tissues.<sup>[45, 98-102]</sup>

Over the past few years, tremendous progress has been made in the development of printable hydrogel systems which involves a variety of polymers. According to the polymer source, these hydrogel forming polymers can be broadly divided into natural polymers and synthetic polymers. In addition, these polymers can also be classified more specifically based on their composition (into natural polymers including proteins/polypeptides, polysaccharides or glycosaminoglycans; and synthetic polymers including polyols, polyethers or polyesters), electrical charge nature (into neutral, cationic, anionic, or amphoteric polymer), degradation behavior (into biodegradable and non-biodegradable polymer) and crosslinking type (into physical crosslinking, chemical crosslinking, or irradiation crosslinking polymer). Several excellent review papers have summarized the currently progresses on printable hydrogels.<sup>[28-29, 52, 99, 101, 103-105]</sup>

Here, we will only take a detailed look at the most common used hydrogel-forming polymers that are suitable for TE and RM applications through the extrusion-based 3D printing technology. It should be noted that all the polymers mentioned below are normally utilized in blending systems between different materials since the single material

always cannot meet the manufacturing needs, while the blending system combines the advantages of two or multiple materials and consequently be able to overcome the limitations to achieve the demand material properties.<sup>[45, 106]</sup>

### 2.2.1 Hydrogel Inks Based on Natural Polymers

The hydrogel-forming natural polymers, also referred to as biopolymers, are derived from various organisms including human, animals, plants, and bacteria.<sup>[104, 107]</sup> In the following, the most commonly used natural occurring polymer based hydrogel inks in the extrusion-based 3D printing technology will be discussed in detail.

*Alginate hydrogel.* Alginate, regarded as a safe and biocompatible materials by the U. S. Food and Drug Administration (FDA), is a hydrophilic linear unbranched anionic polysaccharide extracted from brown algae or bacteria.<sup>[108-111]</sup> It is actually a block copolymer of (1,4)-linked  $\beta$ -D-mannuronate (M) and  $\alpha$ -L-guluronate (G) blocks, and that the ratio of G to M block as well as the length of each block varies depending on the natural source. As only the G-blocks of alginate are believed to participate in intermolecular cross-linking with di/trivalent cations to form hydrogels, the polymer composition (i.e., M/G ratio, sequence, G-block length) and molecular weight are thus two critical factors affecting the physical properties of alginate and its resultant hydrogels. Alginate can form gel under mild conditions through different mechanisms, making it particularly attractive and known as one of the most frequently used polymers for biomedical applications. At pH-values below 3, alginate self-assembles into acidic gels by the formation of intermolecular hydrogen bonds.<sup>[112-113]</sup> Alternatively, a physical hydrogel can also form by cooperative binding with divalent or trivalent cations such as  $\text{Ca}^{2+}$ ,  $\text{Mg}^{2+}$ ,  $\text{Sr}^{2+}$ ,  $\text{Ba}^{2+}$  or  $\text{Al}^{3+}$  which can interact with carboxylic acid groups in the polymer chains.<sup>[114-117]</sup> The viscosity of alginate solution and its overall stiffness after gelation is a function of the polymer concentration and its molecular weight.<sup>[118-119]</sup> For extrusion-based printing, it has been demonstrated that printing of pre-crosslinked alginate or using a coaxial nozzle-assisted cross-linker deposition system shows promising results in terms

of printing accuracy.<sup>[120]</sup> Despite the advantages, ionically cross-linked alginate hydrogels have the disadvantage of limited mechanical properties and difficult to control degradation behavior under physiological conditions. In addition, cells in alginate have limited cell adhesion, spreading and proliferation unless surface modifications are applied, for instance, modifying using cell adhesion ligands containing arginine-glycine-aspartic acid (RGD) amino acid sequence to enhance interactions with cells.<sup>[121]</sup>

*Chitosan hydrogel.* Chitosan, structurally similar to natural glycosaminoglycans, is a biodegradable linear polysaccharide produced by N-deacetylation of chitin.<sup>[122]</sup> It has been widely explored for various biomedical applications due to its low price, biocompatibility, as well as antibacterial and antifungal properties.<sup>[123-130]</sup> In general, chitosan is insoluble in neutral conditions, but easily soluble in the presence of acid due to the protonation of free amino groups on glucosamine.<sup>[131]</sup> Therefore, a lot of chitosan derivatives have been prepared aiming to enhance their solubility and processibility.<sup>[132-134]</sup> Chitosan can form hydrogels through various physical or chemical crosslinking methods.<sup>[135-137]</sup> When combined with an extrusion-based 3D printer, chitosan hydrogels have been used in the fabrication of various TE scaffolds, such as bone, skin, and cartilage.<sup>[138-141]</sup> Nevertheless, the slow gelation rate and low mechanical properties remains big drawbacks that hinders chitosan hydrogels for further development.

*Hyaluronic acid hydrogel.* Hyaluronic acid (HA) is a water-soluble and degradable linear non-sulfated glycosaminoglycan which can be found in almost every connective tissues.<sup>[142-143]</sup> HA and its derivatives have been used for decades as medical products in clinic, and have nowadays found applications as functional biomaterials for TE and RM applications.<sup>[143-148]</sup> The tunable physical and biological properties of HA-based hydrogels make them a promising candidate for 3D bioprinting process, although HA by itself does not have the suitable rheological properties for extrusion-based printing and exhibits the poor mechanical properties and rapid degradation features.<sup>[149-150]</sup> Therefore, in order to endows the resulting system with enhancing printability, stability and mechanical properties, chemical modification becomes indispensable before utilization of HA as the

3D printable materials. For instance, after functionalized with UV-curable methacrylate, the obtained methacrylated hyaluronic acid (HAMA) becomes a suitable hydrogel for extrusion-based printing with high printability capacity.<sup>[18, 151-152]</sup>

*Cellulose hydrogel.* Cellulose is the most abundant polysaccharide in nature that can be easily extracted from plants and bacteria.<sup>[153]</sup> Although the cellulose itself is insoluble in water and other common organic solvents, the cellulose derivatives such as methylcellulose (MC), carboxymethylcellulose (CMC) and hydroxypropyl methylcellulose (HPMC) are water-soluble and have been used for preparing hydrogels through either physical or chemical crosslinking methods.<sup>[154-155]</sup> Among them, the most widely used MC exhibits a typical reversible thermogelation behavior upon heating and cooling, depending on the polymer concentration, molecular weight and co-solutes, in particular the salts.<sup>[156-157]</sup> This reversible gelation is a result of the synergism of the hydrophobic interaction among methyl substituents with the intermolecular hydrogen bonding interaction among hydroxyl groups. With development of the cellulose chemistry and processing technology, cellulose-based materials have been widely used for many advanced applications such as smart healthcare, printed biomedical scaffolds and electronics.<sup>[158-160]</sup> In this context, Wang et al. has reviewed the development and assessment of cellulose materials for 3D printing, with a special focus paid on extrusion based 3D printing.<sup>[161]</sup>

*Fibrin hydrogel.* Fibrin is one of the essential proteins involved in blood clotting and wound healing, and has been used for various biomedical applications, for instance, as a carrier in drug delivery systems<sup>[162]</sup> or as a scaffolding material in TE applications, particularly vascular grafts.<sup>[163]</sup> Fibrin gel has attractive features like excellent mechanical properties, cytocompatibility, biodegradability, and bioactivity to promote cell growth, angiogenesis and differentiation.<sup>[164-166]</sup> Furthermore, for the biomedical applications, fibrin has binding sites RGD and alanine-glycine-aspartic acid-valine (AGDV) for native ECM proteins and heparin-binding domains.<sup>[164-165]</sup> Currently, fibrin has been successfully printed for neural stem cell culture.<sup>[166-167]</sup>

*Silk hydrogel.* Silks are a kind of natural protein fibers produced by *Arthropoda* such as spiders of the class *Arachnida* as well as insects of the order *Lepidoptera*, and have been used in TE and RM applications.<sup>[11, 168]</sup> The silk fibroin scaffolds, in comparison with other scaffolds, have several advantages like slow degradation, outstanding mechanical properties, non-toxicity, absence of immunogenicity and low bacterial adherence.<sup>[169-172]</sup> Because of these properties, silk protein-based materials have been studied a popular choice as biomaterial inks.<sup>[173-175]</sup> However, this kind of natural polymers have some disadvantage like need to mix with other polymers to optimize the rheology profile related with printing process.<sup>[176-179]</sup>

*Collagen hydrogel.* Collagen is a triple-helical biocompatible protein that abundant in mammalian species and marine organisms.<sup>[180-182]</sup> It is a main organic component of ECM, and can be degraded naturally by the matrix metalloproteinases.<sup>[183]</sup> The collagen biomaterial can create an ECM-mimetic microenvironment that is advantageous for promoting various cell functions such as cell adhesion, migration, spreading, proliferation and differentiation with a minimal immunological reaction.<sup>[182, 184-186]</sup> Collagen type I, the most commonly used collagen type, has been used in 3D printing as a growth substrate for 3D cell culture and as a scaffold material for cellular therapies.<sup>[187]</sup> Acid-soluble collagen can be crosslinked when the pH, temperature and ionic strength are adjusted to near physiological conditions, which makes it a good candidate for *in situ* bioprinting applications without harming cells dispersed in the ink materials.<sup>[49, 188-189]</sup> Currently, Collagen type I has been printed in combination with different cell types, and combined with other natural or synthetic materials to enhance the printing capability and the mechanical properties of native collagen.<sup>[190]</sup> However, the commonly used collagen type I also has some disadvantages, such as slow gelation rate, limited long-term stability and poor mechanical properties.<sup>[191]</sup>

*Gelatin hydrogel.* Gelatin is a class of proteinaceous substances that is derived from the parent protein collagen by denaturation and hydrolysis.<sup>[180, 192]</sup> Gelatin, retaining the natural cell-adhesive motifs RGD but less immunogenic compared to its precursor



material collagen, has been widely applied to TE and RM, and recently in 3D (bio)printing field due to their biocompatibility, ease gelation, low cost, non-immunogenicity, and completely biodegradable behavior *in vivo*.<sup>[193-195]</sup> Aqueous gelatin solution is thermoresponsive and solidifies below their upper critical solution temperature (UCST) of around 30 °C, depending on the polymer concentration.<sup>[196]</sup> Gelatin hydrogels are mechanical weak and unstable under physiological conditions, and thus require additional crosslinking cues to improve its printability and stability.<sup>[197-198]</sup> For extrusion-based printing, the most commonly used is the one after chemical modification with methacrylate, which is known as gelatin methacrylate (GelMA). The printability of GelMA is generally dependent on concentration, UV exposure time and cell density, also the intensity and duration of UV curing can affect cell viability, hydrogel density and stiffness.<sup>[199-200]</sup> Additionally, gelatin has been used as sacrificial material to fabricate 3D scaffolds with open fluidic channels.<sup>[201]</sup>

*Matrigel hydrogel.* Matrigel is a gelatinous mixture of basement membrane proteins produced by mouse Engelbreth-Holm-Swarm sarcoma cells.<sup>[202-203]</sup> It is also a thermosensitive material with gelation occurring rapidly around 24-37 °C depends on the concentration, but this gelation is not reversible. In order to extrude Matrigel, it is necessary to possess a temperature-controlled printing system to retain the Matrigel matrix at 4 °C in a liquefied solution state. Otherwise, the dispensing needle clogs and makes printing very challenging. Although Matrigel has been widely studied as biomaterial inks and showed a higher cell survival rate than those in alginate or agarose hydrogels,<sup>[204-207]</sup> it should be noted that Matrigel may promote tumorigenicity and growth of the tumor cells *in vivo* due to the presence of growth factors.<sup>[208]</sup>

*Agarose hydrogel.* Agarose is a linear polysaccharide generally extracted from red seaweed.<sup>[209-210]</sup> It is water-soluble at temperatures above 65 °C, and form a gel in a temperatures range from 17 to 40 °C, depending on the polymer concentration, molecular weight and chemical modification. The gelation mechanism of agarose relies on the formation of intermolecular hydrogen bonds upon cooling, thereby leading to the

aggregation of double helices *via* the physical entanglement of anhydro bridges on individual molecules.<sup>[211]</sup> The resulting agarose hydrogels has the desired abilities for 3D cell encapsulation and stable mechanical properties to mimic native cell niche.<sup>[211-213]</sup> The most suitable agarose for extrusion-based 3D printing process is low-gelling-temperature agarose, which can be extruded feasibly in liquid state and solidifies rapidly when printed onto a cooling stage.<sup>[214]</sup>

*Decellularized extracellular matrix.* The ECM is a complex biomaterial, secreted by cells, which primarily composed of many types of protein (e.g., collagen, fibronectin, laminin) and show various physical nature depending on the protein types and their complexes.<sup>[215-217]</sup> Removal of cellular components from the ECM leaves the matrix known as decellularized extracellular matrix (dECM). The dECM retains physiological cues to mimic the native microenvironmental niche and can, therefore, preserve a more well-matched biochemical complexity of the native tissue compared with the hydrogels composed of individual ECM components like collagen. Currently, the use of dECM hydrogels has significantly increased in the fields of cancer research, drug or cell delivery, as well as in the TE and RM applications as a new paradigm of biomaterial ink.<sup>[218-221]</sup> Very recently, the applications of state-of-art dECM-based bioinks has been comprehensively reviewed by Kim and Cho.<sup>[222]</sup>

### 2.2.2 Hydrogel Inks Based on Synthetic Polymers

Besides the polymers of biological origin, synthetic polymers represent another class of suitable precursors for generating hydrogel inks. Here again, only a few commonly used synthetic polymers in extrusion-based printing will be discussed below.

*Poly(N-isopropylacrylamide) hydrogel.* Poly(N-isopropylacrylamide) (PNIPAAm) is the most extensively studied synthetic polymer which is thermoresponsive and undergoes a rapid coil-globular phase transition in aqueous solution at a Lower Critical Solution Temperature (LCST) around 32 °C, and thus forms the thermoresponsive PNIPAAm hydrogel.<sup>[223-224]</sup> Such temperature-induced transition is a reversible process, and the

polymer changes between a hydrophilic state below LCST and a hydrophobic state above LCST.<sup>[225]</sup> The LCST of PNIPAAm is very close to human body temperature (37 °C), and can be tuned as desired by incorporating co-monomer units, which therefore make the PNIPAAm-based hydrogels particularly suitable for various biomedical applications and recently has been used as ink material for extrusion-based 3D printing technology.<sup>[226-229]</sup> However, PNIPAAm hydrogels are normally optically turbid and nonbiodegradable. In addition, this stimuli-responsive hydrogels are also an attractive and versatile materials for 4D printing fields, which can adopt different shapes and forms when subjected to different environmental stimuli.<sup>[230-232]</sup>

*Poly(ethylene glycol) hydrogel.* PEG is the most widely used synthetic biomaterial that is approved by FDA.<sup>[233-236]</sup> PEG itself is a very hydrophilic and hydrolytically non-degradable polymer with high solubility in water.<sup>[237]</sup> The mobile, non-ionic and highly hydrated features make PEG exhibit effectively antifouling property to both protein adsorption and cell adhesion and, therefore, is considered currently a gold-standard of synthetic biomaterials, although there is also some dispute among scientist.<sup>[238-241]</sup> Various PEG-based hydrogels with tunable physicochemical and biological properties have attracted considerable attention in TE fields, especially recently utilized after being integrated with the advanced extrusion 3D printing systems.<sup>[98, 242-244]</sup>

*Pluronic F127 hydrogel.* A well-known example of PEG-based polymer is poloxamers, which is a kind of nonionic ABA-type triblock copolymers comprising two flanking hydrophilic PEG blocks (A block) and a thermoresponsive polypropylene glycol (PPG) central block (B block). Within this family, Pluronic F127 (F127, also known as Poloxamer 407)) is of particular interest due to their outstanding reversible thermogelling properties at relatively low temperatures close to room temperature. The gelation mechanism of F127 aqueous solutions has been investigated extensively, and is generally considered based on the intermolecular association of PPG blocks leading to the formation of physically cross-linked micelle structures above the critical micelle temperature and polymer concentration.<sup>[152, 245-247]</sup> F127 are non-toxic FDA approved for use as food

additives and pharmaceutical ingredients.<sup>[248-249]</sup> Because of these features, F127 has been investigated for decades and used for various biomedical applications including drug delivery,<sup>[250-253]</sup> RM,<sup>[254]</sup> and biofabrication.<sup>[255]</sup> It is well known that F127 has a great potential in extrusion-based printing process, and normally requires a thermally controlled nozzle system to solidify the ink when extrusion take place.<sup>[40, 256]</sup> Various spatially well-defined 3D constructs has been printed accurately using F127-based hydrogels.<sup>[49, 254-255, 257]</sup> Additionally, researchers have considered F127 as a sacrificial material (or fugitive ink) or a support material to create vascular networks.<sup>[256, 258-259]</sup> Nevertheless, F127 hydrogel has very poor stability and weak mechanical properties, therefore, chemical modification or blending with other polymers are necessary to improve its physical and mechanical properties. In addition, there are several studies have found issues for the *in vivo* application of F127, especially at a high solution concentration of 30 wt%.<sup>[260-262]</sup> Therefore, there is always needs for the development of more promising synthetic alternatives.

*Poly(2-oxazoline) hydrogel.* POx, combining a high synthetic versatility and good biocompatibility, has long been discussed as promising alternative to the well-established PEG systems.<sup>[239, 263]</sup> Furthermore, it serves as a diverse biomaterial platform for hydrogel preparation, has recently also found applications in the fields of biofabrication, which will be described in detail in the following chapter 2.5.3.

### 2.2.3 Naturally Derived *versus* Synthetic Polymers for 3D Printing

In summary, natural derived polymers possess inherent good cytocompatibility and sometimes bioactivity as well. Therefore, except for using in non-biological 3D printing, natural polymers are more attractive for 3D biological printing and often show positive cell modulation. However, implementation of these materials in biofabrication can also be challenging due to their variable printability, lack of tailorability and generally weak mechanical properties. Although some of these limitations can be overcome by modification of the polymers to enable further crosslinking and stabilization of the

extruded inks, the reproducibility of the 3D constructs printed with natural polymers remains complicated due to their poor purity and large batch-to-batch variations.

Besides natural derived polymers, synthetic polymers are also attractive for printing applications owing to their huge synthetic adaptability regarding to the specific physicochemical properties and lower batch-to-batch variability. In contrast to natural polymers, the printed 3D constructs with high mechanical properties can be easily obtained with hydrogels based on synthetic polymers. Challenges in the use of synthetic polymers often include poor biocompatibility and sometimes toxic degradation products. Particularly when aiming for the biological printing, these materials lacking bioactive molecules provide embedded cells with an inert microenvironment, and thus often resulting in low cell adhesion, migration, and viability. Therefore, bioactive sequences and growth factors are frequently required to be grafted or added to the synthetic hydrogel network to improve the cell viability and modulate the cellular behavior.

#### 2.2.4 Development of Ink Materials - Requirements and Challenges

Despite the great achievements have been made toward fabricating various *in vitro* models and *in vivo* therapeutics, one of the most frequently cited limitation currently in 3D printing field is the lack of available materials, known as (bio)inks, that are not only compatible with the printing process but also can provide the desired printability, mechanical and functional properties.<sup>[11, 45, 50]</sup> Moreover, along with the list of desirable features for printable materials become more specific and complex, creating desired constructs, especially overhangs and tall structures to centimeters, upon deposition of current materials becomes very challenging. Therefore, there is an immense need for further (bio)ink development, with an acute requirement for improved printability.<sup>[11, 18]</sup> For future developments, except a continuous advancement of currently established polymers by post modification, it is also important to develop novel advanced materials to broaden the range of available inks. The requirements and challenges for developing of appropriate ink materials for extrusion-based 3D (bio)printing have been extensively

discussed in some excellent reviews recently.<sup>[20, 45, 50, 52]</sup> In general, the important features of ink material that need to be investigated and optimized are:

(1) suitable gelation mechanisms to facilitate handling and printer deposition with shape fidelity including viscosity, gelation methods and rheological properties;

(2) suitable short-term stability to maintain initial design, ensuring that printed structures do not collapse;

(3) sufficient long-term mechanical stability after post-processing step, and can be chosen based on the required mechanical properties of the construct;

(4) well matched degradation kinetics to the particularly application, and degradation byproducts should be nontoxic;

(5) swelling or contraction characteristics should be considered when designing a construct of particularly size and property;

(6) when aiming at (cell-laden) biological printing purpose, besides the above requirements, materials must be biocompatible for transplantation over the long-term and should not induce undesirable local or systemic responses from the host, and should contribute actively to the biological and functional components of the construct.

## 2.3 Printability Assessment of a Hydrogel (Bio)Ink

The several major aspects need to be considered when developing the hydrogel inks for extrusion-based 3D (bio)printing and assessing of their printability are summarized in **Fig. 2.7**. The several major properties including gelation mechanism, degradation and swelling behavior, biological and mechanical performance are typically carried out and discussed following the well-established standard evaluation methodologies for material science, and therefore are similar from paper to paper. In contrast, the term “printability” is only poorly defined by the literature, and the standard methods allowing a reliable evaluation of printability is still lacking clarity and still needs to be established. Recently, several excellent review articles have summarized the printability assessment methodologies used in the literatures thus far in order to guide the development of new (bio)inks for extrusion-based printing.<sup>[50, 264-269]</sup> Generally, the “printability” describing the degree to which a (bio)ink is suitable for printing is not only related to the behavior of the material when being sheared in the printer nozzle, but also related to the performance and stability after being printed.<sup>[264]</sup>

Hydrogel development for 3D extrusion-based printing			
Gelation mechanism	Degradation & swelling	Biological performance	Mechanical performance
Assessment of ink materials printability			
Rheological requirements	Extrudability	Filament formation	Shape fidelity
flow behavior (viscosity & shear thinning) viscoelastic moduli loss factor yield stress viscoelastic recovery	extrusion force needle types (cylindrical & conical)	filament uniformity filament fusion filament collapse	qualitatively & quantitative evaluation

Fig. 2.7| Hydrogel development for 3D extrusion-based printing, and the printability assessment methodologies for ink materials.

Following the sequence corresponding to the different stages of printing process (pre-, during- and post-printing), the printability assessment currently mainly involves rheology, extrudability, filament formation and shape fidelity evaluations. Firstly, for the printability assessment of a potential ink candidate, it is extremely important to understand and optimize the rheological behavior of the material as it can provide a preliminary prediction for the potential printability based on the key parameters obtained such as flow behavior, yield stress, viscoelastic recovery etc.<sup>[45]</sup> It should be emphasized that any assessments of the cell-free ink may not show the complete picture for the equivalent cell-containing bioink, because cells may have an impact on the rheological properties of mixture.<sup>[270]</sup> Thereafter, further exploring of the printability can be categorized into two main parts. The first one is the behavior of the ink during extrusion, called extrudability, and the second one is its behavior after being printed, named as shape fidelity. In this context, the term shape fidelity, also referred to as printing accuracy, can be used to describe not only the shape retention of single filaments upon extrusion but also of the whole printed construct compared to the original design.<sup>[264]</sup> Since the focus of this dissertation is to develop novel hybrid hydrogel inks and evaluate their printability specifically for extrusion-based 3D printing technology, a detailed introduction with regards to the knowledge of printability evaluation thus far in this community will be given below.

### 2.3.1 Rheological Factors Affecting Printability and Shape Fidelity

Rheology describes both the solid-like elastic (mimic the resting state before and after extrusion) and liquid-like flow (mimic the transition state while passing through the nozzle) behavior of materials under application of an external force.<sup>[45, 271]</sup> Therefore, the rheological properties of a (bio)ink are highly relevant to its printability, and is used as a primary predictor for its printability and shape fidelity.<sup>[266, 272-273]</sup> Several most frequently evaluated key rheological parameters associated with an ideal hydrogel (bio)ink are viscosity, viscoelastic shear moduli (storage or elastic modulus  $G'$  and loss or viscous modulus  $G''$ ), loss factor ( $\tan \delta = G''/G'$ ), linear viscoelastic range (LVER), shear thinning, yield stress or yield point, and viscoelastic recovery after printing.<sup>[266]</sup> Typically,



rheological properties of a pronounced shear-thinning behavior and a rapid viscoelastic recovery with sufficient yield stress are responsible to a high printability and shape fidelity in extrusion printing.

### 2.3.1.1 Viscosity

Viscosity is the resistance of a fluid to flow under the application of stress, and directly influences both the filament formation during printing and the shape fidelity after deposition.<sup>[45, 106]</sup> During printing, an increase in viscosity can allow the formation of a uniform filament rather than a droplet at the needle tip. After deposition, if viscosity is too low, then the material may flow too fast after printing and thus resulting in the deposited strands spread out on the surface. Therefore, the printing fidelity generally increases with increasing viscosity, as a high viscosity impedes both the surface tension-driven droplet formation and the quick collapse of deposited structures.

The main factors determining the viscosity of polymer solution are the molecular weight and concentration.<sup>[271]</sup> For a given ink system, increasing the ink viscosity by increasing the polymer concentration is normally considered a traditional way to improve the ink materials printability. However, (bio)inks with too high of viscosity implies an increase of the applied pressure required for extrusion, and subsequent shear stress placed on the cells which may cause permanent cell damage and death in the bioink.<sup>[274-275]</sup> Additionally, increasing the viscosity by increasing the polymer concentrations can result in a restrictive environments for cell proliferation, migration, and tissue formation.<sup>[276-277]</sup> Therefore, it is important to select this parameter depending on the available printer and intended applications (non-biological or biological printing) to ensure both the easily extrusion, best print fidelity, and some cases high cell viability.

### 2.3.1.2 Shear Thinning

Shear thinning refers to a type of non-Newtonian fluid behavior in which the viscosity decreases as shear rate increases.<sup>[278]</sup> This property is typically desired for materials used in extrusion-based 3D printing as it is related directly to the ease extrusion

of an ink material and a temporary maintenance of the printed shape after extrusion but before secondary crosslinking occur.<sup>[65]</sup> Furthermore, when used for bioprinting process, such shear thinning character can address potential issues with shear stress caused cell death during the fabrication process without the cost of resolution loss, and concurrently prevents cell sedimentation in the ink. However, for this category of (bio)inks, secondary cross linking after printing is typically required to ensure the long-term shape stability of the printed constructs.<sup>[279]</sup>

Shear-thinning can be quantitatively assessed using a rotational rheometer to measure the viscosity under increasing shear rate. One of the most commonly used models is the Ostwald-de Waele model, which is defined as

$$\eta = k \dot{\gamma}^{n-1},$$

where  $\eta$  is viscosity,  $k$  is a constant called consistency index,  $\dot{\gamma}$  is the shear rate, and  $n$  is the shear-thinning index (also referred to as flow index or power-law index sometimes).<sup>[280]</sup> A shear-thinning index  $n < 1$  identifies shear-thinning characters,  $n > 1$  shear thickening characters, whereas  $n = 1$  designates Newtonian fluids. Here, it is important to distinguish the shear thinning and thixotropic materials as there is a very distinct difference between them. Shear thinning is time-independent, whereas thixotropy is not. The latter behavior is unfavorable for the printing process and the shape fidelity and should therefore be excluded during ink design. Because time-dependency of the viscosity profile may render extrusion printing more complex, such as printing parameters of extrusion pressure would need to be continuously adjusted to preserve a constant flow of the material.

### 2.3.1.3 Viscoelastic Moduli and Loss Factor

As mentioned before, the (bio)inks for extrusion printing ideally should display both flow and shape retention properties. While passing through a nozzle, inks should flow smoothly with minimal internal resistance, especially in the presence of cells. After being

deposited, the material properties should be opposite and behave an elastic shape retention property, with immediate buildup of internal forces to resist further flow and deformation. Such property of displaying viscous flow and elastic shape retention is known as viscoelasticity property, and can be described using two parameters: storage (or elastic) modulus  $G'$  and loss (or viscous) modulus  $G''$ . The  $G'$  is a measure of the amount of energy elastically stored during deformation and therefore is associated with elastic shape retention. In contrast, the  $G''$  measures the amount of energy dissipated by the material and therefore is linked to the viscous flow.

The  $G'$  and  $G''$  are typically measured as a function of the frequency and amplitude *via* oscillatory rheology, and from which two other relevant rheological parameters known as the damping factor or loss factor  $\tan \delta$  ( $G''/G'$ ) and the LVER can also be obtained. Corresponding to the ratio between loss and storage modulus, the damping factor  $\tan \delta$  carries information on the balance between the viscous and elastic deformation properties. Small value of  $\tan \delta$  represents a material with a predominant  $G'$  value, that is a more solid-like behavior, resulting in a stable hydrogel. Since  $\tan \delta$  can be measured in a few minutes with scarcely experimental bias, it is normally considered a useful quantitative parameter for quick screening of a (bio)ink. For instance, using gelatin and alginate as model hydrogels, Gao and Gillispie et al. investigated the influence of the loss factor  $\tan \delta$  on the printing outcome and defined a range between 0.25 and 0.45 as excellent compromise between extrusion uniformity and structural integrity.<sup>[281]</sup> In this context, just as the authors mentioned, it should be kept in mind that the suggested values do not necessarily apply to other (bio)inks, i.e., different types of materials may require different parameters.

#### 2.3.1.4 Yield Stress

Besides the elastic modulus  $G'$ , shape retention capability can also be described by the yield stress ( $\tau$ ) or yield point, which represents the minimal stress that must be exceeded to initiate material flow, and is correlated to the crosslinking and entanglements

degree within the ink materials.<sup>[45]</sup> A deposited material with sufficient yield stress will not flow unless the acting forces (including gravity determined by the filament own weight and by the weight of all layers above it, and surface tension) overcome this yield threshold value. Increased yield stress of an ink generally improves filament formation, shape fidelity and stiffness of the final construct. Furthermore, the presence of a yield stress also prevents cell or any additive particles settling in the hydrogel precursor reservoir during printing.

The yield stress can be measured in rotational rheology mode and analyzed by using two tangents, one in the plateau-region of the viscosity where the hydrogel is deformed elastically, and one in the region where the viscosity drops indicating the permanent deformation occurs. In addition, the yield point can also be assessed based on the elastic properties in oscillatory rheology (described in detail in the Chapter 7.1 - equipment and methods of measurement), which is more recommended as the test in rotational rheology mode is subject more easily to instrumental bias. It is important to note that a high viscosity can only delay the collapse of a deposited 3D structure, while the presence of a sufficient yield stress can potentially prevent the flow and collapse of a printed structure.

### 2.3.1.5 Viscoelastic Recovery

The last crucial parameter for achieving high shape fidelity printing of the 3D constructs is the viscoelastic recovery ability, also known as regelation property. After deposition of the (bio)ink onto the collector, the material must solidify rapidly to preserve the shape of the printed construct. Otherwise, the printed strands and 3D objects would not exhibit shape fidelity and probably just spread on the substrate. This viscoelastic recovery property and transition kinetics can be investigated by measuring the recovery of the viscosity<sup>[272]</sup> or the shear moduli<sup>[272, 282]</sup> over time under an alternatively changing shear force. The reversible network is broken at high shear forces during dispensing, and it reforms after the shear forces are removed. Ideally, such transition should be instantaneous and complete recovery over several cycles.

### 2.3.2 Extrudability and Filament Formation

Besides the rheological characterization to predict the printability, further visual screening and quantifying of whether an appropriate continuous uniform linear filament are formed upon extrusion have been proposed as initial steps to assess and identify the optimal printer settings.<sup>[272, 283-284]</sup> The capability to extrude a proper uniform filament is directly associated with the inherent ink properties especially the rheological shear-thinning and shear-recovery behavior. Beyond that, the outcome of a print can be significantly affected by the ink conditions such as concentration, crosslinking degrees, and by the printing conditions such as extrusion force, printing speed, nozzle type (diameter, length, geometry) and nozzle-platform distance.<sup>[275, 281, 285-288]</sup>

As one of the most important components of printability, the capability to extrude a uniform filament has been thoroughly studied and characterized by researchers in different manners, including from categorizing the filament just after extrusion but before deposition (filament drop test into the air) to categorizing and quantifying filament shape upon deposition (by visual observing and measuring the dimensions of printed filaments and compared with the designed one) (**Fig. 2.8**).<sup>[264]</sup> First is the filament drop test by extruding a filament into the air to observe whether discontinuous droplets or continuous filaments is formed. The formed discontinuous droplets upon extrusion will not be able to print a 3D structure. Once a continuous filament can be extruded into the air, the filament state and uniformity upon deposited on a substrate will be investigated and optimized as it plays a major role in the generating of high shape fidelity constructs.<sup>[264, 281, 289]</sup> Any improper-deposition of the filaments, either under-deposition (incomplete printing) or over-deposition (excessive material deposition) of the filaments, will result in an unacceptable printing outcome. At the same time, materials that can only form non-uniform filaments (also referred to as irregular fibers, like bumpy or rough surface) are also deemed unprintable especially for the manufacturing of complex geometries and larger constructs. Because all these extruded inappropriate filaments might deviate from the intended path during printing and, thus resulting in unstable constructs with poor

shape fidelity or even causing the overall print to fail due to the accumulation of such inaccuracies from layer to layer.

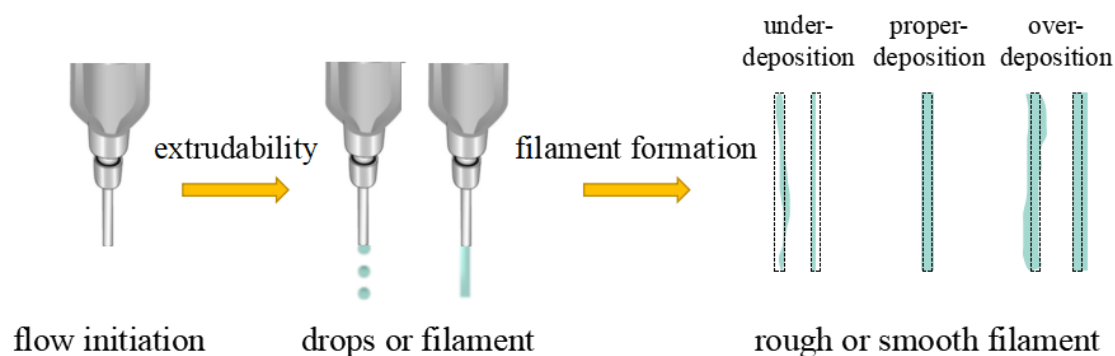


Fig. 2.8| Visual assessment of the extrudability and filament formation of (bio)inks. The dash line represented the design area added for better visualization.

### 2.3.3 Filament Fusion and Filament Collapse

Before further crosslinking step, the printed filaments may display time-dependent creep or collapse due to the limited viscoelasticity properties and tendency to undergo the structural deformations caused by gravity and surface tension, as exemplified by merging of the adjacent filaments or layers.<sup>[166, 266, 290]</sup> Therefore, further assessment methods are introduced and performed in more and more publications, namely the filament fusion testing and the filament collapse testing.

To analyze the filament fusion behavior, a straightforward test was proposed by printing parallel filaments with a stepwise narrowing strand spacing (**Fig. 2.9 a**).<sup>[266, 291]</sup> This test is indicative of the capacity of printing fine details (or referred as printing resolution or printing accuracy) such as small pores or sharp corners. In this meandering pattern, the fused portion of the filament normally starts from the corner of smaller strand space and propagates gradually for decreasing or closing the intra filament spacing of (bio)inks. Thereafter for the filament collapse testing, a commonly used method is by printing a filament over a pillar array with gradually increased gaps distance ( $2L$ ) from 1 to 12 mm, and subsequently measuring the angle ( $\theta$ ) of deflection<sup>[266]</sup> or the area underneath the filament<sup>[283]</sup> to quantify shape fidelity (**Fig. 2.9 b**). Materials that result in a higher sagging or collapsing angle and area are considered to have poorer shape fidelity.

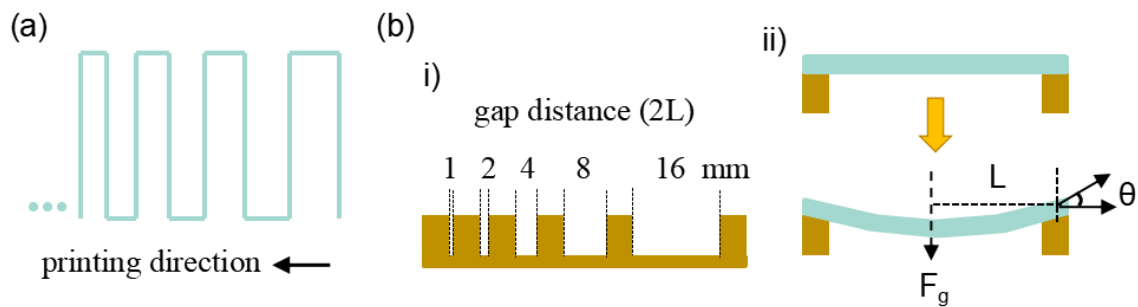


Fig. 2.9| Illustration of the filament fusion (a) and filament collapse (b) tests prior the printing of 3D objects.

Taken together, both the filament fusion and collapse phenomenon are directly linked to the viscoelastic property of a material, more specifically the viscosity and yield stress. Materials which have a higher static viscosity and yield stress possess a better filaments maintenance and, therefore a higher shape fidelity.

### 2.3.4 Shape Fidelity in Printed Structures

Besides the filament fusion and collapse, shape fidelity or geometrical accuracy in the final printed structures is another important aspect of printability evaluation, i.e., the degree of how well the printed features and constructs match their intended design (CAD file) with respect to the size, shape, and location.<sup>[50, 264]</sup> This is typically firstly translates to the image-based analysis of simple structures composed of only 1 or 2 layers, normally a grid pattern (**Fig. 2.10 a**). In the simple x-y planar structures, the filament diameter in terms of width, thickness and circularity are examined across different locations of a printed pattern, and then compared to the original dimensions of the CAD file at the same points directly, or sometimes normalized it further with the needle diameter to obtain an index called spreading ratio.<sup>[292-301]</sup> It is considered that a diameter equal to the designed diameter or a spreading ratio equal to 1 as the most desirable outcome. Particularly, the measured filament diameter at the intersection of two filaments can be considered as an indicator of how well these could be stacked.<sup>[302]</sup> Additionally, researchers have also used the geometry and area of horizontal pores as an outcome measurement and normalized this relative to their design to provide an estimation of the shape fidelity in the x-y plane,

termed as geometric accuracy index.<sup>[50, 53, 288]</sup> In this approach, when a 0-90° laydown pattern is printed, a high geometric accuracy should result in a square or rectangular shape with a printability index equal to 1, while a printability index  $< 1$  or  $> 1$  correspond to a more round or irregular geometry in the x-y plane. Finally, the total area occupied by the whole construct viewed from above rather than the size of its pores,<sup>[303-304]</sup> as well as the total weight of material deposited have also been introduced for printability measurements.<sup>[281]</sup>

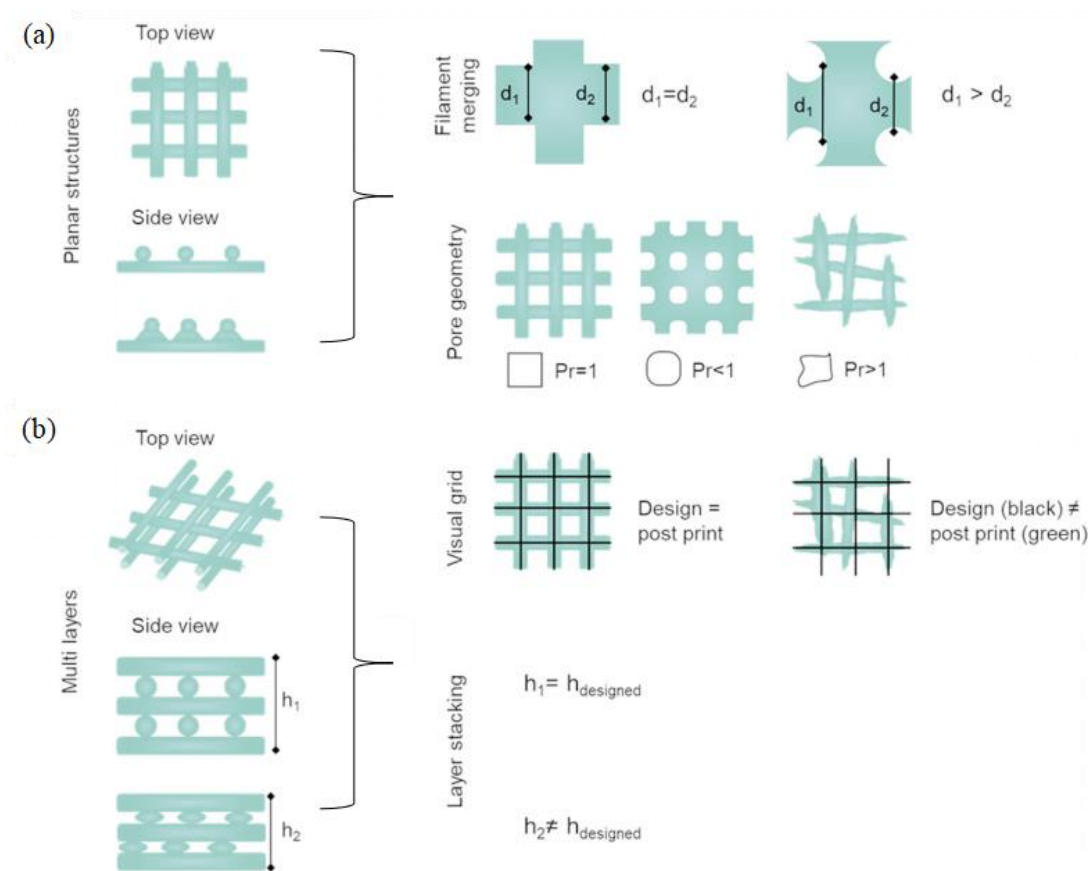


Fig. 2.10| (a) Evaluation in planar structures by measuring the filament diameter and transversal pore geometry. (b) Evaluation in multilayered constructs by measuring the pore geometry and z-axis height. The visible grid of green lines represents the printed structure, the visible grid of black lines represents the computer designed shape. The layer stacking and shape retention ability in multilayered constructs is analyzed by comparing the height of the computer designed sample to the height of printed one ( $h_1$  and  $h_2$ ). Adapted with permission from <sup>[50]</sup>.

Once a reproducible control over the deposition of filaments in 1-2 layers is realized, the shape fidelity of real 3D constructs with multiple layers will be evaluated (**Fig. 2.10 b**).



In addition to the geometric accuracy assessments mentioned above, another important parameter that can be measured at this point is the maximum height reached of a print, also known as layer stacking ability.<sup>[50, 281]</sup> The assessment of ink stackability is also based on comparing the measured height of a printed construct with the theoretical designed one. A height less than the design indicates filament merging and/or collapse, while a height equal to the design refers to an optimal layer stacking. Furthermore, to identify the structural integrity or any additional defects and artifacts within a printed construct, CT imaging and optical coherence tomography (OCT) have been utilized as a novel evaluation technology in 3D printing community.<sup>[297, 305-306]</sup>

### 2.3.5 Summary

The approaches described above provide an important insight into the understanding and assessment of printability from filaments, layers to 3D structures when developing a (bio)ink. In summary, rheology characterization and imaging analysis are established as the major methodologies currently for printability predication and assessment after getting a (bio)ink. Firstly, the rheological characteristics, more specifically the shear thinning and viscoelastic recovery properties is considered linking to the ease extrusion and filament formation ability of a given (bio)ink, while the yield stress and viscoelastic modulus is proposed as an indicator of the resistance of a (bio)ink to fusion and sagging or collapse on a short time scale before further crosslinking. Subsequently, filament formation, fusion and collapse tests in simple x-y planer structures followed by the shape fidelity, layer stacking and construct integrity assessments in complex 3D objects can be performed by various image-based analysis to predict and verify the printability of a given (bio)ink. Importantly, except for the intrinsic material properties, the printability of a (bio)ink material is also linked to the actual printing conditions as even an ideal (bio)ink may result in unacceptable printing outcomes under improper printing conditions.

Furthermore, when aiming for the cell-laden biofabrication specifically, the biological performance of the bioink should also be investigated to evaluate the impact of

the materials as well as the printing process on cell viability and functions, since optimization of the biological properties may likely require an iterative optimization of the ink materials or printing process.<sup>[50]</sup> Last but certainly not the least, the impact of time-dependent effects post printing process, especially in the cases that the construct geometry changes over time in response to specific stimuli (e.g., the hydrogel swelling or shrinking, termed 4D printing), should not be overlooked when design a (bio)ink, as this can result in significant deviations from the computer designed shape.<sup>[307-310]</sup> Looking forward, further efforts are always needed to advance a more comprehensive view of printability upon current assessment methodologies, and to standardize these printability measurements between researchers. Because better assessment techniques will lead to a better understanding of the printability and better comparisons between different (bio)inks, which in turn will aid dramatically the development and applications of next generation (bio)inks.

## 2.4 Approaches to Improve Printability

To improve the printability of a given (bio)ink, many approaches have been introduced over the past years (**Fig. 2.11**).<sup>[311-312]</sup> The most common technique for improving control over the printing process of an ink formulation is increasing polymer concentration, however this approach may cause other issues limiting its suitability for bioprinting, for instance an increased requirement on extrusion pressure, and a reduced hydrogel porosity and water content.<sup>[45, 311]</sup> Beyond that, since the main sources of printing artifacts, i.e., the unwanted deformation and thus poor shape fidelity in generated 3D structures, are gravity, surface tension and time-dependent flow behavior of a (bio)ink prior to stabilization, introducing strategies to refine the (bio)ink intrinsic rheological properties to counteract such forces have been a primary motivation in recent researches.

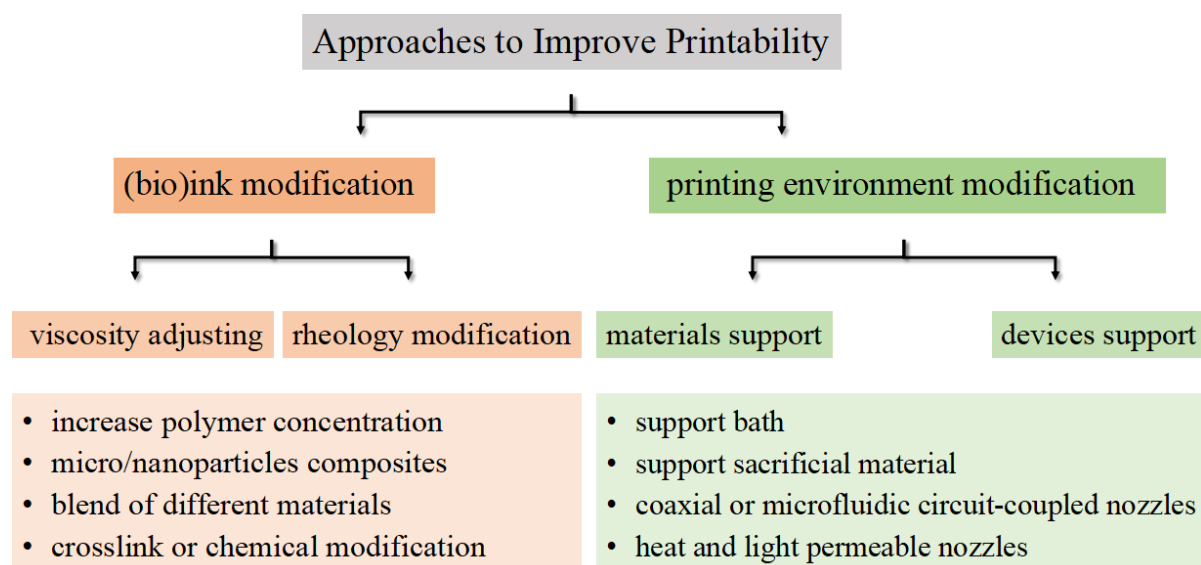


Fig. 2.11 | Approaches to improve printability.

Proposed approaches go from adding viscosity or rheological modifiers (in the form of micro/nanoparticles<sup>[313-314]</sup> or nanofibrous<sup>[315-316]</sup>), blends of different materials,<sup>[317-319]</sup> and pre-crosslinking<sup>[320]</sup> or chemical modification.<sup>[321]</sup> In this context, the clay Laponite, also used in this work, is the most commonly used rheology modifier due to its low cost, chemical resistance and good cytocompatibility.<sup>[322-324]</sup> The Laponite is a kind of synthetic disk-like silicates with a diameter of around 30 nm and a thickness of 1 nm, and can form

aggregates with house-of-cards structures in aqueous solutions due to the negative surface charges and positive charges on the rim.

Besides the above-mentioned approaches by directly modifying the (bio)ink, other introduced approaches are by modifying the surrounding environment in which the printing occurs, or the printer hardware itself to optimize the printability of an ink. For example, the deformation prior to crosslinking can be countered by printing within an environment providing buoyancy, for instance printing into a support bath made of shear thinning polymers, fluidized gels, or granular media.<sup>[282, 325-327]</sup> These methods might enable the printing of (bio)inks with low yield stress and viscosity, which are unprintable with traditional methods. Likewise, sacrificial materials, e.g., thermosensitive hydrogels such as gelatin and poloxamers, can be used to print temporary supports for a (bio)ink, especially when printing complex structures involving overhang geometries or a large size.<sup>[45]</sup> Moreover, in order to accurately control over the (bio)ink deposition and crosslinking kinetics during the printing process, coaxial,<sup>[328-329]</sup> microfluidic circuit-coupled nozzles,<sup>[330]</sup> as well as temperature control and light permeable nozzles<sup>[331-332]</sup> have been designed and used during extrusion. Finally, secondary crosslinking, either physical crosslinking such as thermogelation or chemical crosslinking such as ultraviolet (UV) photopolymerization, is frequently applied during or immediately after the printing process as most of the (bio)inks are too weak to self-supporting for long-terms.<sup>[50, 333]</sup>

To summarize, these proposed approaches have not only successfully improved the printability of existing (bio)inks displaying poor printability, but also substantially expanded the range of suitable (bio)inks for printing which would not be printable when extruded in traditional standard conditions. Further refinement of these methodologies, as well as development of new directions and strategies in (bio)ink design and printability improvement are expected to remain major research topics in biofabrication in the future.

## 2.5 Poly(2-oxazoline)s and Poly(2-oxazine)s

POx can be considered pseudo-polypeptides based on their structural analogy to the naturally occurring polypeptides. It was first synthesized experimentally in the 1960s by four independent research groups,<sup>[334-337]</sup> and subsequently developed as an indirect food additive (poly(2-ethyl-2-oxazoline), PEtOx) on industrial scale in the early 1980s.<sup>[338-339]</sup> Decades later, in 2004, the renewed interest in POx can be traced back to the development of methods for accelerating reaction rates using microwave assisted polymerization.<sup>[340-341]</sup> After that, two very recent important developments on POx that reported by two different research teams are the synthesis of high molar mass, low dispersity polymers,<sup>[342-343]</sup> and the “first in human” clinical trials of a POx-drug conjugate (SER-214).<sup>[344]</sup> These two developments are believed potentially ensuring the continued growth of interests in POx, and promoting its widespread use in the biomedical field.<sup>[339, 345-346]</sup>

### 2.5.1 Synthesis

POx can be synthesized *via* LCROP with a variety of 2-substituted-2-oxazoline monomers (referred to as 2-oxazolines in the following), which thus leads to a variety of physicochemical properties.<sup>[347-348]</sup> The LCROP of 2-oxazolines follows a typical chain-growth polymerization mechanism, *via* three steps including initiation (electrophilic addition), propagation (nucleophilic substitution), and termination with nucleophiles (**Fig. 2.12**). This LCROP route is in general also applicable for the synthesis of polymers poly(2-oxazine)s (POzi), a closely related families of POx, form the corresponding monomers of 2-substituted-2-oxazines (referred to as 2-oxazines in the following). Additionally, 4-substituted and 5-substituted 2-oxazoline monomers are also available for LCROP process, however the reaction rate in chain propagation step slowed down significantly due to steric hindrance.<sup>[349-352]</sup> In the following, each of the polymerization steps, namely the initiation, propagation, and termination, will be discussed in detail further.

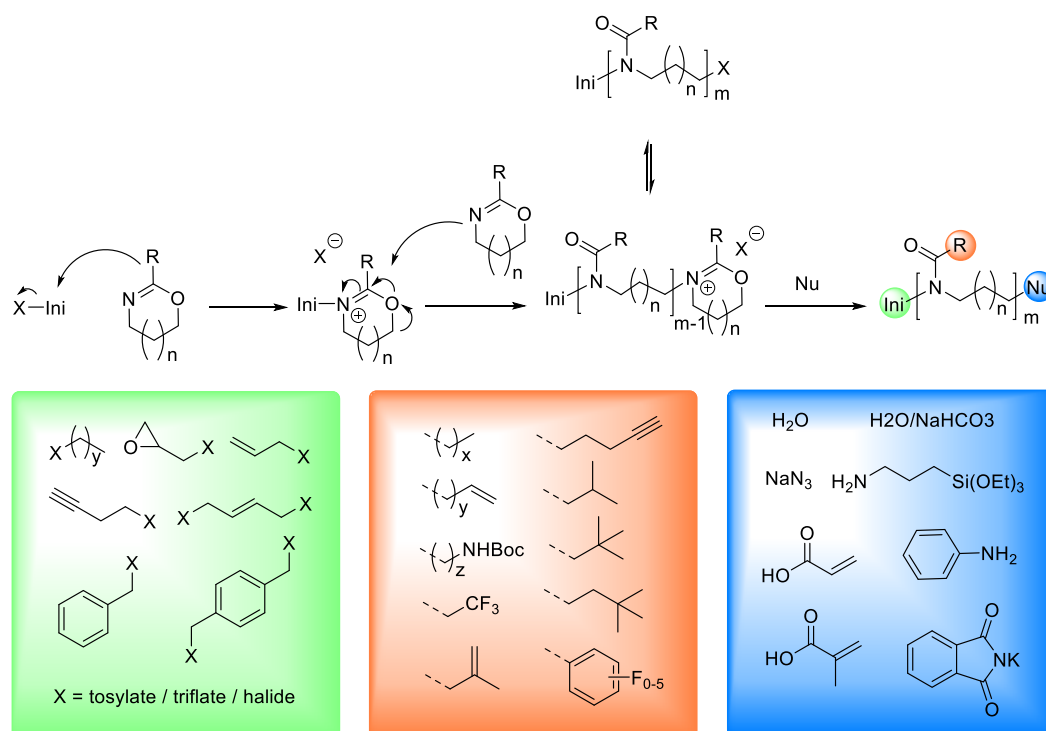


Fig. 2.12| Mechanism of the living cationic ring opening polymerization (LCROP) process of 2-oxazolines ( $n=0$ ) and 2-oxazines ( $n=1$ ), and the well-reported initiators, monomers and terminating agents.

### 2.5.1.1 Initiation

The initiation of LCROP process typically occurs by an exothermic nucleophilic attack of the cyclic imino ether to the electrophilic initiator, and resulting in the formation of an oxazolinium cation.<sup>[353]</sup> The leaving group of initiators acts as the counter ion for the oxazolinium species. As illustrated in **Fig. 2.12**, during initiation, there is an equilibrium between the active, cyclic cationic oxazolinium species and the covalent species depending on the counter ion influences, which plays an important role in the following propagation step. Since an incomplete or slow initiation will lead to a broader molar mass distributions accompanied by higher dispersity, nowadays, the most popular initiators are triflate and tosylate based on their relatively fast initiation.<sup>[354-359]</sup> In addition, one strategy for rapid initiation is using the freshly prepared oxazolinium salts as initiator, which is resonance stabilized species and can be isolated as initiator salt.<sup>[348, 360-361]</sup>

During initiation stage, an  $\alpha$ -end functionality can be introduced into the POx chains by using a functional initiator. It should be kept in mind that the introduction of end-group

functionalities during this stage requires that the functional groups presented in the initiator should not only be compatible with the LCROP of 2-oxazolines and 2-oxazines, but also provide fast initiation to ensure narrow molar mass distributions. Functional groups that are incompatible with the LCROP process might be introduced during initiation by using an appropriate protecting group. By altering the nature of the initiator, POx with various functional  $\alpha$ -end groups such as alkyne,<sup>[362]</sup> amine,<sup>[363]</sup> hydroxyl,<sup>[364]</sup> carboxylic acid<sup>[365]</sup> as well as lipids,<sup>[366-367]</sup> porphyrins<sup>[368]</sup> or saccharides<sup>[369]</sup> have been prepared successfully. Additionally, the initiation step can also be utilized to prepare POx with different architectures such as star-shaped polymers,<sup>[355-356, 370]</sup> and comb copolymers.<sup>[361, 371-373]</sup>

### 2.5.1.2 Propagation

During propagation, the cationic species is responsible for the chain propagation. However, there is an equilibrium between the cationic species and covalent species at any time depending on counter ion and influenced by monomer, solvent, temperature, and concentration (**Fig. 2.12**). In this step, the combination of several different 2-oxazoline monomers into one copolymer result in the multiplicity of possible structures, e.g., statistical (random- or gradient-) copolymers and block copolymers. In addition, after complete monomer consumption, the propagating species can either be terminated or a second monomer can be added exploiting the living cationic nature of the LCROP, which allows the combination of POx and POzi, and enables the direct synthesis of diblock copolymers and multiblock copolymers.

The building block of monomers 2-oxazoline or 2-oxazine for LCROP are either commercially available (**Fig. 2.13**) or accessible *via* synthesis.<sup>[348]</sup> Although the types of commercially available monomers are very limited at present, it is believed that their expansion in the future would strongly promote the development of POx/POzi polymers.<sup>[348]</sup> Apart from this, monomers 2-oxazoline as well as 2-oxazine can be synthesized laboratorial typically from nitriles,<sup>[336]</sup> carboxylic acids,<sup>[374]</sup> aldehydes<sup>[375]</sup> or

from MeOx.<sup>[376-377]</sup> The variation of 2-substitution monomers gives another great possibility to introduce functional groups to POx, such as alkynes and alkenes,<sup>[354, 378]</sup> thiols,<sup>[379-381]</sup> aldehyde moieties,<sup>[377]</sup> amines<sup>[382]</sup> or carboxylic acids groups.<sup>[374]</sup> This functionalization offers a higher degree of freedom in the generation of functional polymers, when the functional group does not influence the polymerization directly if its nucleophilicity is low enough. The number of functional groups per polymer chain is only limited by the degree of polymerization.

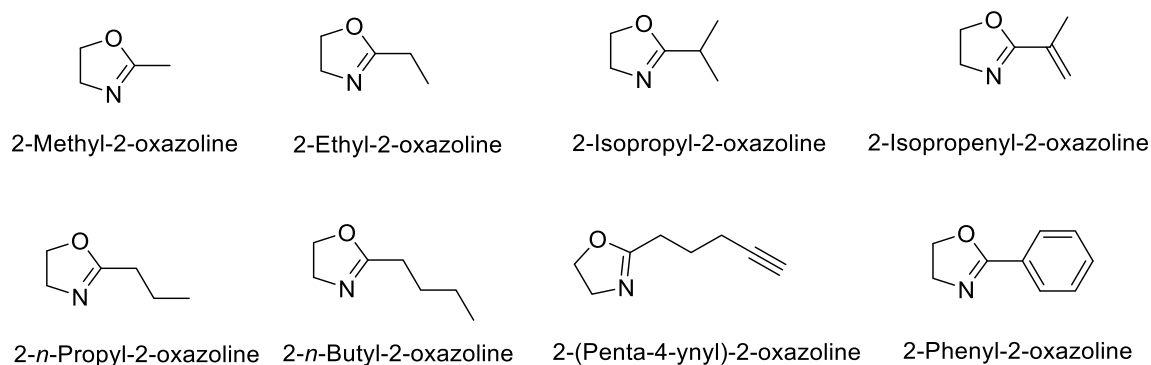


Fig. 2.13| Currently commercially available monofunctionalized 2-substitute-2-oxazoline.

### 2.5.1.3 Termination

In the last step of termination, nucleophiles including water,<sup>[348]</sup> amines,<sup>[383-386]</sup> azides,<sup>[387-388]</sup> acids<sup>[389]</sup> and thiols<sup>[390]</sup> can be utilized as terminating agent for end-capping of the living polymer chain. Likewise, the termination step can also be exploited to introduce various end-functional groups to polymers, which has one major advantage, i.e., the terminator can bear non-compatible/chain transfer LCROP groups as it is only added at the end.

### 2.5.1.4 Summary of the LCROP of 2-oxazolines and 2-oxazines

To summarize, the main advantages of the LCROP of 2-oxazolines and 2-oxazines in terms of synthesis are the high degree of polymerization control with well-defined polymeric structures,<sup>[391]</sup> and the large synthetic versatility with tunable end- and side-group functionalities.<sup>[392]</sup> Nevertheless, the LCROP process is susceptible to some extent of unwanted chain transfer (also referred as  $\beta$ -elimination) and other manners of



uncontrolled termination, especially when aiming at the synthesis of higher molar mass polymers or in the presence of nucleophilic impurities such as water. Therefore, importantly, all chemicals used should be completely dry and extremely pure, otherwise it will lead to an undesired broad molar mass distribution, i.e., high dispersity ( $\mathcal{D}$ ) accompanied by low molar mass impurities.<sup>[392-394]</sup> However, it should be noted that the unwanted chain transfer and termination cannot be suppressed completely in reality. Finally, the LCROP can be further influenced by the solvent, reaction time, temperature and monomer concentration.<sup>[395]</sup>

## 2.5.2 Properties

As described above in the synthesis of POx and POzi, this polymer class enables the synthesis of various functional materials with versatile properties through the variation of monomers and copolymerization of different monomers. Small modification in the side chain or slight elongation of the polymer backbone by only one methylene group per repeat unit will have significant influence on the polymer properties, including the most common studied solubility and thermal properties. Thereupon, such properties of the polymer can be readily tailored simply by the monomer selection and combination according to the needs from specific applications, which is a major advantage for POx and POzi based polymers.

### 2.5.2.1 Aqueous Solubility of Poly(2-oxazoline)s and Poly(2-oxazine)s

The aqueous solubility of POx and POzi strongly depends on the side chain (**Fig. 2.14**). With the shortest methyl, the solubility of poly(2-methyl-2-oxazoline) (PMeOx) is determined by the hydrophilicity of the polyamide backbone, and therefore is highly soluble in water and some of the commonly organic solvents. Increasing the side chain of the polymers leads to a LCST behavior. For PEtOx, values from 60 to 100 °C have been reported.<sup>[396-397]</sup> Further increasing the side chain leads to a further decrease of the LCST until the poly(2-*n*-butyl-2-oxazoline) (P*n*BuOx) which is essentially insoluble in water. Moreover, the cloud point temperature ( $T_{CP}$ ) of the polymer can be varied by changing the

constitution of the side chain as well, for instance the propyl side chain, which is reported of around 25 °C for poly(2-*n*-propyl-2-oxazoline) (P*n*PrOx),<sup>[398]</sup> around 30 °C for poly(2-*cyclo*-propyl-2-oxazoline) (P*c*PrOx),<sup>[399]</sup> and around 40 °C for poly(2-*iso*-propyl-2-oxazoline) (P*i*PrOx).<sup>[399-400]</sup> Here, it is important to take the degree of polymerization (DP), end groups type, as well as the external influences like the presence of salts into account, as they may strongly effect the LCST transition or  $T_{CP}$  of POx.<sup>[401-403]</sup>

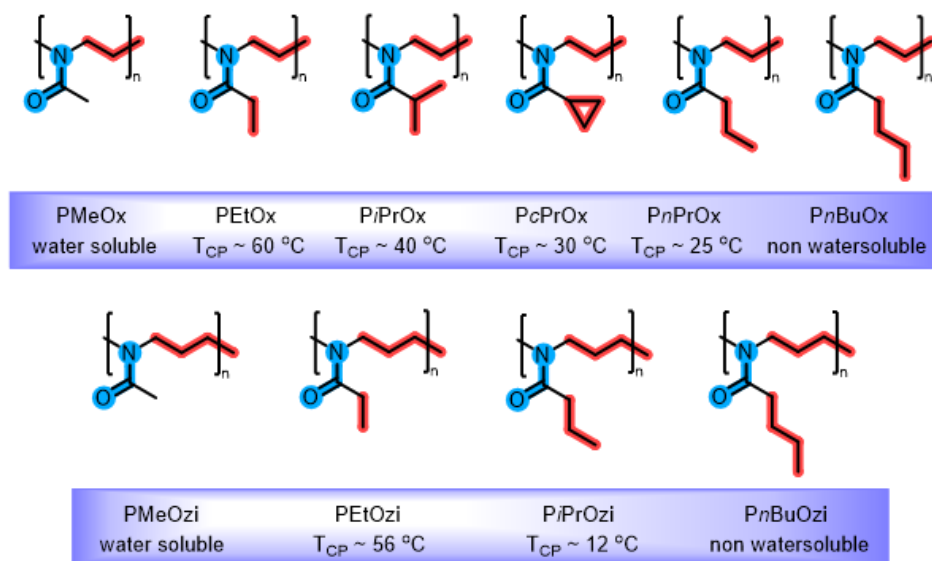


Fig. 2.14| The homologue series of POx and POzi that share the polar amide motif with decreasing water solubility as the 2-alkyl side chain length increases. Polymer with intermediate side chain length display a temperature dependent solubility, namely lower critical solution temperature (LCST) behavior.

Although only very little data is available for POzi, the  $T_{CP}$  of POzi exhibits a similar trend as for POx described above, yet generally lower than that for the corresponding POx (**Fig. 2.14**). For instance, a  $T_{CP}$  of around 56 °C for poly(2-ethyl-2-oxazine) (PEtOzi) and 12 °C for poly(2-*n*-propyl-2-oxazine) (P*n*PrOzi) were reported by Bloksma et al.<sup>[404]</sup> Here the same, poly(2-*n*-butyl-2-oxazine) (P*n*BuOzi) and POzi with longer side-chains appeared completely water insoluble. In addition, benefiting from the LCROP of POx as well as POzi, the solubility of the polymer can be modulated further *via* the copolymerization of different monomers.<sup>[400, 405]</sup> The resulting copolymers are normally amphiphiles, and can self-assemble into aggregates like micelles, cylinders, vesicles or lamellar structures at a critical concentration and temperature in selective solvents.

### 2.5.2.2 Thermal Properties of Poly(2-oxazoline)s and Poly(2-oxazine)s

Regarding the thermal properties, it is well established that POx is thermally stable up to temperatures of  $\sim 300$  °C which is comparable to the PEGs.<sup>[406-408]</sup> For POx of non-branched side chains, the glass transition temperature ( $T_g$ ) decreases almost linearly with increasing chain length due to the increasing flexibility.<sup>[409-410]</sup> The introduction of branched side chains results in completely amorphous POx with low  $T_g$  due to their hindered alignment and resulting decrease in packing density.<sup>[411-412]</sup> Again, the  $T_g$  of the POzi generally follows the trend described for POx, but considerably lower than that for the corresponding POx due to the additional methylene group leads to an increased chain flexibility.

### 2.5.2.3 Cytocompatibility of Poly(2-oxazoline)s and Poly(2-oxazine)s

Except for using as performance materials in the applications like polymer solar cells and thermosensitive fluorescence materials,<sup>[413-414]</sup> most of the research about POx and POzi are focused on the different biomedical applications as biomaterials due to their generally good cytocompatibility.<sup>[239-240, 263, 347, 391, 415-416]</sup> Together with their huge synthetic diversity, these facts make POx a fascinating and promising material platform for biomedical applications, and therefore causing tremendous interest in the studies of POx as PEG substitutes. Compared to PEG, the POx features several advantages such as a higher resistance towards oxidation and a greater diversity of material properties. Although more and more research, either *in vitro* or *in vivo* tests, have been published and confirmed the cytocompatibility of POx-based polymers for biomedical applications, it remains necessary to evaluate these properties systematically for specific POx polymers before the clinical trials.

### 2.5.3 Poly(2-oxazoline)s and Poly(2-oxazine)s Based Hydrogels

Along with the general growing interest in POx and POzi, they have been discussed also a fascinating platform for hydrogel preparation, although the formed hydrogels are mainly brittle due to the inaccessibility of high molar masses or long polymer chains and

the poor chain entanglement. Methods proposed for producing POx and POzi hydrogels were mainly by taking their synthetic advantage of the possibilities to generate functional polymer that can be crosslinked under a variety of conditions. Accordingly, the polymer chains can be crosslinked either covalently or non-covalently, and resulting in chemical or physical hydrogels, respectively. A detailed summary of all works on POx hydrogels has already been provided by some excellent reviews recently,<sup>[339, 417-420]</sup> therefore, only a brief introduction will be given in the following.

### 2.5.3.1 Chemical Hydrogels

Early studies on POx based chemical hydrogels was reported by the group of Saegusa and co-workers in the late 1980s and early 1990s. The authors published a large body of innovative work on POx hydrogels based on several methods: partially hydrolyzing the polymer backbone to introduce functional groups for crosslinking *via* diisocyanate coupling,<sup>[421]</sup> reversible Diels-Alder (DA) reaction of furan and maleimide functionalized polymer side chains,<sup>[422]</sup> photocuring of a pendant coumarin group *via* [2 + 2] cycloaddition,<sup>[423]</sup> disulfide bridge formation of thiol groups,<sup>[380]</sup> and copolymerization between 2-methyl-2-oxazoline (MeOx) and a bis-2-oxazoline.<sup>[424]</sup> Since the work by Saegusa *et al.*, a plethora of chemistry for the preparation of chemical POx-based hydrogels has been described over the past few decades.<sup>[339, 392, 418]</sup>

At present, chemical crosslinked POx-based hydrogels can be subdivided into three major classes (**Fig. 2.15**): (1) hydrogels that are obtained in a one-step reaction using bis/multifunctional monomers; (2) hydrogel prepared *via* the utilization of macromonomers with polymerizable groups; and (3) hydrogels that are fabricated from POx with side- and end-group functionalities and multifunctional cross-linkers. In particular, the side-chain modification is the most common used approach in POx hydrogels preparation, including the use of click thiol-ene coupling chemistry,<sup>[379, 388, 425-428]</sup> and very recently click chemistry of dynamic DA reaction studied again by Nahm *et al.*<sup>[429]</sup> and Hahn *et al.*<sup>[430]</sup>

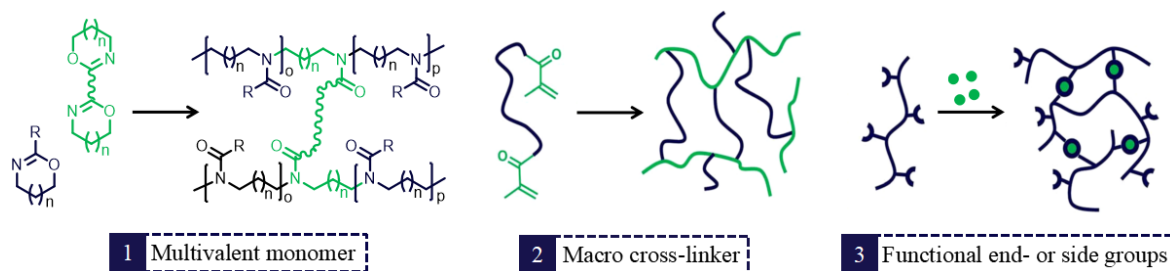


Fig. 2.15| Different strategies to synthesis POx ( $n = 0$ ) or POzi ( $n = 1$ ) based chemical crosslinked hydrogels. Although POzi is mentioned here as well due to the potential transferability of reactions from POx to POzi, no studies on such materials have been reported until today. Reproduced from Ref. <sup>[420]</sup> with permission from the Royal Society of Chemistry.

### 2.5.3.2 Physical Hydrogels

In addition to chemical hydrogels, physical hydrogels, crosslinked in non-covalent way including metal complexation or ionic interactions,<sup>[431-433]</sup> hydrogen bonding<sup>[434-435]</sup> and hydrophobic interactions, have been described as well. For instance, Saegusa and co-workers synthesized a bipyridyl-branched POx and investigated its gelation by means of metal coordination with metal salts like iron (II) sulfate or ruthenium (III).<sup>[431]</sup> Liu et al. synthesized a series of amphiphilic ABA copolymers with a poly(D, L-lactide) segment and two flanking PEO blocks, and observed a sol-gel transition around body temperature.<sup>[436]</sup> Interestingly though, the pure POx/POzi-based systems that exhibit thermogelation behavior in water are rarely reported.

Very recently in 2017, inspired by the synthetic thermogelling Pluronic family, Zahoranova et al. studied various ABA and BAB triblock copolymers based on hydrophilic PMeOx (A) and thermoresponsive PnPrOx (B), but no thermogelation were observed at an investigated temperature range of 10-50 °C.<sup>[437]</sup> Subsequently in the same year, the first solely POx/POzi based thermogelling copolymer that equivalent to thermogelling Pluronic was reported by Lorson *et al.*<sup>[438-439]</sup> They described a thermogelling supramolecular hydrogel of AB-type diblock copolymer comprising hydrophilic PMeOx (A-block) and thermoresponsive PnPrOzi (B-block) as a cytocompatible bioink for 3D bioprinting. In his work, enormous attentions have been paid to the elucidation of the micro- and nanostructure of the hydrogel by using small

angle neutron scattering analysis (SANS), dynamic light scattering (DLS), static light scattering (SLS), and suggested an unusual bi-continuous sponge-like structure of the formed the hydrogels.

Hereafter, a family of POx/POzi copolymer based printable thermogelling platform were described (**Fig. 2.16**), which greatly enriched the current material library suitable for extrusion-based 3D printing. Hoogenboom and Monnery reported thermoresponsive ABA triblock copolymers bearing thermoresponsive outer blocks P*n*PrOx and a more hydrophilic PEtOx inner block that can form hydrogels upon heating an aqueous solution.<sup>[440]</sup> Lübtow *et al.* reported a ABA triblock copolymer features hydrophilic PMeOx A-blocks and a modestly hydrophobic poly(2-*iso*-butyl-2-oxazoline) (PiBuOx) B-block, and investigated the thermogelling capability and printability of the aqueous polymer solutions.<sup>[441]</sup> More recently, Haider *et al.* introduced an alternative in to Lorson's work with the PMeOx block exchanged with a PEtOx block.<sup>[442]</sup> These amphiphiles block copolymers self-assemble into aggregates like micelles, cylinders or vesicles above a critical concentration and above a critical temperature, and thus leading to the gelation. Since the aqueous solution of this class copolymers behave as solid gel when the environment temperature increase above its gelation temperature ( $T_{gel}$ ), they are also referred to systems with LCST phase behavior, and are cataloged as LCST-type thermogelling copolymers. At temperature below LCST, the system is completely miscible (in most cases the solvent is water), whereas above LCST, phase separation occurs and leading to gelation in the specific cases here. Furthermore, such thermogelation process is normally reversible, and behave as flow liquid again under the temperature decrease below to the corresponding  $T_{gel}$ .

In contrast to the LCST-type thermogelling POx/POzi copolymers mentioned above, thermogelling copolymers with UCST behavior, i.e., the so-called UCST-type inverse thermogelling copolymers, have also been reported by Hahn and co-workers. Initially, they reported on a series of ABA-type POx/POzi-based triblock copolymers comprising the same PMeOx as the hydrophilic blocks (A) and aromatic poly(2-phenyl-2-oxazoline)

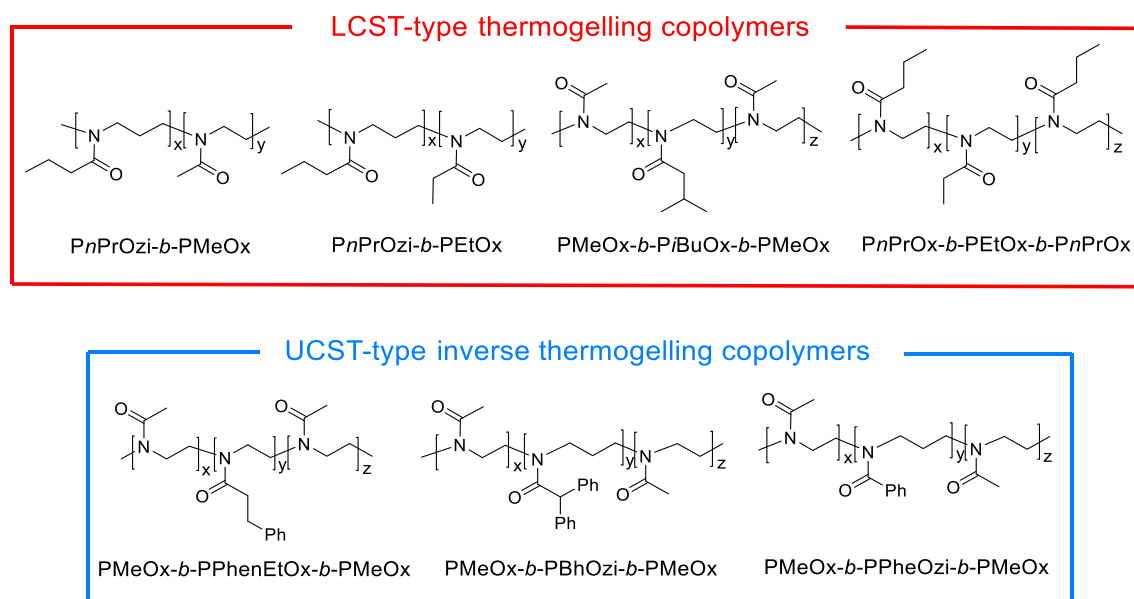


Fig. 2.16| Summary of the representative thermogelable POx/POzi copolymers.

(PPheOx), poly(2-benzyl-2-oxazoline) (PBzOx), poly(2-phenyl-2-oxazine) (PPheOzi), or poly(2-benzyl-2-oxazine) (PBzOzi), respectively, as the hydrophobic block (B). Interesting, only the one with PPheOzi block, i.e., the triblock copolymer PMeOx-*b*-PPheOzi-*b*-PMeOx, exhibits inverse thermogelation at around room temperature at a concentration above 5 wt%, and allows for a significantly improved 3D printability and scaffolds stability after blending with alginate.<sup>[443]</sup> Soon after, Hahn *et al.* introduced another two ABA-type amphiphile triblock copolymer comprising the same PMeOx as the hydrophilic outer A blocks but poly(2-phenethyl-2-oxazoline) (PPhenEtOx) or poly(2-benzhydryl-2-oxazine) (PBhOzi) as the aromatic and hydrophobic central B block that show pronounced thermoresponsive inverse gelation property as well.<sup>[444-445]</sup> In general, all these physical hydrogels, either from LCST-type thermogelling copolymers or UCST-type inverse thermogelling copolymers, exhibited pronounced shear-thinning character and rapid viscoelastic recovery property opening another interesting applications of POx/POzi in the field of biomedical, namely biofabrication.

### 2.5.3.3 Hydrogels for 3D Printing

Benefiting from the great synthetic versatility and good biocompatibility, the POx/POzi-based hydrogel that can be precisely designed with tunable physicochemical

and biological properties was discussed recently a promising ink material for 3D printing technology especially in biofabrication applications.

The POx/POzi chemical hydrogels has been investigated more frequently from an early stage in comparison with the physical hydrogels. However, most of the reported approaches of chemical crosslinked hydrogels are not well-suited for AM technologies. Especially for the most commonly used extrusion-based 3D printing technology, the hydrogels should meet certain criteria with respect to rheological properties, gelation mechanism and kinetics to ensure the desired printability as well as mechanical property. In contrast, recent research on physically thermogelling POx/POzi copolymers exhibit desirable rheological properties for this purpose, in particular a beneficial combination of highly shear-thinning and rapid (re)gelation properties needed for printing process. However, it is still challenging to print real 3D constructs with the current thermogelling POx/POzi system at this point even at an extremely high copolymer concentration due to the remain suboptimal rheological properties. Furthermore, lack of the printing shape fidelity and long-term stability, as well as the extremely poor mechanical property of the printed constructs are frequently cited as other major drawbacks in this community.

Very recently, a pioneering work carried out under the same time as this work, is by DA reaction modification of the copolymers, Hahn *et al.* developed a new system which can be printed and then chemically cured to achieve the long-term scaffold stability.<sup>[446]</sup> Apart from this work, in general, the 3D (bio)printing study of POx/POzi-based hydrogels in AM especially in the biofabrication fields is still at an early stage. Great efforts are urgently needed to overcome the major limitations suffered by such polymers currently, and to realize more sophisticated printing design. Therefore, this will be the focus of this work, to develop more advanced novel hybrid hydrogel (bio)inks based on POx/POzi specifically for extrusion-based 3D printing technology.



## 3 | Motivation



As a transformative manufacturing technology that emerged in the late 1980s, AM (more commonly referred to as 3D printing) has recently evolved into a powerful biofabrication technology, particularly in the fields of TE and RM. Biofabrication *via* 3D printing is a very promising and rapidly growing approach that allows the rapid fabrication of customized complex 3D functional and cell-laden tissue-like scaffolds with a significantly high freedom in design. The generated scaffolds by 3D printing technology have already been used as *in vitro* models for drug screening and diseased tissue studies, and more importantly, are expected to serve as a potentially alternative to the urgently needed donor organs for transplantation in the future.

Despite the tremendous progress that has been made, there are still major challenges that hamper its further development, in particular the shortage of high-performance printable materials. These materials are called (cell-free) biomaterial inks or (cell-laden) bioinks and serve as a crucial basis for the printing process. In order to realize the printing of complex structures with high shape fidelity and specific functionality, the (bio)inks formulated from either naturally derived or synthetic polymers can only be considered as a potential candidate when the numerous certain requirements have been fulfilled. However, to find an “ideal” combination of all these requirements, i.e., the printability, shape fidelity, gelation behavior, mechanical properties as well as biological performance, in one material is a huge challenge and, therefore remains a major research topic in the field of material science and biofabrication.

In the context of this dissertation, based on the very recently reported and progressively expanding thermogelling POx/POzi copolymers, a series of novel hybrid hydrogel (bio)inks are developed and investigated comprehensively with regards to their suitability for extrusion-based 3D printing applications.

The first step is the synthesis and characterization of the diblock copolymers POx-*b*-POzi, and then to formulate the (bio)inks with these copolymers (**Fig. 3.1**). Here, a total of three different hybrid hydrogel (bio)inks were developed. Initially, aiming to improve the

printability of such copolymers, a hybrid system of Laponite XLG and POx-*b*-POzi was designed. Subsequently, in order to increase the spectrum of properties and potential applications of POx-based hydrogels, a POx-*b*-POzi/poly(N, N-dimethylacrylamide) (PDMAA)/clay hybrid hydrogel system was proposed, which can be chemically cured by free radical polymerization post-fabrication. Finally, to combine the advantages and offset the drawbacks of the individual components of thermogelling POx/POzi copolymers and alginate, a POx-*b*-POzi/alginate (Alg)/clay hybrid hydrogel ink was developed which can be used for the cell-laden printing process. After obtaining a potential (bio)ink, in general, the secondly step is to investigate their critical properties related to the extrusion-based printing process, including rheological properties and printability assessments. After that, the micro-morphology, swelling behavior, printing diversity, as well as the mechanical property and biological performance of the hydrogels (in bulk or after printing) were systemically investigated.

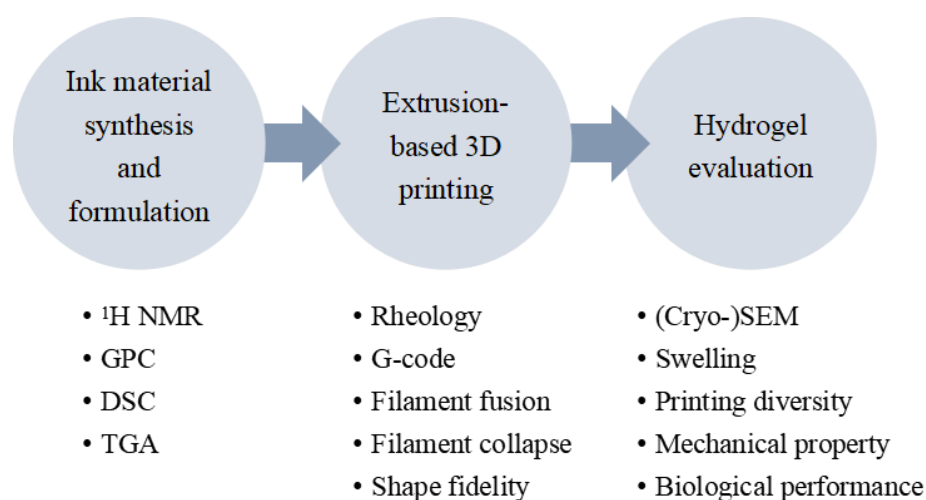


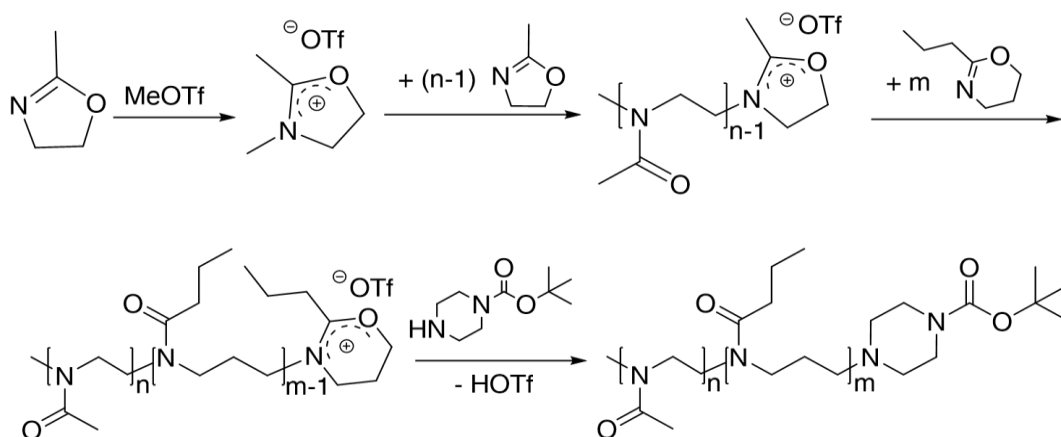
Fig. 3.1| Schematic representation of the workflow of this research.

## 4 | Results and Discussion



## 4.1 Synthesis of Poly(2-oxazoline)-*b*-Poly(2-oxazine) Copolymers

As outlined previously, the aim of the present study was to improve the extrusion-based 3D printability as well as the long-term mechanical property of POx and POzi based thermoresponsive copolymers. Although a small library of POx/POzi based thermogelling copolymers either exhibiting LCST-type or UCST-type thermoresponsive behavior were introduced in recent years, this work was designed and conducted based on an exemplarily diblock copolymer PMeOx-*b*-PnPrOzi, which was reported in 2017 and considered the first solely POx/POzi thermogelation systems.<sup>[447]</sup> Therefore, three batches of amphiphilic and thermoresponsive diblock copolymer comprising a hydrophilic PMeOx block and a thermoresponsive PnPrOzi block with a constant DP of 100-100 were synthesized by LCROP (**Scheme 4.1**). We chose a polymerization degree of 100 for both blocks as this yields a hydrogel with a  $T_{gel}$  at slightly below room temperature, which we deemed favorable for this proof-of-concept. Short block lengths will lead to higher  $T_{gel}$ .



Scheme 4.1| Schematic presentation of one-pot two-stage synthesis of diblock copolymer PMeOx-*b*-PnPrOzi. Methyl trifluoromethylsulfonate (MeOTf) was used as initiator and 1-Boc-piperazine (Boc-Pip) as terminating agent.

In all cases, methyl trifluoromethylsulfonate (MeOTf) was used as initiator and 1-Boc-piperazine (Boc-Pip) as terminating agent. The monomer MeOx was commercially available, and used after distillation. As for the monomer 2-*n*-propyl-2-oxazine (nPrOzi), it was synthesized by an adapted standard procedure,<sup>[448]</sup> and kindly provided by M.Sc.

Lukas Hahn. Since higher temperatures are necessary for the LCROP of 2-oxazines, benzonitrile (PhCN) was chosen as the solvent due to its relatively higher boiling point in comparison with the commonly used solvent acetonitrile (ACN).

Following the optimized conditions for LCROP in our group,<sup>[447, 449]</sup> in total, three batches of the diblock copolymers PMeOx-*b*-PnPrOzi (Batch ID: HUC-01.1, HUC-01.2, HUC-01.3) have been synthesized successively and characterized (**Fig. 4.1**, and **Tab. 4.1**). The proton nuclear magnetic resonance (<sup>1</sup>H NMR) spectroscopy and gel permeation chromatography (GPC) has been utilized to determine the polymer composition and to evaluate the copolymerization. From the signals of chemical shifts around 2.1 ppm attributed to CH<sub>3</sub> of PMeOx (peaks d in **Fig. 4.1**) and around 0.9 ppm attributed to CH<sub>3</sub> of PnPrOzi (peaks g in **Fig. 4.1**) in the <sup>1</sup>H NMR spectrum, the relative block lengths and diblock copolymer composition was determined *via* end group analysis, indicating that the desired diblock copolymer was obtained with reasonable control and definition.

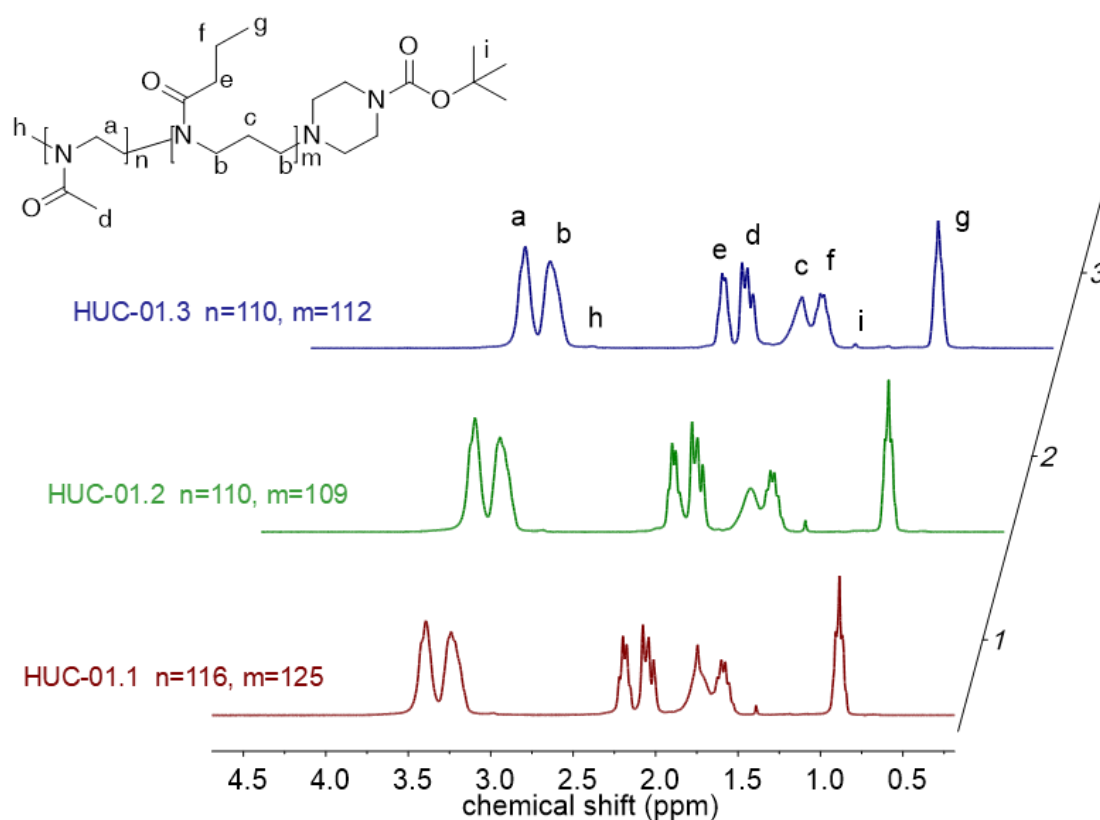


Fig. 4.1| Chemical structure of the synthesized diblock copolymer PMeOx-*b*-PnPrOzi and the corresponding <sup>1</sup>H NMR spectrum (CDCl<sub>3</sub>; 300 MHz; 298 K).



Table 4.1| Polymer composition (PC), molar masses ( $\text{kg mol}^{-1}$ ), and dispersity of the synthesized PMeOx-*b*-PnPrOzi diblock copolymer obtained *via*  $^1\text{H}$  NMR and GPC with HFIP as eluent.

Batch ID	PC, exp <sup>a</sup>	$M_n$ <sup>a</sup>	$M_n$ <sup>b</sup>	$M_w$ <sup>b</sup>	$\mathcal{D}$ <sup>b</sup>
HUC-01.1	Me-PMeOx <sub>116</sub> - <i>b</i> -PnPrOzi <sub>125</sub> -BOC	26	7.7	9.9	1.3
HUC-01.2	Me-PMeOx <sub>110</sub> - <i>b</i> -PnPrOzi <sub>109</sub> -BOC	23	7.3	9.7	1.3
HUC-01.3	Me-PMeOx <sub>110</sub> - <i>b</i> -PnPrOzi <sub>112</sub> -BOC	24	8.5	11.3	1.3

<sup>a</sup> Determined by end-group analysis ( $^1\text{H}$  NMR spectroscopy in  $\text{CDCl}_3$ , 300 MHz, 298 K).

<sup>b</sup> Determined from GPC in HFIP with KTFA (3 g/L) at 313 K and calibrated against PEG standards.

The dispersity  $\mathcal{D}$  ( $M_w/M_n$ ) obtained by GPC analysis is a measure of the distribution of molar mass of a polymer and, therefore directly reflects the control over the polymerization. From the GPC traces of three batches of PMeOx-*b*-PnPrOzi (**Fig. 4.2**), it revealed that the diblock copolymers were synthesized with reasonable control ( $\mathcal{D} = 1.3$ ) and high reproducible (low batch-to-batch variations), which is a crucial aspect in the field of biomaterials research. A slight variation between individual batches is inevitable as the polymerization is a statistical process that can only be controlled to a certain extend.

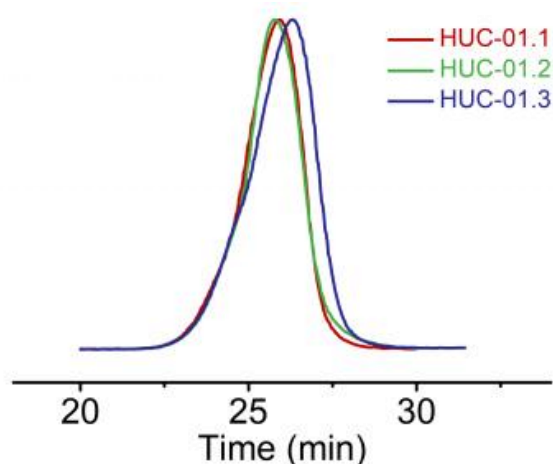


Fig. 4.2| GPC elution profile of the synthesized diblock copolymer.

Additionally, it should be noted that the molar mass determined from GPC is not an absolute value, but is calibrated based on the PEG standards, so it may deviate from the value calculated *via* end group analysis from  $^1\text{H}$  NMR spectroscopy. Of course,  $^1\text{H}$  NMR

does also not directly give the absolute value but through the calibration of the integrals to the signal of the terminator fragment (peaks i in **Fig. 4.1**). This can also easily lead to misinterpretations due to the variations in spectral quality and during integration processing.

## 4.2 Temperature Dependent Rheological Properties of PMeOx-*b*-PnPrOzi Copolymer Solutions

Rheological properties of the copolymer aqueous solutions, as a major strategy and factor for predicting and determining the printability of materials, is one of the most important parts in this research. After obtaining the well-characterized diblock copolymers PMeOx-*b*-PnPrOzi, its rheological properties as well as the influence of the copolymer concentrations on the rheological properties was investigated systematically (**Tab. 4.2**). The influence of block length, end group, monomer type, solvent as well as the synthetic batches on the thermogelling behavior of the copolymer aqueous solutions has been carefully investigated in Lorson's dissertation.<sup>[439]</sup> The study of this part (chapter 4.2) was conducted using the third batch copolymer HUC-01.3.

Table 4.2| The influence of copolymer concentrations on the rheological properties. The rheological data and parameters of PMeOx-*b*-PnPrOzi hydrogels (from 20 to 35 wt %) obtained from temperature sweep, amplitude sweep, frequency sweep, dynamic oscillatory (osc.) stress sweep, and rotational (rot.) steady stress sweep and steady rate sweep experiments.

PMeOx- <i>b</i> -PnPrOzi (wt%)	T <sub>gel</sub> (°C)	G' <sub>gel</sub> (kPa)	LVER (%)	Tanδ	σ <sub>0 (osc.)</sub> (Pa)	σ <sub>0 (rot.)</sub> (Pa)	σ <sub>f (osc.)</sub> (Pa)	n
20	18.8	3.38	1.1	0.066	42.4	67.5	148.1	0.152
25	17.8	4.48	1.8	0.060	219.5	260.7	513.9	0.084
30	12.9	3.59	3.8	0.070	77.9	128.9	232.4	0.001
35	13.2	2.11	6.9	0.147	54.3	62.6	159.8	0.135

First is the thermogelling behavior investigation of the copolymer aqueous solutions. Under oscillation mode, temperature sweeps from 5 to 45 °C were performed on the four group of hydrogel samples with the concentrations ranging from 20 to 35 wt% (**Fig. 4.3 a**). It was found that all the samples showed a relatively sharp sol-gel transition at a certain temperature which is defined as the gelation temperature (T<sub>gel</sub>) that corresponding to the intersection of storage modulus (G') and loss modulus (G''). Comparable with the reported thermogelling behavior for 20 wt% of this solution (T<sub>gel</sub> and G' around 17 °C and 4 kPa,

respectively),<sup>[447]</sup> the  $T_{\text{gel}}$  of the 20 wt% solution (black curve) in this study is 19 °C. After gelation,  $G'$  reaches a plateau at about 3.4 kPa. In the process of this gelation transition, the amphiphilic polymer molecular chain exhibits a temperature-sensitive aggregation behavior, i.e., as the temperature increases, the polymer chains self-assemble into vesicles *via* hydrophobic interaction and molecular chain entanglement, and thus leading to gelation.

With the increasing of polymer concentration, the  $T_{\text{gel}}$  was decreasing gradually and then reached a plateau around 13 °C (**Fig. 4.3 b**). From 20 wt% (the reported required critical polymer concentration for gelation), to 25 wt%, 30 wt%, the corresponding  $T_{\text{gel}}$  decreased from 18.8 °C to 17.8 °C, 12.9 °C. Thereafter, further increasing of the polymer concentration to 35 wt% led no further decrease in the  $T_{\text{gel}}$ , which remained at about 13 °C. On the contrary, in the investigated concentration range, the strength (reflected in the value of  $G'$ ) of the formed hydrogel showed a trend of gradually increasing and then decreasing, along with the increasing of the polymer solution concentration, with a peak value of 4.5 kPa at 25 wt%. This is because after reaching the critical gelation concentration, an increase of the polymer concentration accelerated the self-assembly rate of polymer chains and enhanced the crosslinking density of hydrogel and, thus resulting in

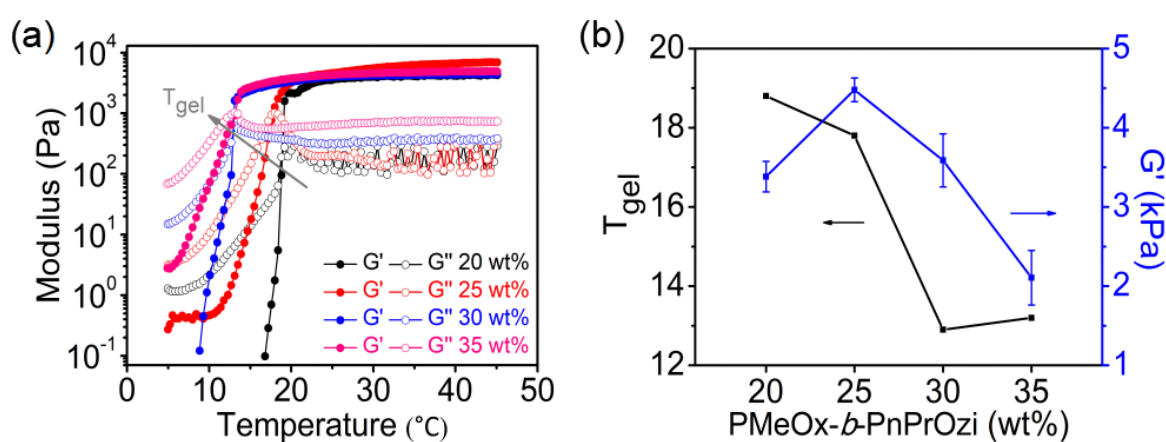


Fig. 4.3| (a) PMeOx-*b*-PnPrOzi copolymer concentration dependent rheology properties of PMeOx-*b*-PnPrOzi hydrogels during temperature sweeps from 5 to 45 °C. (b) PMeOx-*b*-PnPrOzi copolymer concentration dependent  $T_{\text{gel}}$  and the corresponding  $G'$  of the resulting hydrogel obtained from temperature sweeps.

a reduced  $T_{gel}$  and enhanced hydrogel strength. However, further increasing of the polymer concentration excessively led to an extremely viscous solution which we assume that may restrict the flexibility and self-assembly behavior of the polymer chains, and thus resulting in an inhomogeneous hydrogel network, and decreased hydrogel strength ( $G'$ ).

In order to further study the viscoelastic behavior of the samples at various concentrations, a series of rheological tests were conducted. First, at a constant angular frequency of 10 rad/s, amplitude sweeps were carried out to determine the linear viscoelastic range (LVER) of the hydrogels (**Fig. 4.4 a**). It was found that as the polymer concentration increases, the LVER value of the formed hydrogel increases from 1.1% to

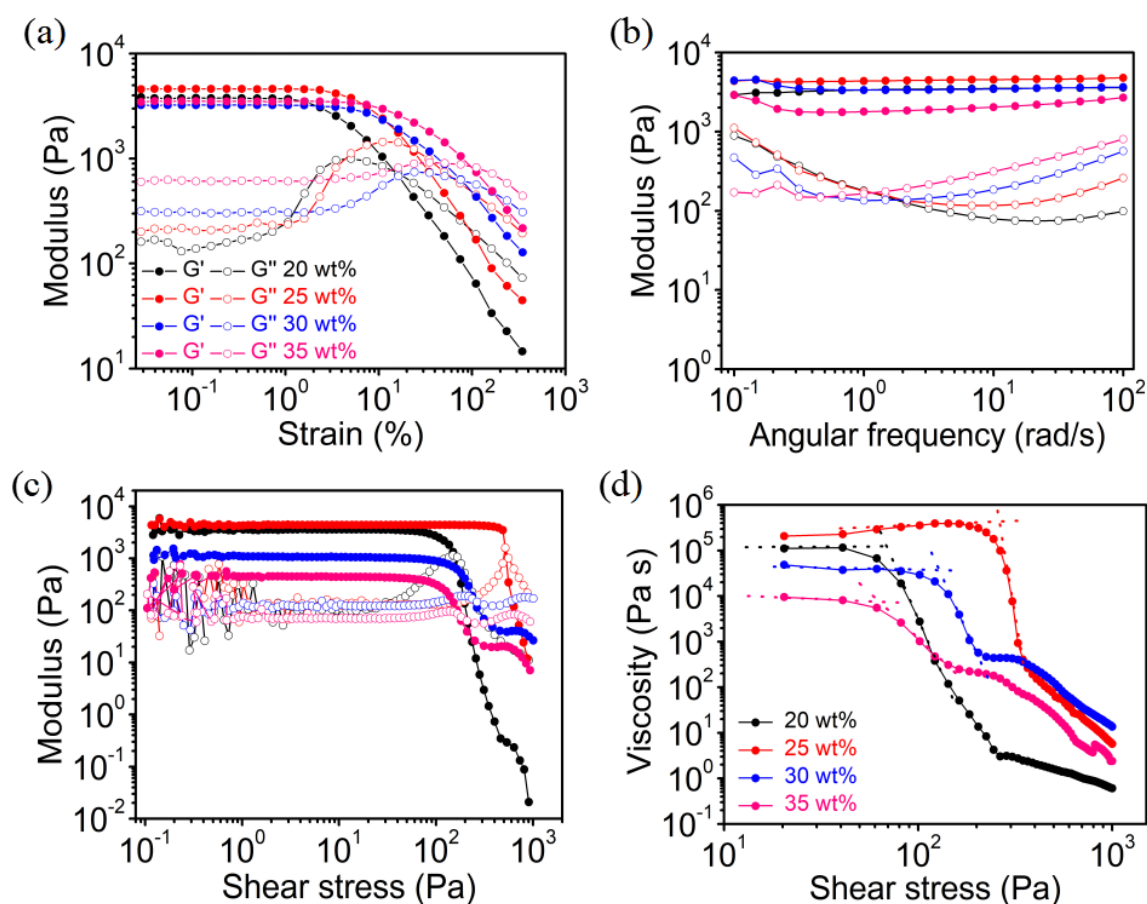


Fig. 4.4| PMeOx-*b*-PnPrOzi copolymer concentration dependent rheology properties of PMeOx-*b*-PnPrOzi hydrogels at 25 °C. (a) Amplitude sweeps at constant angular frequency of 10 rad/s to determine the LVER of the hydrogels. (b) Dependence of  $G'$  and  $G''$  on angular frequency at constant strain of 0.1%. (c) Shear stress-modulus results. (d) Shear stress-viscosity results.

6.9% (**Tab. 4.2**). Subsequently, under a fixed strain of 0.1% (within the LVER), frequency sweeps were performed (**Fig. 4.4 b**). In the investigated angular frequency range, the  $G'$  of hydrogels remained basically stable, and showed a similar changing trend as that observed in temperature sweeps under the variation of concentrations (**Fig. 4.3**). Taking these two factors ( $G'$  and  $G''$ ) into consideration together, the loss factor ( $G''/G' = \tan \delta$ ) is proposed as another systematic approach to assess viscoelastic property of the materials. A lower loss factor ( $G' \gg G''$ ) indicating an elastic dominated character, while a higher loss factor ( $G' \approx G''$ ) indicating a viscosity dominated character. It is obvious that all the formed hydrogels exhibited an elastic dominated character ( $\tan \delta \approx 0.1$ ). Moreover, a considerable increase of the loss factor was observed at 35 wt% meaning an increased viscosity character.

As described above in subchapter 2.3.1, the yield point/stress of the printable hydrogel can be determined in two ways, namely in a shear stress sweep in oscillation mode and in rotation mode, respectively. From the results shown in **Fig. 4.4 c-d** and summarized in **Tab. 4.2**, it was found that the yield stress of the hydrogel first increased and subsequently decreased along with increasing of the polymer concentration, which is in consistence with polymer concentration effect on the hydrogel strength. This again confirmed that hydrogel strength can be improved by increasing the polymer concentration, while further increasing the polymer concentration excessively would lead to an opposite effect. The yield stress obtained from the two methods can both be used as laboratory reference value.

Shear thinning character and recovery properties are two crucial factors for realizing high quality extrusion-based 3D printing. Here, the fluid behavior and recovery performance of samples at different concentrations were studied (**Fig. 4.5**). It was found that all the samples exhibited a pronounced shear thinning (shear thinning index  $n \ll 1$ ) behavior and rapid recovery properties (in the order of seconds). However, from the power-law fitting results of the shear thinning curves (**Tab. 4.2**), as the concentration changes from 20 wt% to 35 wt%, the values of  $n$  first decreased and then increased,

indicating an enhanced and then decreased shear thinning behavior. In addition, the time-dependent recovery test results indicating an excellent recovery property of the materials. Again, not surprisingly, the recovery performance of the material also shows a similar changing that improved firstly and then weakened under the continues polymer concentration increasing.

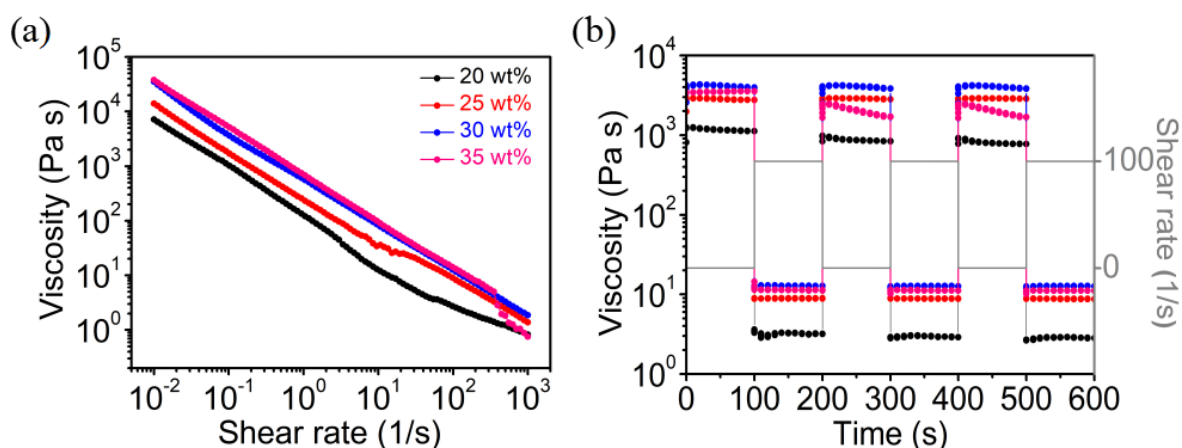


Fig. 4.5| PMeOx-*b*-PnPrOzi copolymer concentration dependent rheology properties of PMeOx-*b*-PnPrOzi hydrogels at 25 °C. (f) Shear thinning behaviors. (g) Recovery properties under the applied shear rate of  $0.1 \text{ s}^{-1}$  and  $100 \text{ s}^{-1}$ .

In summary, although the traditional method of increasing the polymer concentration can be a way to improve the hydrogels printability and strength, such improvement is generally very limited and normally leads to additional undesirable negative effects, such as excessive viscosity and thus more strict requirements on the extrusion process. Especially when used for cell-laden printing purposes, this may lead to damage on cell viability, and restrictions on cell metabolism and other necessary activities during the later cultivation and maturation process. Therefore, there remains a huge demand on developing novel methods and strategies to improve the printed scaffolds shape fidelity and stability of POx/POzi-based thermogelling materials.

### 4.3 Development of Novel Hybrid Hydrogels Based on PMeOx-*b*-PnPrOzi Copolymers

After obtaining the three batches of PMeOx-*b*-PnPrOzi diblock copolymers and the basically investigating of the thermogelling behavior, aiming to improve their extrusion-based 3D printability as well as the long-term mechanical flexibility of the printed scaffolds, three different hybrid hydrogels system based on PMeOx-*b*-PnPrOzi were designed and investigated. Unless otherwise noted, each batch of the diblock copolymer corresponds to each individual hybrid hydrogel system's study, i.e., batch HUC-01.1 for the study of subchapter 4.3.1, batch HUC-01.2 for the study of subchapter 4.3.2, and batch HUC-01.3 for the study of subchapter 4.3.3.

#### 4.3.1 PMeOx-*b*-PnPrOzi/clay Hybrid Hydrogels

In this part, a hybrid hydrogel system of nanoclay Laponite XLG and the thermoresponsive block copolymer PMeOx-*b*-PnPrOzi (named briefly as PMeOx-*b*-PnPrOzi/clay) was described as a novel biomaterial ink, and discussed its critical properties relevant for extrusion-based printing, including viscoelastic properties and printability.

*The work described in this subchapter was already published: “Improving printability of a thermoresponsive hydrogel biomaterial ink by nanoclay addition” by C. Hu; L. Hahn; M. S. Yang; A. Altmann; P. Stahlhut; J. Groll and R. Luxenhofer published recently in Journal of Material Science, 2021, 56, 691–705.<sup>[450]</sup> The text and figures of the following pages 68-86 are may identical with the publication with permission.*

##### 4.3.1.1 Preparation and Characterization of PMeOx-*b*-PnPrOzi/clay Hybrid Hydrogels

The PMeOx-*b*-PnPrOzi/clay hybrid hydrogel was prepared by dissolving the diblock copolymer PMeOx-*b*-PnPrOzi in a 2 wt% clay aqueous solution at 7 °C. After complete



dissolution, the mixture was incubation at room temperature for 10 min to trigger the thermogelation (**Fig. 4.6 a**). Like the pristine copolymer solution that behaves a sol-gel transition above a critical concentration (20 wt%) and temperature ( $T_{gel}$ ),<sup>[441, 447]</sup> the PMeOx-*b*-PnPrOzi/clay mixture shows reversible thermogelation behavior (**Fig. 4.6 b**). The sol-gel transition reverses and the PMeOx-*b*-PnPrOzi/clay gel liquefies again when the temperature drops below the  $T_{gel}$ . Furthermore, this hybrid hydrogel is extrudable and can achieve a *in situ* thermogelation immediately when pipetted into a pre-warmed 37 °C water (**Fig. 4.6 c**).

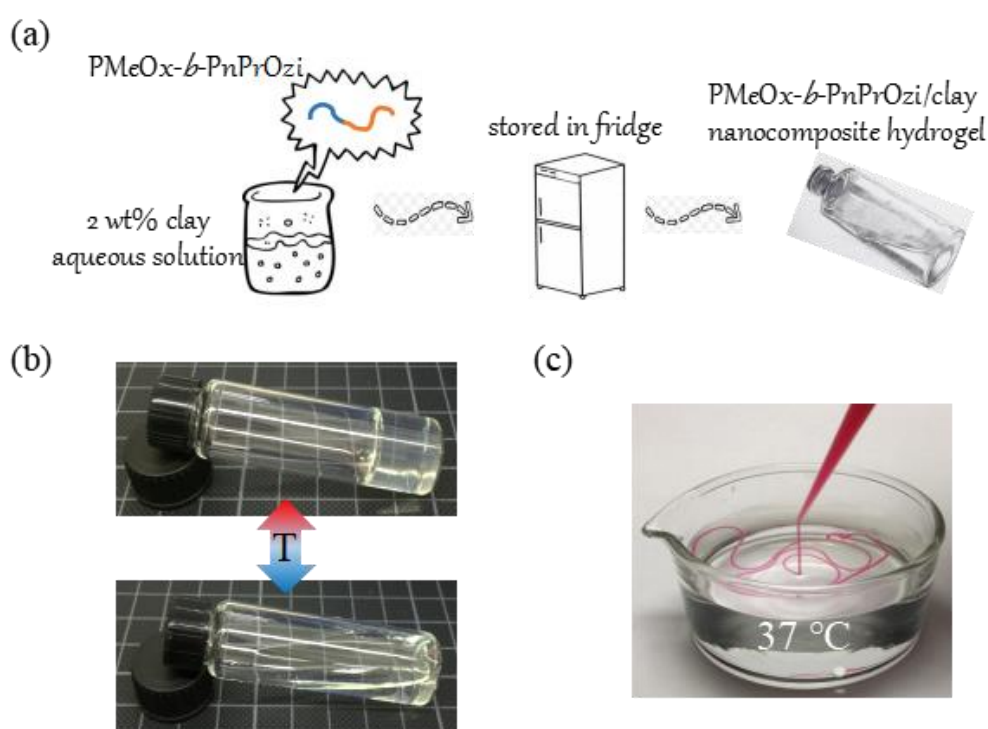


Fig. 4.6| (a) Schematic illustration the preparation of PMeOx-*b*-PnPrOzi/clay hybrid hydrogel. (b) Photographs indicating the thermal reversible sol-gel transition of PMeOx-*b*-PnPrOzi/clay hydrogel. (c) Photograph demonstrating the injectable and *in situ* thermal gelation properties of PMeOx-*b*-PnPrOzi/clay hydrogel (dyed red by carmine).

In the absence of clay, the copolymers self-assemble into spherical vesicles of several 100 nm, and lead macroscopic physical gelation with a sponge-like network above a critical concentration and temperature.<sup>[439, 441]</sup> When comes to the PMeOx-*b*-PnPrOzi/clay hybrid system, we hypothesize that the nanoclay particles interact with copolymer vesicles, probably by adsorbing onto their surface *via* hydrogen bonding. XRD results confirmed

that the copolymer PMeOx-*b*-PnPrOzi interacts strongly with the clay platelets as shown by the disappearance of the typical aggregation peak of clay (**Fig. 4.7 a**). Interestingly, the incorporation of clay into the copolymer matrix did not affect the transparency of gels, which again indicating that the clay particles were dispersed in the gels uniformly (**Fig. 4.7 b**).

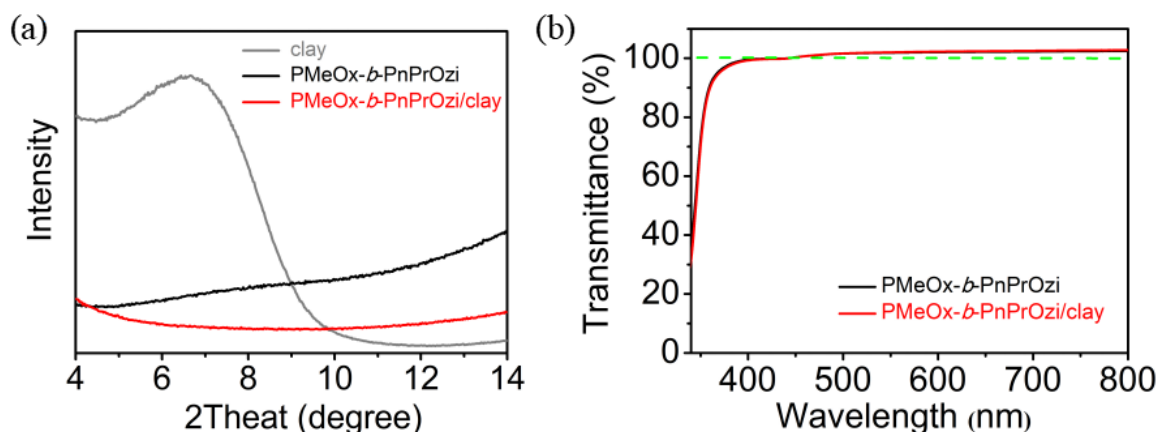


Fig. 4.7| (a) XRD characterization of the samples. (b) Transmittance test of PMeOx-*b*-PnPrOzi and PMeOx-*b*-PnPrOzi/clay hydrogels in the visible range (a green dashed line at 100% transmittance is added for better visibility).

Subsequently, the composition and thermal property of the dried hybrid hydrogels were studied by TGA and DSC analysis (**Fig. 4.8**). As expected, the nanoparticle clay is thermostable and showed only a slightly weight loss from moisture (92 wt% remained at 900 °C) (**Fig. 4.8 a**). In contrast, for both the pure copolymer PMeOx-*b*-PnPrOzi and hybrid system PMeOx-*b*-PnPrOzi/clay, a pronounced weight loss was found from 300 to 700 °C corresponding to the decomposition of the component PMeOx-*b*-PnPrOzi in the hydrogels. The degradation onset was 300 °C and 285 °C, respectively. Although this effect is very minor and might irrelevant for the applications of the hydrogel, it indicates that the clay leads to an earlier thermal degradation of PMeOx-*b*-PnPrOzi copolymer. The residual mass difference at 900 °C reflects the composition of the PMeOx-*b*-PnPrOzi/clay hybrid system. Compared with the PMeOx-*b*-PnPrOzi, an extra residual of 8.5 wt% for PMeOx-*b*-PnPrOzi/clay was observed and attributed to the added clay Laponite XLG, which is comparable to the theoretical composition of clay (8 wt%) in the hybrid system.

The glass transition temperature ( $T_g$ ) is defined as the midpoint of the step in the heating curves. For the block copolymer, two  $T_g$ -values were found due to the (micro)phase separation of the PMeOx block and the PnPrOzi block in bulk (**Fig. 4.8 b**). In the case of PMeOx-*b*-PnPrOzi/clay, a very minor decrease was observed in the first  $T_g$  of PnPrOzi block, while the second  $T_g$  of PMeOx block appears to be attenuated. This might indicate that the added clay preferentially interacts with the hydrophilic block PMeOx.

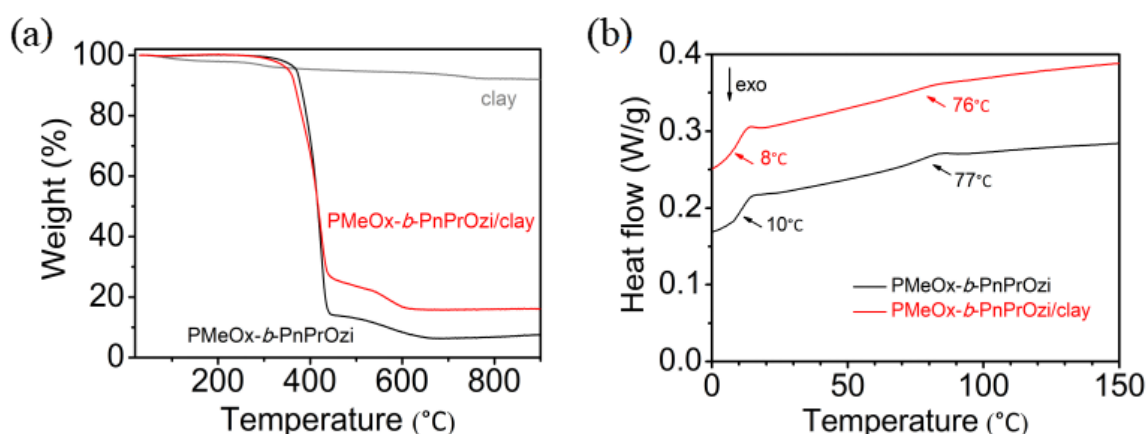


Fig. 4.8| (a) TGA and (b) DSC analysis of the samples.

#### 4.3.1.2 Rheological Properties of PMeOx-*b*-PnPrOzi/clay Hydrogels

Clay Laponite is one of the most widely used rheology modifier for 3D printability improvement of (bio)inks.<sup>[323, 451]</sup> Previously, Laponite RDS has been combined with polymer Pluronic F127 and investigated with regards to the rheological properties. While at a 1 wt% of Laponite RDS addition only slight effects were observed, the  $T_{gel}$  increased and the  $G'$  decreased significantly when 2 wt% and 3 wt% Laponite were added.<sup>[452]</sup> Although the authors did not touch on this aspect, one still can assume that such clay addition would have an influence to the printability of Pluronic F127. To the best of our knowledge, the interaction between POx and clay has not or very less been studied before this contribution. In addition, it is of great interest to understand how clay affects the thermoresponsive rheological properties of copolymer PMeOx-*b*-PnPrOzi. Thereupon, we investigated the rheological behavior of PMeOx-*b*-PnPrOzi/clay hydrogel in detail, to better assess the performance under dynamic printing conditions.

Initially, a 20 wt% PMeOx-*b*-PnPrOzi/clay hydrogel was selected as a representative concentration, with the plain PMeOx-*b*-PnPrOzi hydrogel of same concentration (20 wt%) as control. To analyze the thermogelling property, temperature sweeps were performed by recording  $G'$  and  $G''$  under a dynamic oscillation condition (**Fig. 4.9 a**), in which the intersection of  $G'$  and  $G''$  ( $G' = G''$ ) defines the gelation point and the corresponding temperature as  $T_{\text{gel}}$ . At a low temperature,  $G'' > G'$  indicates a flowable sol state. Along with the temperature increase, both the moduli increase first moderately and then rapidly when close to the  $T_{\text{gel}}$  (15 and 17 °C, respectively), and finally reaching plateau values at around 25 °C. This behavior is consistent with the observations in test-tube inversion tests. Importantly, the plateau extends well beyond the physiological relevant temperature of 37 °C. Compared with the plain PMeOx-*b*-PnPrOzi hydrogel of  $T_{\text{gel}}$  17 °C and  $G'_{\text{max}}$   $3.3 \pm 0.2$  kPa (the values are of around  $T_{\text{gel}}$  18 °C and  $G'_{\text{max}}$  3.4 kPa for batch HUC-01.3 in chapter 4.2, which suggesting a low batch-to-batch variation), the clay added hybrid PMeOx-*b*-PnPrOzi/clay hydrogel exhibits a lower  $T_{\text{gel}}$  of 15 °C and a well enhanced  $G'_{\text{max}}$   $5.3 \pm 0.3$  kPa. Furthermore, a heating-cooling cycle temperature sweep for the PMeOx-*b*-PnPrOzi/clay hybrid hydrogel was performed and revealed a minor hysteresis of 2 °C for the  $T_{\text{gel}}$ , which is attributed to the extra physical interactions between the copolymers and clay in system during the sol-gel transition. Above the  $T_{\text{gel}}$ , the heating and cooling curves overlapped very well, confirming that the transition was completely reversible (**Fig. 4.9 b**).

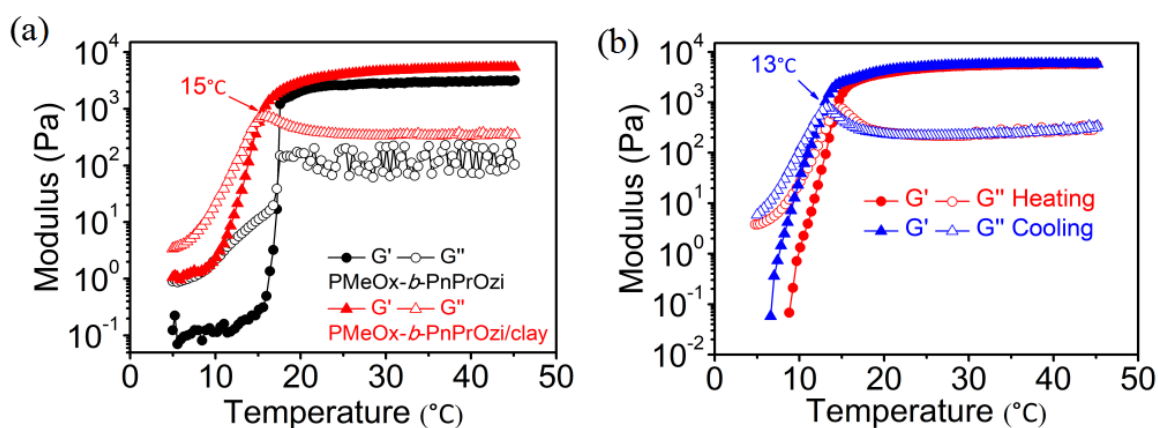


Fig. 4.9| (a) Temperature-dependent rheological properties of the hydrogels. (b) A cyclic temperature sweep of PMeOx-*b*-PnPrOzi/clay hydrogel under a heating/cooling rate of  $0.05 \text{ }^\circ\text{C s}^{-1}$ .

Then, the effect of block copolymer/clay concentrations on the thermogelling properties of PMeOx-*b*-PnPrOzi/clay hydrogels was investigated (**Fig. 4.10 a**). The  $G'_{\max}$  increases with increasing polymer concentration and stabilizes at around 5-6 kPa eventually, meanwhile, the  $T_{\text{gel}}$  decreases along with increasing polymer concentration (**Fig. 4.10 b**). Interesting to note, the critical thermal gelation concentration of the PMeOx-*b*-PnPrOzi/clay hybrid system was decreased to 15 wt% (although the  $T_{\text{gel}}$  for 15 wt% is quite high) from the 20 wt% for plain PMeOx-*b*-PnPrOzi, which is considered beneficial as the additive clay is much cheaper and commercially available compared to the copolymers.

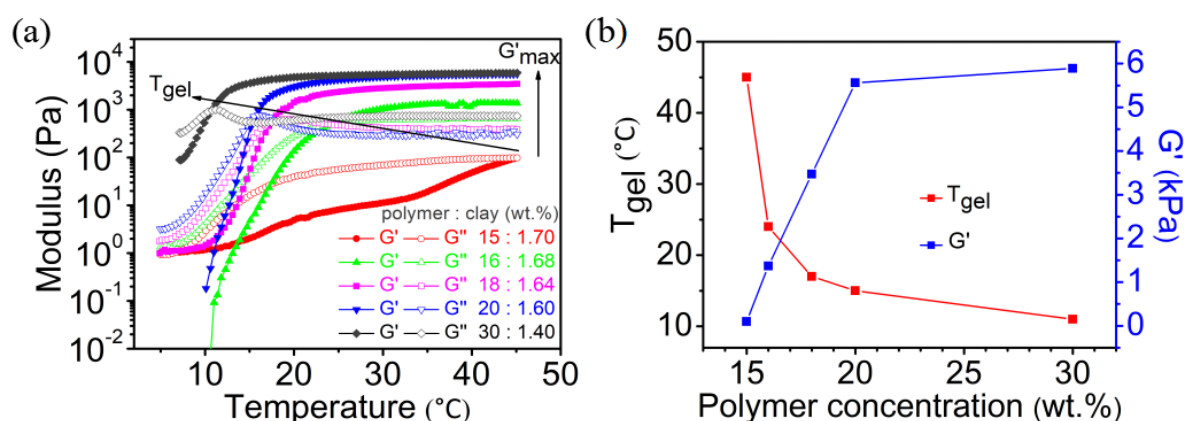


Fig. 4.10| (a) Temperature-dependent rheological properties of PMeOx-*b*-PnPrOzi/clay hydrogels with varying compositions. (b) Composition dependent thermogelation properties of PMeOx-*b*-PnPrOzi/clay hydrogels.

Using the gelatin-alginate as model hydrogels, Gao and Gillispie et al. proposed the loss factor ( $G''/G' = \tan \delta$ ) to assess printability and defined a range between 0.25 and 0.45 as excellent compromise for high printability.<sup>[281]</sup> Accordingly, the loss factor  $\tan \delta$  of the hydrogels in this study were extracted from frequency sweeps (**Tab. 4.3**). It is obvious that 15 wt% PMeOx-*b*-PnPrOzi/clay (with 1.7 wt% clay) hydrogel is more viscous in character ( $\tan \delta \approx 1$ ;  $G' < 0.1$  kPa), though it did form a gel as evidenced by  $G' \geq G''$ . Nevertheless, all the others formed hydrogels show a more elastic character ( $\tan \delta < 0.5$ ), particularly the 20 wt% PMeOx-*b*-PnPrOzi/clay hydrogel with 1.6 wt% clay ( $\tan \delta \approx 0.05$ ;  $G' \approx 5.5$  kPa). In contrast, the  $\tan \delta$  of the pristine 20 wt% PMeOx-*b*-PnPrOzi is slightly lower ( $\approx 0.04$ ). It is obvious that these values lie significantly outside the range suggested

by Gao and Gillispie. Our results suggest that different materials types may require different parameters. Therefore, the search for a universally predictive parameter for good printability is still ongoing.

Table 4.3| The loss factor  $\tan \delta$  of PMeOx-*b*-PnPrOzi/clay hydrogels with varying compositions obtained *via* rheological measurements in oscillatory temperature sweeps mode.

PMeOx- <i>b</i> -PnPrOzi:clay (wt%)	15:1.70	16:1.68	18:1.64	20:1.60	30:1.40
$\tan \delta (G''/G')$	1.0	0.47	0.11	0.05	0.13

The dynamic amplitude sweeps were conducted to determine the LVER, where the plateau of  $G'$  and  $G''$  is referred to as the LVER. Clearly, the apparent LVER for PMeOx-*b*-PnPrOzi/clay hybrid hydrogel (marked as the shaded pink area) extends further than that for the PMeOx-*b*-PnPrOzi hydrogel (marked as the shaded grey area) (**Fig. 4.11 a**), suggesting that the PMeOx-*b*-PnPrOzi/clay hybrid hydrogel is more elastic and stable to oscillating strain. The onset of the  $G'$  decrease and  $G''$  increase indicates that the inner structure of the hydrogels is suffering a damage. Consequently, a strain value of 0.1% (within the LVE range) was selected for the subsequent frequency sweep experiments (**Fig. 4.11 b**). It was found that the  $G'$  was relatively stable and higher than the  $G''$  in the whole investigated frequency range, demonstrating that both PMeOx-*b*-PnPrOzi and PMeOx-*b*-PnPrOzi/clay showed and well maintained the typical gel-phase from low to high shear

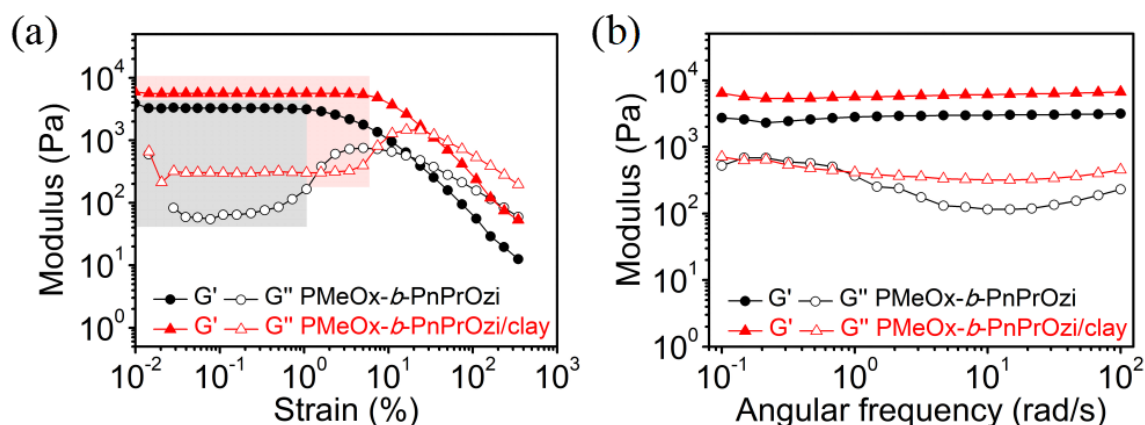


Fig. 4.11| (a) Amplitude sweeps of hydrogels, where the marked grey and pink areas represent the LVE range of PMeOx-*b*-PnPrOzi and PMeOx-*b*-PnPrOzi/clay hydrogels, respectively. (b) Dependence of  $G'$  and  $G''$  on the angular frequency of hydrogels.

frequency. Again, the  $G'$  of the PMeOx-*b*-PnPrOzi/clay hybrid hydrogel is approximately 2 times higher than that of PMeOx-*b*-PnPrOzi, which corroborating the earlier results and supporting the idea of additional physical interaction, i.e., hydrogen bonds between copolymer chains and clay platelets, which contribute to the increase of  $G'$ .

Overall, the rheological analysis performed above shows that the hybrid hydrogel PMeOx-*b*-PnPrOzi/clay has stronger physical crosslinks under dynamic external forces than the pure PMeOx-*b*-PnPrOzi hydrogel. Additionally, both two of the hydrogels exhibited a rapid and essentially reversible transition between sol and gel state (within 10 s), which is confirmed by the structure recovery testing under alternant strains of 0.1% and 100% of 10 times (**Fig. 4.12**).

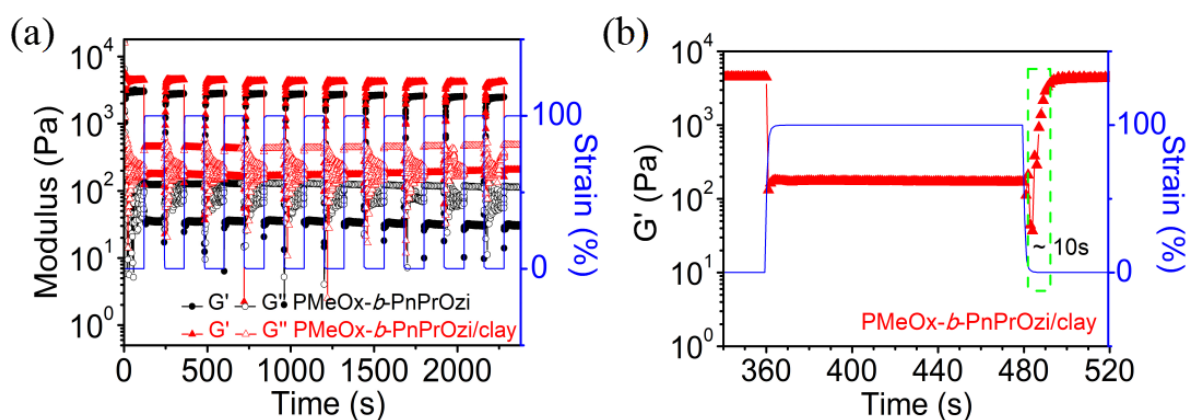


Fig. 4.12| (a) Structure recovery testing for hydrogels under applied alternant strains of 0.1% and 100%. (b) Enlarged  $G'$  curve of PMeOx-*b*-PnPrOzi/clay hydrogel in structure recovery testing results for better visibility of the recovery property. The green dashed frame highlights the time needed for full structure recovery.

In the steady-state flow test, it was obvious that the viscosity of hydrogels decreased markedly with the increasing shear rate, indicating a pronounced shear-thinning behavior (**Fig. 4.13**). The flow index  $n$  and the consistency index  $K$  obtained by power-law expression fitting the shear rate-viscosity profile show that PMeOx-*b*-PnPrOzi/clay hydrogel ( $n = 0.02$ ,  $k = 367.2$ ) has an enhanced shear-thinning property, in comparison with plain PMeOx-*b*-PnPrOzi hydrogel ( $n = 0.11$ ,  $k = 132.8$ ).<sup>[267]</sup> The shear thinning property of plain PMeOx-*b*-PnPrOzi hydrogel prepared from the polymer batch HUC-01.3 in chapter 4.2 is characterized as  $n = 0.15$ ,  $k = 142.7$ , which again suggesting a low batch-

to-batch variation. Furthermore, PMeOx-*b*-PnPrOzi/clay hydrogel exhibited a higher viscosity than PMeOx-*b*-PnPrOzi hydrogel across the entire investigated shear rate range. Such enhanced shear thinning behavior with an increased zero-shear viscosity is considered a desirable feature for printing, as it can facilitate not only the efficient extrusion of the inks, but also a temporary shape maintenance prior to crosslinking due to the rapid viscosity recovery after removing the shear force.

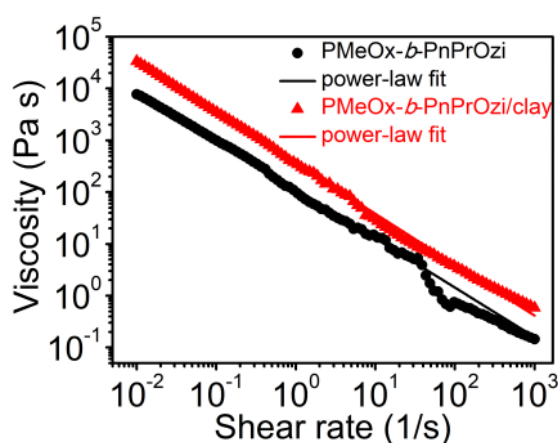


Fig. 4.13| Steady-state flow profile of the hydrogels including power law fit.

Furthermore, the hysteresis loop test was performed by placing the hydrogels to a cycle of increasing and subsequent decreasing shear rate (**Fig. 4.14**). Surprisingly, neither sample showed thixotropic behavior, but rather rheopectic. Although the hysteresis in absolute values of the hybrid hydrogel was more pronounced which can be seen from the

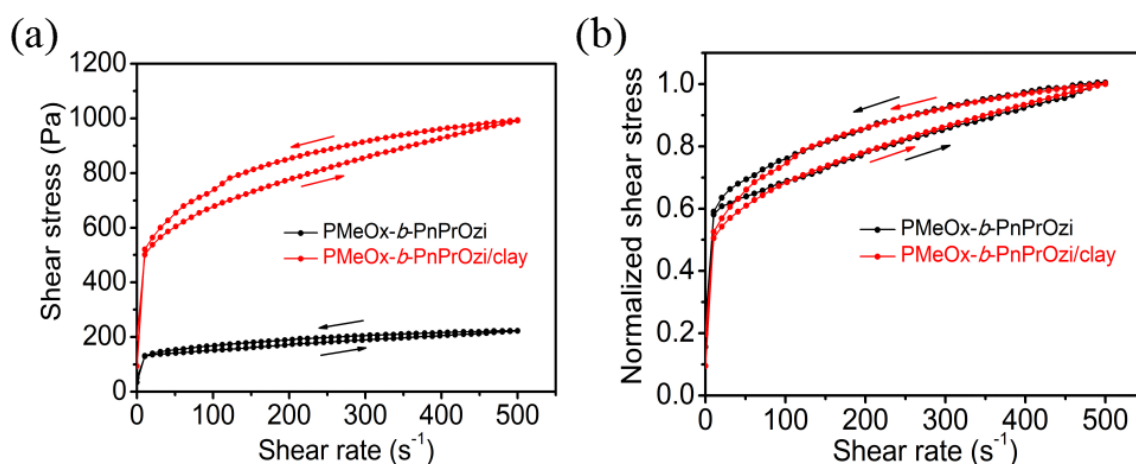


Fig. 4.14| (a) Hysteresis loop tests of PMeOx-*b*-PnPrOzi and PMeOx-*b*-PnPrOzi/clay hydrogels. (b) Normalized hysteresis loops.



much higher shear stress of the hybrid hydrogel (**Fig. 4.14 a**), the relative hysteresis of the both samples was the same, as can be seen readily after the data normalization (**Fig. 4.14 b**).

Yield stress is referred as the minimum stress required for materials to flow. It is a critical parameter to prevent the collapse of structures just being printed and thus achieve high shape fidelity. The steady stress sweeps revealed that the addition of clay enhanced the yield stress of the hybrid hydrogel to around 240 Pa, while that of the pristine PMeOx-*b*-PnPrOzi hydrogel was only 140 Pa (**Fig. 4.15**).

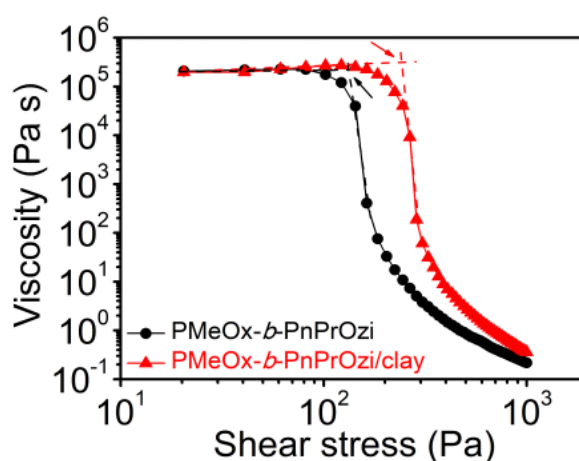


Fig. 4.15| Steady stress sweeps for hydrogels. The intersection of the dashed lines is commonly referred to as the yield stress (arrows).

Finally, the viscosity recovery ability of the materials after extrusion was examined in a rotational rheology mode. Corroborating with the previous elastic recovery test results (**Fig. 4.12**), excellent viscosity recovery that completed within few seconds was observed and still a recovery of over 85% was observed even after ten consecutive cycles (**Fig. 4.16 a**). Although such profound viscosity recovery was observed in both hydrogel samples under the alternant of low ( $0.1 \text{ s}^{-1}$ ) and high ( $100 \text{ s}^{-1}$ ) shear rates (**Fig. 4.16 b**), the PMeOx-*b*-PnPrOzi/clay hybrid hydrogel has a 4.4 times higher quasi-static viscosity ( $\approx 4000 \text{ Pa}\cdot\text{s}$ ) when compared to the pristine ( $\approx 900 \text{ Pa}\cdot\text{s}$ ). This, together with the enhanced yield stress derived above from **Fig. 4.15**, will likely contribute to printability improvement of the PMeOx-*b*-PnPrOzi/clay hybrid hydrogel, and thus achieving a high printing shape fidelity.

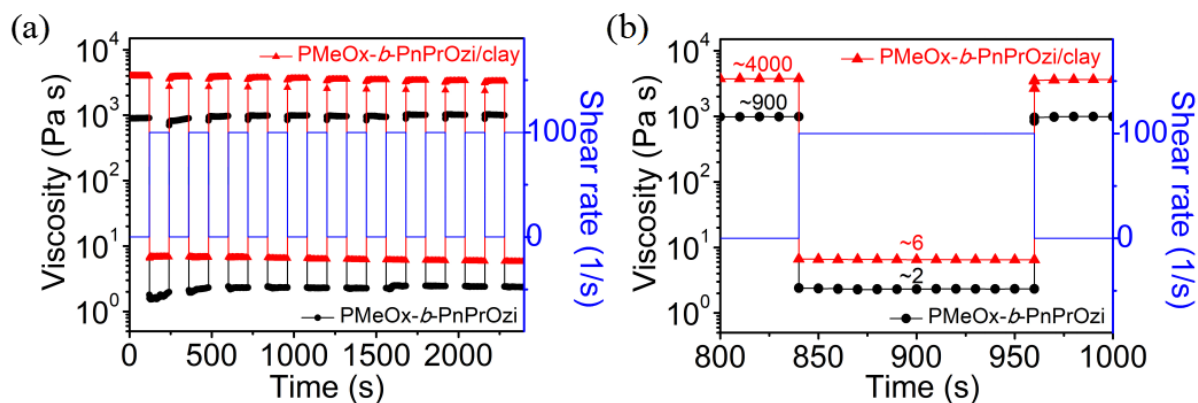


Fig. 4.16| (a) Viscosity recovery with time at alternant shear rates of  $0.1 \text{ s}^{-1}$  and  $100 \text{ s}^{-1}$ . (b) More detailed view of a) for better visibility of the recovery property.

#### 4.3.1.3 Printability of PMeOx-*b*-PnPrOzi/clay Hybrid Hydrogels

After the extensive rheological property analysis, the printability of the hydrogels was evaluated by using a commercially available extrusion-based 3D printer from CELLINK (**Fig. 4.17**). Here, it should be noted that the thermogelling property of this hydrogels is highly beneficial as it will facilitate mixing of the materials and filling of the syringe in the cold, liquid state.

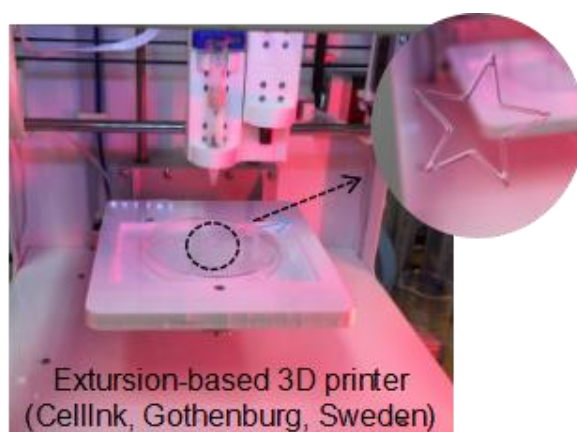


Fig. 4.17| Extrusion-based 3D printer used for printing of the hydrogels.

For 3D printing, initially, a 2D pattern with stepwise increasing filament distances from 0.75 mm to 1 mm, 1.25 mm and 1.5 mm were printed under an extrusion pressure of 110 kPa for strand-fusion assessment. Obviously, the clay addition shows a benefit. When printing with the pristine PMeOx-*b*-PnPrOzi, significant strand fusion was observed at a strand-to-strand distance below 1.25 mm, indicating this is the minimal strand-to-strand

distance can be achieved (red arrows, **Fig. 4.18 a**). In addition, for a planar grid pattern printed with pristine PMeOx-*b*-PnPrOzi, an extreme low-quality printing was observed accompany with fiber fusion at intersections, as indicated by red circles in **Fig. 4.18 b**. In contrast, the same grid was printed successfully without any notable strand fusion when using the hybrid hydrogel PMeOx-*b*-PnPrOzi/clay as ink, i.e., a high shape fidelity with the strands excellently defined. This significant improvement of printing shape fidelity is attributed to the improved rheological properties by addition of clay, specifically the enhanced  $G'$  and yield stress. With a  $\tan \delta$  value 0.05 for the present hybrid hydrogel showing an ideal printability, which clearly outside of the reported range of 0.25 - 0.45 for ideal printing of the gelatin-alginate systems by Gao et al, we therefore can conclude that the value of  $\tan \delta$  alone is not well suited to assess the printability across different materials, i.e., different type of materials may require different parameters.

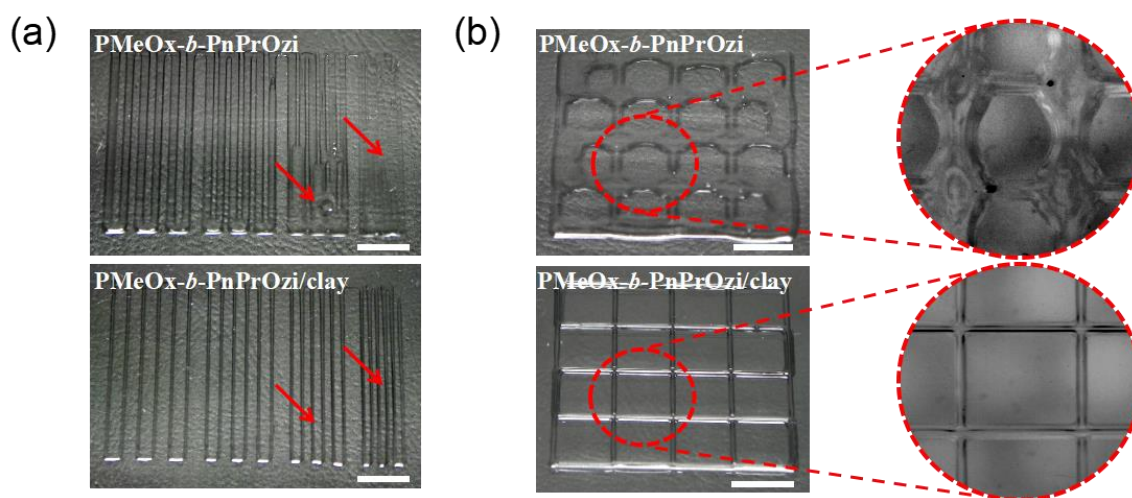


Fig. 4.18| (a) 2D printed patterns for assessing the minimal strand-to-strand distance and strand fusion of the inks (red arrows are guiding for eyes). (b) Optical and stereomicroscopic images of the printed three layers 5 x 5 grid with a base area of  $20 \times 20 \text{ mm}^2$  (amplified in dashed red circles). Scale bars: 5 mm.

Subsequently, the printing versatility of the PMeOx-*b*-PnPrOzi/clay hybrid hydrogel was examined by printing various shapes, including six layers of grid (extrusion pressure 220 kPa), letters “GEL” and a star (extrusion pressure 190 kPa) (**Fig. 4.19 a**). The intersections of grid structure, the resolution of “GEL” and sharp corners of the star are resolved excellently. The printability improvement is obvious when comparing the strands

quality of the hybrid hydrogel ink with the pristine prints (**Fig. 4.19 b**). Moreover, the printing results demonstrate a better self-supporting capability of the hybrid hydrogel, as opposed to the pristine hydrogel (**Fig. 4.19 c**).

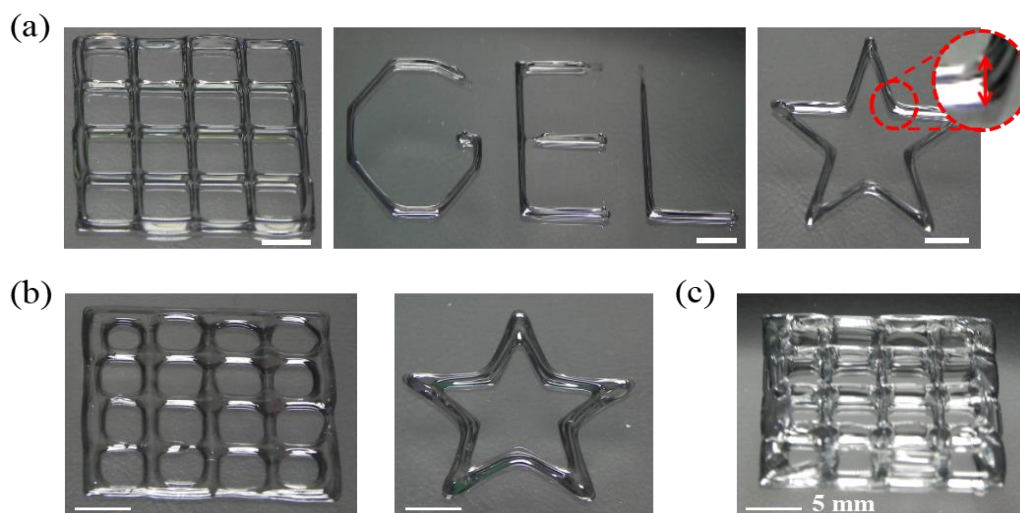


Fig. 4.19| (a) Optical images of 3D printed six layers of a grid, letters “GEL” and a five-pointed star with PMeOx-*b*-PnPrOzi/clay hydrogel. (b) Optical images of the printed six layers grid and a five-pointed star with PMeOx-*b*-PnPrOzi hydrogel. (c) Photograph of a 3D printed 20 layers cube with PMeOx-*b*-PnPrOzi/clay hydrogel. Scale bars: 5 mm.

It is known that clay aqueous dispersions form a house-of-cards microstructure at rest. From the rheological measurements and printability assessment, it is apparent that the addition of clay strengthens the overall rheological property and therefore printability of the hybrid hydrogel. However, how the microstructure is affected remains unclear at the moment. Therefore, we investigated the micromorphology of the clay, pristine copolymer hydrogel and copolymers/clay hybrid hydrogel using the cryo-SEM after flash freezing of the samples in liquid nitrogen slush (**Fig. 4.20**). It is clearly that the house-of-card structure of clay dispersion was confirmed. It can be hypothesized that this structure may

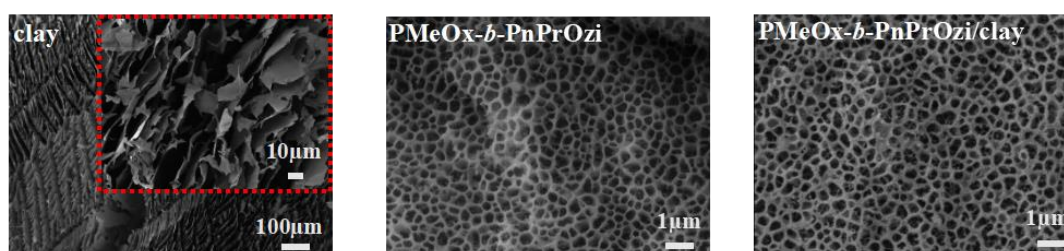


Fig. 4.20| Cryo-SEM images of clay, PMeOx-*b*-PnPrOzi and PMeOx-*b*-PnPrOzi/clay gels.

function as a self-supporting internal scaffold contributing to the rheological and printing performance improvement of the PMeOx-*b*-PnPrOzi/clay hybrid hydrogels. Additionally, no obvious difference was observed between the two hydrogels, i.e., the addition of clay does not seem to have a significant effect on the pore shape and size. Both the pristine PMeOx-*b*-PnPrOzi and hybrid PMeOx-*b*-PnPrOzi/clay hydrogels exhibited a typical hydrogel microstructure with uniform microporous.

#### 4.3.1.4 Clay Influence on The Printing Window of PMeOx-*b*-PnPrOzi/clay Hybrid Hydrogels

The clay mineral Laponite is the most widely investigated nanofillers that was first reported by Haraguchi et al. as a multifunctional crosslinker to form nanocomposite (NC) hydrogel.<sup>[453-454]</sup> Nowadays, it has been used as rheology modifier for improving the printability of materials, especially in the extrusion-based 3D printing community.<sup>[455-458]</sup> They can form aggregates with house-of-cards structures in aqueous solutions due to the negative surface charges and positive charges on the rim, and forming gels above a critical concentration (**Fig. 4.21**). However, the gelation of pure clay is time-consuming, and normally results in extremely weak gels ( $G'$  of only around 100 Pa for 2 wt% clay). Therefore, clay is commonly used as reinforcing additives to improve mechanical strength, biological effects as well as the printability of materials, rather using or printing directly. Here, its improvement to the printability, as pioneered recently by Gelinsky and Huang groups, is of particular interest for the present purpose.

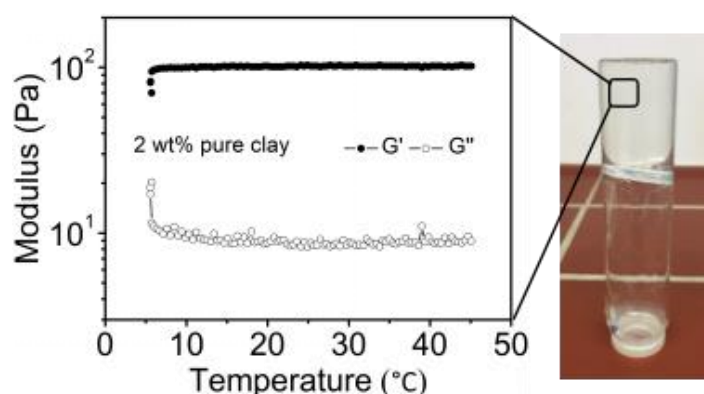


Fig. 4.21| Gelation performance of pure clay aqueous solution.

Again, a systematic rheological study was conducted to investigate the effect of clay addition on the hydrogel properties (Tab. 4.4). Under a constant diblock copolymer PMeOx-*b*-PnPrOzi (also known as POx-*b*-POzi) concentration of 20 wt%, the thermogelling performance of the hydrogels with a various clay concentration from 1 to 4 wt% was studied, and compared with the pristine 20 wt% hydrogel (Fig. 4.22). From the temperature sweeps, it was found that as the clay concentration increases, the thermogelation transition temperature ( $T_{gel}$ ) of the nanocomposites decreases gradually, from  $\sim 19$  °C of the pristine 20 wt% hydrogel to  $\sim 11$  °C of the nanocomposites with 4 wt% clay. Meanwhile, the elastic strength ( $G'$ ) of the hydrogel increased to over 8.4 kPa, which is about twice the strength of the pristine 20 wt% PMeOx-*b*-PnPrOzi hydrogel.

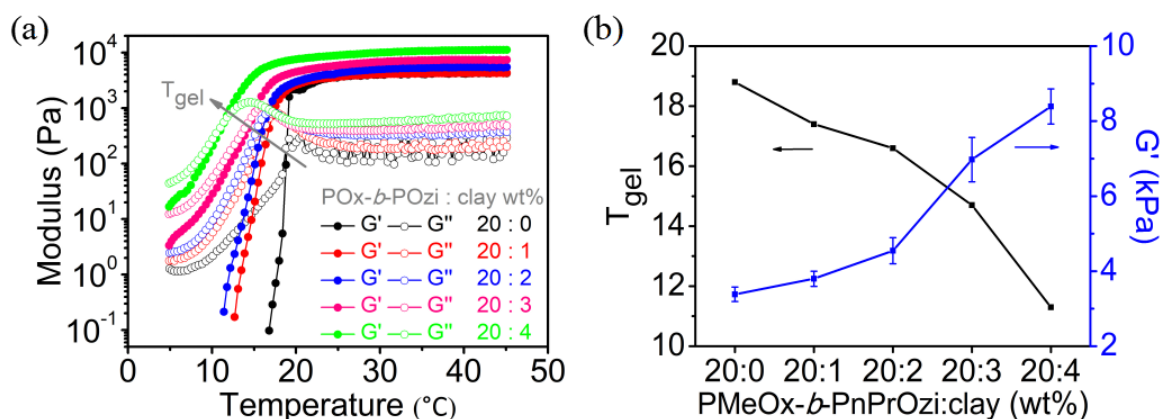


Fig. 4.22| Clay concentration dependent rheology properties of PMeOx-*b*-PnPrOzi/clay hydrogels. (a) Temperature sweeps from 5 to 45 °C. (b) Clay concentration dependent  $T_{gel}$  of the hydrogels, and the corresponding  $G'$  obtained from frequency sweeps at 25 °C.

Table 4.4| Summary of rheological data and parameters of PMeOx-*b*-PnPrOzi/clay hydrogels (20/0 to 20/4 wt%) obtained from temperature sweep, amplitude sweep, frequency sweep, dynamic oscillatory stress sweep, steady stress sweep, and steady rate sweep experiments. “nd” means no value was obtained due to the limit in dynamic oscillatory stress sweeps.

PMeOx- <i>b</i> -PnPrOzi/clay (wt%)	$T_{gel}$ (°C)	$G'_{gel}$ (kPa)	LVER (%)	Tan $\delta$	$\sigma_{0 (osc.)}$ (Pa)	$\sigma_{0 (rot.)}$ (Pa)	$\sigma_{f (rot.)}$ (Pa)	n
20/0	18.8	3.38	1.1	0.066	42.4	65.8	148.1	0.152
20/1	17.4	3.80	1.9	0.064	134.7	145.8	271.1	0.043
20/2	16.6	4.55	3.4	0.089	265.8	275.0	504.5	0.081
20/3	14.7	6.98	3.9	0.096	353.2	362.6	674.5	0.064
20/4	11.3	8.39	5.5	0.066	478.5	433.7	nd	0.069

The amplitude and angular frequency sweep results of the hydrogels are shown in **Fig. 4.23 a-b**, and summarized in **Tab. 4.4**. Both the LVER and strength ( $G'$ ) of the hydrogel increase with the increasing amount of clay doping. Then the yield point of each sample was determined by two established testing programs (**Fig. 4.23 c-d**, and **Tab. 4.4**). Not surprisingly, the yield stress of the hydrogel increases with increasing amount of clay addition. More importantly, this enhancement effect by clay addition is much more pronounced than that by increasing the copolymer concentration (**Tab. 4.2**), which indicate that the composite with clay would be a better alternative method to improve the printability and strength of the hydrogel.

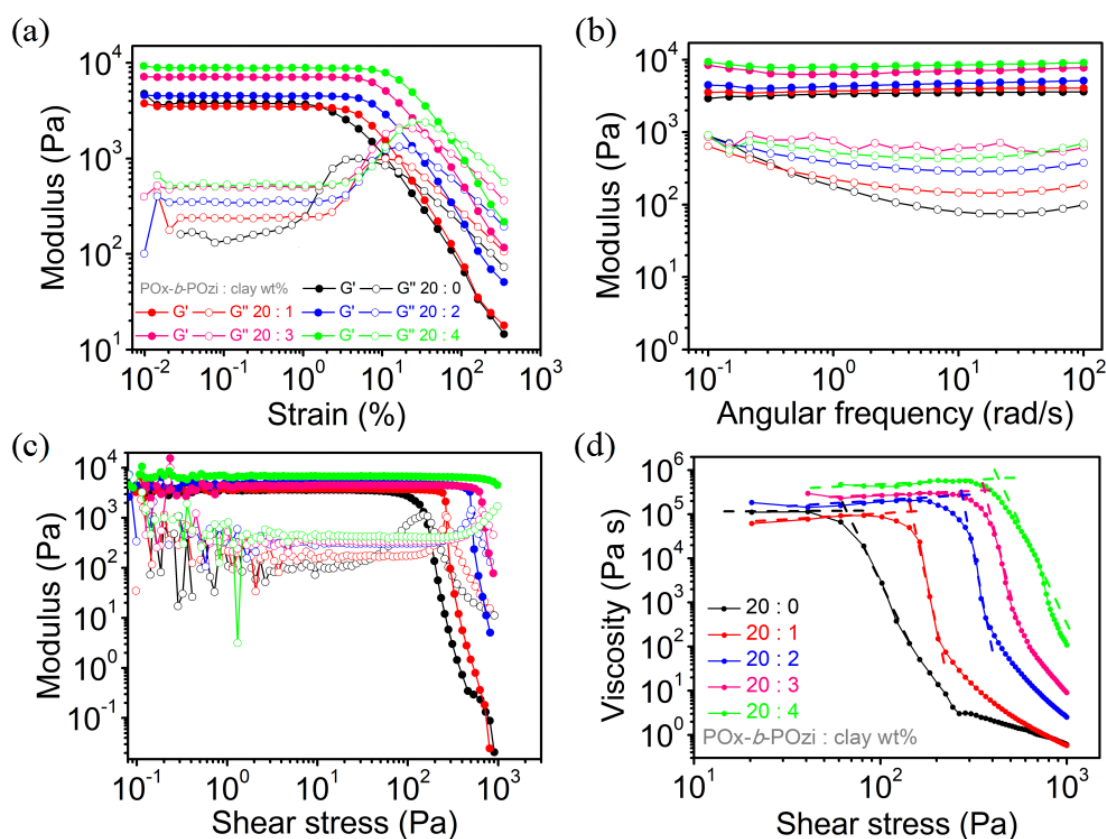


Fig. 4.23| (a) Amplitude sweeps at constant angular frequency of 10 rad/s to determine the LVE range of the hydrogels. (b) Dependence of  $G'$  and  $G''$  on angular frequency at constant strain of 0.1%. (c) Shear stress-modulus results. (d) Shear stress-viscosity results.

Subsequently, the shear thinning and recovery properties of the nanocomposite hydrogels were studied (**Fig. 4.24**). All samples showed a significant shear thinning character with shear thinning index  $n$  far less than 1 (**Fig. 4.24 a**, and **Tab. 4.4**). The flow

index  $n$  of the nanocomposites dropped from 0.15 to 0.07 at an increasing amount of clay addition from 0 to 4 wt%, indicating an enhanced shear-thinning behavior. Additionally, all the nanocomposite hydrogels maintained a rapid recovery property under alternative of high ( $100 \text{ s}^{-1}$ ) and low ( $0.1 \text{ s}^{-1}$ ) shear rates (**Fig. 4.24 b**). Interestingly, the clay addition increased the viscosity of the nanocomposite systems without undermine their recovery property.

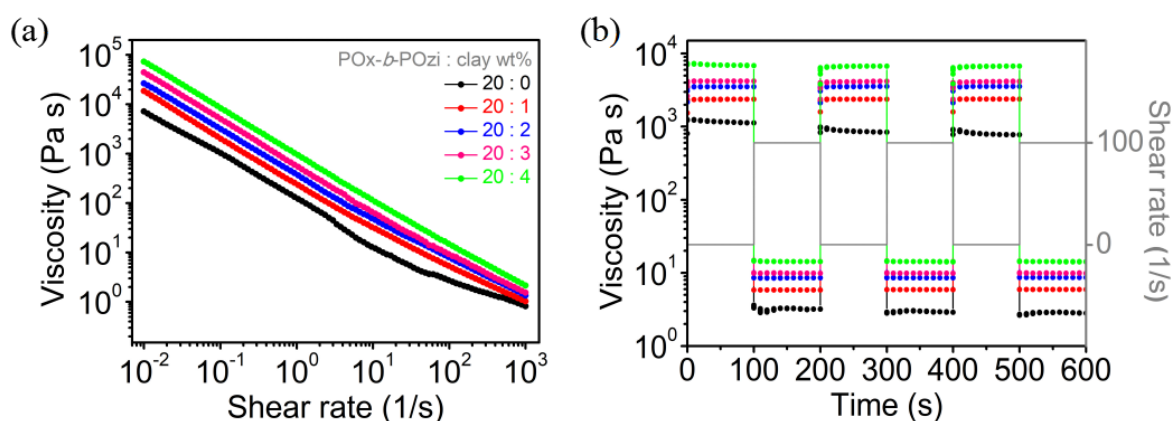


Fig. 4.24| (a) Shear thinning behaviors. (b) Recovery properties under the applied shear rate of  $0.1 \text{ s}^{-1}$  and  $100 \text{ s}^{-1}$ .

Finally, combining the practical 3D printing evaluation with the rheological measurements results above, a printing window in an investigated concentration range of PMeOx-*b*-PnPrOzi 10-20 wt% and clay 0-4 wt% was obtained for this PMeOx-*b*-PnPrOzi/clay hybrid hydrogel ink (**Fig. 4.25**). The addition of clay obviously reduced the

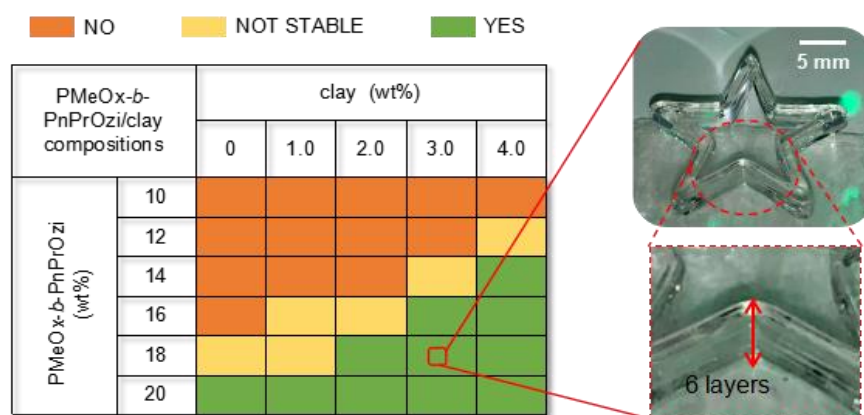


Fig. 4.25| Printing window of the PMeOx-*b*-PnPrOzi/clay hybrid hydrogel, and the photos of a printed 6 layers "star" with a selected composition. This data was made in collaboration with my bachelor student Phan Tuong Vy Dinh.



critical gelation concentration required for thermogelation of the diblock copolymer, for instance, compared with a critical gelation concentration of 20 wt% of plain polymer, the doping of 4 wt% clay allows the thermogelation happen at a copolymer concentration of 14 wt%. Thereafter, the printing of true 3D structures with high resolution and high shape fidelity was realized using the developed novel PMeOx-*b*-PnPrOzi/clay hybrid hydrogel inks. However, it should be kept in mind that one cannot increase the clay addition amount indefinitely in actual ink material design and application, as this would eventually cause the system too sticky to be processed and printed conveniently.

#### 4.3.1.5 Conclusion

In conclusion, we have successfully adjusted the rheological properties of the synthetic thermoresponsive PMeOx-*b*-PnPrOzi hydrogel by the addition of clay Laponite XLG (**Fig. 4.26**). The thermoresponsive character was well retained with only a slightly decreased gelation temperature. More importantly, the PMeOx-*b*-PnPrOzi/clay hybrid hydrogels exhibited markedly enhanced viscoelastic properties such as storage modulus, yield stress and shear-thinning behavior. Such changes are highly desirable for extrusion-based 3D printing and, therefore resulting in a significantly improved printability. The filaments fusion was markedly suppressed, which allowed a drastically improved shape fidelity. Furthermore, both the component PMeOx-*b*-PnPrOzi and clay are biocompatible. Therefore, this newly developed thermoresponsive hybrid hydrogel is very promising to expand the options available to researchers for 3D (bio)printing. Additionally, this hybrid material platform, could be interesting for many other research fields, such as drug delivery, sacrificial or support-bath printing, and thermoresponsive self-protection.

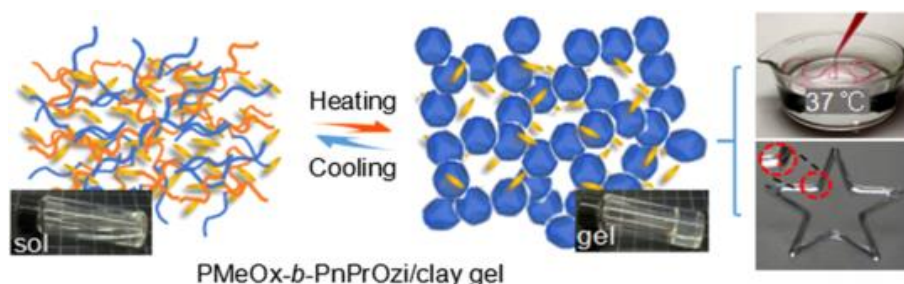


Fig. 4.26| Improving printability of a thermoresponsive hydrogel ink by clay addition.

Although the printability of this thermogelling PMeOx-*b*-PnPrOzi diblock copolymer has been significantly improved by clay addition, the developed novel PMeOx-*b*-PnPrOzi/clay hybrid hydrogel inks still suffer major limitations such as poor mechanical strength and low scaffolds stability due to the existing weak physical crosslinking network. The printed structures cannot be used for load-bearing applications that are more like the actual situations. In addition, the printed scaffolds will be diluted and dissolved quickly upon the surrounding temperature decreasing below the  $T_{gel}$  and/or the addition of excess solutions such as culture medium during the culture stages (**Fig. 4.27**). Therefore, developing suitable additional crosslinking methods to ensure the long-term stability of the printed structure is of great significance to further promote the wide application of the currently POx/POzi-based ink materials.

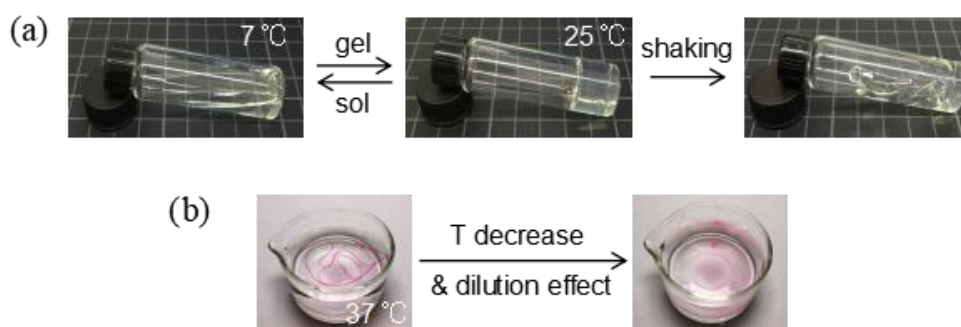


Fig. 4.27| The performance of the PMeOx-*b*-PnPrOzi/clay hybrid hydrogel under an applied external shear force (a) and under temperature decreasing or culture in water (b).

### 4.3.2 PMeOx-*b*-PnPrOzi/PDMAA/clay Hybrid Hydrogels

Hydrogels that can be processed with AM techniques and concomitantly have favorable mechanical properties are attractive for many advanced applications. Herein, another 3D printable organic-inorganic hybrid interpenetrating network (IPN) hydrogel was developed based on the previous PMeOx-*b*-PnPrOzi/clay hybrid hydrogel, and was characterized systemically in term of the rheological property, swelling behavior, composition, mechanical property, as well as the extrusion-based printability.

*The work described in this subchapter was already published: “Development of a 3D printable and highly stretchable ternary organic-inorganic nanocomposite hydrogel” by C. Hu; M. S. Haider; L. Hahn; M. S. Yang and R. Luxenhofer published recently in Journal of Materials Chemistry B, 2021, 9, 4535–4545.<sup>[459]</sup> The text and figures of the following pages 87-105 are may identical with the publication with permission.*

#### 4.3.2.1 POx-*b*-POzi/PDMAA/clay Hydrogel Preparation

The ternary PMeOx-*b*-PnPrOzi/PDMAA/clay hydrogel, named shortly as POx-*b*-POzi/PDMAA/clay in the following, was prepared using a two-step approach. First, all the components were mixed in the desired ratios and allowing to undergo the thermogelation transition. Subsequently, the DMAA in the mixtures was polymerized by free radical

Table 4.5| Screening experiments for optimizing the system composition in view of rheological property and mechanical strength.

composition <sup>a</sup>	POx- <i>b</i> -POzi (g)	DMAA (g)	MBAA/KPS <sup>b</sup> (g)	DI-water (g)	2 wt% clay solution (g)
30:15:0	1.2	0.6	0.003	2.2	/
30:15:1.2	1.2	0.6	0.003	/	2.2
30:10:0	1.2	0.4	0.002	2.4	/
30:10:2	1.2	0.4	0.002	/	2.4

<sup>a</sup> The composition is labeled as x: y: z, where x is the mass fraction of block copolymer POx-*b*-POzi, y is the mass fraction of monomer DMAA, z means the mass fraction of clay. <sup>b</sup> The cross linker N, N'-methylenebisacrylamide (MBAA) and KPS are both 0.5 wt% of DMAA. ”/” means not added.

polymerization initiated by potassium persulfate (KPS) under 60 °C. In order to find an optimized hydrogel composition, several initial screening experiments were carried out for the ternary hydrogel precursors of different composition with respect to their rheological behavior and mechanical properties (Tab. 4.5-4.6).

Table 4.6 | Screening experiments for the amount of cross linker MBAA.

No.	PO <sub>x</sub> - <i>b</i> -POzi (g)	DMAA (g)	MBAA (g)	KPS (g)	2 wt% clay solution (g)
1	1.2	0.4	0.0004	0.002	2.4
2	1.2	0.4	0.0020	0.002	2.4
3	1.2	0.4	0.0040	0.002	2.4

A sharp sol to gel transition at room to physiological relevant temperature ( $T_{gel}$ ) will ensure a rapid gelation under a mild condition. This together with a relatively higher storage modulus  $G'$  of formed gel will facilitate the instant shape maintenance of print structures. As thermogelation of the mixture hinges on the thermoreversible hydrophobic interactions, the addition of significant amounts of DMAA could affect the thermogelation (Fig. 4.28). In fact, when a 15 wt% DMAA was added, the  $T_{gel}$  of the sample increased significantly, i.e., the thermogelation behavior was weakened somehow. In contrast, at a 10 wt% DMAA addition, the effect was rather minor. Therefore, we concluded that the sample with composition 30:10:1.2 showed the desired thermogelation performance with a  $T_{gel}$  near 27 °C and  $G'$  over 4.5 kPa.

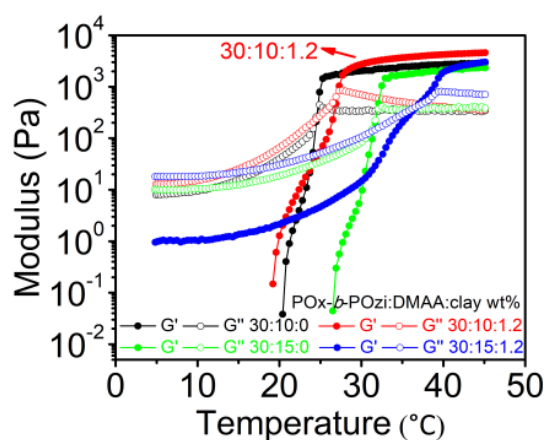


Fig. 4.28 | Temperature dependent rheological measurements to investigate the thermogelling property of mixtures with different compositions (without MBAA and initiator KPS).

In addition, the mechanical properties of the samples after chemical curing were investigated to understand the mechanical strength and elongation of the hydrogels with different compositions (**Fig. 4.29**). Although increasing the amount of monomer DMAA will enhance the mechanical strength of the hydrogel, it will over-compromise the thermogelling property of the hydrogel system and, thus result in a poor printability. As expected, the clay addition enhanced the overall performance of the hydrogel, especially the elongation at break. These results confirmed that the hydrogel precursor composition of 30:10:1.2 would be an optimized combination for the hydrogels in present purpose.

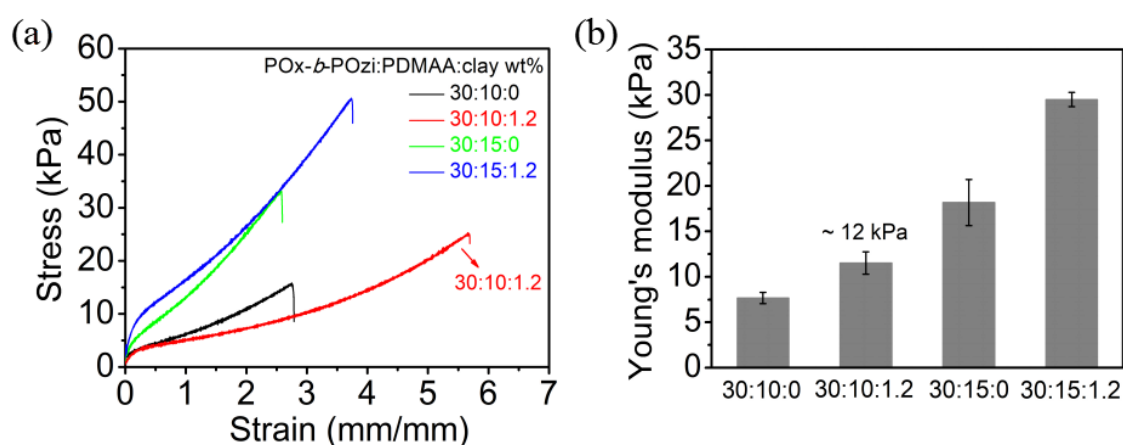


Fig. 4.29| Screening experiments for optimizing the hydrogel composition in view of the mechanical strength. (a) Tensile stress-strain curves of hydrogels with different compositions. (b) The corresponding Young's modulus of the hydrogels obtained from the tensile stress-strain curves.

Finally, the influence of crosslinker MBAA on the mechanical properties of the hydrogel was investigated (**Fig. 4.30**). By comparing the mechanical strength of hydrogels crosslinked by 1 wt% and 0.1 wt% MBAA, it can be found that a higher amount of crosslinker will result in an enhanced mechanical strength because of the increased crosslinking density, but significantly decreased breaking elongation. In contrast, a lower crosslinker amount will lead to a decreased crosslinking density or even an incomplete crosslinking and, thus a rather softer hydrogel was obtained showing a decreased breaking strength while increased breaking elongation. Therefore, with this method of changing the crosslinking agent amount, the mechanical properties of the hydrogels can be adjusted

within a certain range accordingly. Here, a medium crosslinker amount of 0.5 wt% was chosen for further study as the resulting hydrogel has both a suitable strength and long elongation. Taken together, the hydrogel precursor composition (30:10:1.2) of a 2 wt% clay aqueous solution as solvent (the final clay concentration is 1.2 wt%), polymer concentration of 40 wt% (the weight ratio of DMAA:POx-*b*-POzi is 1:3), and the crosslinker MBAA and initiator KPS of 0.5 wt% relative to the weight of DMAA was selected as the optimized composition for the following experimental demonstration.

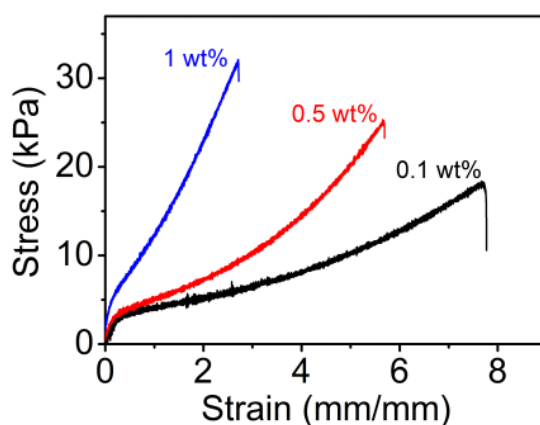


Fig. 4.30| The effect of chemical crosslinker MBAA amount on the mechanical properties of POx-*b*-POzi/PDMAA/clay hydrogel (30:10:1.2).

The hybrid hydrogel was prepared by a two-step approach (**Fig. 4.31 a**). In the first step, a homogeneous POx-*b*-POzi/DMAA/clay mixture (with MBAA/KPS) dissolved thoroughly in 7 °C fridge was transferred into a mold in the cold, and subsequently allowed to complete the thermogelation at room temperature. As described before, inducted by this temperature change, the thermosensitive diblock copolymer POx-*b*-POzi self-assembles into spherical vesicles, and aggregates into a sponge-like network leading the formation of a macroscopic physical hydrogel.<sup>[447]</sup> As we have studied and found in the binary POx-*b*-POzi/clay system in subchapter 4.3.1, the inorganic additive of clay does not negatively affect this thermogelation. In the second step, the DMAA in the mixture was polymerized at 60 °C for 6 h to produce the POx-*b*-POzi/PDMAA/clay IPN hydrogel. As we expected, the freshly prepared hydrogel precursor before chemical crosslinking showed a clear reversible thermogelation behavior (**Fig. 4.31 b**). After

completing the chemical curing step, the hybrid hydrogel lost its reversible thermogelation property, and transformed from a transparent to white/opaque hydrogel. Notably, the resulting hydrogel can sustain a high stretching deformation, and recover to some extent quickly upon the release of the external force without any observable damage (**Fig. 4.31 c**).

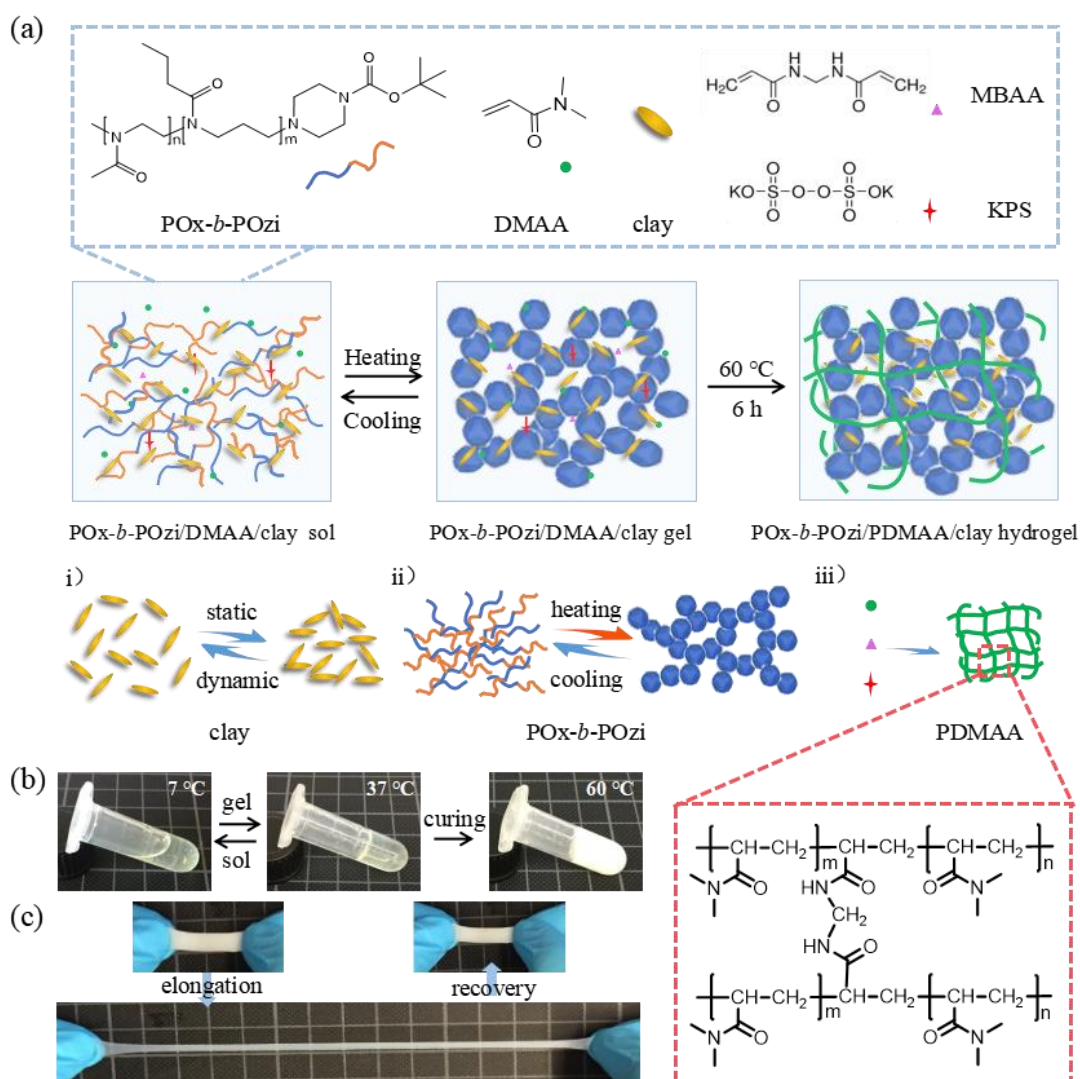


Fig. 4.31| (a) Schematic illustration for the preparation of POx-*b*-POzi/PDMAA/clay hydrogel via the strategy of thermogelation and subsequent free radical polymerization from three components: i) clay Laponite XLG, ii) thermoresponsive diblock copolymer POx-*b*-POzi and iii) chemically crosslinked PDMAA network. (b) Photographs indicating the thermal reversible sol-gel transition of POx-*b*-POzi/DMAA/clay mixture and the state after curing. (c) Photographs demonstrating the highly stretchability and recovery of POx-*b*-POzi/PDMAA/clay hydrogel.

In this context, we also designed and investigated acrylic acid (AA) and 2-hydroxyethylmethacrylate (HEMA) as alternative to DMAA in the hydrogel precursors

(Fig. 4.32). However, distinct from DMAA, these monomers affected the thermogelation of POx-*b*-POzi in an unfavorable manner. All the investigated compositions remained in a gel state throughout the investigated temperature range of 5 - 45 °C. We hypothesize that these monomers compete more effectively with the water molecules, preventing hydration of the nPrOzi block at lower temperatures and, thereby restricting the liquefaction of the gels.

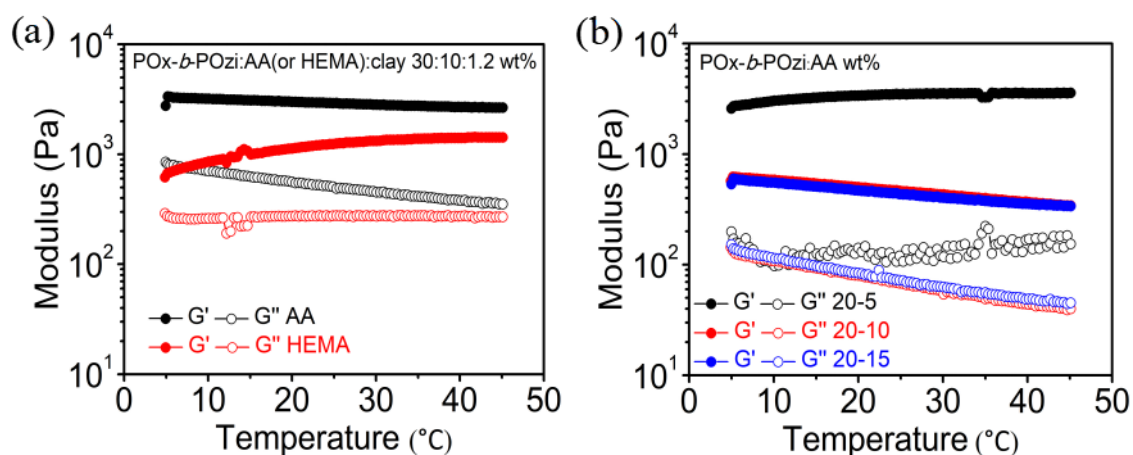


Fig. 4.32 | Temperature dependent rheology properties of (a) POx-*b*-POzi/AA/clay and POx-*b*-POzi/HEMA/clay system with a hydrogel composition of 30:10:1.2, and (b) POx-*b*-POzi/AA system with different compositions.

#### 4.3.2.2 Rheological Properties of POx-*b*-POzi/DMAA/clay Precursor

Rheological analysis was performed to understand the viscoelastic property and to predict the printability of POx-*b*-POzi/DMAA/clay system prior to chemical crosslinking. Initially, a temperature sweep was carried out in the dynamic oscillation mode to investigate the thermogelling behavior of the POx-*b*-POzi/DMAA/clay precursor mixture. The intersection of  $G'$  and  $G''$  defines the gelation point, and the corresponding temperature referred to as  $T_{gel}$  (Fig. 4.33). At low temperatures, the mixture behaves as liquid ( $G'' > G'$ ). Upon temperature increasing, both the  $G'$  and  $G''$  increase, and at around 25 °C ( $T_{gel}$ ),  $G'$  surpasses the  $G''$  and reach a plateau value around 6 kPa, indicating the formation of a solid gel. Here, in comparison with the result of POx-*b*-POzi/DMAA/clay mixture without MBAA and KPS (Fig. 4.28), a slightly lower  $T_{gel}$  and higher  $G'$  was observed and attributed to partial polymerization of DMAA during the testing.



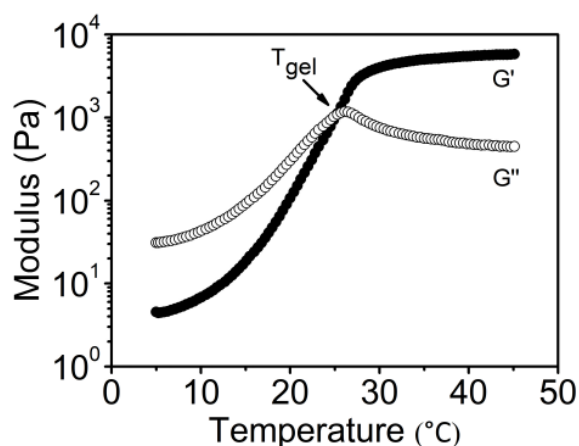


Fig. 4.33| Thermogelation behavior of POx-*b*-POzi/DMAA/clay precursor mixture.

At 37 °C (above  $T_{gel}$ ), an amplitude sweep was conducted to assess the LVER of the precursor mixture, which was determined as the onset of decrease of  $G'$  (Fig. 4.34 a). Subsequently, a frequency sweep was performed under a constant strain of 0.1% (within the LVER) at 37 °C (Fig. 4.34 b). The result showed a dominating  $G'$  value over  $G''$  in the whole investigated frequency range, indicating a relatively stable gel-like character of the precursor mixture when under a temperature above its gelation temperature ( $T_{gel}$ ).

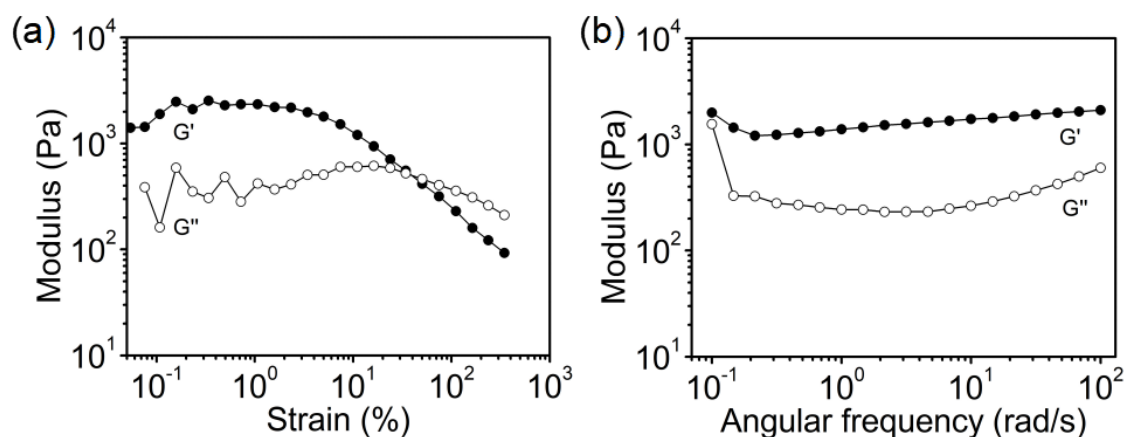


Fig. 4.34| Amplitude sweep (a) and Frequency sweep (b) for the POx-*b*-POzi/DMAA/clay precursor mixture at 37 °C .

Furthermore, we found that the viscosity of mixture decreases significantly under the increasing of the shear rate, confirming that the POx-*b*-POzi/DMAA/clay system remains a pronounced shear-thinning hybrid material system (Fig. 4.35). Again, as mentioned previously, the thermogelling and shear-thinning are two very valuable properties for the

extrusion-based 3D printing, which facilitate not only the smooth extrusion out of the materials during printing but also the 3D printed features maintenance after printing.

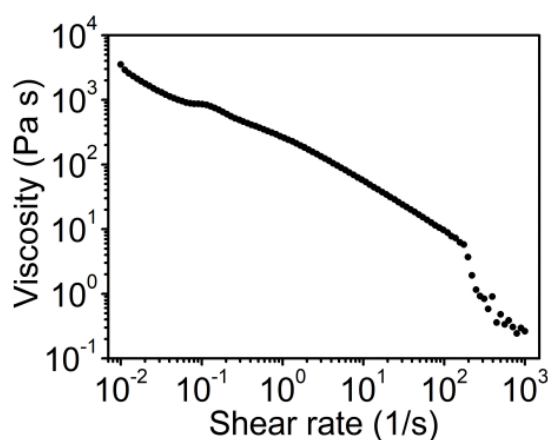


Fig. 4.35| Shear-thinning behavior of the hydrogel.

#### 4.3.2.3 Mechanical Properties of POx-*b*-POzi/PDMAA/clay Hydrogel

Besides the investigation of rheological properties for printability assessment, the mechanical properties of the hydrogel after chemical curing were studied as well. From the mechanically tensile stress-strain testing, we found that the hybrid hydrogel became highly stretchable after chemical curing (**Fig. 4.36 a**). The resulting hydrogel exhibited a remarkable elongation at break of over 550%, accompanied with a Young's modulus of 12 kPa and a breaking strength of 25 kPa, respectively (**Fig. 4.36 b**). Although it has been reported that nanocomposite IPN hydrogels often show excellent mechanical properties, we believe this report is the first report showing such highly stretchable hydrogels based on POx.

Subsequently, the cyclic loading-unloading tests under various predefined maximum strains of 100%, 200% and 300% were conducted to understand the energy dissipation capacity of the hybrid hydrogels (**Fig. 4.36 b**). Apparent hysteresis loops were observed in the loading-unloading cycle tests of hydrogels, suggesting that there are non-covalent interactions existing in the hydrogel network which can dissipate energy effectively during the deformation and thus, resulting in the hysteresis effect and remarkable stretchability. After releasing the tensile force applied on hydrogels, the strain recovered

accompanied with only a small hysteresis below 50%. This result shows that the developed hybrid hydrogel has a strong elastic nature but also that some plastic deformation occurs under a large strain loading, indicating an irreversible fracture of the partial chemical crosslinked networks.

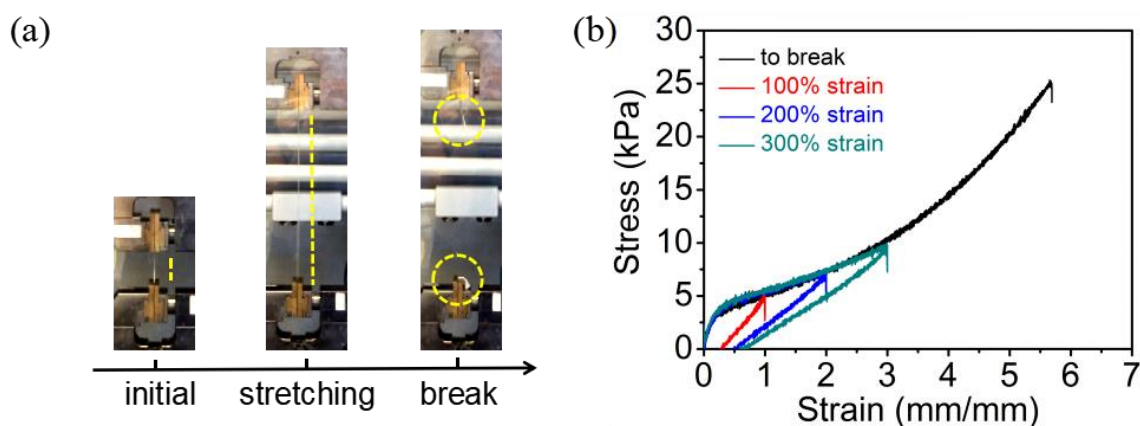


Fig. 4.36| (a) Photographic images during the tensile test of POx-*b*-POzi/PDMAA/clay hydrogels. The dashed yellow lines are added for better visibility of hydrogels. (b) Tensile stress-strain curve of POx-*b*-POzi/PDMAA/clay hydrogel and cyclic tensile loading-unloading curves measured at different strains.

Moreover, 10-times consecutive cyclic tensile loading-unloading tests were performed to investigate the fatigue resistance property (**Fig. 4.37 a**). During the consecutive loading-unloading cycles, the apparent hysteresis loops decreased gradually particularly after the first loading cycle. In general, an inverse relationship was observed between the hysteresis loop and the residual strain throughout the entire loading-unloading tests, i.e., a gradual decrease of hysteresis loop area with a gradual increase of residual strain. Interestingly, the tensile stress was also reduced in the successive cycles, without appearance of any visible cracks and fractures. This result suggest that the energy dissipation is mainly due to the destruction and reconstruction of the internal physical networks. In addition, loading-unloading cyclic tests at higher critical strains of 400% and 500% showed a similar behavior as with lower strains (**Fig. 4.37 b-c**). It is worth noting that when the strained hydrogels were allowed to recover for 2 h at room temperature after the loading-unloading test, the sample can recover their original dimensions to some extend (**Fig. 4.37 d**).

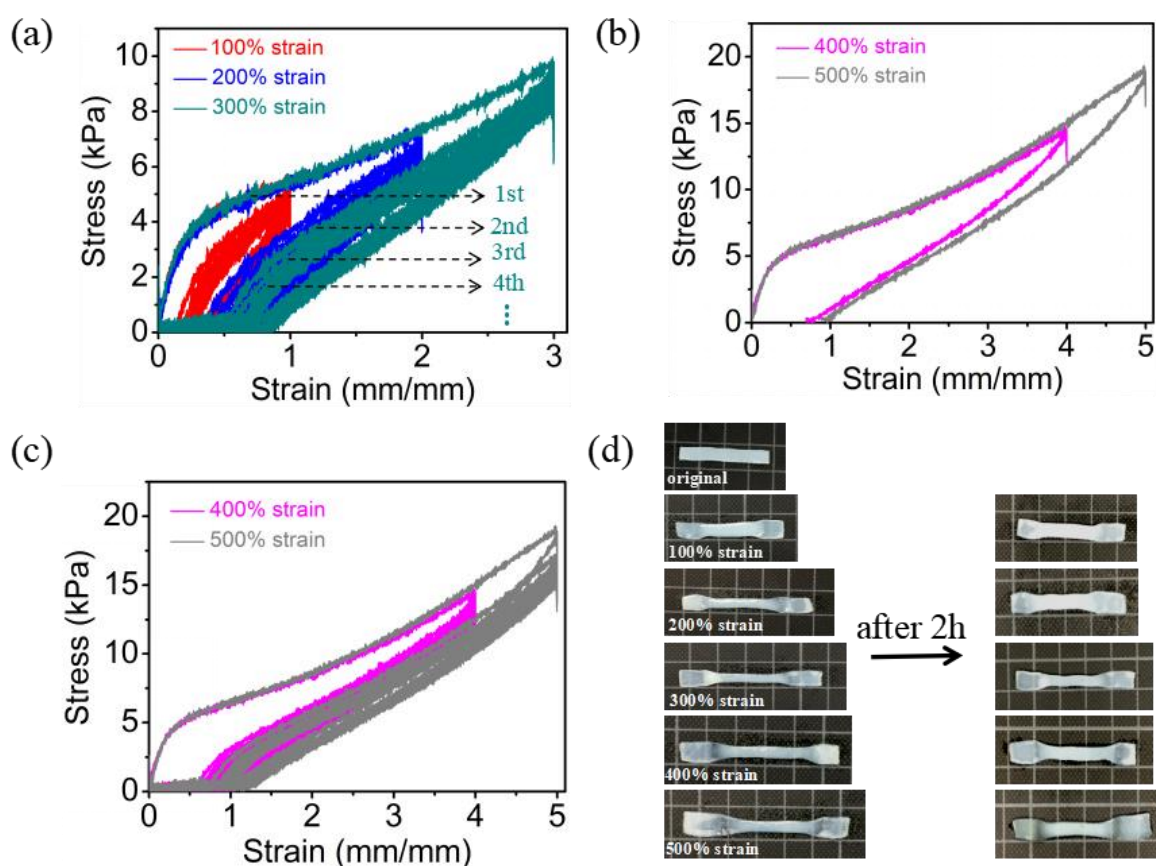


Fig. 4.37| (a) Ten-times consecutive tensile loading-unloading curves at different strains. (b) The cyclic tensile loading-unloading curves and, (c) Ten-times consecutive tensile loading-unloading curves at the maximum strains of 400% and 500%. (d) The recovery of hydrogels after 10 times consecutive cyclic tensile loading-unloading tests at different stretching strain after a recovering time of 120 min.

Finally, a uniaxial compressive test was conducted to evaluate the compressive strength of the hybrid IPN hydrogel (**Fig. 4.38**). From the compressive stress-strain curve, a compressive modulus of  $0.16 \pm 0.01$  kPa was determined. The hydrogel can sustain a large compressive deformation of 80% without visible fracture, and showing a compressive strength of 320 kPa. It should be noted that all these mechanical tests were conducted at room temperature. Although the PDMAA network was chemically crosslinked and the hybrid hydrogel had lost its apparent thermoresponsive behavior, there remains a thermoresponsive component POx-*b*-POzi in the IPN hydrogel. Therefore, it would be interesting to further study the changes in mechanical properties of this IPN hydrogel with the temperature in the future.

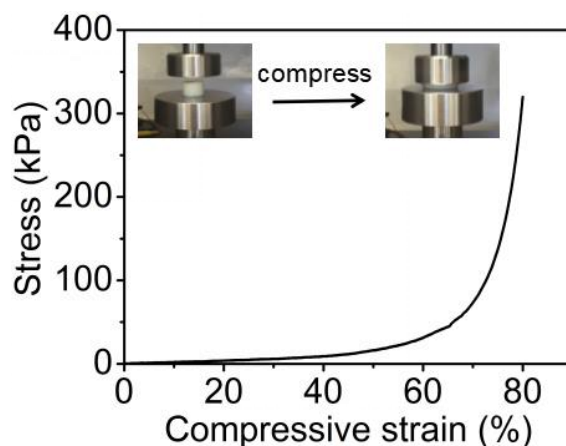


Fig. 4.38| Compressive stress-strain test of POx-*b*-POzi/PDMAA/clay hydrogel.

#### 4.3.2.4 Characterizations of POx-*b*-POzi/PDMAA/clay Hydrogel

The swelling behavior of the ternary hybrid hydrogels was investigated in deionized (DI) water at 37 °C (**Fig. 4.39**). The hydrogels swelled rapidly in the first 6 h, and then tended to level off after 24 h. After that, only minor increase of the swelling ratio was observed, and the swelling ratio after 4 days was found to be 1100%, which is in the expected range for hydrogels containing POx and PDMAA network.<sup>[460-462]</sup> At the same time, the sol content of the hydrogels was determined as  $39.94 \pm 0.05$  %, i.e., the corresponding gel content is around 60.06 %. Considering that the original solid content of PDMAA/clay in the dry hybrid hydrogel is about 27.18 % (POx-*b*-POzi is around 72.82 %), it is obvious that a considerable amount of POx-*b*-POzi remained in the hydrogel despite extensive washing. This can be because that the copolymer POx-*b*-POzi

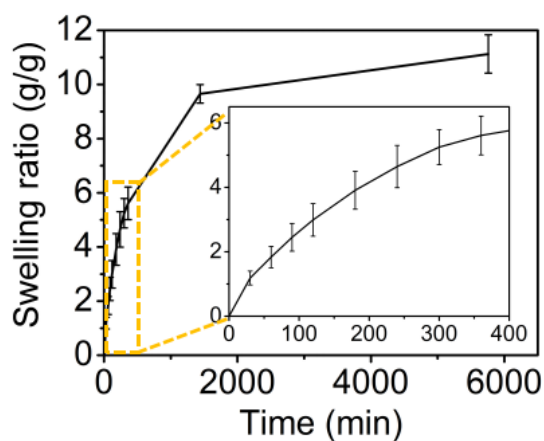


Fig. 4.39| Swelling behavior of POx-*b*-POzi/PDMAA/clay hydrogel.

is very effectively physically trapped and/or in part covalently attached to the PDMAA/clay network through the virtue of chain transfer reactions during the free radical polymerization.

Furthermore, DSC characterization was conducted on the dried gels before (POx-*b*-POzi/DMAA/clay), after chemical crosslinking (POx-*b*-POzi/PDMAA/clay), and after sol-extraction (POx-*b*-POzi/PDMAA/clay extr.) (**Fig. 4.40**). The physical hydrogel POx-*b*-POzi/DMAA/clay before chemical crosslinking has two  $T_g$  at 8.8 °C and 78.8 °C, corresponding to the two blocks of POx-*b*-POzi (**Fig. 4.40**, black trace).<sup>[450]</sup> In contrast, the POx-*b*-POzi/PDMAA/clay hydrogels after chemical crosslinking showed three  $T_g$  values both before and after extraction (**Fig. 4.40**, red and blue traces). The newly appeared  $T_g$  of around 127 °C was attributed to the newly formed PDMAA polymer chain.<sup>[460]</sup> The appearance of three individual  $T_g$  values in the crosslinked IPN gels, especially after extensive extraction, confirmed the presence of the copolymer POx-*b*-POzi in the developed hydrogels. Important to note, without the PDMAA network, the POx-*b*-POzi/clay hydrogels would dissolve rapidly in water. Compared with the  $T_g$  of

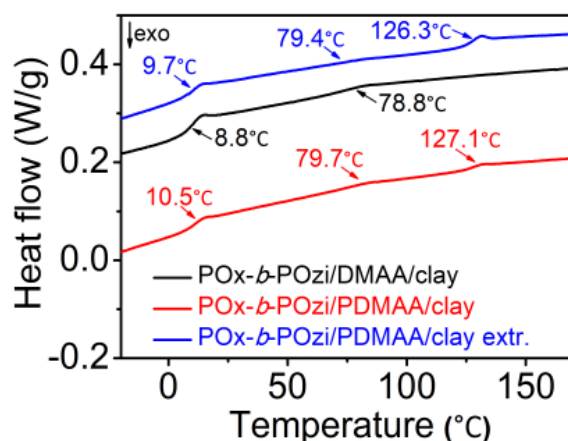


Fig. 4.40| DSC analysis of the dried hydrogels POx-*b*-POzi/DMAA/clay before chemical crosslinking, POx-*b*-POzi/PDMAA/clay after chemical crosslinking, and POx-*b*-POzi/PDMAA/clay extr. after sol-extraction.

copolymer POx-*b*-POzi in the POx-*b*-POzi/DMAA/clay physical network, the slight increase in the  $T_g$  of POx-*b*-POzi in the POx-*b*-POzi/PDMAA/clay and POx-*b*-POzi/PDMAA/clay extr. chemical networks can be attributed to the chain transfer

reactions, which allowed covalently linking of the POx-*b*-POzi to the PDMAA and thus, reducing its chain segment mobility.

#### 4.3.2.5 3D Printing

3D printing of the developed POx-*b*-POzi/DMAA/clay hybrid hydrogel precursor was conducted by using a commercially available extrusion-based 3D printer BIO X form CELLINK (Gothenburg, Sweden) (**Fig. 4.41**).

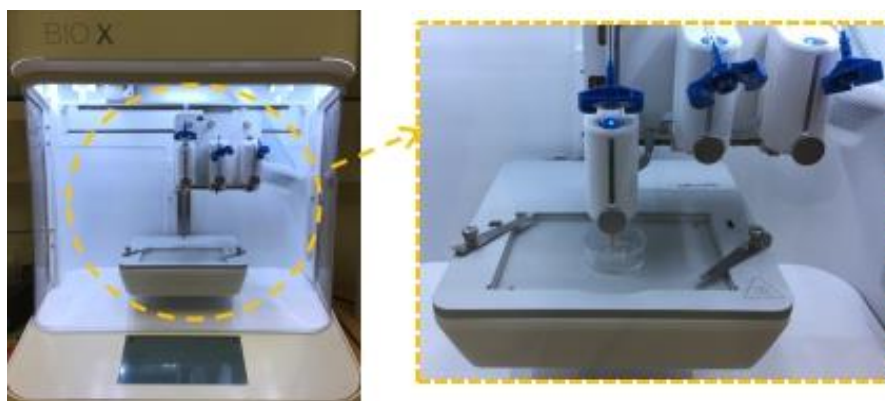


Fig. 4.41| Extrusion-based printer for the printing of POx-*b*-POzi/DMAA/clay mixtures.

Initially, a 20-layer hollow five-pointed star ( $7.28 \times 7.28 \times 5$  mm) and a 20-layer cube ( $10 \times 10 \times 5$  mm) were designed and printed under an extrusion pressure of 190 kPa and 155 kPa, respectively (**Fig. 4.42**). The POx-*b*-POzi/DMAA/clay system could be extruded smoothly through a fine needle (23 G), and then recovery to solid-like gel state immediately upon being deposited onto a 37 °C print bed. Here, the combination of the remarkable shear thinning character and rapid thermogelling property, allows avoidance of using extra crosslinking agents at this point and facilitates the high-quality printing process without undesirable fusion and collapse of the printed structures. The designed 3D constructs of a star and a cube were printed successfully with high shape-fidelity and layer-stackability, demonstrating that the proposed POx-*b*-POzi/DMAA/clay mixture might be an ideal ink candidate for the extrusion-based printing technology. Unsurprisingly, the printed constructs without further chemical curing treatment collapsed gradually upon the environment temperature drops below the  $T_{gel}$ , again confirming the

reversible thermogelling property of the POx-*b*-POzi/DMAA/clay ink system (**Fig. 4.42 b**). In contrast, the printed constructs retained their structural integrity for a long time when the surrounding temperature was kept above the  $T_{gel}$ , for example when being incubated in 60 °C silicone oil (**Fig. 4.42 c**).

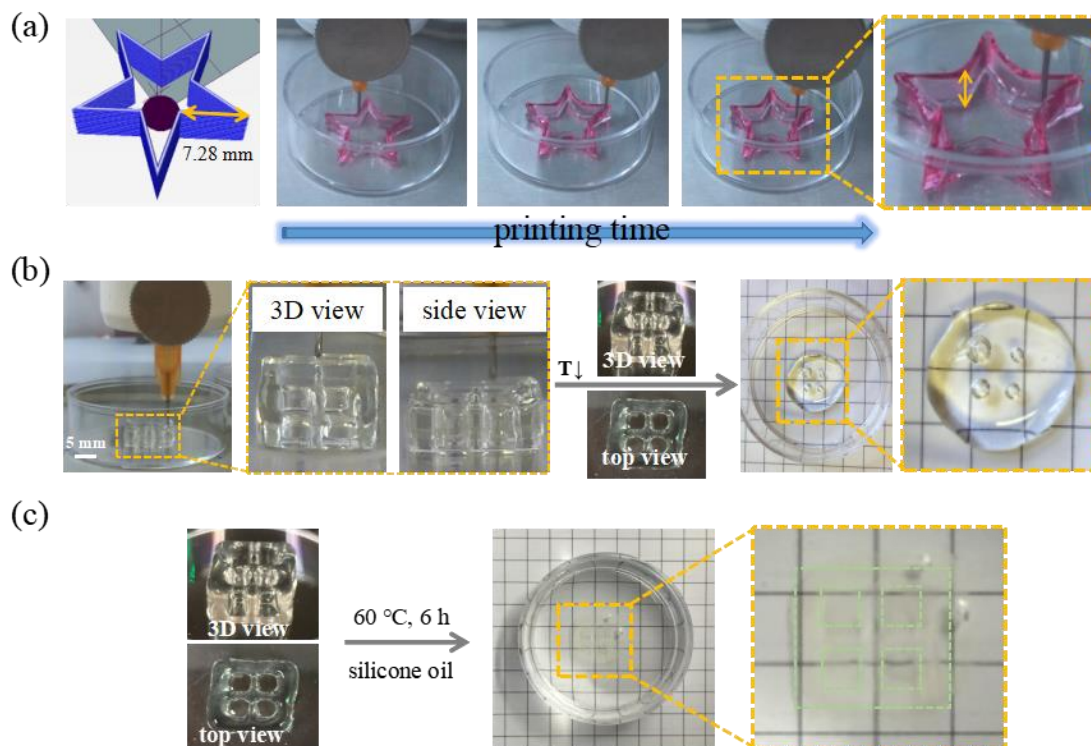


Fig. 4.42| Extrusion-based 3D printing of the POx-*b*-POzi/DMAA/clay hybrid hydrogel ink. (a) Screen shots to show the printing process of a 20-layer hollow five-pointed star ( $7.28 \times 7.28 \times 5$  mm). The ink was dyed red by carmine. (b) 3D printing of a 20-layer cube ( $10 \times 10 \times 5$  mm). The printed cube collapsed gradually when the surrounding temperature drops below the  $T_{gel}$ . (c) Photographs of the printed 20-layer cube, and its long-term stability in 60 °C silicone oil. The dashed green line was added for better visibility of the printed colourless cube.

Due to the weak adhesion between sequentially deposited layers during the printing process, the mechanical properties of the AM materials generated in a layer-by-layer fashion are typically inferior to those of the corresponding bulk materials. In order to investigate the influence of printing process on the hydrogel's mechanical properties, we printed a solid rectangular stripe and then chemically cured for mechanical testing. In one design, the printing direction was along the uniaxial stretching direction, in the other, the printing direction was perpendicular to it (**Fig. 4.43 a**). The sample cut from a molded



bulk hydrogel was used as control. Remarkably, no significant effect of the printing process on the mechanical property of hydrogels was observed (**Fig. 4.43 b**). In fact, the Young's modulus of the printed hydrogels ( $11.43 \pm 1.06$  kPa in case of parallel printing, and  $10.22 \pm 0.93$  kPa in case of perpendicular printing) were essentially identical to the one measured for bulk samples ( $11.51 \pm 1.22$  kPa). Furthermore, the printing process has no significant influence on the breaking elongation, which remained at over 550%. Interestingly, the hydrogel printed in perpendicular direction exhibited a significantly higher toughness when compared to the molded and parallel-printed one.

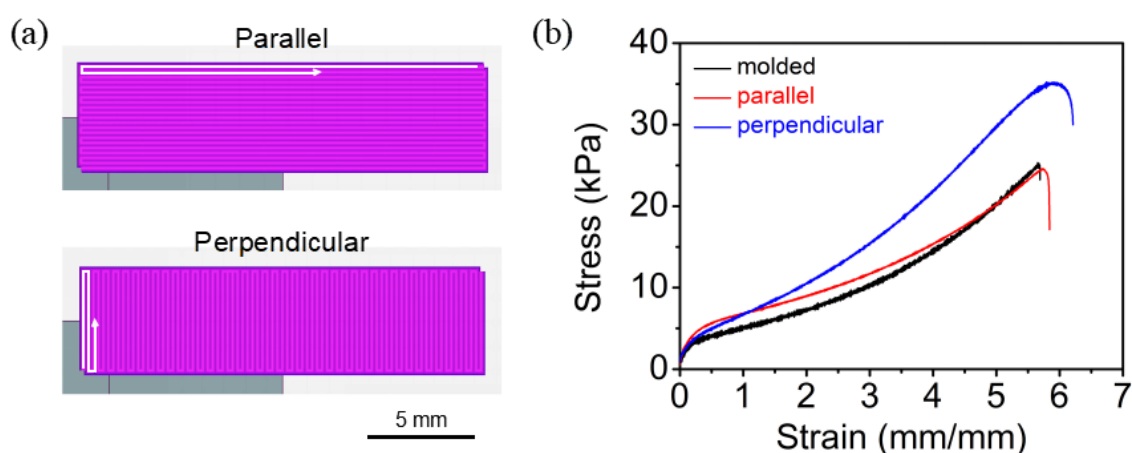


Fig. 4.43| (a) Designed model of the hydrogel stripes printed with parallel or perpendicular filament orientation. (b) The stress-strain curves of hydrogel stripes printed parallel and perpendicular to the uniaxial stretching direction, and compared to molded bulk material.

The fact that the materials manufactured layer-by-layer do not suffer with respect to their mechanical properties is only surprising on first sight and when thinking about layer-by-layer manufacturing of polymer melts. When a strand of the polymer melt is extruded onto a solidified strand, the mobility and thus the entanglement of the macromolecular will be severely hampered by the fact that the previous polymer strand is already solid and the next solidifies rapidly. Here, we print shear-thinning hydrogels, which are much softer viscoelastic solid-like gels that lack a primary phase boundary between layers. Therefore, they are prone to fuse on a molecular level much more effectively. In addition, in the subsequent curing step, we polymerize a low molar mass monomer DMAA, which leads to the formation of an IPN hydrogel that naturally spans the hypothetical layer boundaries

from the printing process. However, this does not explain why the perpendicularly printed hydrogel showed a higher toughness.

In fact, we also made another unexpected observation. The hydrogel stripes printed in perpendicular to its long axis extended along the long axis, while the stripes printed in parallel to its long axis extended perpendicular to it (**Fig. 4.44**). Although the same structure should be generated in theory according to the designed G-code, it in fact does not when the same printing parameters were applied (extrusion pressure and printing speed). This may be related to the much more directional turns in the perpendicular print, where the printhead must decelerate and accelerate again. We assume that the higher toughness is likely related to a discrepancy between the theoretical G-code and the actual extruded structure. Such discrepancy has been recently discussed in a groundbreaking paper by Dalton and co-workers for the melt electro-writing.<sup>[463]</sup> We propose that such study would be of great interest to the direct extrusion-based ink writing community.

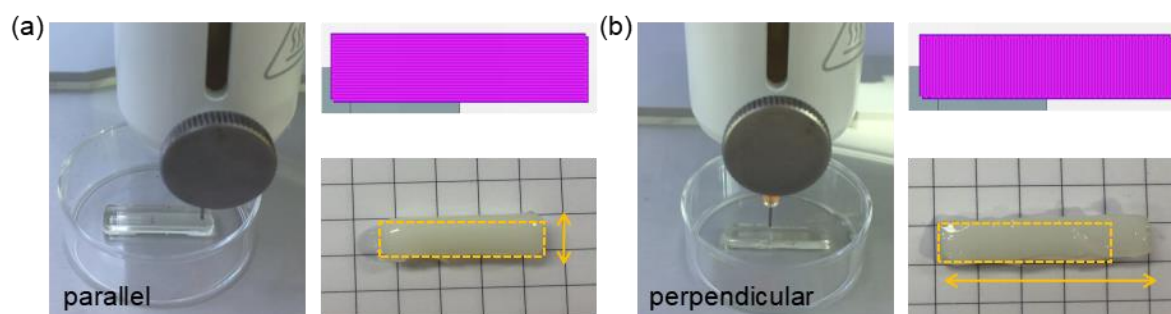


Fig. 4.44| Photographs to show the 3D printing process, top view of the designed stripes ( $20 \times 5 \times 5$  mm) and printed hydrogels with parallel (a) and perpendicular (b) filament orientation to the uniaxial stretching direction. The yellow arrow indicates the merging direction, and the yellow dashed box represents the theoretical size of the hydrogel.

Thereafter, various 3D constructs were designed and printed for further assessment of the printability of POx-*b*-POzi/DMAA/clay hydrogel ink and its performance after chemical curing. Initially, a 12-layer cuboid ( $20 \times 5 \times 6$  mm) was printed under an extrusion pressure of 190 kPa, and then chemically cured by incubating the printed structure at 60 °C overnight to initiate the free radical polymerization of monomer DMAA (**Fig. 4.45 a**). Here, argon-purged silicone oil was used as a protective bath during the

chemical crosslinking aiming to avoid the dehydration and oxygen-induced inhibition on the polymerization of DMAA. Successfully, a printed and chemically crosslinked POx-*b*-POzi/PDMAA/clay hydrogel cuboid was obtained with a size of around  $18 \times 5 \times 6$  mm. Comparing the printed cuboid size with designed one, this indicated some dimension shrinkage which can be attributed to the imperfect free radical polymerization as well as the loss of water despite the silicone oil protection. The resulting cuboid exhibited a remarkable mechanical flexibility upon stretching and compression (**Fig. 4.45 b-c**), which is in good agreement with the mechanical test results described above in subchapter 4.3.2.3. After reaching a swelling equilibrium in water, the printed POx-*b*-POzi/PDMAA/clay hydrogel cuboid increased in volume over 6-fold ( $31 \times 10 \times 11$  mm), confirming a highly gel swelling ratio (**Fig. 4.45 d**).

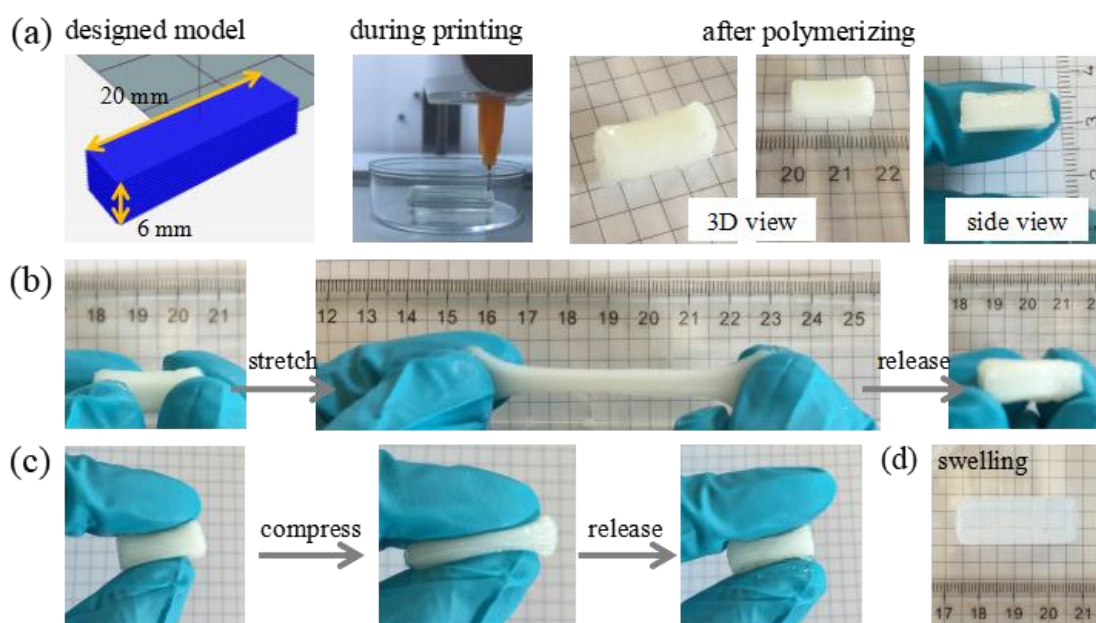


Fig. 4.45| (a) The images during 3D printing and after chemical curing of a designed 12-layers cuboid. (b-c) After chemically curing, the printed cuboid exhibited a high mechanical flexibility under holding, stretching, and compressing. (d) The chemically cured printed cuboid after completely swelling in DI water at room temperature. The photo background is  $5 \times 5$  mm grid.

Subsequently, a 16-layer “U-shape” structure ( $10 \times 10 \times 8$  mm) and an 18-layer “T-shape” structure ( $10 \times 10 \times 9$  mm) were designed and printed under an extrusion pressure of 190 kPa. The 3D constructs were printed successfully with high shape fidelity and,

exhibited an excellent mechanical flexibility after chemical curing (**Fig. 4.46**). In general, the thermoresponsive POx-*b*-POzi diblock copolymer lays a foundation for the excellent printability of the POx-*b*-POzi/DMAA/clay hybrid system in high shape fidelity, while the DMAA allows chemical curing of the printed constructs post-fabrication to result in an excellent mechanical flexibility with high stretchability.

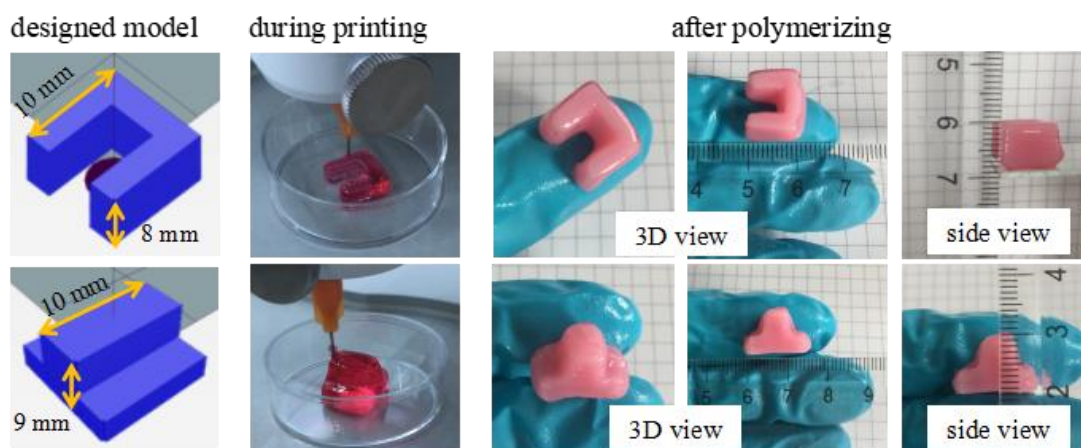


Fig. 4.46| 3D printing of various constructs, and the corresponding printed results after chemical curing (dyed red by carmine). The photo background is  $5 \times 5$  mm grid.

#### 4.3.2.6 Conclusion

In conclusion, a 3D printable POx-based POx-*b*-POzi/DMAA/clay ternary hybrid hydrogel was developed, which can be further chemically cured by free radical polymerization (**Fig. 4.47**). The resulting POx-*b*-POzi/PDMAA/clay hydrogels represent a clay reinforced IPN with good mechanical flexibility and high stretchability. Good 3D printability was demonstrated by the printing of various structures with high stackability and shape fidelity. As expected, the chemical crosslinking treatment eliminates the original reversible thermogelation property of the POx-*b*-POzi based hybrid system, and resulting in a long-term mechanical stable hydrogel. The added clay improved both the printability and mechanical properties of the final IPN hybrid hydrogel. Hopefully, the novel hybrid IPN hydrogel presented here would expand the material toolbox available for extrusion-based 3D printing community, and may be interesting for a wide range of applications including TE, drug delivery, soft robotics, and AM in general. Additionally, it

is also expected to further promote the application of POx-based materials in the field of hydrogels.

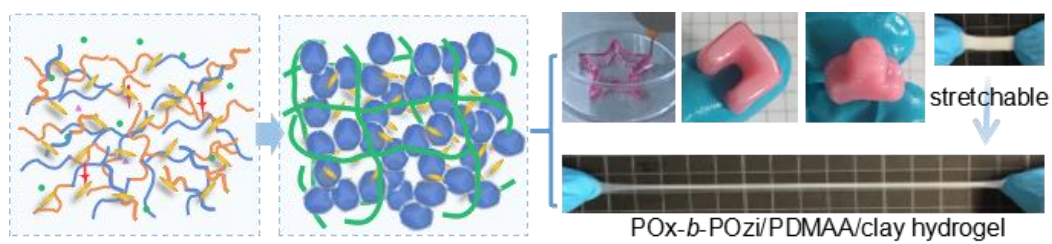


Fig. 4.47| Development of a 3D printable and highly stretchable ternary organic-inorganic POx-*b*-POzi/PDMAA/clay hybrid hydrogel.

### 4.3.3 PMeOx-*b*-PnPrOzi/Alg/clay Hybrid Hydrogels

As highlighted in the introduction, the further development of 3D bioprinting technology highly depends upon the availability of suitable bioinks. In this part, an advanced hybrid hydrogel bioink was developed based on the synthetic POx-*b*-POzi/clay thermogelling system described above and a natural polysaccharides sodium alginate. Again, systematical investigations were conducted on this newly proposed hydrogel, in terms of their preparation, characterization, rheological property, mechanical property, extrusion-based printability, as well as the cell-laden printing capability.

*The work described in this subchapter was already published: “A thermogelling organic-inorganic hybrid hydrogel with excellent printability, shape fidelity and cytocompatibility for 3D bioprinting” by C. Hu; T. Ahmad; M. S. Haider; L. Hahn; P. Stahlhut; J. Groll and R. Luxenhofer published recently in Biofabrication, 2022, 14, 025005.<sup>[464]</sup> The text and figures of the following pages 106-128 are may identical with the publication with permission.*

#### 4.3.3.1 Preparation of POx-*b*-POzi/Alg/clay Hybrid Hydrogel

In preliminary hydrogel composition optimizing experiments, hydrogels with various compositions were prepared and analyzed with regards to their thermogelling property (**Tab. 4.7**, and **Fig. 4.48**). In specific, 20 wt% POx-*b*-POzi diblock copolymer was combined with 1, 2 and 3 wt% sodium alginate, respectively. The temperature sweep results of these precursor mixtures showed that higher weight concentrations of sodium alginate make the precursor mixture solution highly viscous and, thus increased loss factor  $\tan \delta$  ( $G''/G'$ , mainly due to the significantly increase in  $G''$  representing for viscous character) resulting in a weakened thermogelling property. Therefore, unless otherwise noted, the precursor mixture with 20 wt% POx-*b*-POzi and 1 wt% sodium alginate was chosen for the detailed investigations, named shortly as POx-*b*-POzi/Alg (20/1; w/w) in the following. Furthermore, a clay added ternary mixture with 20 wt% POx-*b*-POzi, 1

wt% alginate and 1.5 wt% clay was prepared and investigated as well in this study, which is named shortly as POx-*b*-POzi/Alg/clay (20/1/1.5; w/w) in the following.

Table 4.7| Compositions of the hydrogels studied in this work. \*

sample	compositions (% w/w)		
	POx- <i>b</i> -POzi	Alg	clay
<b>POx-<i>b</i>-POzi/Alg</b>	<b>20</b>	<b>1</b>	-
POx- <i>b</i> -POzi/Alg	20	2	-
POx- <i>b</i> -POzi/Alg	20	3	-
<b>POx-<i>b</i>-POzi/Alg/clay</b>	<b>20</b>	<b>1</b>	<b>1.5</b>

\* Post-crosslinking by 1 wt% (0.09 mol L<sup>-1</sup>) CaCl<sub>2</sub>, or 0.3 mol L<sup>-1</sup> FeCl<sub>3</sub>·6H<sub>2</sub>O or 0.3 mol L<sup>-1</sup> TbCl<sub>3</sub>·6 H<sub>2</sub>O accordingly. Dyed by carmine in where needed.

\* Unless otherwise noted, the POx-*b*-POzi/Alg (20/1 wt%) and POx-*b*-POzi/Alg/clay (20/1/1.5 wt%) hydrogels which were marked in bold were used for further study.

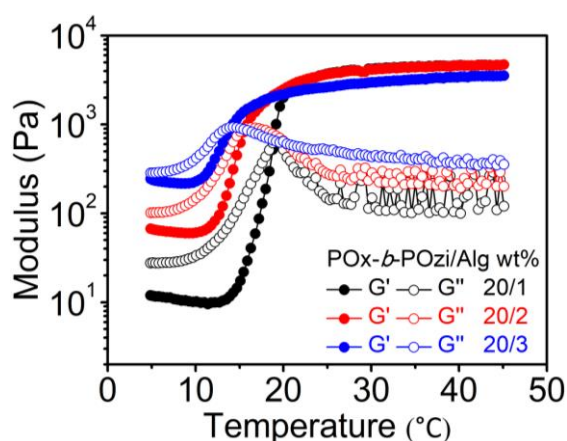


Fig. 4.48| Thermogelling property of the POx-*b*-POzi/Alg hydrogel precursor solutions with a constant POx-*b*-POzi copolymer concentration of 20 wt% and various Alg concentration from 1 to 3 wt%.

Specifically, the POx-*b*-POzi/Alg/clay hybrid hydrogel was prepared using a two-step approach (**Fig. 4.49 a**). In the first step, the dry components of clay, Alg and POx-*b*-POzi were added in the desired ratios in sequence into the DI water, and then allowed to dissolve at 7 °C to obtain a homogeneous solution. Subsequently, the mixture was placed at warm to room temperature for few minutes allowing to trigger and complete the thermogelation. It should be noted that the thermogelation behavior at this point is

completely reversible upon heating/cooling, which is highly beneficial as it facilitates mixing of the material such as cells and (air-bubble free) filling of the syringe in the cold, liquid state (**Fig. 4.49 b**). In the second step, the hydrogel was allowed immersing into a 1 wt% (0.09 M)  $\text{CaCl}_2$  solution overnight at room temperature, to trigger the ionotropic crosslinking of Alg, resulting in a mechanical flexible  $\text{POx-}b\text{-POzi/Alg/clay}$  hybrid hydrogel.

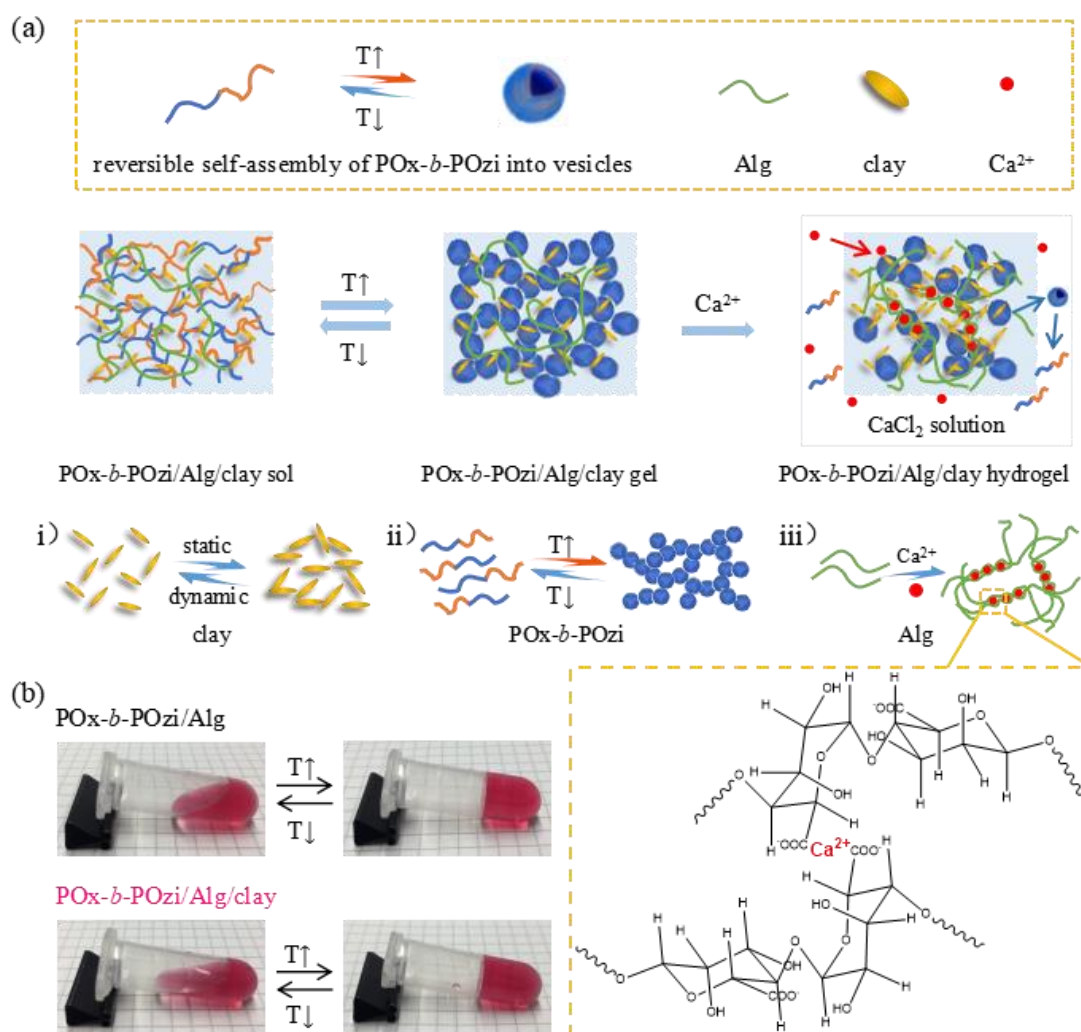


Fig. 4.49| (a) Schematic illustration for the preparation of  $\text{POx-}b\text{-POzi/Alg/clay}$  hydrogel via the strategy of thermogelation and subsequent ionic crosslinking of Alg with  $\text{Ca}^{2+}$ . (b) Photographs demonstrating the thermo-reversible sol-gel transition of  $\text{POx-}b\text{-POzi/Alg}$  and  $\text{POx-}b\text{-POzi/Alg/clay}$  hydrogel precursor solutions before ionic crosslinking (dyed by carmine).

During this physically ionic crosslinking process, free  $\text{Ca}^{2+}$  ions diffused into the hydrogel networks and crosslinked the Alg polymer chain through coordination with -



COO<sup>-</sup> groups. Concomitantly, significant amount of the POx-*b*-POzi diblock copolymer diffused out of the hydrogel network gradually and dissolved in the CaCl<sub>2</sub> solution bath, especially in the first 2 h, as demonstrated by a decreasing in the gel content (**Fig. 4.50 a**). The POx-*b*-POzi/Alg hybrid hydrogel without clay was also prepared in the same way.

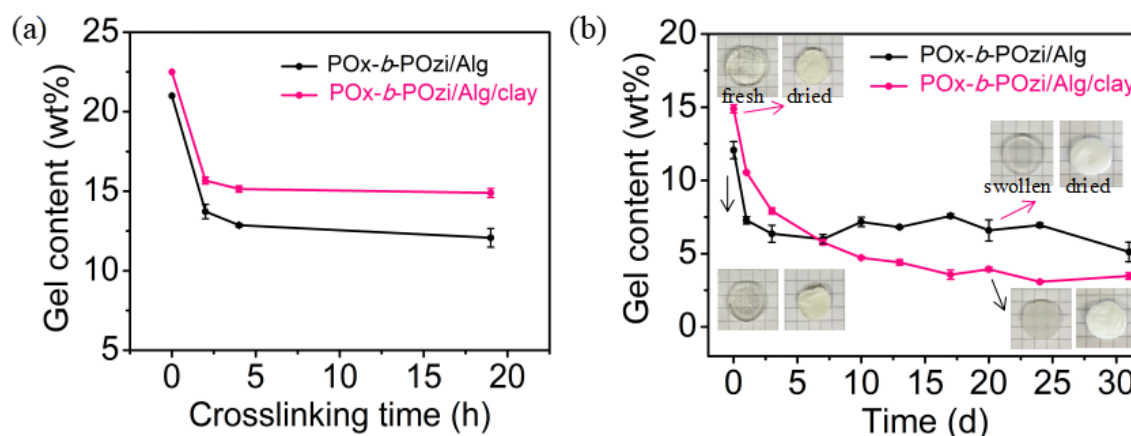


Fig. 4.50| (a) Ionic crosslinking time dependent gel content of the hydrogels. (b) Determination of gel content of the hydrogels after Ca<sup>2+</sup> crosslinking in DI water at 37 °C. Insert photographs represented the corresponding hydrogel appearance at different stages, the background is 5 × 5 mm grid.

Subsequently, the long-term stability of the hybrid hydrogels in DI water was evaluated over a one-month period by measuring the solid/gel content over time (**Fig. 4.50 b**). Both POx-*b*-POzi/Alg and POx-*b*-POzi/Alg/clay hybrid hydrogel experienced an obvious decrease of gel content, especially in the first day, and then reached a plateau after 7 days. Finally, a solid content of around 6.6 wt% for POx-*b*-POzi/Alg hydrogel, 4.1 wt% for POx-*b*-POzi/Alg/clay hydrogel were determined, respectively. At this point, we assumed that predominantly the POx-*b*-POzi diblock copolymer is leached from the hydrogel network while the ionically crosslinked Alg and clay nanoplatelets remain behind. However, some copolymer must remain trapped in the hydrogel network to explain the final solid content. It is important to note that the shape and dimension of the hydrogels did not suffer any visible change, which is very favorable as this may avoid the need for complex calculations for swelling or shrinkage of 3D printed constructs (the insert photographs in **Fig. 4.50 b**).

Furthermore, the swelling behavior of the hybrid hydrogels were studied with respect to their swelling kinetics in DI water at room temperature until the equilibrium was reached (**Fig. 4.51**). Both the hydrogels showed a fast swelling rate in an initial stage, and gradually plateaued off at an equilibrium swelling ratio of 480% for the POx-*b*-POzi/Alg hybrid hydrogel, and 840% for the POx-*b*-POzi/Alg/clay hybrid hydrogel. Regarding the significant higher equilibrium swelling ratio determined for the POx-*b*-POzi/Alg/clay hydrogel when compared with the POx-*b*-POzi/Alg hybrid hydrogel, we would attribute it to the presence of highly hydrophilic component clay Laponite XLG.

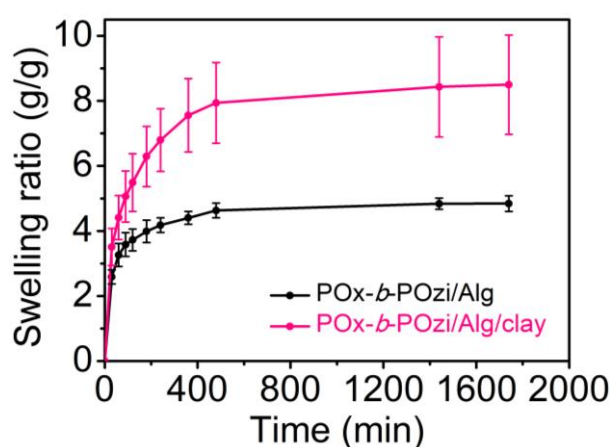


Fig. 4.51| Swelling behavior of the hydrogels in water at room temperature.

SEM images of the hybrid hydrogels after 7 days extraction (POx-*b*-POzi/Alg extr. and POx-*b*-POzi/Alg/clay extr.) suggested that the hydrogels network become more uniform with significant thinner pore walls in comparison with the freshly prepared hydrogels (**Fig. 4.52**). Yellow arrows in Fig. 4.52-left were added as a guide for eye to the thick patches of hydrogel pore walls. Here, it should keep in mind that the materials were freeze-dried before SEM, which might change the internal structure. Interestingly, for the POx-*b*-POzi/Alg/clay hybrid hydrogel, it appears that a typical layered house-of-cards structure of clay Laponite XLG can be observed after 7 days thoroughly extraction. As the majority of POx-*b*-POzi is extracted out, the clay appears to dominant hydrogel network morphology. Presumably, in the hydrogel network, the ionic crosslinked Alg and remaining very less POx-*b*-POzi diblock copolymer bind with the clay nanoplatelets *via* electrostatic and H-bonding interaction.

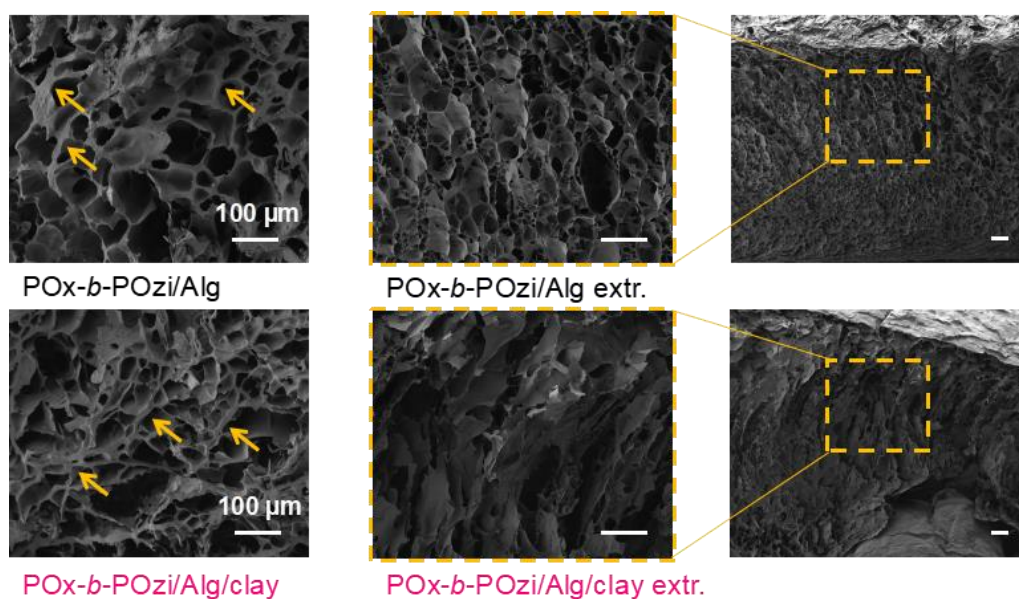


Fig. 4.52| SEM images of the hydrogels before (POx-b-POzi/Alg; POx-b-POzi/Alg/clay), and after (POx-b-POzi/Alg extr.; POx-b-POzi/Alg/clay extr.) thorough extraction. The yellow arrow added as a guide for the eye to thick patches of hydrogel pore walls.

#### 4.3.3.2 Rheological Properties of POx-b-POzi/Alg/clay Precursor Solution

Rheological measurements were carried out to understand the viscoelastic property and to predict the printability of the hydrogel precursors.<sup>[50, 267]</sup> Initially, a dynamic oscillation temperature sweep was performed to investigate the thermogelling behavior of the samples, wherein the intersection of  $G'$  and  $G''$  defines as the gelation point and the corresponding temperature as the  $T_{gel}$  (Fig. 4.53). Like the reported pristine POx-b-POzi

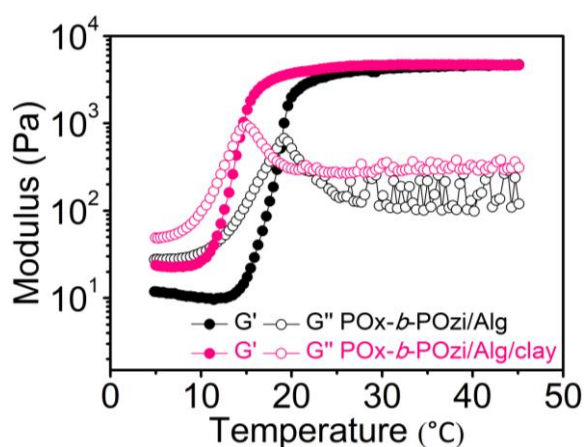


Fig. 4.53| A plot of the temperature sweep from 5 to 45 °C of the POx-b-POzi/Alg and POx-b-POzi/Alg/clay hydrogel precursor solutions.

hydrogel ( $T_{\text{gel}} \approx 17 \text{ }^{\circ}\text{C}$ ,  $G'_{\text{max}} \approx 3.3 \text{ kPa}$ ),<sup>[447, 450]</sup> the POx-*b*-POzi/Alg/clay and POx-*b*-POzi/Alg mixtures exhibited a typical and comparable thermogelling behavior with an increased  $G'_{\text{max}} \approx 4.5 \text{ kPa}$ . Addition of Alg lead to a slight increase in the  $T_{\text{gel}} (\approx 19 \text{ }^{\circ}\text{C}$  for POx-*b*-POzi/Alg). In contrast, when also clay was added, a minor decrease in the  $T_{\text{gel}} (\approx 15 \text{ }^{\circ}\text{C}$  for POx-*b*-POzi/Alg/clay) was observed. Notably again, such remarkable thermoresponsive sol-gel transition is generally very beneficial for (bio)ink material handling.

An amplitude sweep was carried out to determine the LVE range (**Fig. 4.54 a**). Clearly, the clay addition leads to a larger LVER, which is in line with observations for the plain POx-*b*-POzi system.<sup>[450]</sup> Subsequently, dynamic frequency sweeps under a constant strain of 0.1% (within the LVER) showed a dominating  $G'$  value over  $G''$  in the whole investigated frequency range of 0.1-100  $\text{rad s}^{-1}$ , indicating a stable solid-like gel character (**Fig. 4.54 b**).

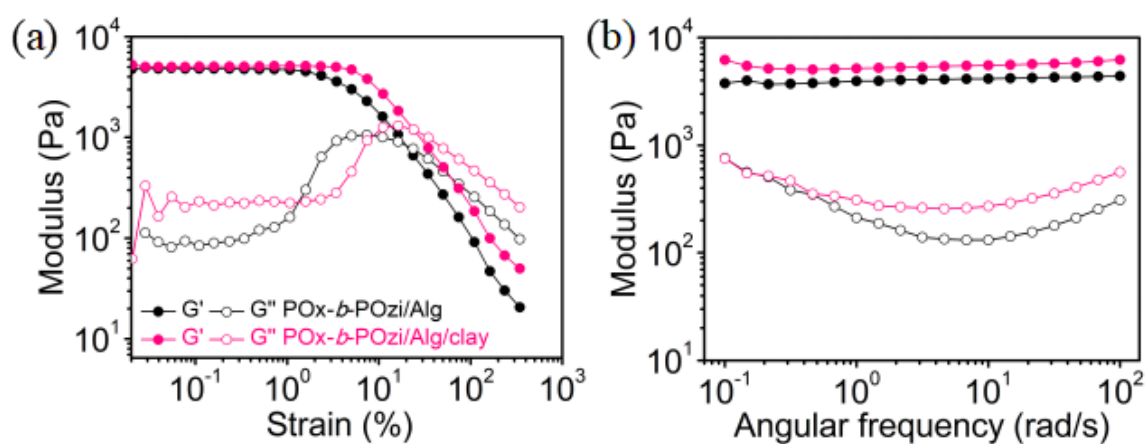


Fig. 4.54| Rheological characterization of the POx-*b*-POzi/Alg and POx-*b*-POzi/Alg/clay hydrogel precursor solutions. (a) Amplitude sweeps performed under a constant angular frequency of  $10 \text{ rad s}^{-1}$  to determine the LVE range. (b) Frequency sweep performed under an applied strain of 0.1%.

Subsequently, from the dynamic oscillatory stress sweep, a well improved yield stress  $\approx 210 \text{ Pa}$  was determined for POx-*b*-POzi/Alg/clay mixture, compared to only  $\approx 80 \text{ Pa}$  for POx-*b*-POzi/Alg (**Fig. 4.55 a**). Such pronounced yield stress improvement was corroborated in a rotational steady stress sweep, which yielded  $\approx 180 \text{ Pa}$  for POx-*b*-

POzi/Alg/clay and  $\approx 90$  Pa for POx-*b*-POzi/Alg (**Fig. 4.55 b**). Compared with the yield stress of  $\approx 140$  Pa for plain POx-*b*-POzi hydrogel,<sup>[450]</sup> it appears that the addition of 1 wt% Alg generally decreases the yield stress of the POx-*b*-POzi diblock copolymer system while clay addition increases it and overcompensates the loss from Alg addition.

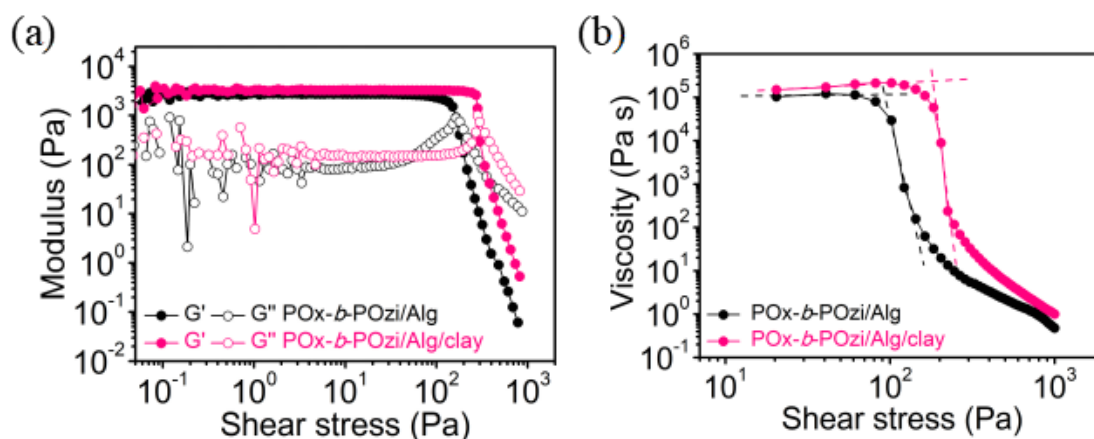


Fig. 4.55 | Yield point characterization of the hydrogel precursor solutions. (a) Development of  $G'$  and  $G''$  modulus with increasing shear stresses. (b) Applied shear stress dependent viscosity of the hydrogel precursor solutions at 37 °C. The intersection of dashed lines is commonly referred to as the yield point.

Furthermore, another important parameter, namely the shear-thinning character of the materials, was investigated. For both mixtures, a remarkable viscosity decreasing over five orders of magnitude was observed along with the increasing of shear rate from 0.01 to 1000  $s^{-1}$ , indicating their pronounced shear-thinning behavior (**Fig. 4.56 a**). By fitting the shear rate-viscosity profile using a power-law expression, the flow index  $n$  and consistency index  $K$  were obtained. As we observed before in chapter 4.3.1 for POx-*b*-POzi/clay, the clay addition led to an enhanced shear-thinning character (POx-*b*-POzi/Alg/clay;  $n = 0.07$  and  $K = 368.4$  vs POx-*b*-POzi/Alg;  $n = 0.14$  and  $K = 246.5$ ). Important to note, the addition of Alg does lead to an increased system viscosity, irrespective of shear and temperature, which is considered directly relevant for e.g., dispersing cells into the hydrogel or others handling.

Finally, a rapid viscosity recovery property was observed for both mixtures (**Fig. 4.56 b**). Such pronounced instantaneously viscosity recovery upon the altering of applied shear

rate from high ( $100 \text{ s}^{-1}$ ) to low ( $0.1 \text{ s}^{-1}$ ) is highly desirable for materials used for extrusion-based 3D bioprinting. Because this, together with the shear-thinning property, can facilitate an efficient extrusion of the bioink through fine nozzles without affecting the cell viability, and subsequently retain the shape of the printed objects with high-fidelity upon deposited onto the print-bed.

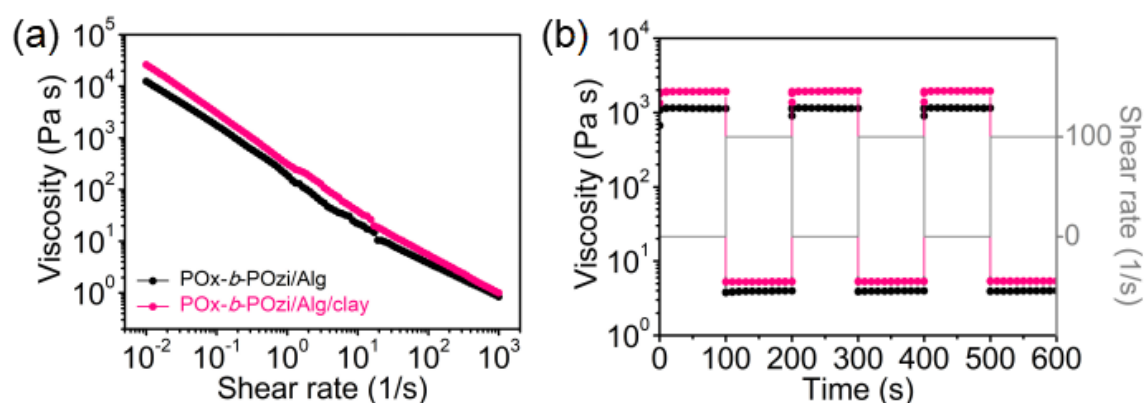


Fig. 4.56| (a) Shear thinning behavior of the hydrogel precursor solutions. (b) Recovery property under alternative applied shear rate of  $0.1 \text{ s}^{-1}$  and  $100 \text{ s}^{-1}$  of the POx-*b*-POzi/Alg (black line) and POx-*b*-POzi/Alg/clay (magenta line) hydrogel precursor solutions.

In summary, the rheological analysis results revealed that both POx-*b*-POzi/Alg and POx-*b*-POzi/Alg/clay hybrid systems exhibited a thermogelling behavior with pronounced shear-thinning and rapid viscosity-recovery properties, suggesting their great potential as ink material for extrusion-based bioprinting. However, in comparison, the POx-*b*-POzi/Alg/clay is supposed to be a better bioink candidate, not only due to the already reported bioactive effect of clay in biological study, but also because of the comprehensively improvement in rheological property by clay addition, in specific the enhance shear thinning character and yield stress, which are the crucial parameters for excellent printing performance prediction. The rapid thermogelation, shear-thinning and structure recovery of the hydrogel precursor solutions is excellently suited for temporarily maintaining of the printed shapes. However, any additional mechanical stress or excess water or aqueous media addition after printing would destroy and dissolve the printed structures easily. To prevent this, the influence of ionic crosslinking of Alg component in the present hybrid material after printing is studied next.

### 4.3.3.3 Mechanical Properties of POx-*b*-POzi/Alg/clay Hydrogel

During and after the ionic curing by  $\text{Ca}^{2+}$ , the mechanical properties of the hybrid hydrogels were evaluated by rheological frequency sweep and mechanical compression tests. Initially, dependence of the average elastic module  $G'$  on angular frequency after different crosslinking times was measured (**Fig. 4.57**). During incubation in  $\text{CaCl}_2$  solution, free  $\text{Ca}^{2+}$  ions diffuse into hydrogel network and crosslinked the Alg, resulting in a gradually stiffening hydrogel, as reflected by the continuous increase in  $G'$ . Both POx-*b*-POzi/Alg and POx-*b*-POzi/Alg/clay hydrogels reached a plateau after 4 h, and showed the maximum  $G'$  of  $32.4 \pm 3.3$  kPa and  $29.2 \pm 2.6$  kPa, respectively, suggesting a  $G'$  increase of more than 6-fold in comparison with the non-crosslinked samples.

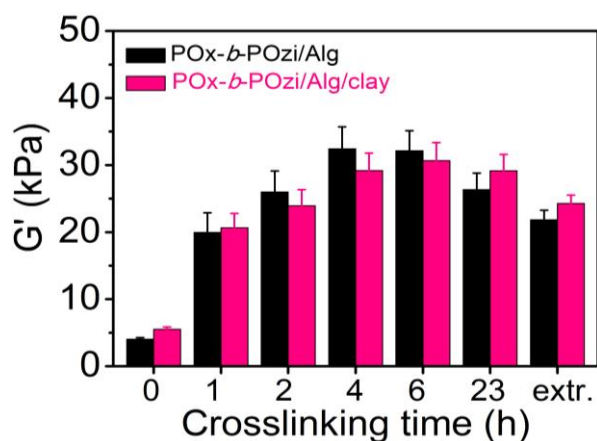


Fig. 4.57| Development of storage moduli ( $G'$ ) of POx-*b*-POzi/Alg and POx-*b*-POzi/Alg/clay hydrogels over time after addition of  $\text{Ca}^{2+}$  as a crosslinker. The  $G'$  after extensive extraction are shown for comparison.

Of course, the required crosslinking time is highly dependent on the hydrogel dimensions, i.e., the needed crosslinking time will increase when the thickness of hydrogel increases, and vice versa. After 23 h immersing in  $\text{CaCl}_2$  solution, a minor decrease of  $G'$  was observed, which can be attributed to the continuous extraction of POx-*b*-POzi copolymer from the hydrogels (**Fig. 4.50 a**). In fact, after 7 days of thorough extraction, the hydrogels reached a swelling equilibrium whereby the  $G'$  decreased slightly to  $21.8 \pm 1.4$  kPa for POx-*b*-POzi/Alg and  $24.3 \pm 1.2$  kPa for POx-*b*-POzi/Alg/clay. No significant differences in  $G'$  values between the  $\text{Ca}^{2+}$  ionically crosslinked hydrogels were found.

Subsequently, mechanical compression testing was conducted on the hybrid hydrogels after ionic crosslinking by  $\text{Ca}^{2+}$  (**Fig. 4.58**, and **Tab. 4.8**). It was found that the compressive stress at break for POx-*b*-POzi/Alg/clay hydrogel ( $238 \pm 13$  kPa) was slightly higher while comparable to the POx-*b*-POzi/Alg hydrogel ( $204 \pm 14$  kPa). In contrast, the compressive Young's modulus of POx-*b*-POzi/Alg/clay hydrogel ( $94.6 \pm 9.1$  kPa) was improved significantly due to the addition of clay Laponite XLG, and was around 3 times higher than that for the POx-*b*-POzi/Alg hydrogel ( $35.0 \pm 0.6$  kPa).

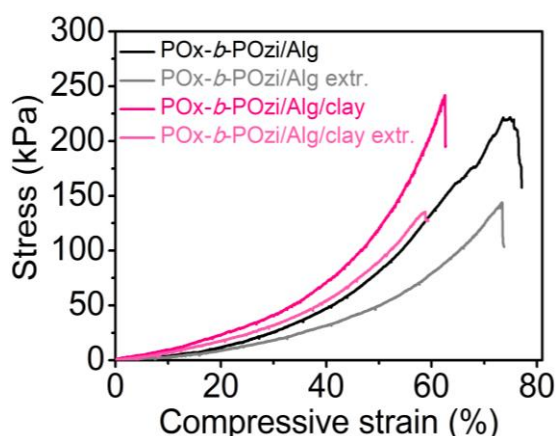


Fig. 4.58| Stress-strain curve under compression for various hydrogel samples before and after extensive extraction in DI water.

Table 4.8| Compression testing of the hydrogels. #

hydrogels	Young's modulus (kPa)	compression strength (kPa)	breaking strain (%)
POx- <i>b</i> -POzi/Alg	$35.0 \pm 0.6$	$203.8 \pm 14.4$	$72.2 \pm 4.3$
POx- <i>b</i> -POzi/Alg extr.#	$30.5 \pm 0.9$	$139.4 \pm 2.8$	$72.4 \pm 0.8$
POx- <i>b</i> -POzi/Alg/clay	$94.6 \pm 5.9$	$237.9 \pm 13.4$	$61.9 \pm 1.1$
POx- <i>b</i> -POzi/Alg/clay extr.#	$65.5 \pm 9.1$	$131.3 \pm 3.8$	$57.8 \pm 2.5$

# The compression testing of hydrogels was carried out after immersion in DI water for 7 d. The DI water was exchanged every day.

Moreover, after reaching the swelling equilibrium in DI water, both the compressive strength and Young's modulus of the two hybrid hydrogels decreased obviously, which became  $131.3 \pm 3.8$  kPa and  $65.5 \pm 9.1$  kPa for POx-*b*-POzi/Alg/clay hydrogel, and  $139.4 \pm 2.8$  kPa and  $30.5 \pm 0.9$  kPa for POx-*b*-POzi/Alg hydrogel, respectively. Interestingly,



compared with the POx-*b*-POzi/Alg hydrogel, the Young's modulus decreasing was more obvious in case of POx-*b*-POzi/Alg/clay hybrid hydrogel, which can be attributed to the higher swelling degree of the latter, absorbing more water and thus had a bigger impact. Additionally, there was no significant difference observed in the fracture strain before and after extraction (**Tab. 4.8**).

Finally, photographs during the compression test of POx-*b*-POzi/Alg/clay hybrid hydrogel was shown in **Fig. 4.59**. Combining with the measured stress-strain curve described above, this hydrogel is mechanical stable to sustain a compressive deformation to some extent, although it fractured eventually under a relatively high deformation over 50%. In comparison with the POx-*b*-POzi/PDMAA/clay hybrid hydrogel (can sustain a large compressive deformation of 80% without visible collapsing) described in chapter 4.3.2, POx-*b*-POzi/Alg/clay hybrid hydrogel network is more brittle and fridge.

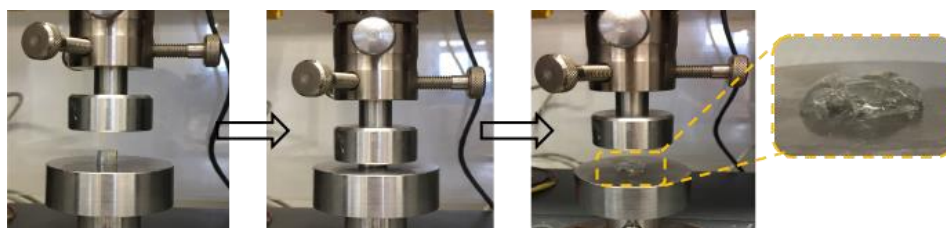


Fig. 4.59| Photographs during the compression test of POx-*b*-POzi/Alg hybrid hydrogel.

#### 4.3.3.4 3D Printing

3D printability of the hybrid hydrogel precursors was investigated by an extrusion-based 3D printer, the same one used in subchapter 4.3.2 (**Fig. 4.41**). Here, all the printing was performed at room temperature, and the printed structure was deposited on a heated 37 °C print-bed (a physiological relevant temperature above the  $T_{gel}$  of ink). Initially, a 12-layer hollow five-pointed star and a 12-layer grid were printed using POx-*b*-POzi/Alg under an extrusion pressure of 80 kPa. Subsequently, the printed structures were crosslinked by immersion into a CaCl<sub>2</sub> solution bath for 6 h. The final structures proved to be mechanical flexible and robust with respect to manual handling and compression (**Fig. 4.60 a-b**). This result suggested that the highly shear-thinning character and rapid

viscosity recovery property of the POx-*b*-POzi/Alg mixture allows the smooth extrusion of uniform filaments through the fine needle (23 G). More importantly, the obtained 3D structures remained geometrical stable without obvious volumetric swelling and collapse after 7 days incubation in DI water (**Fig. 4.60 b**).

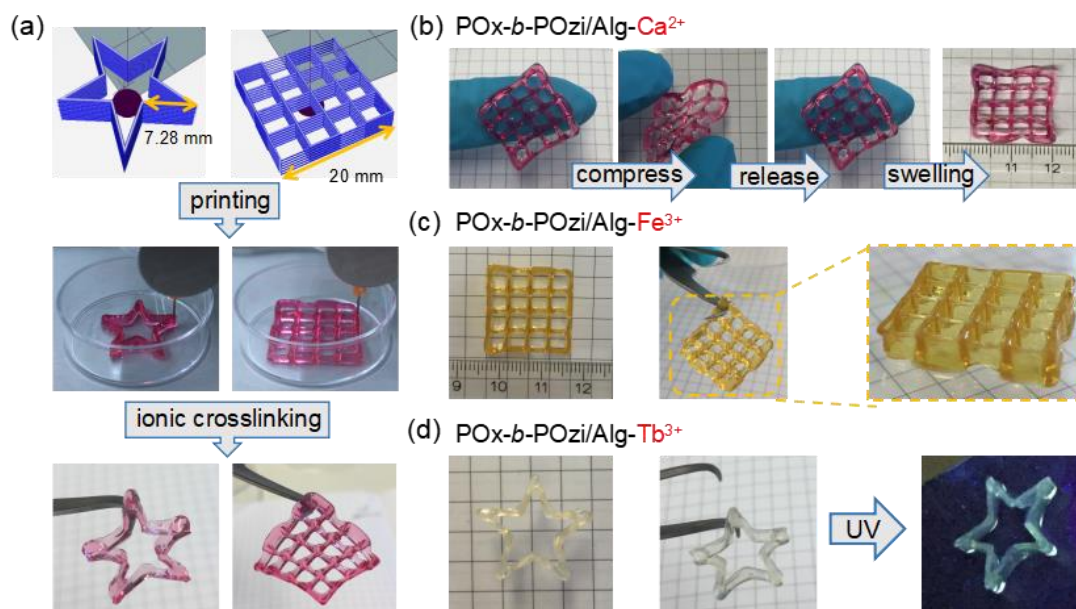


Fig. 4.60| Extrusion-based 3D printing of POx-*b*-POzi/Alg hydrogel ink. (a-b) Illustration of the CAD models of a 12-layer five-point star and a 12-layer grid and the 3D printing process. After printing, the structures were cured by immersion into a CaCl<sub>2</sub> solution by which removed the fugitive support ink concomitantly. The obtained structures were mechanical flexible under compressing, and remained stable after equilibrium swelling in DI water. Hydrogels dyed using carmine. As crosslinkers, also FeCl<sub>3</sub>·6H<sub>2</sub>O (c) and TbCl<sub>3</sub>·6H<sub>2</sub>O (d) were employed. Crosslinking using TbCl<sub>3</sub>·6H<sub>2</sub>O imparts photoluminescent (excitation under UV light) properties in the scaffolds. The photo background is 5 × 5 mm grid.

Alternatively, the printed structures are also be ionically cured using other multivalent cations, as demonstrated in this study by Fe<sup>3+</sup> and Tb<sup>3+</sup>, simply by exchanging the CaCl<sub>2</sub> aqueous solution to FeCl<sub>3</sub>·6H<sub>2</sub>O or TbCl<sub>3</sub>·6H<sub>2</sub>O aqueous solution. Consequently, the printed structures crosslinked by Fe<sup>3+</sup> appeared yellow, and the printed structures crosslinked by Tb<sup>3+</sup> were photoluminescent (**Fig. 4.60 c-d**). Although this aspect was not investigated in detail in this contribution, it should be clear that different crosslinking ions may have an impact on the mechanical properties. The successful printing of different 3D structures with high shape fidelity and mechanical flexibility demonstrated that POx-*b*-

POzi/Alg hybrid hydrogel can be a potential ink candidate for extrusion-based 3D printing technology.

Subsequently, the printability of three different hydrogel inks were investigated in detail, i.e., POx-*b*-POzi, POx-*b*-POzi/Alg and POx-*b*-POzi/Alg/clay.<sup>[266]</sup> Firstly, a serrated mold with a stepwise increasing gap from 1, 2, 4, 8 to 16 mm was utilized for the filament collapse test under an extrusion pressure of 110 kPa (**Fig. 4.61 a**). When using POx-*b*-POzi/Alg/clay as the ink, the printed strand could hang on the mold relatively stable even for a gap of up to 16 mm, with only a filament sagging after an extended time due to the gravity. In contrast, the hydrogel ink POx-*b*-POzi and POx-*b*-POzi/Alg were much weaker and the printed filament broken off quickly at a smaller bridging gap of only 4 and 8 mm, respectively.

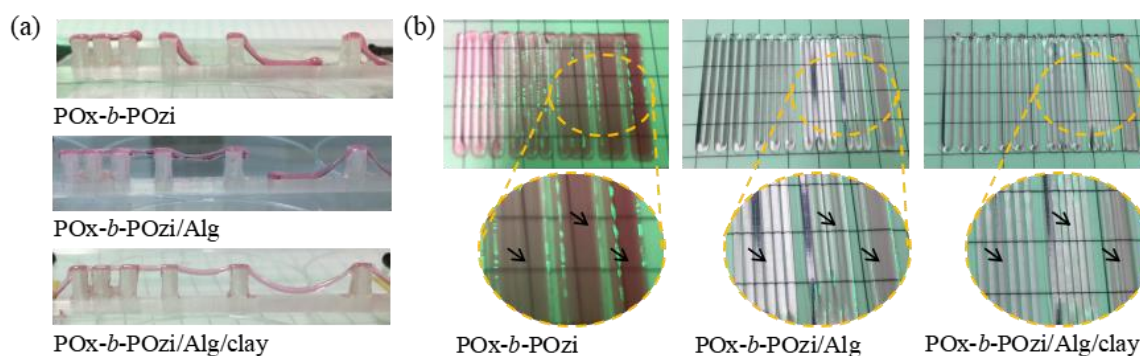


Fig. 4.61| (a) Filament collapse test of the hydrogel inks with a stepwise increase in gap from 1, 2, 4, 8 to 16 mm. (b) Filament fusion test of the hydrogel inks with a stepwise increasing strand-to-strand distance from 0.5, 0.75, 1.0, 1.25 to 1.5 mm.

For assessment of the filament fusion and the minimal printable strand-to-strand distance, a 2D pattern with a stepwise increasing strand-to-strand distance from 0.5 to 0.75, 1, 1.25 and 1.5 mm were printed, known as the filament fusion test (**Fig. 4.61 b**). Obviously, this test is highly dependent on the printing conditions such as printing speed, extrusion pressure and nozzle type. Here, all the printing tests were carried out with a 23 G needle with an inner diameter of 0.33 mm at a fixed printing speed of 4 mm s<sup>-1</sup> and extrusion pressure of 70 kPa. As expected, printability in an order of POx-*b*-POzi/Alg/clay > POx-*b*-POzi/Alg > POx-*b*-POzi was observed. For the hydrogel ink POx-*b*-POzi and

POx-*b*-POzi/Alg, obvious filament fusion was observed at strand-to-strand distances below 1.25 and 1 mm, respectively. In contrast, for the hybrid hydrogel ink POx-*b*-POzi/Alg/clay, the same pattern was printed nicely without any notable strand fusion. The printed strands remained excellently defined even at strand-to-strand distances at 0.5 mm. Again, the rheological benefit from the clay addition is clear and can be attributed specifically to the enhanced shear-thinning character and yield stress resulting in this significant improved filaments stackability and shape fidelity.

Accordingly, the printable height of 3D structures was extended successfully, as demonstrated here by the printing of a 24-layer grid and a 20-layer five-point star (**Fig. 4.62**). Even such a high construct did not buckle noticeably under their own weight. The intersections of the printed grid as well as the sharp corners of the printed star were all well resolved. Again, the mechanically stable and flexible hydrogel scaffolds were obtained after the ionic curing by  $\text{Ca}^{2+}$ . Importantly, the resulting 3D structures maintained their structural dimension and integrity excellently even after 7 days of incubation in DI water, and still exhibited a remarkable mechanical flexibility under a high compression deformation.

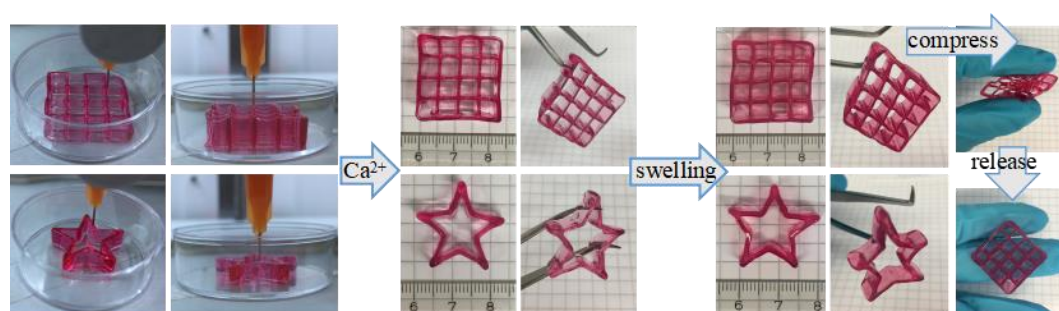


Fig. 4.62| 3D printing and ionic crosslinking of a 24-layer grid and a 20-layer star with POx-*b*-POzi/Alg/clay, and the corresponding performance after swelling 7 days.

Finally, for the demonstration purposes, a few of Arabic numerals were designed and printed in a high shape fidelity, which remained clear to identify after reaching swelling equilibrium (**Fig. 4.63 a**). More challenging, various structures featuring suspended filaments over 10 mm and separating in z-axis were printed successfully with high shape fidelity, without the requirement of any other additional sacrificial materials or support

baths (**Fig. 4.63 b**). The printed construct with a single-layer suspended mesh in middle is able to hold target objects for example molecular sieves granules, showing its relatively stable mechanical property and load-bearing capacity (**Fig. 4.63 c**). These demonstrates an extraordinary printability design freedom possible, and great potential in more sophisticated applications when using POx-*b*-POzi/Alg/clay hybrid hydrogel.

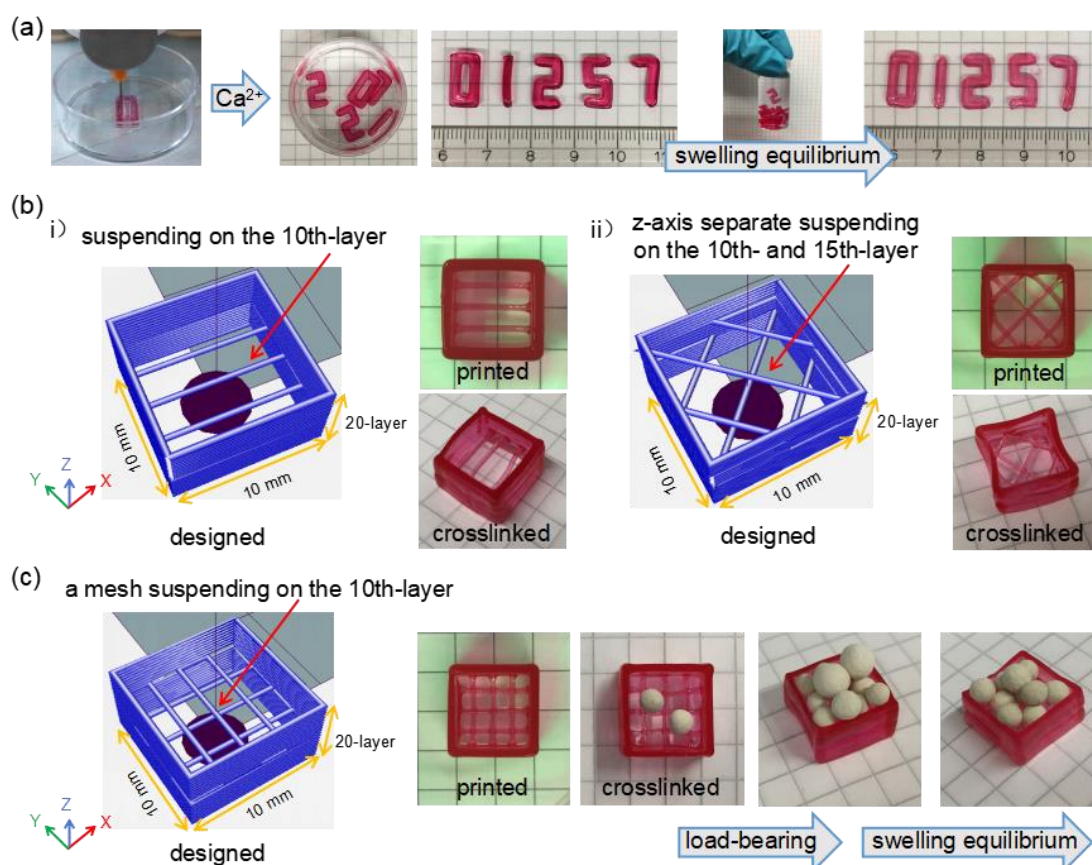


Fig. 4.63| (a) 3D printing of 4-layer numeral with POx-*b*-POzi/Alg/clay hydrogel ink. (b) 3D printing of different 20-layer constructs line-grids with suspended filaments able to hold molecular sieves granules. The extrusion pressure is 110 kPa. Scaffolds dyed using carmine. The photo background is 5 × 5 mm grid.

It is important to note that the layers (height) of the printing structures shown above is not the limit of this POx-*b*-POzi/Alg/clay hybrid hydrogel ink. The printable height of 3D structures can be extended further to over centimeters, i.e., the printing of taller structure, which is considered another major challenge in the field of 3D printing in addition to the printing of suspended structures. For demonstration purpose, a 60-layer hollow cube with a height of 18 mm was printed (**Fig. 4.64**).

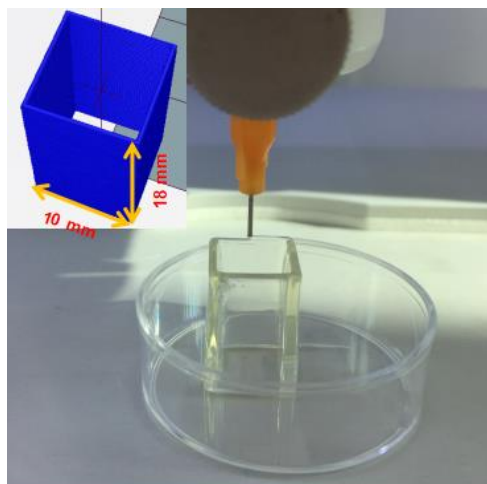


Fig. 4.64| 3D printing of a 60-layer hollow cube with POx-*b*-POzi/Alg/clay hydrogel ink.

#### 4.3.3.5 Cytocompatibility and 3D Cell-laden Printing

*This subchapter (4.3.3.5) was done in collaboration with Dr. Taufiq Ahmad. I was responsible for the preparation and 3D printing of the bioink. Dr. Taufiq Ahmad was responsible for taking care of the cells and collecting the data for analysis.*

In order to be considered as a suitable bioink, the developed hybrid hydrogel must be cytocompatible. Using the WST-1 assay, no significant reduction in metabolic activity of NIH 3T3 cells were observed when incubated with 1, 1.5, 5, and 10 wt% solutions of POx-*b*-POzi, POx-*b*-POzi/Alg, and POx-*b*-POzi/Alg/clay in growth media over 24 h (**Fig. 4.65 a**). In fact, the cell-laden hydrogel showed a significant increase in cell number from day 1 to day 3. Optical microscopy analysis revealed a throughout homogenous distribution of cells throughout in POx-*b*-POzi/Alg and POx-*b*-POzi/Alg/clay groups with distinct increase in cell number on day 3 (**Fig. 4.65 b**). In contrast, the cells in POx-*b*-POzi hydrogel started aggregation at day 1 and formed relatively large aggregates at day 3. This observation can be attributed to the gradually dissolution of POx-*b*-POzi in culture media to form a viscous solution, which resulted in cell aggregation and settlement at bottom of the culture plates. Therefore, we excluded the plain POx-*b*-POzi from further studies. Corroborating the impression from optical microscopy, WST-1 assay showed a significant increase in metabolic activity at day 3 in POx-*b*-POzi/Alg and POx-*b*-

POzi/Alg/clay groups indicating the proliferation of fibroblasts in gels with no significant difference between the groups (**Fig. 4.65 c**).

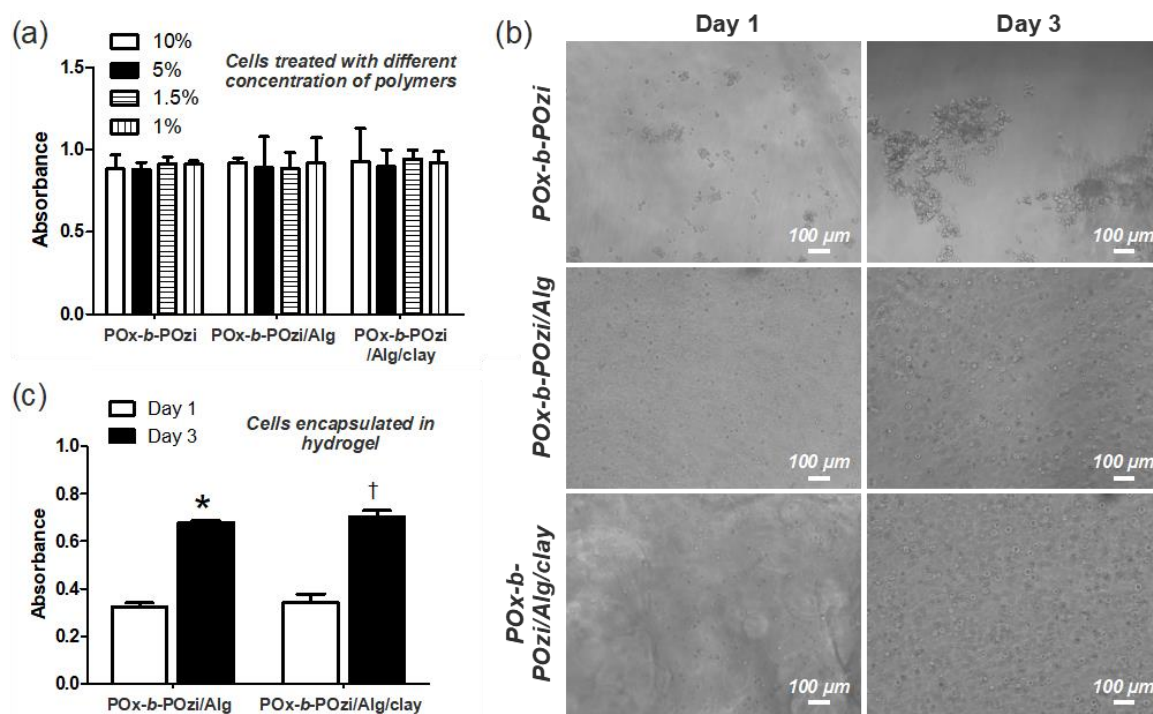


Fig. 4.65| Cytocompatibility of bioink. (a) WST-1 assay of fibroblast treated with different concentrations of POx-*b*-POzi, POx-*b*-POzi/Alg and POx-*b*-POzi/Alg/clay in growth media (n=4). (b) Optical microscope images of cell-laden POx-*b*-POzi, POx-*b*-POzi/Alg, and POx-*b*-POzi/Alg/clay hydrogels. (c) WST-1 assay of cell-laden POx-*b*-POzi/Alg and POx-*b*-POzi/Alg/clay (n=4). \* and † indicates  $P < 0.05$  compared to POx-*b*-POzi/Alg at day 1 and POx-*b*-POzi/Alg/clay at day 1, respectively.

Further, the distribution, proliferation, and viability of fibroblasts in the 3D bioprinted constructs were investigated. Herein, 8-layer grids with a base area of  $12 \times 12 \text{ mm}^2$  were printed using POx-*b*-POzi/Alg and POx-*b*-POzi/Alg/clay hybrid hydrogel bioinks, and then ionically crosslinked in  $\text{Ca}^{2+}$  solution for 10 min. Subsequently, the printed structures were transferred into growth culture media for cell culture. Important to note that the cells were distributed homogeneously in 3D bioprinted constructs of POx-*b*-POzi/Alg and POx-*b*-POzi/Alg/clay hydrogels (**Fig. 4.66**). The printed constructs using both hydrogel bioinks exhibited a good structural stability over 5 days of cell culture. Corroborating the results from cell-free printing, the POx-*b*-POzi/Alg/clay bioink exhibited a better printability. We should point out that the presence of cells and cell

culture media was not detrimental to the 3D printability, which is likely to be connected to the fact that the main bioink component relies on non-ionic polymer amphiphile. Again, the optical images suggested a significant increase in cell number from day 1 to day 5.

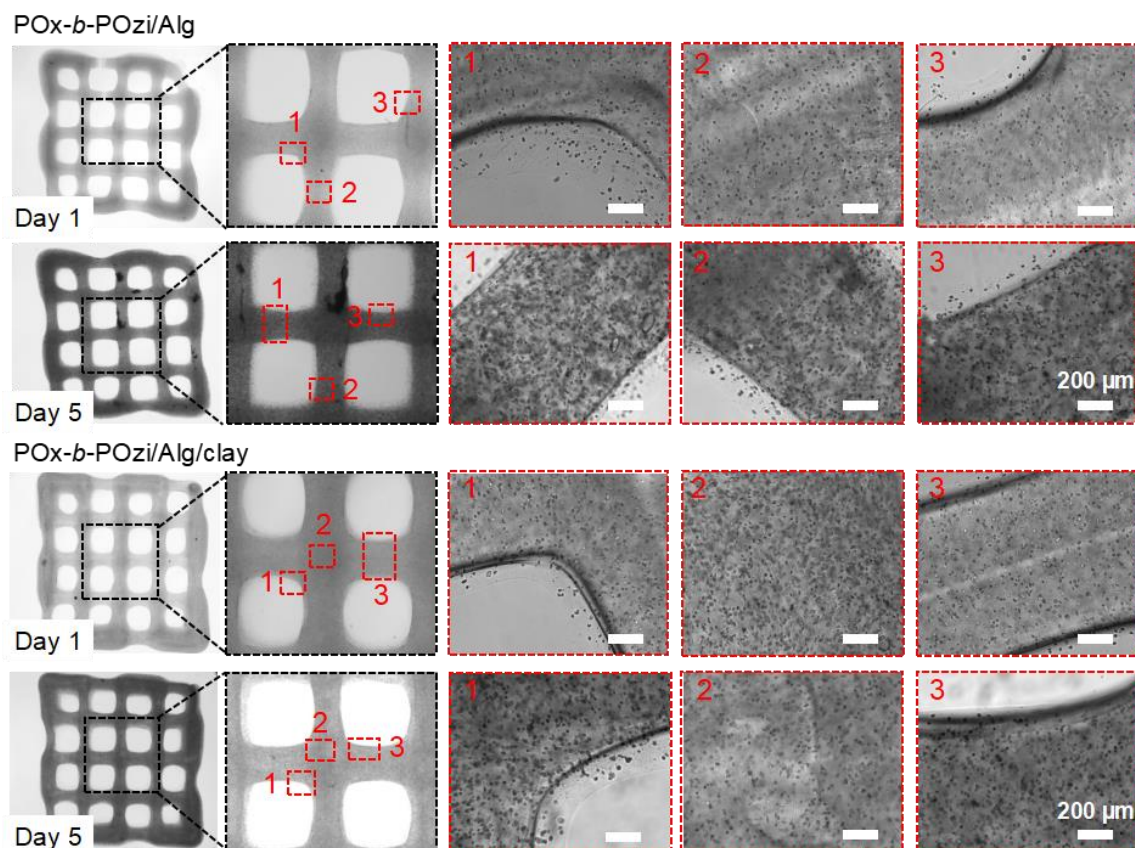


Fig. 4.66| Optical microscope images to visualize cell distribution at day 1 and day 5 in cell-laden 3D bioprinted 8-layer grids (12 × 12 mm) using *POx-b-POzi/Alg* and *POx-b-POzi/Alg/clay* bioinks, respectively. All printing were carried out under an extrusion pressure of 100 kPa. Scale bar 200 μm in all images.

Consistently, the DNA content in *POx-b-POzi/Alg* and *POx-b-POzi/Alg/clay* bioprinted structures increased significantly from day 1 to day 5 (Fig. 4.67 a). In *POx-b-POzi/Alg* and *POx-b-POzi/Alg/clay*, the DNA content increased about 1.6- fold at day 3 and about 2-fold at day 5. The *POx-b-POzi/Alg/clay* group exhibited a minor but statistically significant increase in DNA contents in comparison with the *POx-b-POzi/Alg* group at day 5. In addition, we evaluated the cells viability in *POx-b-POzi/Alg/clay* bioprinted samples at day 1 and day 5 using live/dead staining (Fig. 4.67 b). It is clearly apparent that the majority of cells were viable.



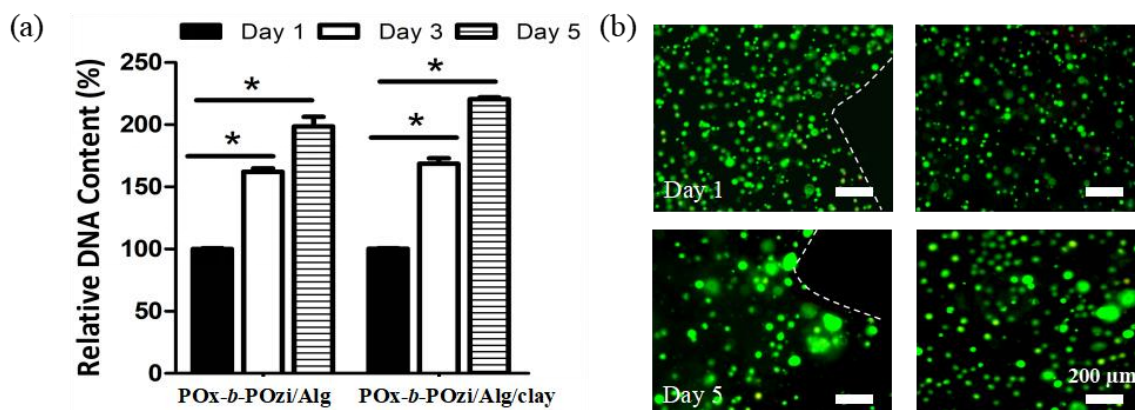


Fig. 4.67| (a) DNA quantification within POx-*b*-POzi/Alg and POx-*b*-POzi/Alg/clay bioprinted construct (n=6) demonstrating cells proliferation at day 1, day 3, and day 5. (b) Live and dead staining in bioprinted constructs using POx-*b*-POzi/Alg/clay at day 1 and day 5. \* indicate  $p < 0.05$ . All printing were carried out under an extrusion pressure of 100 kPa. Scale bar 200  $\mu\text{m}$  in all images.

Furthermore, we extended the culture time and evaluated the viability of cells in POx-*b*-POzi/Alg/clay bioprinted samples at day 1, 3, 5, 7, 14, and 21 using live/dead staining (**Fig. 4.68 a**). Again, it is clearly apparent that most cells were viable throughout the culture time. However, we observed that cells started to form aggregates from day 3, and we observed a significant increase in the size of cell aggregates with the passage of culture. We assumed that our bioink lacks the cell-adhesion cues, which eventually led to the clustering of proliferating cells. Further, we have seen migration of large aggregates (**Fig. 4.68a** at day 7) towards the periphery of bioink, which may be due to intrinsic pressure built in the bioink matrix by cell aggregates, which pushes them towards the edge. Similarly, at 14 and 21 days, cell aggregates at the periphery fused and formed large cell clusters at and around the bioink matrix. Apart from the aggregation, it is obvious that our developed bioink platform is highly cytocompatible, maintaining the viability of cells throughout the culture. However, we have observed very a few dead cells around the periphery near cell aggregates, which may be due to the large size of cell aggregates causing hypoxia. Finally, we performed immunofluorescence staining to evaluate the cell distribution in the bioink and the deposition of collagen type-I (**Fig. 4.68 b**). Overall, F-actin staining revealed the roundish morphology of single cells, which started the

formation of aggregates with time. Similarly, the deposition of collagen type-I increased with the passage of culture time.

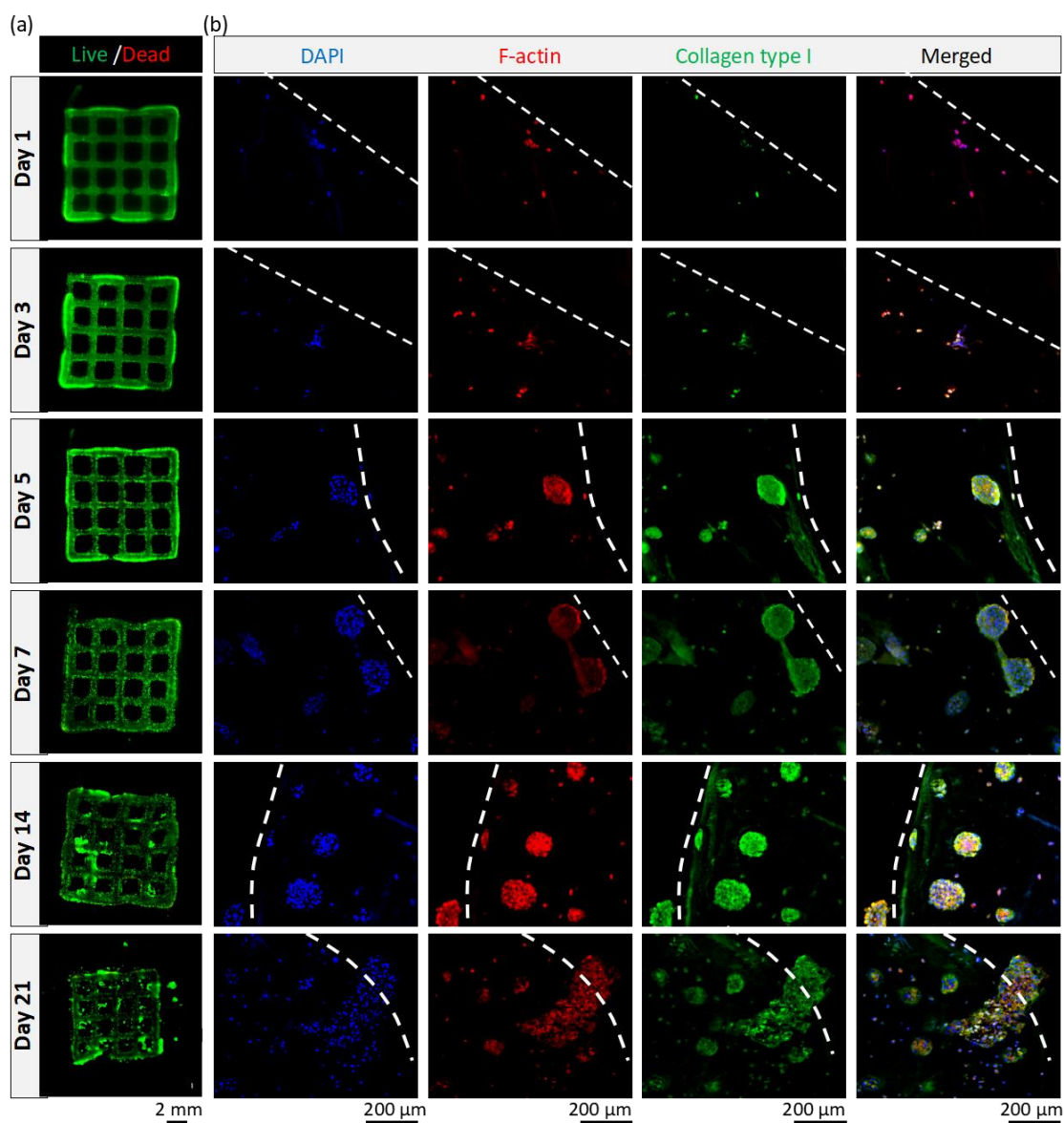


Fig. 4.68| Cells (NIH 3T3 fibroblasts) distribution, viability, and collagen type-1 deposition in POx-*b*-POzi/Alg/clay bioprinted constructs (a) Live and dead of cells in bioprinted constructs at day 1, 3, 5, 7, 14, and 21, scale bar = 2mm and (b) Immunostaining of cells in bioink (DAPI for nucleus, F-actin for cytoskeleton, and Collagen type-I) at day 1, 3, 5, 7, 14, and 21, white dotted line indicates edge of bioink, scale bar = 200 μm.

Important to note, at this point, the bioink does not contain any bio-instructive cues such as peptide moieties for effectively cell adhesion or functional differentiation; however, these can easily be introduced by modify the alginate with RGD or mixing with alternative bioactive materials like gelatin. In summary, this newly developed hybrid

hydrogel bioink exhibited excellent cytocompatibility, bio-printability and long-term structural stability, which may be opening new and improve paths to fabricate complex architectures whilst maintaining a cell-permissive environment. Although demonstrated only for alginate at this point, it should be obvious that this hybrid approach would be rather interesting for other bioink materials which may suffer from a less than optimal printability on their own.

#### 4.3.3.6 Conclusion

In this part, an advanced POx-*b*-POzi/Alg/clay hybrid hydrogel was introduced as a bioink for extrusion-based 3D bioprinting (**Fig. 4.69**). A dual-step crosslinking approach was presented that exploited a primary thermogelling of the diblock copolymer POx-*b*-POzi to achieve an improvement in rheological profiles beneficial for extrusion-based printing, while the secondary ionic crosslinking with Ca<sup>2+</sup> ions provided the long-term construct stabilization and mechanical flexibility. Excellent printability was demonstrated

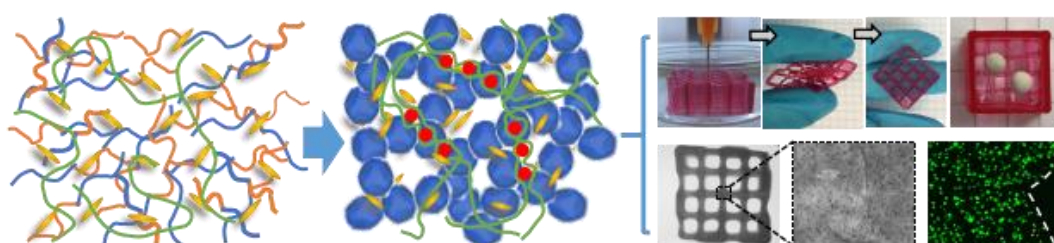


Fig. 4.69| A thermogelling organic-inorganic hybrid hydrogel with excellent printability, shape fidelity and cytocompatibility for 3D bioprinting.

by various constructs printing with high shape fidelity and layers stackability, and supported by a detailed rheological characterization. More importantly, the printing of very challenging constructs that have suspended filaments or a height over centimeters were achieved successfully with the POx-*b*-POzi/Alg/clay hybrid hydrogel. The post-printing ionic crosslinking of Alg could also be realized by other di/trivalent cations, as exemplified by using Fe<sup>3+</sup> and Tb<sup>3+</sup>. Additionally, the 3D cell-laden bioprinting using the hybrid hydrogel and post-printing crosslinking process using Ca<sup>2+</sup> ions demonstrated that this printing process was well tolerated by the embedded cells, highlighting the feasibility

of this novel hybrid hydrogels for 3D bioprinting applications. The presented hybrid approach, utilizing the beneficial properties of the thermogelling POx-*b*-POzi diblock copolymer base material should help to open new opportunities for the fabrication of complex architectures needed in the fields of drug delivery and biofabrication.

# 5 | Summary and Outlook



Motivated by the great potential offered by the combination of additive manufacturing technology and hydrogels, especially in the field of tissue engineering and regenerative medicine, a series of novel hybrid hydrogel inks were developed based on the recently described thermogelling poly(2-oxazoline)s-*block*-poly(2-oxazine)s diblock copolymers, which may help to expand the platform of available hydrogel inks for this transformative 3D printing technology (**Fig. 5.1**).

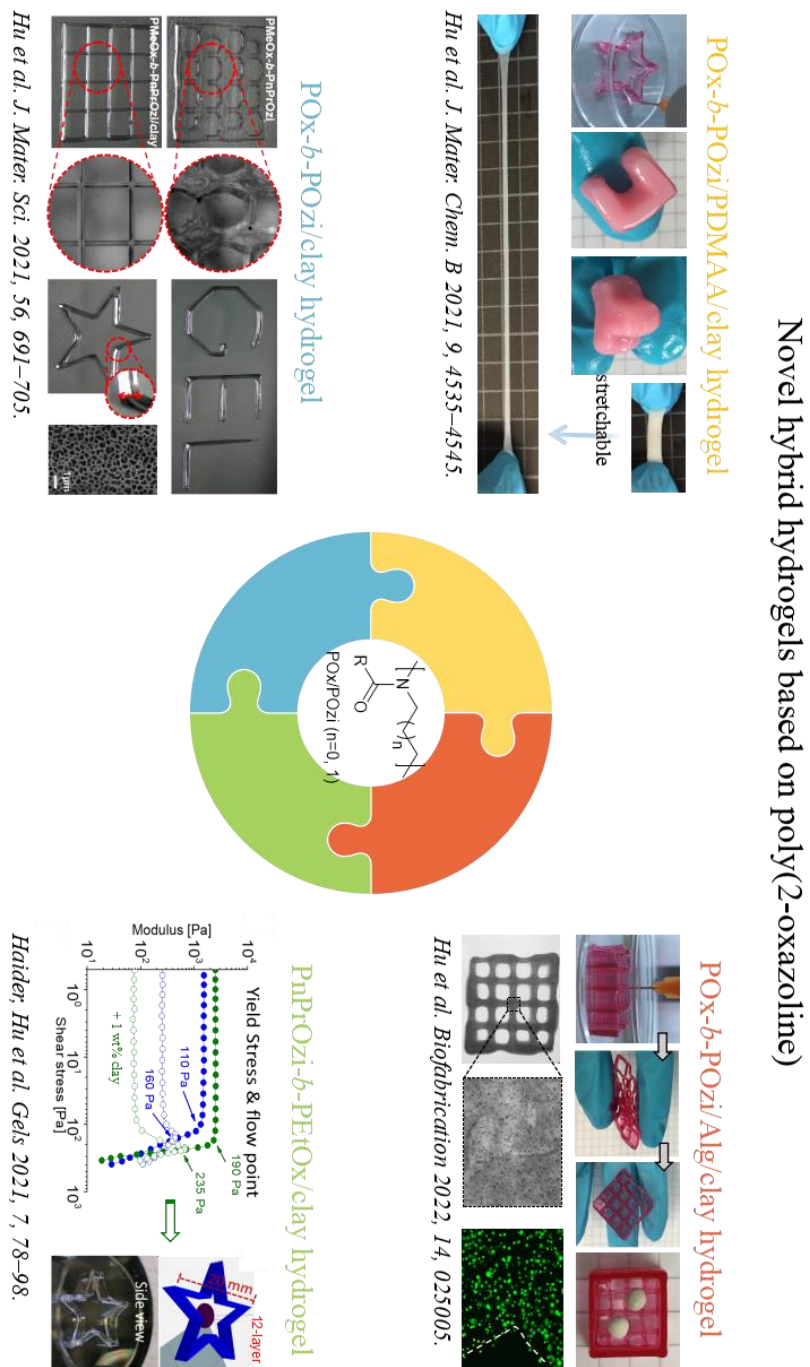


Fig. 5.1 | Novel hybrid hydrogels based on poly(2-oxazoline).

In the present thesis, the first reported thermogelling polymer solely consisting of POx and POzi, i.e., the diblock copolymer PMeOx-*b*-PnPrOzi comprising a hydrophilic block (PMeOx) and a thermoresponsive block (PnPrOzi), was selected and used as a proof-of-concept for the preparation of three novel hybrid hydrogels. Therefore, three batches of the diblock copolymers with a DP of 100 were synthesized for the study of three different hybrid hydrogels with a special focus on their suitability as (bio)inks for extrusion-based 3D printing. The PMeOx-*b*-PnPrOzi diblock copolymer solution shows a temperature induced reversible gelation behavior above a critical polymer concentration of 20 wt%, as described for the Pluronic F127 solution but with a unique gelation mechanism, working through the formation of a bicontinuous sponge-like structure from the physically crosslinked vesicles. Specially, its intrinsic shear thinning behavior and excellent recovery property with a certain yield point make it a promising ink candidate for extrusion-based printing technology.

Increasing the polymer concentration is the most traditional approach to improve the printability of an ink material, and serve as the major strategy available to improve the printability of PMeOx-*b*-PnPrOzi systems prior to this work. From the analysis of rheological properties related to printability, it came a conclusion that increasing the copolymer concentration does improve the hydrogel strength and thus the printability. However, such improvement is very limited and usually leads to other problems such as more viscous systems and stringent requirements on the printers, which are not ideal for the printing process and applications especially in the cell-embedded biofabrication field.

### ***POx-*b*-POzi/clay Hybrid Hydrogel***

An alternative method proposed to improve the printability of this thermoresponsive hydrogel ink is through nanoclay (Laponite XLG) addition, i.e., the first hybrid hydrogel system of PMeOx-*b*-PnPrOzi/clay (also named shortly as POx-*b*-POzi/clay) in this thesis. To optimize the viscoelastic properties of the ink material, Laponite XLG acted as a reinforcement additive and a physically crosslinker was blended with the copolymers.



Compared with the pristine copolymer solution of PMeOx-*b*-PnPrOzi, the hybrid PMeOx-*b*-PnPrOzi/clay solution well retained the temperature induced gelation performance of the copolymers.

The obtained hybrid hydrogels exhibited a rapid *in situ* reversible thermogelation at a physiological relevant  $T_{gel}$  of around 15 °C and a rapid recovery of viscoelastic properties within a few seconds. More importantly, with the addition of only a small amount of 1.2 wt% clay, it exhibited obviously enhanced shear thinning character ( $n = 0.02$ ), yield stress (240 Pa) and mechanical strength (storage modulus over 5 kPa). With this novel hybrid hydrogel, real three-dimensional constructs with multiple layers and various geometries are generation with greatly enhanced shape fidelity and resolution. In this context, the thermogelling properties of the hybrid hydrogels over a copolymer concentration range of 10-20 wt% and a clay concentration of 0-4 wt% were systematically investigated, and from which a printable window was obtained from the laboratory as a reference.

In fact, the printing performance of an ink is not only determined by the intrinsic physicochemical properties of the material, but is also influenced by the external printing environments as well as the printer parameter settings. All the printing experiments in this study were conducted under a relatively optimized conditions obtained from preliminary experiments. In future work, the relationship between material rheology properties, printer parameters and printing performance could be systematically explored. Such a fundamental study will help to develop models that allows the prediction and comparison of printing results from different researches based on the parameters available through rheology, which is very beneficial for further development of more advanced ink systems.

Although the printability has been significantly improved by the addition of nanoclay Laponite XLG, the hybrid hydrogels and their printed constructs still suffer from some major limitations. For example, these materials are still thermoresponsive, which will cause the printed constructs to collapse when the environment temperature changes below their  $T_{gel}$ . In addition, the formed hydrogel constructs are mechanical too weak for load-

bearing applications, and the allowed incubation time is very limited during media exchange/addition as it will lead to dissolution of the hydrogels due to dilution effects. Therefore, it is essential to establish a second (chemical or physical) crosslinking mechanism that allows further solidification of the gels after printing. It should be kept in mind that the second crosslinking step will eliminate the thermoresponsive behavior of the gels and thus the possibility of cell recovery. In this case, besides through the traditional approach of copolymer modification to realize further crosslinking, like one of the well-known post-polymerization modification approach Diels-Alder reaction,<sup>[430]</sup> designing of interpenetrating networks (IPN) hydrogels serves as one of the major strategy for advanced (bio)ink preparation.<sup>[311]</sup> Therefore, the second hybrid hydrogel system of PMeOx-*b*-PnPrOzi/PDMAA/clay (also named shortly as POx-*b*-POzi/PDMAA/clay) was developed in this thesis, which is a 3D printable and highly stretchable ternary organic-inorganic IPN hydrogel.

#### ***POx-*b*-POzi/PDMAA/clay Hybrid Hydrogel***

The nanocomposite IPN hydrogel combines a thermoresponsive hydrogel with clay described above and *in situ* polymerized poly(N, N-dimethylacrylamide). Before *in situ* polymerization, the thermoresponsive hydrogel precursors exhibited thermogelling behavior ( $T_{gel} \sim 25$  °C,  $G' \sim 6$  kPa) and shear thinning properties, making the system well-suited for extrusion-based 3D printing. After chemical curing of the 3D-printed constructs by free radical polymerization, the resulting IPN hydrogels show excellent mechanical strength with a high stretchability to a tensile strain at break exceeding 550%. The hybrid hydrogel can sustain a high stretching deformation and recover quickly due to the energy dissipation from the non-covalent interactions. With this hybrid hydrogel, integrating with the advanced 3D-printing technique, various 3D constructs can be printed and cured successfully with high shape fidelity and geometric accuracy.

In this context, we also investigated the possibility of acrylic acid (AA) and 2-hydroxyethylmethacrylate (HEMA) as alternative hydrogel precursors. However, the

---

addition of these two monomers affected the thermogelation of POx-*b*-POzi in an unfavorable manner, as these monomers competed more effectively with water molecules, preventing the hydration of *n*PrOzi block at lower temperatures and therefore, the liquefaction of the gels. Furthermore, the influence of the printing process and direction on the mechanical properties of the hydrogel was investigated and compared with the corresponding bulk materials obtained from a mold. No significant effects from the additive manufacturing process were observed due to a homogeneous adhesion and merging between sequentially deposited layers. In the future, further studies on the specific performance differences among hydrogels fabricated at different printing directions/speeds would be of great interest to the community, as this allows for a more accurately control and better predict of the printed structures.

This newly developed hybrid IPN hydrogel is expected to expand the material toolbox available for hydrogel-based 3D printing, and may be interesting for a wide range of applications including tissue engineering, drug delivery, soft robotics, and additive manufacturing in general. However, in this case, the low toxicity from the monomer DMAA and other small molecules residuals in the polymerized hydrogels made this hybrid hydrogel not ideal for bioprinting in the field of biofabrication. For this problem, cyto-/biocompatible monomers such as polyethylene glycol diacrylate (PEGDA) can be used as an alternative, while the overall properties of the hydrogels including mechanical properties should be re-evaluated accordingly. Moreover, the swelling behavior of the hydrogels should also be taken into account, as it may most likely affect the mechanical strength and geometry size of the printed scaffold, but is often be overlooked after printing. For example, regarding the specific hybrid hydrogel POx-*b*-POzi/PDMAA/clay in this work, an equilibrium swelling ratio of 1100% was determined. The printed hydrogel cuboid experienced a volume increasing over 6-fold after equilibrium swelling in water, and became mechanical fragile due to the formation of a swollen hydrogel network absorbing large amount of water.

### ***POx-*b*-POzi/Alg/clay Hybrid Hydrogel***

In the final part of this dissertation, to enable the cell-loaded bioprinting and long-term cell culture, the third hybrid hydrogel system POx-*b*-POzi/Alg/clay was introduced by replacing the monomer DMAA to the natural polysaccharides alginate. Initially, detailed rheological characterization and mechanical tests were performed to evaluate their printability and mechanical properties. Subsequently, some simple patterns were printed with the optimized hydrogel precursor solutions for the preliminary filament fusion and collapse test before proceeding to more complex printings. The fibers showed a sufficient stability which allows the creation of large structures with a height of a few centimeters and a suspended filament up to centimeter. Accordingly, various 3D constructs including suspended filaments were printed successfully with high stackability and shape fidelity. The structure after extrusion was physical crosslinked easily by soaking in CaCl<sub>2</sub> solution and, thereafter exhibited a good mechanical flexibility and long-term stability. Interestingly, the mechanical strength and geometry size of the generated scaffolds were well maintained over a culture period of weeks in water, which is of great importance for clinical applications. In addition, the post-printing ionic crosslinking of alginate could also be realized by other di/trivalent cations such as Fe<sup>3+</sup> and Tb<sup>3+</sup>.

Subsequently, the cell-laden printing with this hybrid hydrogel and post-printing crosslinking by Ca<sup>2+</sup> ions highlighting its feasibility for 3D bioprinting. WST-1 assay of fibroblast suggested no-dose dependent cytocompatibility of the hydrogel precursor solution. The cell distribution was uniform throughout the printed construct, and proliferated with high cell viability during the 21 days culture. The presented hybrid approach, utilizing the beneficial properties of the POx-*b*-POzi base material, could be interesting for a wide range of bioprinting applications and potentially enabling also other biological bioinks such as collagen, hyaluronic acid, decellularized extracellular matrix or cellulose based bioinks. Although the results look promising and the developed hydrogel is an important bioink candidate, the long-term *in vitro* cell studies with different cell lines and clinical model establishment are still under investigation, which remains a long road but is of great importance before realizing real clinical application.

Last but not least, the improvement to the printability of thermogelling POx/POzi-based copolymers by the clay Laponite XLG was also demonstrated in another thermogelling copolymer PEtOx-*b*-PnPrOzi. This suggests that the addition of clay may be a general strategy to improve the printability of such polymers. Despite these advances in this work which significantly extended the (bio)material platform of additive manufacturing technology, the competition is still fierce and more work should be done in the further to reveal the potential and limitations of this kind of new and promising candidate (bio)ink materials. It is also highly expected for further creative works based on the thermogelling POx/POzi polymers, such as crosslinking in Ca<sup>2+</sup> solution containing monomer acrylamide to prepare printable and mechanically tough hydrogels, research on POx-based support bath material, and print of clinically more relevant sophisticated structures such as 3D microvascular networks omnidirectionally.



# 6 | Zusammenfassung und Ausblick





Motiviert durch das große Potenzial, das die Kombination von additiver Fertigungstechnologie und Hydrogelen insbesondere im Bereich des Tissue Engineering und der regenerativen Medizin bietet, wurde eine Reihe neuartiger Hybrid-Hydrogeltinten auf der Grundlage der kürzlich beschriebenen thermogelierenden Poly(2-oxazolin)s-*block*-Poly(2-oxazin)s-diblock-copolymere entwickelt, die dazu beitragen können, die Plattform der verfügbaren Hydrogeltinten für diese transformative 3D-Drucktechnologie zu erweitern (Abb. 6.1).

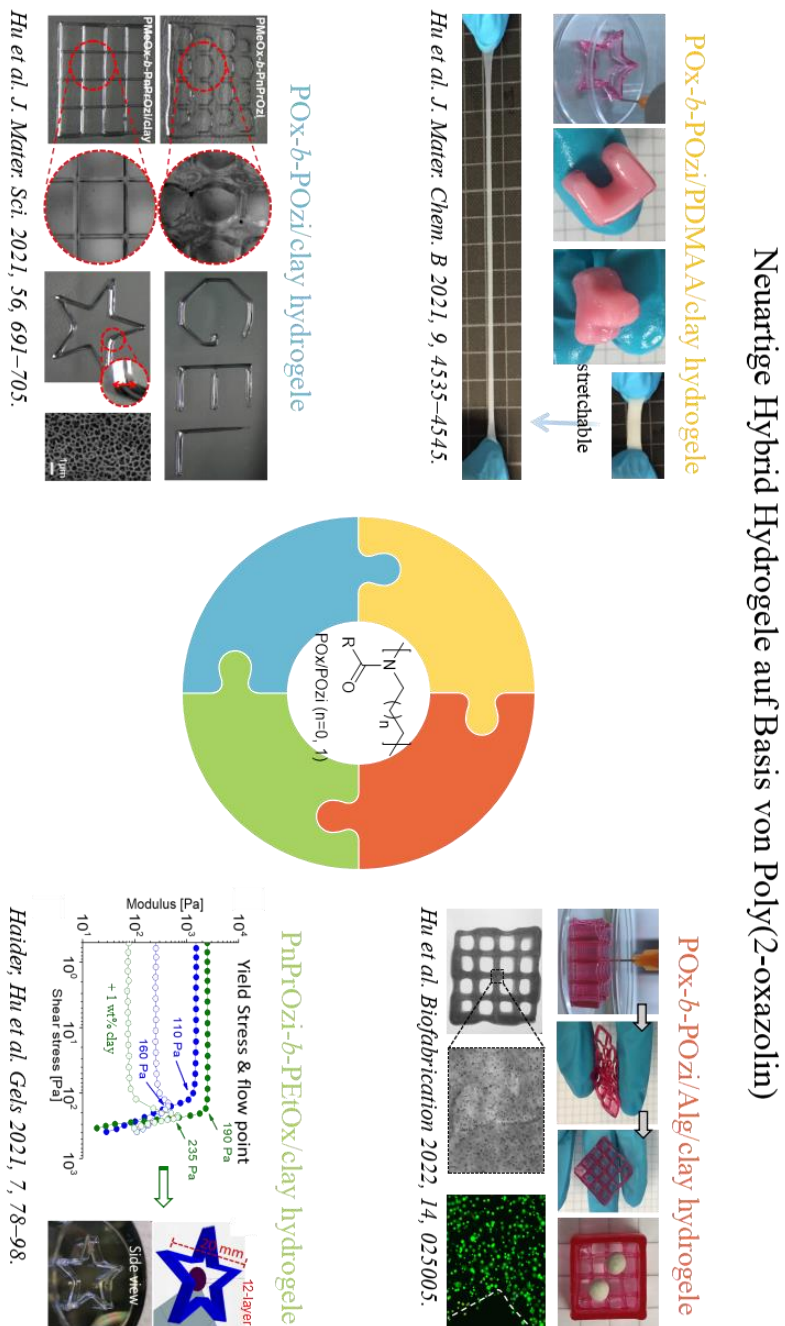


Abb. 6.1 | Neuartige Hybridhydrogele auf Basis von Poly(2-oxazoline).

In der vorliegenden Arbeit wurde das erste bekannte thermogelierende Polymer, das ausschließlich aus POx und POzi besteht, d.h. das Diblock-Copolymer PMeOx-*b*-PnPrOzi, das einen hydrophilen Block (PMeOx) und einen thermoresponsiven Block (PnPrOzi) umfasst, ausgewählt und als Proof-of-Concept für die Herstellung von drei neuartigen Hybridhydrogelen verwendet. Daher wurden drei Chargen der Diblock-Copolymere mit einem DP von 100 für die Untersuchung von drei verschiedenen Hybrid-Hydrogelen synthetisiert, wobei der Schwerpunkt auf ihrer Eignung als (Bio-)Tinten für den extrusionsbasierten 3D-Druck lag. Die PMeOx-*b*-PnPrOzi Diblock-Copolymer-Lösung zeigt ein temperaturinduziertes reversibles Gelierverhalten oberhalb einer kritischen Polymerkonzentration von 20 Gew.-%, wie für die Pluronic F127-Lösung beschrieben, jedoch mit einem einzigartigen Geliermechanismus, der durch die Bildung einer bikontinuierlichen, schwammartigen Struktur aus den physikalisch vernetzten Vesikeln zustande kommt. Insbesondere das intrinsische Scherverdünnungsverhalten und die hervorragende Rückstelleigenschaft mit einer bestimmten Fließgrenze machen sie zu einem vielversprechenden Tintenkandidaten für die extrusionsbasierte Drucktechnologie.

Die Erhöhung der Polymerkonzentration ist der traditionellste Ansatz zur Verbesserung der Bedruckbarkeit eines Druckfarbenmaterials und diente vor dieser Arbeit als Hauptstrategie zur Verbesserung der Bedruckbarkeit von PMeOx-*b*-PnPrOzi-Systemen. Die Analyse der rheologischen Eigenschaften, die mit der Druckfähigkeit zusammenhängen, ergab, dass eine Erhöhung der Copolymerkonzentration die Festigkeit des Hydrogels und damit die Druckfähigkeit verbessert. Diese Verbesserung ist jedoch sehr begrenzt und führt in der Regel zu anderen Problemen wie zähflüssigeren Systemen und strengen Anforderungen an die Drucker, was für den Druckprozess und die Anwendungen insbesondere im Bereich der zelleingebetteten Biofabrikation nicht ideal ist.

### ***POx-*b*-POzi/clay Hybrid Hydrogel***

Eine alternative Methode zur Verbesserung der Druckbarkeit dieser thermoresponsiven Hydrogeltinte ist die Zugabe von Nanoclay (Laponite XLG), d. h. das

erste hybride Hydrogelsystem aus PMeOx-*b*-PnPrOzi/clay (in dieser Arbeit auch kurz als POx-*b*-POzi/clay bezeichnet). Um die viskoelastischen Eigenschaften der Tinte zu optimieren, wurde Laponite XLG als Verstärkungsadditiv eingesetzt und ein physikalischer Vernetzer mit den Copolymeren gemischt. Im Vergleich zur ursprünglichen Copolymerlösung von PMeOx-*b*-PnPrOzi behielt die hybride PMeOx-*b*-PnPrOzi/clay-Lösung die temperaturinduzierte Gelierleistung der Copolymere gut bei.

Die erhaltenen Hybrid-Hydrogele zeigten eine schnelle reversible Thermogelierung *in situ* bei einer physiologisch relevanten  $T_{gel}$  von etwa 15 °C und eine rasche Erholung der viskoelastischen Eigenschaften innerhalb weniger Sekunden. Noch wichtiger ist, dass die Zugabe einer geringen Menge von 1.2 Gew.-% clay zu einer deutlichen Verbesserung der Scherverdünnung ( $n = 0.02$ ), der Fließspannung (240 Pa) und der mechanischen Festigkeit (Speichermodul über 5 kPa) führte. Mit diesem neuartigen Hybrid-Hydrogel lassen sich echte dreidimensionale Konstrukte mit mehreren Schichten und verschiedenen Geometrien mit deutlich verbesserter Formtreue und Auflösung erzeugen. In diesem Zusammenhang wurden die Thermogel-Eigenschaften der Hybrid-Hydrogele über einen Copolymer-Konzentrationsbereich von 10-20 Gew.-% und einer clay-Konzentration von 0-4 Gew.-% systematisch untersucht, wobei ein druckbares Fenster als Referenz aus dem Labor gewonnen wurde.

Die Druckleistung einer Tinte wird nicht nur durch die physikalisch-chemischen Eigenschaften des Materials bestimmt, sondern auch durch die äußeren Druckbedingungen und die Einstellungen der Druckerparameter beeinflusst. Alle Druckexperimente in dieser Studie wurden unter relativ optimierten Bedingungen durchgeführt, die durch Vorversuche ermittelt wurden. In zukünftigen Arbeiten könnte die Beziehung zwischen den rheologischen Eigenschaften des Materials, den Druckerparametern und der Druckleistung systematisch erforscht werden. Eine solche grundlegende Studie wird dazu beitragen, Modelle zu entwickeln, die die Vorhersage und den Vergleich von Druckergebnissen aus verschiedenen Untersuchungen auf der Grundlage der über die Rheologie verfügbaren

Parameter ermöglichen, was für die weitere Entwicklung fortschrittlicherer Tintensysteme sehr nützlich ist.

Obwohl die Druckbarkeit durch die Zugabe von Nanoclay Laponite XLG erheblich verbessert wurde, weisen die hybriden Hydrogele und ihre gedruckten Konstrukte immer noch einige wesentliche Einschränkungen auf. Zum Beispiel sind diese Materialien immer noch thermoresponsiv, was dazu führt, dass die gedruckten Konstrukte kollabieren, wenn die Umgebungstemperatur unter ihre  $T_{\text{gel}}$ -Temperatur fällt. Außerdem sind die gebildeten Hydrogelkonstrukte mechanisch zu schwach für lasttragende Anwendungen, und die zulässige Inkubationszeit ist während des Medien austauschs/der Medienzugabe sehr begrenzt, da sie aufgrund von Verdünnungseffekten zur Auflösung der Hydrogele führt. Daher ist es wichtig, einen zweiten (chemischen oder physikalischen) Vernetzungsmechanismus zu schaffen, der eine weitere Verfestigung der Gele nach dem Druck ermöglicht. Dabei ist zu bedenken, dass der zweite Vernetzungsschritt das thermoresponsive Verhalten der Gele und damit die Möglichkeit der Rückgewinnung von Zellen. In diesem Fall ist neben dem traditionellen Ansatz der Copolymermodifikation zur weiteren Vernetzung, wie z. B. der bekannten Diels-Alder-Reaktion,<sup>[430]</sup> die Entwicklung von Hydrogelen mit interpenetrierenden Netzwerken (IPN) eine der wichtigsten Strategien für die Herstellung fortschrittlicher (Bio-)Tinten.<sup>[311]</sup> Daher wurde in dieser Arbeit das zweite hybride Hydrogelsystem PMeOx-*b*-PnPrOzi/PDMAA/clay (auch kurz als POx-*b*-POzi/PDMAA/clay bezeichnet) entwickelt, das ein 3D-druckbares und hoch dehnbares ternäres organisch-anorganisches IPN-Hydrogel ist.

### ***POx-*b*-POzi/PDMAA/clay Hybrid Hydrogel***

Das Nanokomposit-IPN-Hydrogel kombiniert ein thermoresponsives Hydrogel mit dem oben beschriebenen clay Laponite XLG und in situ polymerisiertem Poly(N,N-dimethylacrylamid). Vor der In-situ-Polymerisation zeigten die thermoresponsiven Hydrogelvorläufer ein Thermogelling-Verhalten ( $T_{\text{gel}} \sim 25 \text{ }^\circ\text{C}$ ,  $G' \sim 6 \text{ kPa}$ ) und scherverdünnende Eigenschaften, wodurch sich das System gut für den

extrusionsbasierten 3D-Druck eignet. Nach der chemischen Aushärtung der 3D-gedruckten Konstrukte durch radikalische Polymerisation zeigen die resultierenden IPN-Hydrogele eine ausgezeichnete mechanische Festigkeit mit einer hohen Dehnbarkeit bis zu einer Bruchdehnung von über 550 %. Das Hybridhydrogel kann eine hohe Dehnungsverformung aushalten und sich aufgrund der Energiedissipation durch die nicht-kovalenten Wechselwirkungen schnell erholen. Mit diesem Hybrid-Hydrogel können in Verbindung mit der fortschrittlichen 3D-Drucktechnik verschiedene 3D-Konstrukte mit hoher Formtreue und geometrischer Genauigkeit gedruckt und ausgehärtet werden.

In diesem Zusammenhang untersuchten wir auch die Möglichkeit von Acrylsäure (AA) und 2-Hydroxyethylmethacrylat (HEMA) als alternative Hydrogelvorläufer. Die Zugabe dieser beiden Monomere wirkte sich jedoch ungünstig auf die Thermogelierung von POx-*b*-POzi aus, da diese Monomere effektiver mit Wassermolekülen konkurrierten und die Hydratation des nPrOzi-Blocks bei niedrigeren Temperaturen und damit die Verflüssigung der Gele verhinderten. Darüber hinaus wurde der Einfluss des Druckverfahrens und der Druckrichtung auf die mechanischen Eigenschaften des Hydrogels untersucht und mit den entsprechenden aus einer Form gewonnenen Massenmaterialien verglichen. Es wurden keine signifikanten Auswirkungen des additiven Herstellungsverfahrens beobachtet, da die nacheinander aufgetragenen Schichten homogen aneinander haften und miteinander verschmelzen. In Zukunft wären weitere Studien zu den spezifischen Leistungsunterschieden zwischen Hydrogelen, die mit unterschiedlichen Druckrichtungen und -geschwindigkeiten hergestellt wurden, von großem Interesse für die Fachwelt, da dies eine genauere Kontrolle und bessere Vorhersage der gedruckten Strukturen ermöglicht.

Dieses neu entwickelte hybride IPN-Hydrogel wird voraussichtlich die Materialpalette für den hydrogelbasierten 3D-Druck erweitern und könnte für eine Vielzahl von Anwendungen interessant sein, darunter Tissue Engineering, Medikamentenverabreichung, Soft Robotics und additive Fertigung im Allgemeinen. In diesem Fall war das Hybrid-Hydrogel jedoch aufgrund der geringen Toxizität des

Monomers DMAA und anderer kleiner Moleküle, die in den polymerisierten Hydrogelen zurückblieben, nicht ideal für das Bioprinting im Bereich der Biofabrikation. Für dieses Problem können zyto-/biokompatible Monomere wie Polyethylenglykoldiacrylat (PEGDA) als Alternative verwendet werden, wobei die Gesamteigenschaften der Hydrogele einschließlich der mechanischen Eigenschaften entsprechend neu bewertet werden sollten. Darüber hinaus sollte auch das Quellverhalten der Hydrogele berücksichtigt werden, da es sich höchstwahrscheinlich auf die mechanische Festigkeit und die Geometriegröße des gedruckten Gerüsts auswirkt, aber nach dem Druck oft übersehen wird. Für das in dieser Arbeit verwendete Hybrid-Hydrogel POx-*b*-POzi/PDMAA/clay wurde zum Beispiel ein Gleichgewichtsquellverhältnis von 1100 % ermittelt. Der gedruckte Hydrogelquader erfuhr nach der Gleichgewichtsquellung in Wasser eine Volumenzunahme um das 6-fache und wurde aufgrund der Bildung eines gequollenen Hydrogelnetzwerks, das eine große Menge Wasser absorbiert, mechanisch brüchig.

### ***POx-*b*-POzi/Alg/clay Hybrid Hydrogel***

Im letzten Teil dieser Dissertation wurde das dritte hybride Hydrogelsystem POx-*b*-POzi/Alg/clay eingeführt, um das zellbeladene Bioprinting und die langfristige Zellkultur zu ermöglichen, indem das Monomer DMAA durch das natürliche Polysaccharid Alginat ersetzt wurde. Zunächst wurden eine detaillierte rheologische Charakterisierung und mechanische Tests durchgeführt, um die Druckbarkeit und die mechanischen Eigenschaften zu bewerten. Anschließend wurden einige einfache Muster mit den optimierten Hydrogel-Vorläuferlösungen gedruckt, um die Fusion und das Koaleszieren der Stränge zu testen, bevor komplexere Drucke durchgeführt wurden. Die Stränge wiesen eine ausreichende Stabilität auf, die die Herstellung großer Strukturen mit einer Höhe von einigen Zentimetern und einem hängenden Filament von bis zu einem Zentimeter ermöglicht. Dementsprechend wurden verschiedene 3D-Konstruktionen, einschließlich hängender Filamente, erfolgreich mit hoher Stapelbarkeit und Formtreue gedruckt. Die Struktur wurde nach der Extrusion durch Eintauchen in CaCl<sub>2</sub>-Lösung leicht physikalisch vernetzt und wies danach eine gute mechanische Flexibilität und Langzeitstabilität auf.

Interessanterweise blieben die mechanische Festigkeit und die geometrische Größe der erzeugten Gerüste über einen Kulturzeitraum von mehreren Wochen in Wasser erhalten, was für klinische Anwendungen von großer Bedeutung ist. Darüber hinaus könnte die ionische Vernetzung von Alginat nach dem Druck auch mit anderen zwei- oder dreiwertigen Kationen wie  $\text{Fe}^{3+}$  und  $\text{Tb}^{3+}$  erfolgen.

Anschließend wurde das Hybrid-Hydrogel mit Zellen verdruckt und nach dem Druck durch  $\text{Ca}^{2+}$ -Ionen vernetzt, was seine Eignung für das 3D-Bioprinting unterstreicht. Der WST-1-Test an Fibroblasten zeigte, dass die Hydrogelvorläuferlösung dosisunabhängig zytokompatibel ist. Die Zellen verteilten sich gleichmäßig über das gesamte gedruckte Konstrukt und vermehrten sich während der 21-tägigen Kultur mit hoher Zellebensfähigkeit. Der vorgestellte hybride Ansatz, der die vorteilhaften Eigenschaften des POx-*b*-POzi-Basismaterials nutzt, könnte für ein breites Spektrum von Bioprinting-Anwendungen interessant sein und möglicherweise auch andere biologische Biotinten wie Kollagen, Hyaluronsäure, dezellularisierte extrazelluläre Matrix oder auf Zellulose basierende Biotinten ermöglichen. Obwohl die Ergebnisse vielversprechend aussehen und das entwickelte Hydrogel ein wichtiger Biotinten-Kandidat ist, sind die langfristigen In-vitro-Zellstudien mit verschiedenen Zelllinien und die Etablierung eines klinischen Modells noch in der Forschung, was ein langer Weg ist, aber von großer Bedeutung, bevor eine echte klinische Anwendung realisiert werden kann.

Nicht zuletzt wurde die Verbesserung der Druckfähigkeit von thermogelierenden POx/POzi-Copolymeren durch den clay Laponite XLG auch bei einem anderen thermogelierenden Copolymer PEOx-*b*-PnPrOzi nachgewiesen. Dies deutet darauf hin, dass die Zugabe von Ton eine allgemeine Strategie zur Verbesserung der Druckfähigkeit solcher Polymere sein könnte. Trotz dieser Fortschritte in dieser Arbeit, die die (Bio-)Materialplattform der additiven Fertigungstechnologie erheblich erweitert hat, ist der Wettbewerb immer noch hart, und es sollte weiter daran gearbeitet werden, das Potenzial und die Grenzen dieser Art von neuen und vielversprechenden Kandidaten für (Bio-)Tintenmaterialien aufzuzeigen. Weitere kreative Arbeiten auf der Grundlage der

thermogelierenden POx/POzi-Polymere erwartet, z. B. die Vernetzung in einer Ca<sup>2+</sup>-haltigen Lösung, die das Monomer Acrylamid enthält, um druckbare und mechanisch widerstandsfähige Hydrogele herzustellen, die Erforschung von POx-basiertem Badematerial und der Druck klinisch relevanterer komplexer Strukturen wie mikrovaskulärer 3D-Netzwerke in allen Richtungen.



# 7 | Experimental



## 7.1 Equipment and Methods of Measurement

### *Glovebox*

A *LabMaster 130* (MBraun, Garching, Germany) comprising nitrogen atmosphere (5.0, Linde AG, Germany) was used to store chemicals.

### *Proton nuclear magnetic resonance (<sup>1</sup>H NMR)*

The chemical structure of the diblock copolymer PMeOx-*b*-PnPrOzi was confirmed by <sup>1</sup>H NMR on a Fourier 300 (300.12 MHz) Bruker BioSpin (Rheinstetten, Germany) system at 298 K with CDCl<sub>3</sub> as solvent. The chemical shift of the signals is indicated in ppm. Spectra were calibrated using residual solvent signals of CDCl<sub>3</sub> 7.26 ppm.

### *Gel permeation chromatography (GPC)*

GPC was performed on Agilent 1260 Infinity, System Polymer Standards Service (Mainz, Germany) with hexafluoroisopropanol (HFIP) containing 3 g L<sup>-1</sup> potassium trifluoroacetate (KTFA) as eluent; precolumn: 50 mm × 8 mm PSS PFG linear M; 2 columns: 300 mm × 8 mm PSS PFG linear M (particle size 7 μm; pore size 0.1-1000 kDa). The columns were kept at 40 °C and the flow rate was 0.7 mL min<sup>-1</sup>. Prior to each GPC measurement, the sample was filtered through a 0.2 μm Teflon filter from Thermo Scientific (Schwerte, Germany) to remove particles, if any. Calibration was performed using PEG standards.

### *Cryogenic scanning electron microscopy (Cryo-SEM)*

*Cryo-SEM* was performed using the Zeiss Crossbeam 340 field emission SEM (Oberkochen, Germany), where the as-prepared samples were flash-frozen (2 x 1 mm pellet) in the liquid nitrogen slurry. Then, samples were freeze fractured and freeze etched at -85 °C for 15 min and sputtered subsequently with platinum (3 nm) before the observation (at -140 °C). The Cryo-SEM images were obtained at an acceleration voltage of 2.00 kV for pure clay, and 8.00 kV for all the other hydrogel samples.

### *Scanning Electron Microscopy (SEM)*

The prepared hydrogels were frozen within the liquid nitrogen and lyophilized afterwards. The resulting dried hydrogel samples were then mounted on aluminum sample holders with conductive carbon tape, and sputtered with platinum in a sputter coater Leica Microsystems ACE 400 (Wetzlar, Germany). The morphology of the samples was subsequently analyzed using the Crossbeam 340 field emission scanning electron microscope Carl Zeiss Microscopy (Oberkochen, Germany) at an acceleration voltage ETH 2.0 kV.

### *X-ray diffraction (XRD)*

XRD was analyzed with the Bruker D8 Discover powder diffractometer (Karlsruhe, Germany) in a range of 5 - 60° (2 $\theta$ ).

### *UV-vis-NIR*

The UV-vis-NIR Cary 5000 from Agilent Technologies (Santa Clara, United States) was used to measure the optical transparency of as-prepared hydrogels at 37 °C.

### *Thermogravimetric analysis (TGA)*

TGA of the hydrogels was performed on the thermal gravimetric analyzer *TG 209F1 IRIS* from Netzsch (Selb, Germany) under a nitrogen flow. The sample (5 - 10 mg) was added to an aluminum oxide crucible and then heated from 30 to 900 °C with a heating rate of 10 K min<sup>-1</sup> while detecting the mass loss. The software *NETZSCH Proteus – Thermal Analysis – V.5.2.1* was used to evaluate the obtained spectra.

### *Dynamic Scanning Calorimetry (DSC)*

DSC analysis was performed on a DSC 204 F1 Phoenix equipped with a CC200 F1 controller from Netzsch (Selb, Germany). The dynamic scans were recorded in nitrogen atmosphere with a heating rate of 10 K min<sup>-1</sup> in a range of 25 °C - 240 °C, and subsequently cooled to -50 °C. The sample was heated and cooled two additional times

from -50 to 200 °C (three heating and two cooling cycles). For DSC tests, samples (5 - 10 mg) were placed into flat bottom aluminum pans with crimped-on lids (pierced on the top).

### *Stereomicroscopy*

The printed constructs were imaged by using a stereomicroscope Carl Zeiss Discovery V.20 (Jena, Germany) sometimes to visually characterize the shape fidelity post fabrication.

### *Rheology*

Rheological measurements were performed using a MCR 301 rheometer from Anton Paar (Ostfildern, Germany) employing a 25 mm diameter parallel-plate geometry. A Peltier system was employed for temperature control. The measuring gap was 0.35 mm, unless otherwise noted. The samples were prepared and stored in 7 °C fridge prior to measurement. By default, the sample was applied to the bottom plate which was kept at 20 °C. After moving the upper plate to the trim position, excess material was removed with a spatula to avoid the interference during measurements.

For measurements, firstly, under a fixed angular frequency of 10 rad s<sup>-1</sup> and amplitude of 0.5%, temperature sweeps from 5 to 45 °C were conducted at a heating rate of 0.05 °C s<sup>-1</sup> to study the thermogelling behavior of the samples. Then, different rheological test programs shown below was performed accordingly.

(1) Cyclic heating-cooling temperature sweeps in a range of 5 - 45 °C under a fixed angular frequency of 10 rad s<sup>-1</sup> and a constant strain of 0.5%. The heating and cooling rate was 0.05 °C s<sup>-1</sup>.

(2) Amplitude sweeps with a oscillation strain amplitudes of 0.01-500% at a constant angular frequency of 10 rad s<sup>-1</sup>, from where the linear viscoelastic (LVE) range of the samples can be determined.

(3) Frequency sweeps in an angular frequency range of 0.1-100 rad s<sup>-1</sup> at a constant strain of 0.1% (within the LVE range obtained from the amplitude sweep). Particularly,

for the ionically crosslinked hydrogels, the crosslinking kinetics were monitored at different time with this oscillatory mode. Here, the measuring gap was set according to the specific gel size so that the z-axial force was almost to zero. After predefined crosslinking times, the immersed hydrogels were removed from the crosslinking solution, the excess surface liquid was removed using blotting paper, and the frequency sweep was performed.

(4) Steady-state shear flow from a shear rate range of  $0.01 - 1000 \text{ s}^{-1}$  to characterize the shear thinning behavior. The data were fitted using the power-law expression  $\eta = K(\dot{\gamma})^{n-1}$  established by Ostwald–de Waele, where  $K$  is the consistency index,  $n$  is the flow index, and  $\dot{\gamma}$  is the applied shear rate.

(5) To investigate recovery properties, two measurement programs were used accordingly. Time sweeps of shear flow with alternating shear rate of  $0.1 \text{ s}^{-1}$  and  $100 \text{ s}^{-1}$  under rotational mode. Time sweeps with alternating oscillation strain of 0.1% and 100% at a fixed angular frequency of  $10 \text{ rad s}^{-1}$  under oscillatory mode.

(6) Hysteresis loop tests in a shear rate range from 0 to  $500 \text{ s}^{-1}$ .

(7) Dynamic oscillatory stress sweeps and steady stress sweeps to evaluate the yield stress and yield point of the gel samples. In the dynamic oscillatory stress sweep, yield stress was evaluated using onset determination, i.e., the point where the  $G'$  start decreasing and  $G''$  start increasing, and the flow point is determined as the crossing of storage and loss modulus ( $G' = G''$ ) by definition. In the steady stress sweep (rotational rheology mode), the corresponding shear stress where the viscosity starts decreasing by several orders of magnitude is recommended as the yield stress. It can be analyzed by using two tangents, one in the plateau-region of the viscosity where the hydrogel is deformed elastically, and one in the region where the viscosity drops indicating the permanent deformation occurs.

Except for temperature sweeps, all tests were performed at  $37 \text{ }^\circ\text{C}$  unless otherwise stated. An aqueous solvent trap was used in all experiments to mitigate drying effects.

---

### *Extrusion-based 3D Printing*

3D printing of the PMeOx-*b*-PnPrOzi/clay hybrid hydrogels in Chapter 4.3.1 were performed using the extrusion-based 3D bioprinter Inkredible form CELLINK (Gothenburg, Sweden) equipped with a pneumatic driven print head (syringe dispenser, DD-135N) and a 0.20 mm inner diameter precision needle from Nordson EFD (Oberhaching, Germany). The extrusion pressure was controlled and varied from 110 to 220 kPa according to different user-defined printing structures which are programmed by G-code. The hydrogels were loaded into a printing cartridge in liquid form immediately after taking out from the 7 °C refrigerator, mounted in the 3D printer, and driven pneumatically through the nozzle to print the hydrogel onto polystyrene plates at room temperature. The printing speed was fixed at 600 mm min<sup>-1</sup> in all printing experiments.

Printing experiments of the PMeOx-*b*-PnPrOzi/PDMAA/clay hybrid hydrogels in Chapter 4.3.2 were performed using the extrusion-based 3D bioprinter BIO X from CELLINK (Gothenburg, Sweden) equipped with pneumatic driven print head and a 0.33 mm inner diameter precision needle (23G). The extrusion pressure was controlled and varied according to different user-defined printing structures which are programmed by G-code. The prepared POx-*b*-POzi/DMAA/clay hydrogel was loaded as the ink into a printing cartridge in liquid (cooled) form conveniently because of its thermogelling property, and then kept in 7 °C fridge before printing to eliminate bubbles. To avoid the dehydration effect and the inhibition on DMAA polymerization by oxygen, silicone oil which was purged with argon gas for few hours was used as protective bath, and kept at 60 °C prior to use. After that, the POx-*b*-POzi/DMAA/clay-loaded printing cartridge was mounted in the 3D printer immediately after taking out from the fridge, and driven pneumatically through the nozzle to print the hydrogel on a petri dish placed on 37 °C print-bed. The printing speed was fixed at 5 mm s<sup>-1</sup> in all printing experiments. Immediately after printing, the printed structures were chemically cured by transferring the petri dish to the 60 °C oven for 6 h for DMAA polymerization, where the pre-heated 60 °C argon-purified silicone oil was used as protective bath. Thereafter, the cured 3D

structures of POx-*b*-POzi/PDMAA/clay hydrogel were obtained after removing the silicone oil bath.

For printing of the PMeOx-*b*-PnPrOzi/Alg/clay hybrid hydrogels in Chapter 4.3.3, an extrusion-based 3D bioprinter CELLINK BIO X (Gothenburg, Sweden) was used. The prepared hydrogel precursor solution was loaded as the ink material into a printing cartridge in liquid (cooled) form conveniently because of its thermogelling property, and then kept in a 7 °C fridge to eliminate bubbles before printing. For printing, the ink loaded pneumatic syringe dispenser was equipped with a 0.33 mm inner diameter precision needle (23 G), and then driven pneumatically through the nozzle to extrude the hydrogel ink onto the preheated 37 °C print-bed in a layer-by-layer deposition mode. An extrusion pressure ranging from 70 to 110 kPa was applied. The printing speed was fixed at 4 mm s<sup>-1</sup> in all printing experiments. Immediately after the printing, the printed structures were physically cured by immersing into CaCl<sub>2</sub> (or FeCl<sub>3</sub>·6H<sub>2</sub>O, TbCl<sub>3</sub>·6H<sub>2</sub>O) aqueous solution at room temperature to complete the Alg crosslinking followed by washing twice with DI water.

### *Mechanical Tests*

The mechanical performance of the developed hydrogels was investigated by a universal testing machine Zwick Roell Z010 (Ulm, Germany) at room temperature. Force sensors of 100 N for tensile tests and 10 kN for compressive tests were applied respectively. In tensile tests, the hydrogel sample was cut into long stripes with a length of 35 mm and a cross-sectional area of 5 × 1 mm. The original gauge length between the clamps of every sample was recorded followed by test performed at a constant velocity of 100 mm min<sup>-1</sup>. The nominal stress was determined as the loading force divided by the original specimen cross-sectional area, the nominal strain was defined as the deformed length divided by the original gauge length, and the tensile Young's modulus were calculated from the slope of the linear region in the 0-20% strain range of the stress-strain curves. In the hysteresis measurements, hydrogels were initially loaded to a predetermined



---

strain and then unloaded to zero force at a constant velocity of  $100 \text{ mm min}^{-1}$ . Such cyclic loading-unloading tensile tests were programmed to repeat 10 times.

Additionally, the cylinder-shape POx-*b*-POzi/PDMAA/clay hydrogel (12 mm diameter, 7 mm height), and cylindrical POx-*b*-POzi/Alg/clay hydrogel discs (10 mm diameter, 6 mm height) were prepared for compression tests at a constant compression speed of  $0.7 \text{ mm min}^{-1}$  and  $1 \text{ mm min}^{-1}$ , respectively. The compressive Young's modulus was determined in the 0-20% initial linear strain region. For all tests, the samples surface was greased with olive oil to prevent water evaporation during testing. Each measurement was performed in triplicate and results are reported as the mean  $\pm$  standard deviation.

#### *Swelling ratio (SR)*

The SR of the hydrogel was assessed using a gravimetric method. Initially, the dry weight ( $W_d$ ) of hydrogels was noted, followed by immersion in DI water at room temperature. At predefined time points, the wet hydrogels were taken, the excess surface liquid was cleared using blotting paper, and the swelled weight ( $W_t$ ) was recorded. The study was conducted under identical conditions in triplicates, and the SR was calculated using the equation  $SR = (W_t - W_d)/W_d$ .

#### *Sol content and solid content*

Sol content of the hydrogels were calculated using a formula  $(M_0 - M_1)/M_0$  ( $n=3$ ), where  $M_0$  is the dry mass of the as-prepared hydrogel and  $M_1$  is the final mass of lyophilized hydrogel after allowing it to swell for three days in DI water at  $37^\circ\text{C}$  with the water replaced every 12 h.

Solid content (gel content) of the hydrogels was calculated using the formula  $M_1/M_0$  ( $n=3$ ), where  $M_0$  and  $M_1$  are the weight of the swollen hydrogels and the corresponding weight of lyophilized swollen hydrogels after incubation for regular intervals in DI water at room temperature, respectively. The DI water was replaced every day.

#### *Cell culture and cytocompatibility of bioink*

The murine-derived NIH 3T3 fibroblast were maintained under standard culture conditions (37 °C and 5% CO<sub>2</sub>) in DMEM supplemented with 10% FBS and 1% P/s. The WST-1 assay was performed to evaluate the compatibility of bioink via treatment of different concentration of bioink in growth media and encapsulation of cells in bioink. Briefly,  $1 \times 10^5$  fibroblasts were cultured overnight in 96 well plate. Next day, POx-*b*-POzi (20 wt%), POx-*b*-POzi/Alg (20 : 1 wt%), and POx-*b*-POzi/Alg/clay (20 : 1 : 1.5 wt%) hydrogel precursor solutions (ink materials) prepared in filtered-sterile DI water were further sterilized under UV light for 1h and diluted into 10, 5, 1.5, and 1 wt% in ice-cold fresh growth media. About 100  $\mu$ L of each diluted polymer in growth media was added to their assigned cell groups (n=4) and incubated for 24 h under standard culture conditions. Thereafter, treated media was carefully removed and cells were washed with PBS. Subsequently, cells were treated with freshly prepared WST-1 reagent solution for 1 h according to manufacturer's instruction and absorbance values were recorded at 450 nm using Spark 20M multimode microplate reader (Tecan, Germany). Further, fibroblasts, with density of  $1 \times 10^6$  cell per mL, were incorporated into hydrogel precursor solutions (POx-*b*-POzi (20 wt%), POx-*b*-POzi/Alg (20 : 1 wt%), and POx-*b*-POzi/Alg/clay (20 : 1 : 1.5 wt%)) and were thoroughly mixed on ice bath. Then, 100  $\mu$ L of cell-laden hydrogel solutions were added into specified wells of each group (n=4) in pre-warmed 96 well plate. While POx-*b*-POzi/Alg and POx-*b*-POzi/Alg/clay groups were followed by ionic crosslinking for 10 min with 1 wt% CaCl<sub>2</sub> aqueous solution filtered through a sterile 0.2  $\mu$ m membrane, a widely used and acceptable processing conditions in cell study. Thereafter, CaCl<sub>2</sub> solution was removed and crosslinked hydrogels were washed thrice in PBS. About 100  $\mu$ L of fresh media was added into each well and cell-laden hydrogels were incubated under standard culture conditions. Finally, WST-1 assay was performed at day 1 and day 3 as described before.

#### *Cells proliferation and viability in 3D bioprinted constructs*

To investigate the proliferation and viability of cells in bioprinted construct, fibroblast ( $1 \times 10^6$  cells per mL) were incorporated into POx-*b*-POzi/Alg (20 : 1 wt%) and

POx-*b*-POzi/Alg/clay (20 : 1 : 1.5 wt%) hydrogel precursor solutions (ink materials) as discussed earlier. Thereafter, still on ice bath, the bioinks were transferred into the pneumatic syringe dispenser equipped with the needle of 23 G, and then printed as the previously described. Subsequently, bioprinted constructs were treated with pre-sterile CaCl<sub>2</sub> solution (1 wt%) for 10 min for ionic crosslinking following 3-time washing in PBS. About 3 mL of growth media was added into each sample and media was changed on every alternative day and cell distribution in bioprinted constructs was analyzed at day 1 and day 5 using optical microscope. The DNA assay was performed to assess the proliferation of cells in each group (n=6) at day 1, 3, and 5. Briefly, samples were collected on each interval of times, washed thrice in PBS, and treated with 300 µL of RIPA buffers (150 mM Trizma-base, 150 mM NaCl, 1% sodium deoxycholate, 0.1% SDS, and 1% Triton X-100 in distilled water). The samples were chopped in RIPA buffers and supernatants were collected after centrifugation at 12,000 rpm for 10 min. Then, DNA assay was performed using with Quant-iT PicoGreen dsDNA assay kits (Invitrogen, Carlsbad, CA, USA) according to the manufacturer's guidelines.

Then, we examined the viability and distribution of the cells in POx-*b*-POzi/Alg/clay bioprinted constructs using Live and Dead assay and immunofluorescence staining. The cell-laden constructs were incubated under standard culture conditions and analyzed at 1, 3, 5, 7, 14, and 21 days. For the Live and Dead assay, we treated the constructs in a working solution of ethidium homodimer (1:500) and calcein-AM (1:1000) prepared in DPBS for 30 min. Then, the images of live and dead cells were acquired using a fluorescent microscope (Zeiss Axioimager Z1 microscope). For immunofluorescence staining, the constructs were fixed in 4% paraformaldehyde solution overnight at 4 °C. After that, constructs were frozen in OCT (Surgipath, Leica, Richmond, IL, USA) compound at -20 °C overnight. Then, we prepared 10 µm thick sections using a Cryostat Cryocut microtome (Leica Biosystems GmbH, Wetzlar, Germany). Next, samples were washed in PBS for 20 min to dissolve OCT and treated with 0.1% Tween 20 solution in PBS for permeabilization for 20 min. Following permeabilization, samples were treated

with blocking buffers (2% bovine serum albumin (BSA)) for 1 hr at 37 °C. Subsequently, overnight incubation of samples with collagen type-I antibody (1:100) at 4 °C. The next day, samples were washed in PBS five times and incubated with a secondary antibody solution composed of Alexa fluor 488 anti-mouse (1:200) and Rhodamine Phalloidin (1:1000) in blocking buffers for 2 h. Then, samples were washed in PBS five times, mounted with DAPI mounting medium, and observed under fluorescence microscopy.

## 7.2 Reagents and Solvents

All substances and reagents for the polymer synthesis and hydrogel preparation were obtained from Sigma-Aldrich (Steinheim, Germany), Acros (Geel, Belgium) or Thermo Fisher Scientific (Waltham, USA) and were used as received unless otherwise stated. Deuterated solvents for NMR analysis were obtained from Deutero GmbH (Kastellaun, Germany). Reagents used for synthesis of PMeOx-*b*-PnPrOzi (POx-*b*-POzi) diblock copolymer, specifically the initiator methyl trifluoromethylsulfonate (MeOTf), monomer 2-methyl-2-oxazoline (MeOx), and solvent benzonitrile (PhCN) were dried by refluxing over CaH<sub>2</sub> under dry argon atmosphere followed by subsequent distillation. Another monomer 2-*n*-propyl-2-oxazine (nPrOzi) was synthesized and kindly provided by Lukas Hahn. It was synthesized by an adapted standard procedure, distilled over CaH<sub>2</sub>, distilled, and stored under dry argon.

Laponite XLG ([Mg<sub>5.34</sub>Li<sub>0.66</sub>Si<sub>8</sub>O<sub>20</sub>(OH)<sub>4</sub>] Na<sub>0.66</sub>) was purchased from BYK-Chemical GmbH (Wesel, Germany) and used as received. VIVAPHARM® Alginate PH176 (Alg) is extracted from brown algae, approved as a pharmaceutical excipient, and obtained from JRS PHARMA GmbH & Co KG (Rosenberg, Germany). Deionized (DI) water was used throughout the experiments. Murine NIH 3T3 fibroblast (ATTC-Number CRL-1658) were purchased from ATCC (Manassas, VA, USA). Dulbecco's Modified Eagle Medium (DMEM) was from Sigma-Aldrich (Schnelldorf, Germany), Water-soluble tetrazolium (WST-1) was from Roche (Basel, Switzerland), Fetal bovine serum (FBS) was from Gibco (Darmstadt, Germany) and Penicillin and streptomycin (P/s) solution were purchased from Biochrom AG (Berlin, Germany). Rhodamine Phalloidin Reagent, anti-collagen type-I, and Alexa fluor 488 anti-mouse secondary antibody was purchased from Abcam (Cambridge, UK).

## 7.3 Methods

### 7.3.1 Polymer Synthesis

Unless otherwise stated, all LCROP of 2-oxazolines and 2-oxazines were carried out according to the following procedure.

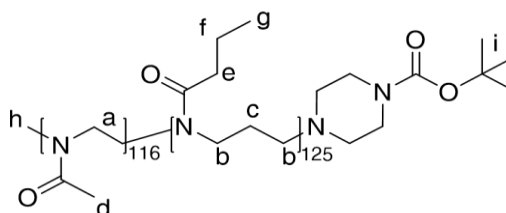
The initiator MeOTf and monomer MeOx of the first block were dissolved in dry PhCN at room temperature under dry and inert conditions in a flame-dried flask. The reaction mixture was placed in an oil bath and heated to 120 °C at least for 4 h. Full monomer conversion was verified by <sup>1</sup>H NMR spectroscopy before addition of the monomer of the second block. The second block nPrOzi dissolved in dry PhCN was added after the reaction mixture cooled to ambient temperature, and then placed back in an oil bath at 140 °C overnight. Termination with Boc-Pip was carried out with 3 eq with respect to the initiator for overnight at 40 °C. Subsequently, after cooling to room temperature, an excess of potassium carbonate was added and the mixture was stirred for at least 5 h. Thereafter, the solvent was removed at reduced pressure and the residual was dissolved in deionized water, dialyzed against deionized water using a dialysis membrane (molecular weight cut-off (MWCO) of 10 kDa) for 2 days and then freeze-dried to obtain the final product.

#### ***PMeOx-b-PnPrOzi Diblock Copolymer, HUC-01.1***

Lab notebook-ID:	HUC-01.1	
Initiation:	MeOTf	50 µL (0.46 mmol, 1 eq)
Monomer 1 <sup>st</sup> block:	MeOx	3.99 g (46.88 mmol, 100 eq)
Monomer 2 <sup>nd</sup> block:	nPrOzi	5.99 g (47.14 mmol, 100 eq)
Termination:	Boc-Pip	0.26 g (1.40 mmol, 3 eq)
Solvent (1/2):	PhCN	9.43 mL/11.67 mL

Reaction time (1/2):	4.5 h/14 h
Yield:	9.06 g (90.78%)
M:	25.97 kg/mol
GPC (HFIP):	$M_n=7.7$ kg/mol, $\bar{D}=1.28$
$^1\text{H NMR}$ :	(300 MHz, 298.15 K, $\text{CDCl}_3$ ): $\delta[\text{ppm}] = 3.45$ (br, 482H, $\text{H}^a$ ); 3.30 (br, 505H, $\text{H}^b$ ); 3.04 (br, 4H, $\text{H}^h$ ); 2.26-2.24 (br, 273H, $\text{H}^c$ ); 2.14-2.07 (br, 348H, $\text{H}^d$ ); 1.81 (br, 344H, $\text{H}^e$ ); 1.66-1.64 (br, 274H, $\text{H}^f$ ); 1.45 (s, 9H, $\text{H}^i$ ); 0.95 (br, 374H, $\text{H}^g$ )

Chemical structure:

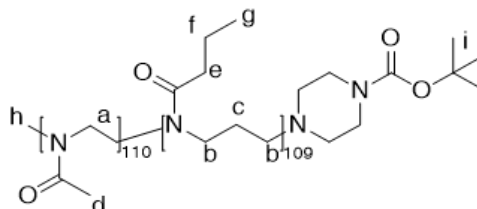


### *POx-b-POzi Diblock Copolymer, HUC-01.2*

Lab notebook-ID:	HUC-01.2
Initiation:	MeOTf 0.48 g (2.92 mmol, 1 eq)
Monomer 1 <sup>st</sup> block:	MeOx 24.92 g (292.8 mmol, 100 eq)
Monomer 2 <sup>nd</sup> block:	nPrOzi 37.27 g (293.0 mmol, 100 eq)
Termination:	Boc-Pip 1.63 g (8.76 mmol, 3 eq)
Solvent (1/2):	PhCN 56.58 mL/70.02 mL
Reaction time (1/2):	5.5 h/14 h
Yield:	60 g
M:	23.43 kg/mol
GPC (HFIP):	$M_n=7.32$ kg/mol, $\bar{D}=1.32$

$^1\text{H}$  NMR: (300 MHz, 298.15 K,  $\text{CDCl}_3$ ):  $\delta$ [ppm] = 3.44 (br, 451H,  $\text{H}^{\text{a}}$ ); 3.28 (br, 437H,  $\text{H}^{\text{b}}$ ); 2.24-2.22 (br, 263H,  $\text{H}^{\text{c}}$ ); 2.12-2.05 (br, 330H,  $\text{H}^{\text{d}}$ ); 1.77 (br, 213H,  $\text{H}^{\text{e}}$ ); 1.64-1.62 (br, 225H,  $\text{H}^{\text{f}}$ ); 1.43 (s, 9H,  $\text{H}^{\text{g}}$ ); 0.91 (br, 328H,  $\text{H}^{\text{h}}$ )

Chemical structure:

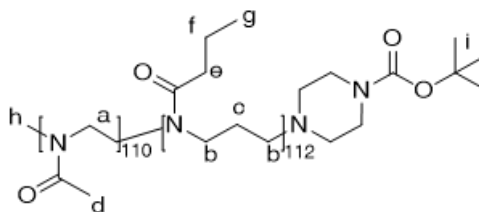


### *POx-b-POzi Diblock Copolymer, HUC-01.3*

Lab notebook-ID:	HUC-01.3	
Initiation:	MeOTf	0.48 g (2.92 mmol, 1 eq)
Monomer 1 <sup>st</sup> block:	MeOx	24.81 g (292.8 mmol, 100 eq)
Monomer 2 <sup>nd</sup> block:	nPrOzi	37.65 g (293.1 mmol, 101 eq)
Termination:	Boc-Pip	1.63 g (8.76 mmol, 3 eq)
Solvent (1/2):	PhCN	56.58 mL/70.02 mL
Reaction time (1/2):	6 h/14 h	
Yield:	58.3 g (93%)	
M:	24 kg/mol	
GPC (HFIP):	$M_n=8.5$ kg/mol, $D=1.3$	
$^1\text{H}$ NMR:	(300 MHz, 298.15 K, $\text{CDCl}_3$ ): $\delta$ [ppm] = 3.45 (br, 425H, $\text{H}^{\text{a}}$ ); 3.30 (br, 448H, $\text{H}^{\text{b}}$ ); 2.25-2.23 (br, 241H, $\text{H}^{\text{c}}$ ); 2.13-2.07 (br, 330H, $\text{H}^{\text{d}}$ ); 1.77 (br, 260H, $\text{H}^{\text{e}}$ ); 1.66-1.64 (br, 234H, $\text{H}^{\text{f}}$ ); 1.45 (s, 9H, $\text{H}^{\text{g}}$ ); 0.94 (br, 336H, $\text{H}^{\text{h}}$ )	



Chemical structure:



### 7.3.2 Hybrid Hydrogels Preparation

#### *PMeOx-*b*-POzi/clay Hybrid Hydrogels*

The PMeOx-*b*-PnPrOzi/clay nanocomposite hybrid hydrogels were prepared by thermogelation of an aqueous solution consisting of clay Laponite XLG and PMeOx-*b*-PnPrOzi diblock copolymers. Specifically, 2 wt% Laponite XLG aqueous sol was prepared by dispersing the appropriate amount of dry Laponite XLG powder in deionized water with continuous stirring to ensure the thorough hydration of Laponite powder, until a homogeneous and transparent clay sol was obtained (at least 24 h). The sol was stored in sealed containers to prevent evaporation, and shaken before use. Subsequently, the dry PMeOx-*b*-PnPrOzi was added to the 2 wt% clay sol to reach the desired polymer final concentration (15, 16, 18, 20 and 30 wt%) and stored at 7 °C overnight to allow complete dissolution (**Tab. 7.1**). Accordingly, the final clay concentration also changed with different polymer concentrations. For example, at 15 wt% polymer, the clay concentration was 1.7 wt%, while at 30 wt% polymer, the clay concentration was 1.4 wt%. Afterwards, the mixture solution can undergo a thermogelation at room temperature rapidly and form the stable PMeOx-*b*-PnPrOzi/clay hybrid hydrogels.

For reference, a 20 wt% PMeOx-*b*-PnPrOzi hydrogel without clay was also prepared accordingly. Unless otherwise noted, the hydrogels used throughout this study comprised PMeOx-*b*-PnPrOzi at a concentration of 20 wt% and a final clay concentration of 1.6 wt%. All samples were stored at 7 °C until used.

Tab. 7.1| Preparation of PMeOx-*b*-PnPrOzi/clay hybrid hydrogels.

PMeOx- <i>b</i> -PnPrOzi:clay (wt%)	15:1.70	16:1.68	18:1.64	20:1.60	30:1.40
PMeOx- <i>b</i> -PnPrOzi (g)	0.15	0.16	0.18	0.20	0.30
2 wt% clay sol (g)	0.85	0.84	0.82	0.80	0.70

### ***POx-*b*-POzi/PDMAA/clay Hybrid Hydrogels***

The POx-*b*-POzi/PDMAA/clay nanocomposite hybrid hydrogels were prepared by thermogelation and free radical polymerization from the initial solutions consisting of clay, POx-*b*-POzi, DMAA, N, N'-methylenebisacrylamide (MBAA), and initiator potassium persulfate (KPS). Exemplarily, the preparation of POx-*b*-POzi/PDMAA/clay hydrogel was performed as follows where the mass fraction of POx-*b*-POzi, PDMAA and clay were 30, 10 and 1.2 wt%. First, 2 wt% clay aqueous stock solution was prepared by dispersing the accurate amount of dry Laponite XLG powder in deionized water with continuous stirring to ensure the thorough hydration of Laponite powder, until a homogeneous and transparent solution was obtained (at least 24 h). Second, 0.4 g DMAA and 1.2 g lyophilized POx-*b*-POzi copolymer were added into 2.4 g 2 wt% clay solution. Thereafter, the mixture was stored at 7 °C overnight to allow complete dissolution followed by the addition of 0.002 g MBAA and 0.002 g initiator KPS, which are both at 0.5 wt% relative to the weight of DMAA, to obtain a homogeneous dispersion. Subsequently, the dispersion was transferred into a reaction cell consisting of two polymethyl methacrylate (PMMA) plates separated by a polyvinyl chloride (PVC) spacer to produce a physical cross-linked POx-*b*-POzi/DMAA/clay hydrogel at room temperature. Third, the mold was placed in an oven at 60 °C for 6 h to initiate the free radical polymerization of DMAA. The developed POx-*b*-POzi/PDMAA/clay hydrogels were obtained after taken out of the mold. For comparison, the hydrogel POx-*b*-POzi/PDMAA without clay was also prepared using DI water to replace 2 wt% clay aqueous solution as solvent.

***POx-b-POzi/Alg/clay Hybrid Hydrogel***

The POx-*b*-POzi/Alg/clay nanocomposite hybrid hydrogel was prepared *via* thermogelation of the initial blend solutions consisting of POx-*b*-POzi, Alg and clay, followed by ionic crosslinking step. Specifically the preparation of POx-*b*-POzi/Alg/clay hydrogel (20 : 1 : 1.5 wt%) was performed as follows. Initially, 0.015 g clay and 0.01 g Alg were dispersed in 0.775 g DI water with continuous stirring for few minutes. Subsequently, 0.2 g lyophilized POx-*b*-POzi copolymer was added into the mixture, and then stored at 7 °C (for at least 24 h) to allow complete polymer dissolution and to obtain a homogeneous dispersion. The dispersion was then transferred to a defined mold in cold state, and kept at room temperature for ten minutes to trigger the thermogelation process of POx-*b*-POzi/Alg/clay solution. Successively, the mold was immersed into 1 wt% CaCl<sub>2</sub> aqueous solution overnight to complete the further curing step of ionic crosslinking with Ca<sup>2+</sup>. The final POx-*b*-POzi/Alg/clay hydrogels were obtained followed by washing twice with DI water. For comparison, different POx-*b*-POzi/Alg hydrogels without clay were also prepared. In addition, the ionic crosslinking diversity of the hydrogels was also confirmed by replacing the CaCl<sub>2</sub> solution for ionic crosslinking step with FeCl<sub>3</sub>·6H<sub>2</sub>O (0.3 mol L<sup>-1</sup>) or TbCl<sub>3</sub>·6H<sub>2</sub>O (0.3 mol L<sup>-1</sup>) solution.



# Bibliography



- 
- [1] C. Hull, *Apparatus for production of three-dimensional objects by stereolithography*, U. S. Patent 4575330 **1986**, 11.
- [2] J. Edgar, S. Tint, *Johnson Matthey Technol. Rev.* **2015**, 59, 193-198.
- [3] W. Lee, J. C. Debasitis, V. K. Lee, J. H. Lee, K. Fischer, K. Edminster, J. K. Park, S. S. Yoo, *Biomaterials* **2009**, 30, 1587-1595.
- [4] B. Wendel, D. Rietzel, F. Kühnlein, R. Feulner, G. Hülder, E. Schmachtenberg, *Macromol. Mater. Eng.* **2008**, 293, 799-809.
- [5] D. T. Pham, R. S. Gault, *Int. J. Mach. Tools Manuf.* **1998**, 38, 1257-1287.
- [6] R. Bracci, E. Maccaroni, S. Cascinu, *N. Engl. J. Med.* **2013**, 368, 2043-2045.
- [7] J.-P. Kruth, M.-C. Leu, T. Nakagawa, *Cirp Annals* **1998**, 47, 525-540.
- [8] B. Berman, *Bus. Horiz.* **2012**, 55, 155-162.
- [9] J. Groll, T. Boland, T. Blunk, J. A. Burdick, D.-W. Cho, P. D. Dalton, B. Derby, G. Forgacs, Q. Li, V. A. Mironov, *Biofabrication* **2016**, 8, 013001.
- [10] S. V. Murphy, A. Atala, *Nat. Biotechnol.* **2014**, 32, 773-785.
- [11] T. Jungst, W. Smolan, K. Schacht, T. Scheibel, J. Groll, *Chem. Rev.* **2016**, 116, 1496-1539.
- [12] C. J. Ferris, K. G. Gilmore, G. G. Wallace, *Appl. Microbiol. Biotechnol.* **2013**, 97, 4243-4258.
- [13] L. Moroni, T. Boland, J. A. Burdick, C. De Maria, B. Derby, G. Forgacs, J. Groll, Q. Li, J. Malda, V. A. Mironov, *Trends Biotechnol.* **2018**, 36, 384-402.
- [14] R. D. Pedde, B. Mirani, A. Navaei, T. Styan, S. Wong, M. Mehrali, A. Thakur, N. K. Mohtaram, A. Bayati, A. Dolatshahi-Pirouz, *Adv. Mater.* **2017**, 29, 1606061.
- [15] D. Tang, R. S. Tare, L.-Y. Yang, D. F. Williams, K.-L. Ou, R. O. Oreffo, *Biomaterials* **2016**, 83, 363-382.
- [16] R. F. Pereira, C. C. Barrias, P. L. Granja, P. J. Bartolo, *Nanomedicine* **2013**, 8, 603-621.
- [17] P. Bajaj, R. M. Schweller, A. Khademhosseini, J. L. West, R. Bashir, *Annu. Rev. Biomed. Eng.* **2014**, 16, 247-276.
- [18] J. Malda, J. Visser, F. P. Melchels, T. Jüngst, W. E. Hennink, W. J. Dhert, J. Groll, D. W. Hutmacher, *Adv. Mater.* **2013**, 25, 5011-5028.
- [19] W. Sun, B. Starly, A. C. Daly, J. A. Burdick, J. Groll, G. Skeldon, W. Shu, Y. Sakai, M. Shinohara, M. Nishikawa, J. Jang, D. W. Cho, M. Nie, S. Takeuchi, S. Ostrovidov, A. Khademhosseini, R. D. Kamm, V. Mironov, L. Moroni, I. T. Ozbolat, *Biofabrication* **2020**, 12, 022002.
- [20] S. V. Murphy, A. Atala, *Nat. Biotechnol.* **2014**, 32, 773-85.
-

- 
- [21] T. J. Horn, O. L. Harrysson, *Sci. Prog.* **2012**, *95*, 255-282.
- [22] N. J. Mankovich, D. Samson, W. Pratt, D. Lew, J. Beumer III, *Otolaryngol. Clin. N. Am.* **1994**, *27*, 875-889.
- [23] A. J. Megibow, M. A. Bosniak, *Am. J. Roentgenol.* **1980**, *134*, 1273-1274.
- [24] R. Zagoria, *Neuroimag. Clin. N. Am.* **1994**, *4*, 1-8.
- [25] D. Tang, R. S. Tare, L. Y. Yang, D. F. Williams, K. L. Ou, R. O. C. Oreffo, *Biomaterials* **2016**, *83*, 363-382.
- [26] M. Mobaraki, M. Ghaffari, A. Yazdanpanah, Y. Luo, D. K. Mills, *Bioprinting* **2020**, *18*, e00080.
- [27] C. Mandrycky, Z. J. Wang, K. Kim, D. H. Kim, *Biotechnol. Adv.* **2016**, *34*, 422-434.
- [28] K. Holzl, S. Lin, L. Tytgat, S. Van Vlierberghe, L. Gu, A. Ovsianikov, *Biofabrication* **2016**, *8*, 032002.
- [29] T. Jungst, W. Smolan, K. Schacht, T. Scheibel, J. Groll, *Chem. Rev.* **2016**, *116*, 1496-1539.
- [30] R. D. Pedde, B. Mirani, A. Navaei, T. Styan, S. Wong, M. Mehrali, A. Thakur, N. K. Mohtaram, A. Bayati, A. Dolatshahi-Pirouz, M. Nikkhah, S. M. Willerth, M. Akbari, *Adv. Mater.* **2017**, *29*, 1606061.
- [31] U. A. Gurkan, R. El Assal, S. E. Yildiz, Y. Sung, A. J. Trachtenberg, W. P. Kuo, U. Demirci, *Mol. Pharm.* **2014**, *11*, 2151-2159.
- [32] N. Jones, *Nature* **2012**, *487*, 22-23.
- [33] L. Valot, J. Martinez, A. Mehdi, G. Subra, *Chem. Soc. Rev.* **2019**, *48*, 4049-4086.
- [34] S. Derakhshanfar, R. Mbeleck, K. Xu, X. Zhang, W. Zhong, M. Xing, *Bioact. Mater.* **2018**, *3*, 144-156.
- [35] M. K. Włodarczyk-Biegun, A. Del Campo, *Biomaterials* **2017**, *134*, 180-201.
- [36] B. Derby, *science* **2012**, *338*, 921-926.
- [37] C. Ferris, K. Gilmore, G. Wallace, *Appl. Microbiol. Biotechnol.* **2013**, *97*, 4243s-4258s.
- [38] J. K. Placone, A. J. Engler, *Adv. Healthc. Mater.* **2018**, *7*, 1701161.
- [39] S. Khalil, W. Sun, *Mater. Sci. Eng. C* **2007**, *27*, 469-478.
- [40] C. C. Chang, E. D. Boland, S. K. Williams, J. B. Hoying, *J. Biomed. Mater. Res. Part B: Appl. Biomater.* **2011**, *98*, 160-170.
- [41] N. E. Fedorovich, I. Swennen, J. Girones, L. Moroni, C. A. Van Blitterswijk, E. Schacht, J. Alblas, W. J. Dhert, *Biomacromolecules* **2009**, *10*, 1689-1696.
- [42] R. Chang, J. Nam, W. Sun, *Tissue Eng. Part A* **2008**, *14*, 41-48.
-



- 
- [43] K. Jakab, B. Damon, A. Neagu, A. Kachurin, G. Forgacs, *Biorheology* **2006**, *43*, 509-513.
- [44] J. Visser, B. Peters, T. J. Burger, J. Boomstra, W. J. Dhert, F. P. Melchels, J. Malda, *Biofabrication* **2013**, *5*, 035007.
- [45] J. Malda, J. Visser, F. P. Melchels, T. Jungst, W. E. Hennink, W. J. A. Dhert, J. Groll, D. W. Huttmacher, *Adv. Mater.* **2013**, *25*, 5011-5028.
- [46] A. C. Daly, F. E. Freeman, T. Gonzalez-Fernandez, S. E. Critchley, J. Nulty, D. J. Kelly, *Adv. Healthc. Mater.* **2017**, *6*, 1700298.
- [47] G. A. Fielding, A. Bandyopadhyay, S. Bose, *Dent. Mater.* **2012**, *28*, 113-122.
- [48] V. Mironov, R. P. Visconti, V. Kasyanov, G. Forgacs, C. J. Drake, R. R. Markwald, *Biomaterials* **2009**, *30*, 2164-2174.
- [49] C. M. Smith, A. L. Stone, R. L. Parkhill, R. L. Stewart, M. W. Simpkins, A. M. Kachurin, W. L. Warren, S. K. Williams, *Tissue Eng.* **2004**, *10*, 1566-1576.
- [50] A. Schwab, R. Levato, M. D'Este, S. Piluso, D. Eglin, J. Malda, *Chem. Rev.* **2020**, *120*, 11028-11055.
- [51] M. T. Poldervaart, H. Wang, J. van der Stok, H. Weinans, S. C. Leeuwenburgh, F. C. Öner, W. J. Dhert, J. Alblas, *PLoS One* **2013**, *8*, e72610.
- [52] F. You, B. F. Eames, X. Chen, *Int. J. Mol. Sci.* **2017**, *18*, 1597.
- [53] B. Duan, L. A. Hockaday, K. H. Kang, J. T. Butcher, *J. Biomed. Mater. Res. A* **2013**, *101*, 1255-1264.
- [54] R. Gaetani, P. A. Doevendans, C. H. Metz, J. Alblas, E. Messina, A. Giacomello, J. P. Sluijter, *Biomaterials* **2012**, *33*, 1782-1790.
- [55] C. Norotte, F. S. Marga, L. E. Niklason, G. Forgacs, *Biomaterials* **2009**, *30*, 5910-5917.
- [56] F. Xu, J. Celli, I. Rizvi, S. Moon, T. Hasan, U. Demirci, *Biotechnol. J.* **2011**, *6*, 204-212.
- [57] P. De Coppi, G. Bartsch, M. M. Siddiqui, T. Xu, C. C. Santos, L. Perin, G. Mostoslavsky, A. C. Serre, E. Y. Snyder, J. J. Yoo, *Nat. Biotechnol.* **2007**, *25*, 100-106.
- [58] R. J. Klebe, *Exp. Cell Res.* **1988**, *179*, 362-373.
- [59] T. Xu, H. Kincaid, A. Atala, J. J. Yoo, *J. Manuf. Sci. Eng.* **2008**, *130*, 021017.
- [60] T. Xu, J. Olson, W. Zhao, A. Atala, J.-M. Zhu, J. J. Yoo, *J. Manuf. Sci. Eng.* **2008**, *130*, 021013.
- [61] S. Kamisuki, T. Hagata, C. Tezuka, Y. Nose, M. Fujii, M. Atobe, *A low power, small, electrostatically-driven commercial inkjet head*, Proceedings MEMS 98.
-

- IEEE. Eleventh Annual International Workshop on Micro Electro Mechanical Systems. An Investigation of Micro Structures, Sensors, Actuators, Machines and Systems (Cat. No. 98CH36176, IEEE: **1998**, 63-68.
- [62] A. Skardal, D. Mack, E. Kapetanovic, A. Atala, J. D. Jackson, J. Yoo, S. Soker, *Stem Cells Transl. Med.* **2012**, *1*, 792-802.
- [63] X. Cui, K. Breitenkamp, M. Finn, M. Lotz, D. D. D'Lima, *Tissue Eng. Part A* **2012**, *18*, 1304-1312.
- [64] N. A. Sears, D. R. Seshadri, P. S. Dhavalikar, E. Cosgriff-Hernandez, *Tissue Eng. Part B: Reviews* **2016**, *22*, 298-310.
- [65] S. Ji, M. Guvendiren, *Front. Bioeng. Biotechnol.* **2017**, *5*, 23.
- [66] A. Pfister, R. Landers, A. Laib, U. Hübner, R. Schmelzeisen, R. Mülhaupt, *J. Polym. Sci., Part A: Polym. Chem.* **2004**, *42*, 624-638.
- [67] C. M. O'Brien, B. Holmes, S. Faucett, L. G. Zhang, *Tissue Eng. Part B: Rev.* **2015**, *21*, 103-114.
- [68] X. Cui, T. Boland, D. DD'Lima, M. K Lotz, *Recent Pat. Drug Deliv. Formul.* **2012**, *6*, 149-155.
- [69] J. D. Kim, J. S. Choi, B. S. Kim, Y. C. Choi, Y. W. Cho, *Polymer* **2010**, *51*, 2147-2154.
- [70] B. Guillotin, F. Guillemot, *Trends Biotechnol.* **2011**, *29*, 183-190.
- [71] T. Okamoto, T. Suzuki, N. Yamamoto, *Nat. Biotechnol.* **2000**, *18*, 438-441.
- [72] T. Goldmann, J. S. Gonzalez, *J. Biochem. Bioph. Methods* **2000**, *42*, 105-110.
- [73] X. Cui, D. Dean, Z. M. Ruggeri, T. Boland, *Biotechnol. Bioeng.* **2010**, *106*, 963-969.
- [74] T. Xu, C. A. Gregory, P. Molnar, X. Cui, S. Jalota, S. B. Bhaduri, T. Boland, *Biomaterials* **2006**, *27*, 3580-3588.
- [75] T. Xu, J. Jin, C. Gregory, J. J. Hickman, T. Boland, *Biomaterials* **2005**, *26*, 93-99.
- [76] H. Wijshoff, *Phys. Rep.* **2010**, *491*, 77-177.
- [77] E. Tekin, P. J. Smith, U. S. Schubert, *Soft Matter* **2008**, *4*, 703-713.
- [78] Y. Fang, J. P. Frampton, S. Raghavan, R. Sabahi-Kaviani, G. Luker, C. X. Deng, S. Takayama, *Tissue Eng. Part C: Methods* **2012**, *18*, 647-657.
- [79] U. Demirci, G. Montesano, *Lab on a Chip* **2007**, *7*, 1139-1145.
- [80] R. Saunders, L. Bosworth, J. Gough, B. Derby, N. Reis, *Eur. Cells Mater.* **2004**, *7*, 84.
- [81] R. E. Saunders, J. E. Gough, B. Derby, *Biomaterials* **2008**, *29*, 193-203.

- 
- [82] M. Nakamura, A. Kobayashi, F. Takagi, A. Watanabe, Y. Hiruma, K. Ohuchi, Y. Iwasaki, M. Horie, I. Morita, S. Takatani, *Tissue Eng.* **2005**, *11*, 1658-1666.
- [83] J. Bohandy, B. Kim, F. Adrian, *J. Appl. Phys.* **1986**, *60*, 1538-1539.
- [84] J. A. Barron, B. R. Ringeisen, H. Kim, B. J. Spargo, D. B. Chrisey, *Thin Solid Films* **2004**, *453*, 383-387.
- [85] W. Liu, M. A. Heinrich, Y. Zhou, A. Akpek, N. Hu, X. Liu, X. Guan, Z. Zhong, X. Jin, A. Khademhosseini, *Adv. Healthc. Mater.* **2017**, *6*, 1601451.
- [86] F. Guillemot, A. Souquet, S. Catros, B. Guillotin, *Nanomedicine* **2010**, *5*, 507-515.
- [87] V. Dinca, E. Kasotakis, J. Catherine, A. Mourka, A. Ranella, A. Ovsianikov, B. N. Chichkov, M. Farsari, A. Mitraki, C. Fotakis, *Nano Lett.* **2008**, *8*, 538-543.
- [88] M. Colina, P. Serra, J. M. Fernández-Pradas, L. Sevilla, J. L. Morenza, *Biosens. Bioelectron.* **2005**, *20*, 1638-1642.
- [89] B. R. Ringeisen, H. Kim, J. A. Barron, D. B. Krizman, D. B. Chrisey, S. Jackman, R. Auyeung, B. J. Spargo, *Tissue Eng.* **2004**, *10*, 483-491.
- [90] B. Guillotin, A. Souquet, S. Catros, M. Duocastella, B. Pippenger, S. Bellance, R. Bareille, M. Rémy, L. Bordenave, J. Amédée, *Biomaterials* **2010**, *31*, 7250-7256.
- [91] X. Zhai, Y. Ma, C. Hou, F. Gao, Y. Zhang, C. Ruan, H. Pan, W. W. Lu, W. Liu, *ACS Biomate. Sci. Eng.* **2017**, *3*, 1109-1118.
- [92] B. Hopp, T. Smausz, N. Kresz, N. Barna, Z. Bor, L. Kolozsvári, D. B. Chrisey, A. Szabó, A. Nógrádi, *Tissue Eng.* **2005**, *11*, 1817-1823.
- [93] M. Gruene, A. Deiwick, L. Koch, S. Schlie, C. Unger, N. Hofmann, I. Bernemann, B. Glasmacher, B. Chichkov, *Tissue Eng. Part C: Methods* **2011**, *17*, 79-87.
- [94] L. Koch, S. Kuhn, H. Sorg, M. Gruene, S. Schlie, R. Gaebel, B. Polchow, K. Reimers, S. Stoelting, N. Ma, *Tissue Eng. Part C: Methods* **2010**, *16*, 847-854.
- [95] C. Mandrycky, Z. Wang, K. Kim, D.-H. Kim, *Biotechnol. Adv.* **2016**, *34*, 422-434.
- [96] F. P. Melchels, J. Feijen, D. W. Grijpma, *Biomaterials* **2010**, *31*, 6121-6130.
- [97] J. W. Lee, J. Y. Kim, D.-W. Cho, *Int. J. Stem Cells* **2010**, *3*, 85-95.
- [98] N. E. Fedorovich, J. Alblas, J. R. de Wijn, W. E. Hennink, A. J. Verbout, W. J. Dhert, *Tissue Eng.* **2007**, *13*, 1905-1925.
- [99] J. L. Drury, D. J. Mooney, *Biomaterials* **2003**, *24*, 4337-4351.
- [100] Y. S. Zhang, A. Khademhosseini, *Science* **2017**, *356*.
- [101] J. Li, C. Wu, P. K. Chu, M. Gelinsky, *Mater. Sci. Eng. R: Rep.* **2020**, *140*, 100543.
- [102] T. Birman, D. Seliktar, *Adv. Funct. Mater.* **2021**, *31*, 2100628.
- [103] I. T. Ozbolat, M. Hospodiuk, *Biomaterials* **2016**, *76*, 321-343.
- [104] D. M. Kirchmayer, R. Gorkin Iii, *J. Mater. Chem. B* **2015**, *3*, 4105-4117.
-

- 
- [105] P. S. Gungor-Ozkerim, I. Inci, Y. S. Zhang, A. Khademhosseini, M. R. Dokmeci, *Biomater. Sci.* **2018**, *6*, 915-946.
- [106] W. Schuurman, P. A. Levett, M. W. Pot, P. R. van Weeren, W. J. Dhert, D. W. Hutmacher, F. P. Melchels, T. J. Klein, J. Malda, *Macromol. Biosci.* **2013**, *13*, 551-561.
- [107] B. Balakrishnan, R. Banerjee, *Chem. Rev.* **2011**, *111*, 4453-4474.
- [108] J. L. Drury, R. G. Dennis, D. J. Mooney, *Biomaterials* **2004**, *25*, 3187-3199.
- [109] J. Cohen, K. L. Zaleski, G. Nourissat, T. P. Julien, M. A. Randolph, M. J. Yaremchuk, *J. Biomed. Mater. Res. Part A* **2011**, *96*, 93-99.
- [110] J. Jia, D. J. Richards, S. Pollard, Y. Tan, J. Rodriguez, R. P. Visconti, T. C. Trusk, M. J. Yost, H. Yao, R. R. Markwald, *Acta Biomater.* **2014**, *10*, 4323-4331.
- [111] S. Wüst, R. Müller, S. Hofmann, *J. Biomed. Mater. Res. Part A* **2015**, *103*, 2558-2570.
- [112] K. I. Draget, B. T. Stokke, Y. Yuguchi, H. Urakawa, K. Kajiwara, *Biomacromolecules* **2003**, *4*, 1661-1668.
- [113] K. Draget, G. S. Bræk, O. Smidsrød, *Carbohydr. Polym.* **1994**, *25*, 31-38.
- [114] O. Smidsrød, G. Skja, *Trends Biotechnol.* **1990**, *8*, 71-78.
- [115] Ý. A. Mørch, I. Donati, B. L. Strand, G. Skjåk-Bræk, *Biomacromolecules* **2006**, *7*, 1471-1480.
- [116] Y. Si, L. Wang, X. Wang, N. Tang, J. Yu, B. Ding, *Adv. Mater.* **2017**, *29*, 1700339.
- [117] G. T. Grant, E. R. Morris, D. A. Rees, P. J. Smith, D. Thom, *FEBS Lett.* **1973**, *32*, 195-198.
- [118] H.-J. Kong, K. Y. Lee, D. J. Mooney, *Polymer* **2002**, *43*, 6239-6246.
- [119] Z. Y. Wang, Q. Z. Zhang, M. Konno, S. Saito, *Biopolymers: Original Research on Biomolecules* **1994**, *34*, 737-746.
- [120] I. T. Ozbolat, H. Chen, Y. Yu, *Robot. Comput. Integr. Manuf.* **2014**, *30*, 295-304.
- [121] J. Rowley, *Biomaterials* **1999**, *20*, 45-53.
- [122] M. Rinaudo, *Prog. Polym. Sci.* **2006**, *31*, 603-632.
- [123] S.-Y. Ong, J. Wu, S. M. Moochhala, M.-H. Tan, J. Lu, *Biomaterials* **2008**, *29*, 4323-4332.
- [124] T. Chandy, C. P. Sharma, *Biomater. Artif. Cells Artif. Organs* **1990**, *18*, 1-24.
- [125] M. Dash, F. Chiellini, R. M. Ottenbrite, E. Chiellini, *Prog. Polym. Sci.* **2011**, *36*, 981-1014.
- [126] I. M. Van der Lubben, J. C. Verhoef, G. Borchard, H. E. Junginger, *Eur. J. Pharm. Sci.* **2001**, *14*, 201-207.
-

- 
- [127] E. I. Rabea, M. E.-T. Badawy, C. V. Stevens, G. Smaghe, W. Steurbaut, *Biomacromolecules* **2003**, *4*, 1457-1465.
- [128] E. Khor, L. Y. Lim, *Biomaterials* **2003**, *24*, 2339-2349.
- [129] S. V. Madihally, H. W. Matthew, *Biomaterials* **1999**, *20*, 1133-1142.
- [130] M. N. R. Kumar, *React. Funct. Polym.* **2000**, *46*, 1-27.
- [131] C. K. Pillai, W. Paul, C. P. Sharma, *Prog. Polym. Sci.* **2009**, *34*, 641-678.
- [132] I.-Y. Kim, S.-J. Seo, H.-S. Moon, M.-K. Yoo, I.-Y. Park, B.-C. Kim, C.-S. Cho, *Biotechnol. Adv.* **2008**, *26*, 1-21.
- [133] R. Riva, H. Ragelle, A. des Rieux, N. Duhem, C. Jérôme, V. Préat, *Chitosan for biomaterials II* **2011**, 19-44.
- [134] H. Sashiwa, S.-i. Aiba, *Prog. Polym. Sci.* **2004**, *29*, 887-908.
- [135] J. Berger, M. Reist, J. M. Mayer, O. Felt, N. Peppas, R. Gurny, *Eur. J. Pharm. Biopharm.* **2004**, *57*, 19-34.
- [136] L. Vachoud, N. Zydowicz, A. Domard, *Carbohydr. Res.* **1997**, *302*, 169-177.
- [137] D.-y. Teng, Z.-m. Wu, X.-g. Zhang, Y.-x. Wang, C. Zheng, Z. Wang, C.-x. Li, *Polymer* **2010**, *51*, 639-646.
- [138] F. Bastian, M.-E. Stelzmüller, K. Kratochwill, M.-T. Kasimir, P. Simon, G. Weigel, *Biomaterials* **2008**, *29*, 1824-1832.
- [139] L. Ma, C. Gao, Z. Mao, J. Zhou, J. Shen, X. Hu, C. Han, *Biomaterials* **2003**, *24*, 4833-4841.
- [140] Y. Hong, H. Song, Y. Gong, Z. Mao, C. Gao, J. Shen, *Acta Biomater.* **2007**, *3*, 23-31.
- [141] T. Hao, N. Wen, J.-K. Cao, H.-B. Wang, S.-H. Lü, T. Liu, Q.-X. Lin, C.-M. Duan, C.-Y. Wang, *Osteoarthr. Cartilage* **2010**, *18*, 257-265.
- [142] G. Kogan, L. Šoltés, R. Stern, P. Gemeiner, *Biotechnol. Lett* **2007**, *29*, 17-25.
- [143] K. Meyer, *Physiol. Rev.* **1947**, *27*, 335-359.
- [144] H. Oxlund, T. Andreassen, *J. Anat.* **1980**, *131*, 611-620.
- [145] H. Knopf-Marques, M. Pravda, L. Wolfova, V. Velebny, P. Schaaf, N. E. Vrana, P. Lavallo, *Adv. Healthc. Mater.* **2016**, *5*, 2841-2855.
- [146] M. N. Collins, C. Birkinshaw, *Carbohydr. Polym.* **2013**, *92*, 1262-1279.
- [147] C. B. Highley, G. D. Prestwich, J. A. Burdick, *Curr. Opin. Biotechnol.* **2016**, *40*, 35-40.
- [148] S. Gerecht, J. A. Burdick, L. S. Ferreira, S. A. Townsend, R. Langer, G. Vunjak-Novakovic, *Proc. Nat. Acad. Sci.* **2007**, *104*, 11298-11303.
-

- 
- [149] E. Masaeli, V. Forster, S. Picaud, F. Karamali, M. H. Nasr-Esfahani, C. Marquette, *Biofabrication* **2020**, *12*, 025006.
- [150] O. Jeon, S. J. Song, K.-J. Lee, M. H. Park, S.-H. Lee, S. K. Hahn, S. Kim, B.-S. Kim, *Carbohydr. Polym.* **2007**, *70*, 251-257.
- [151] D. L. Nettles, T. P. Vail, M. T. Morgan, M. W. Grinstaff, L. A. Setton, *Ann. Biomed. Eng.* **2004**, *32*, 391-397.
- [152] A. Skardal, A. Atala, *Ann. Biomed. Eng.* **2015**, *43*, 730-746.
- [153] D. Klemm, B. Heublein, H. P. Fink, A. Bohn, *Angew. Chem. Int. Ed.* **2005**, *44*, 3358-3393.
- [154] A. Sannino, C. Demitri, M. Madaghiele, *Materials* **2009**, *2*, 353-373.
- [155] C. Chang, L. Zhang, *Carbohydr. Polym.* **2011**, *84*, 40-53.
- [156] K. Kobayashi, C.-i. Huang, T. P. Lodge, *Macromolecules* **1999**, *32*, 7070-7077.
- [157] S. Thirumala, J. M. Gimble, R. V. Devireddy, *Cells* **2013**, *2*, 460-475.
- [158] M. C. Mulakkal, R. S. Trask, V. P. Ting, A. M. Seddon, *Mater. Des.* **2018**, *160*, 108-118.
- [159] S. Sultan, A. P. Mathew, *Nanoscale* **2018**, *10*, 4421-4431.
- [160] S. F. Kabir, P. P. Sikdar, B. Haque, M. R. Bhuiyan, A. Ali, M. Islam, *Prog. Biomater.* **2018**, *7*, 153-174.
- [161] Q. Wang, J. Sun, Q. Yao, C. Ji, J. Liu, Q. Zhu, *Cellulose* **2018**, *25*, 4275-4301.
- [162] L. Gasperini, J. F. Mano, R. L. Reis, *J. R. Soc. Interface* **2014**, *11*, 20140817.
- [163] P. B. Malafaya, G. A. Silva, R. L. Reis, *Adv. Drug Deliv. Rev.* **2007**, *59*, 207-233.
- [164] P. A. Janmey, J. P. Winer, J. W. Weisel, *J. R. Soc. Interface* **2009**, *6*, 1-10.
- [165] D. A. Cheresch, S. A. Berliner, V. Vicente, Z. M. Ruggeri, *Cell* **1989**, *58*, 945-953.
- [166] Y.-B. Lee, S. Polio, W. Lee, G. Dai, L. Menon, R. S. Carroll, S.-S. Yoo, *Exp. Neurol.* **2010**, *223*, 645-652.
- [167] E. Abelseth, L. Abelseth, L. De la Vega, S. T. Beyer, S. J. Wadsworth, S. M. Willerth, *ACS Biomater. Sci. Eng.* **2018**, *5*, 234-243.
- [168] O. Tokareva, V. A. Michalczechen-Lacerda, E. L. Rech, D. L. Kaplan, *Microb. Biotechnol.* **2013**, *6*, 651-663.
- [169] K. Schacht, T. Scheibel, *Biomacromolecules* **2011**, *12*, 2488-2495.
- [170] G. H. Altman, F. Diaz, C. Jakuba, T. Calabro, R. L. Horan, J. Chen, H. Lu, J. Richmond, D. L. Kaplan, *Biomaterials* **2003**, *24*, 401-416.
- [171] A. Leal-Egaña, T. Scheibel, *Biotechnol. Appl. Biochem.* **2010**, *55*, 155-167.
- [172] L.-D. Koh, Y. Cheng, C.-P. Teng, Y.-W. Khin, X.-J. Loh, S.-Y. Tee, M. Low, E. Ye, H.-D. Yu, Y.-W. Zhang, *Prog. Polym. Sci.* **2015**, *46*, 86-110.
-

- 
- [173] K. Schacht, T. Jüngst, M. Schweinlin, A. Ewald, J. Groll, T. Scheibel, *Angew. Chem. Int. Ed.* **2015**, *54*, 2816-2820.
- [174] M. R. Sommer, M. Schaffner, D. Carnelli, A. R. Studart, *ACS Appl. Mater. Interfaces* **2016**, *8*, 34677-34685.
- [175] F. Agostinacchio, X. Mu, S. Dirè, A. Motta, D. L. Kaplan, *Trends Biotechnol.* **2021**, *39*, 719-730.
- [176] B. Yetiskin, O. Okay, *Polymer* **2017**, *112*, 61-70.
- [177] R. R. Jose, J. E. Brown, K. E. Polido, F. G. Omenetto, D. L. Kaplan, *ACS Biomater. Sci. Eng.* **2015**, *1*, 780-788.
- [178] A. M. Compaan, K. Christensen, Y. Huang, *ACS Biomater. Sci. Eng.* **2017**, *3*, 1519-1526.
- [179] J. B. Costa, J. Silva-Correia, J. M. Oliveira, R. L. Reis, *Adv. Healthc. Mater.* **2017**, *6*, 1701021.
- [180] M. Gómez-Guillén, B. Giménez, M. a. López-Caballero, M. Montero, *Food Hydrocoll.* **2011**, *25*, 1813-1827.
- [181] R. Harkness, *Biol. Rev.* **1961**, *36*, 399-455.
- [182] C. H. Lee, A. Singla, Y. Lee, *Int. J. Pharm.* **2001**, *221*, 1-22.
- [183] S. Gomes, I. B. Leonor, J. F. Mano, R. L. Reis, D. L. Kaplan, *Prog. Polym. Sci.* **2012**, *37*, 1-17.
- [184] M. Guvendiren, J. Molde, R. M. Soares, J. Kohn, *ACS Biomater. Sci. Eng.* **2016**, *2*, 1679-1693.
- [185] J. Glowacki, S. Mizuno, *Biopolymers: Original Research on Biomolecules* **2008**, *89*, 338-344.
- [186] B. Lanfer, F. P. Seib, U. Freudenberg, D. Stamov, T. Bley, M. Bornhäuser, C. Werner, *Biomaterials* **2009**, *30*, 5950-5958.
- [187] M. Achilli, D. Mantovani, *Polymers* **2010**, *2*, 664-680.
- [188] J. Y. Park, J.-C. Choi, J.-H. Shim, J.-S. Lee, H. Park, S. W. Kim, J. Doh, D.-W. Cho, *Biofabrication* **2014**, *6*, 035004.
- [189] B. D. Walters, J. P. Stegemann, *Acta Biomater.* **2014**, *10*, 1488-1501.
- [190] M. Rücker, M. W. Laschke, D. Junker, C. Carvalho, A. Schramm, R. Mülhaupt, N.-C. Gellrich, M. D. Menger, *Biomaterials* **2006**, *27*, 5027-5038.
- [191] C. Helary, I. Bataille, A. Abed, C. Illoul, A. Anglo, L. Louedec, D. Letourneur, A. Meddahi-Pelle, M. M. Giraud-Guille, *Biomaterials* **2010**, *31*, 481-490.
- [192] S. Young, M. Wong, Y. Tabata, A. G. Mikos, *J. Control. Release* **2005**, *109*, 256-274.
-

- 
- [193] A. Kuijpers, P. Van Wachem, M. Van Luyn, J. Plantinga, G. Engbers, J. Krijgsveld, S. Zaat, J. Dankert, J. Feijen, *Journal of Biomedical Materials Research: An Official Journal of The Society for Biomaterials, The Japanese Society for Biomaterials, and The Australian Society for Biomaterials and the Korean Society for Biomaterials* **2000**, *51*, 136-145.
- [194] K. Yue, G. Trujillo-de Santiago, M. M. Alvarez, A. Tamayol, N. Annabi, A. Khademhosseini, *Biomaterials* **2015**, *73*, 254-271.
- [195] H.-W. Kang, Y. Tabata, Y. Ikada, *Biomaterials* **1999**, *20*, 1339-1344.
- [196] C. Michon, G. Cuvelier, B. Launay, *Rheol. Acta* **1993**, *32*, 94-103.
- [197] Q. Xing, K. Yates, C. Vogt, Z. Qian, M. C. Frost, F. Zhao, *Sci. Rep.* **2014**, *4*, 1-10.
- [198] X. Wang, Y. Yan, Y. Pan, Z. Xiong, H. Liu, J. Cheng, F. Liu, F. Lin, R. Wu, R. Zhang, *Tissue Eng.* **2006**, *12*, 83-90.
- [199] L. E. Bertassoni, J. C. Cardoso, V. Manoharan, A. L. Cristino, N. S. Bhise, W. A. Araujo, P. Zorlutuna, N. E. Vrana, A. M. Ghaemmaghmi, M. R. Dokmeci, *Biofabrication* **2014**, *6*, 024105.
- [200] J. Huang, H. Zhang, Y. Yu, Y. Chen, D. Wang, G. Zhang, G. Zhou, J. Liu, Z. Sun, D. Sun, *Biomaterials* **2014**, *35*, 550-566.
- [201] W. Lee, V. Lee, S. Polio, P. Keegan, J. H. Lee, K. Fischer, J. K. Park, S. S. Yoo, *Biotechnol. Bioeng.* **2010**, *105*, 1178-1186.
- [202] H. K. Kleinman, G. R. Martin, *Semin. Cancer Biol.* **2005**, *15*, 378-386.
- [203] C. S. Hughes, L. M. Postovit, G. A. Lajoie, *Proteomics* **2010**, *10*, 1886-1890.
- [204] Z. Li, J. Guan, *Polymers* **2011**, *3*, 740-761.
- [205] N. E. Fedorovich, J. R. De Wijn, A. J. Verbout, J. Alblas, W. J. Dhert, *Tissue Eng. Part A* **2008**, *14*, 127-133.
- [206] N. E. Fedorovich, H. M. Wijnberg, W. J. Dhert, J. Alblas, *Tissue Eng. Part A* **2011**, *17*, 2113-2121.
- [207] J. Snyder, Q. Hamid, C. Wang, R. Chang, K. Emami, H. Wu, W. Sun, *Biofabrication* **2011**, *3*, 034112.
- [208] R. Fridman, G. Giaccone, T. Kanemoto, G. R. Martin, A. F. Gazdar, J. L. Mulshine, *Proc. Nat. Acad. Sci.* **1990**, *87*, 6698-6702.
- [209] S. Arnott, A. Fulmer, W. Scott, I. Dea, R. Moorhouse, D. Rees, *J. Mol. Biol.* **1974**, *90*, 269-284.
- [210] P. Zarrintaj, S. Manouchehri, Z. Ahmadi, M. R. Saeb, A. M. Urbanska, D. L. Kaplan, M. Mozafari, *Carbohydr. Polym.* **2018**, *187*, 66-84.
- [211] D. Velasco, E. Tumarkin, E. Kumacheva, *Small* **2012**, *8*, 1633-1642.
-



- 
- [212] H. A. Awad, M. Q. Wickham, H. A. Leddy, J. M. Gimble, F. Guilak, *Biomaterials* **2004**, *25*, 3211-3222.
- [213] D. F. D. Campos, A. Blaeser, M. Weber, J. Jäkel, S. Neuss, W. Jahnen-Dechent, H. Fischer, *Biofabrication* **2012**, *5*, 015003.
- [214] R. Landers, U. Hübner, R. Schmelzeisen, R. Mülhaupt, *Biomaterials* **2002**, *23*, 4437-4447.
- [215] G. Rijal, *Regen. Med.* **2017**, *12*, 475-477.
- [216] D. Hubmacher, S. S. Apte, *Curr. Opin. Rheumatol* **2013**, *25*, 65-70.
- [217] P. Lu, K. Takai, V. M. Weaver, Z. Werb, *Cold Spring Harb. Perspec. Biol.* **2011**, *3*, a005058.
- [218] G. Rijal, W. Li, *Biomaterials* **2016**, *81*, 135-156.
- [219] M. T. Spang, K. L. Christman, *Acta Biomater.* **2018**, *68*, 1-14.
- [220] F. Pati, J. Jang, D.-H. Ha, S. W. Kim, J.-W. Rhie, J.-H. Shim, D.-H. Kim, D.-W. Cho, *Nat. Commun.* **2014**, *5*, 1-11.
- [221] J. Jang, H.-J. Park, S.-W. Kim, H. Kim, J. Y. Park, S. J. Na, H. J. Kim, M. N. Park, S. H. Choi, S. H. Park, *Biomaterials* **2017**, *112*, 264-274.
- [222] B. S. Kim, S. Das, J. Jang, D.-W. Cho, *Chem. Rev.* **2020**, *120*, 10608-10661.
- [223] H. G. Schild, *Prog. Polym. Sci.* **1992**, *17*, 163-249.
- [224] C. De las Heras Alarcón, S. Pennadam, C. Alexander, *Chem. Soc. Rev.* **2005**, *34*, 276-285.
- [225] M. Heskins, J. E. Guillet, *J. Macromol. Sci.-Chem.* **1968**, *2*, 1441-1455.
- [226] T. Sun, G. Wang, L. Feng, B. Liu, Y. Ma, L. Jiang, D. Zhu, *Angew. Chem. Int. Ed.* **2004**, *43*, 357-360.
- [227] R. A. Stile, K. E. Healy, *Biomacromolecules* **2001**, *2*, 185-194.
- [228] K. Nagase, M. Yamato, H. Kanazawa, T. Okano, *Biomaterials* **2018**, *153*, 27-48.
- [229] M. Nizioł, J. Paleczny, A. Junka, A. Shavandi, A. Dawiec-Liśniewska, D. Podstawczyk, *Bioengineering* **2021**, *8*, 79.
- [230] Y. Dong, S. Wang, Y. Ke, L. Ding, X. Zeng, S. Magdassi, Y. Long, *Adv. Mater. Technol.* **2020**, *5*, 2000034.
- [231] H. Chu, W. Yang, L. Sun, S. Cai, R. Yang, W. Liang, H. Yu, L. Liu, *Micromachines* **2020**, *11*, 796.
- [232] S. Joshi, K. Rawat, C. Karunakaran, V. Rajamohan, A. T. Mathew, K. Koziol, V. K. Thakur, A. Balan, *Appl. Mater. Today* **2020**, *18*, 100490.
- [233] D. L. Elbert, *Acta Biomater.* **2011**, *7*, 31-56.
-

- 
- [234] R. Mooney, S. Haeger, R. Lawal, M. Mason, N. Shrestha, A. Laperle, K. Bjugstad, M. Mahoney, *Tissue Eng. Part A* **2011**, *17*, 2805-2815.
- [235] S. N. Alconcel, A. S. Baas, H. D. Maynard, *Polym. Chem.* **2011**, *2*, 1442-1448.
- [236] A. A. D'souza, R. Shegokar, *Expert Opin. Drug Del.* **2016**, *13*, 1257-1275.
- [237] J. M. Harris, *J. Macromol. Sci. Rev. Macromol. Chem. Phys.* **1985**, *25*, 325-373.
- [238] W. R. Gombotz, W. Guanghui, T. A. Horbett, A. S. Hoffman, *J. Biomed. Mater. Res.* **1991**, *25*, 1547-1562.
- [239] M. Barz, R. Luxenhofer, R. Zentel, M. J. Vicent, *Polym. Chem.* **2011**, *2*, 1900-1918.
- [240] K. Knop, R. Hoogenboom, D. Fischer, U. S. Schubert, *Angew. Chem. Int. Ed.* **2010**, *49*, 6288-6308.
- [241] J. J. Verhoef, T. J. Anchordoquy, *Drug Deliv. Transl Res.* **2013**, *3*, 499-503.
- [242] M. Zhang, T. Desai, M. Ferrari, *Biomaterials* **1998**, *19*, 953-960.
- [243] L. Hockaday, K. Kang, N. Colangelo, P. Cheung, B. Duan, E. Malone, J. Wu, L. Girardi, L. Bonassar, H. Lipson, *Biofabrication* **2012**, *4*, 035005.
- [244] J. A. Burdick, K. S. Anseth, *Biomaterials* **2002**, *23*, 4315-4323.
- [245] Z. Zhou, B. Chu, *J. Colloid Interface Sci.* **1988**, *126*, 171-180.
- [246] M. Bohorquez, C. Koch, T. Trygstad, N. Pandit, *J. Colloid Interface Sci.* **1999**, *216*, 34-40.
- [247] A. Cabana, A. Ait-Kadi, J. Juhász, *J. Colloid Interface Sci.* **1997**, *190*, 307-312.
- [248] W. Zhang, K. Gilstrap, L. Wu, R. B. KC, M. A. Moss, Q. Wang, X. Lu, X. He, *ACS Nano* **2010**, *4*, 6747-6759.
- [249] A. P. Constantinou, T. K. Georgiou, *Eur. Polym. J.* **2016**, *78*, 366-375.
- [250] G. Dumortier, J. L. Grossiord, F. Agnely, J. C. Chaumeil, *Pharm. Res.* **2006**, *23*, 2709-2728.
- [251] A. Paavola, I. Kilpeläinen, J. Yliruusi, P. Rosenberg, *Int. J. Pharm.* **2000**, *199*, 85-93.
- [252] J. Qin, I. Asempah, S. Laurent, A. Fornara, R. N. Muller, M. Muhammed, *Adv. Mater.* **2009**, *21*, 1354-1357.
- [253] S. H. Kwon, S. Y. Kim, K. W. Ha, M. J. Kang, J. S. Huh, Y. M. Kim, Y. M. Park, K. H. Kang, S. Lee, J. Y. Chang, *Arch. Pharmacol Res.* **2007**, *30*, 1138-1143.
- [254] R. N. Shamma, R. H. Sayed, H. Madry, N. S. El Sayed, M. Cucchiari, *Tissue Eng. Part B: Rev.* **2021**, DOI: <http://doi.org/10.1089/ten.teb.2021.0026>.
- [255] E. Gioffredi, M. Boffito, S. Calzone, S. M. Giannitelli, A. Rainer, M. Trombetta, P. Mozetic, V. Chiono, *Procedia Cirp* **2016**, *49*, 125-132.
-

- 
- [256] W. Wu, A. DeConinck, J. A. Lewis, *Adv. Mater.* **2011**, *23*, H178-H183.
- [257] M. Müller, J. Becher, M. Schnabelrauch, M. Zenobi-Wong, *Biofabrication* **2015**, *7*, 035006.
- [258] D. B. Kolesky, R. L. Truby, A. S. Gladman, T. A. Busbee, K. A. Homan, J. A. Lewis, *Adv. Mater.* **2014**, *26*, 3124-3130.
- [259] C. M. Homenick, G. de Silveira, H. Sheardown, A. Adronov, *Polym. Int.* **2011**, *60*, 458-465.
- [260] J. R. Thonhoff, D. I. Lou, P. M. Jordan, X. Zhao, P. Wu, *Brain Res.* **2008**, *1187*, 42-51.
- [261] Z. Liu, D. Liu, L. Wang, J. Zhang, N. Zhang, *Int. J. Mol. Sci.* **2011**, *12*, 1684-1696.
- [262] W. K. Palmer, E. E. Emeson, T. P. Johnston, *Atherosclerosis* **1998**, *136*, 115-123.
- [263] R. Luxenhofer, G. Sahay, A. Schulz, D. Alakhova, T. K. Bronich, R. Jordan, A. V. Kabanov, *J. Controlled Release* **2011**, *153*, 73-82.
- [264] G. Gillispie, P. Prim, J. Copus, J. Fisher, A. G. Mikos, J. J. Yoo, A. Atala, S. J. Lee, *Biofabrication* **2020**, *12*, 022003.
- [265] Y. He, F. Yang, H. Zhao, Q. Gao, B. Xia, J. Fu, *Sci. Rep.* **2016**, *6*, 1-13.
- [266] A. Ribeiro, M. M. Blokzijl, R. Levato, C. W. Visser, M. Castilho, W. E. Hennink, T. Vermonden, J. Malda, *Biofabrication* **2017**, *10*, 014102.
- [267] N. Paxton, W. Smolan, T. Böck, F. Melchels, J. Groll, T. Jungst, *Biofabrication* **2017**, *9*, 044107.
- [268] F. F. Cai, S. Heid, A. R. Boccaccini, *J. Biomed. Mater. Res. B: Appl. Biomater.* **2021**, *109*, 1090-1104.
- [269] M. Champeau, D. A. Heinze, T. N. Viana, E. R. de Souza, A. C. Chinellato, S. Titotto, *Adv. Funct. Mater.* **2020**, *30*.
- [270] M. Kesti, M. Müller, J. Becher, M. Schnabelrauch, M. D'Este, D. Eglin, M. Zenobi-Wong, *Acta Biomater.* **2015**, *11*, 162-172.
- [271] J. M. G. Cowie, V. Arrighi, *Polymers: chemistry and physics of modern materials*. CRC press: 2007.
- [272] N. Paxton, W. Smolan, T. Böck, F. Melchels, J. Groll, T. Jungst, *Biofabrication* **2017**, *9*, 044107.
- [273] E. A. Kiyotake, A. W. Douglas, E. E. Thomas, S. L. Nimmo, M. S. Detamore, *Acta Biomater.* **2019**, *95*, 176-187.
- [274] B. A. Aguado, W. Mulyasasmita, J. Su, K. J. Lampe, S. C. Heilshorn, *Tissue Eng. Part A* **2012**, *18*, 806-815.
-

- 
- [275] K. Hölzl, S. Lin, L. Tytgat, S. Van Vlierberghe, L. Gu, A. Ovsianikov, *Biofabrication* **2016**, 8, 032002.
- [276] S. J. Bryant, K. S. Anseth, *Journal of Biomedical Materials Research: An Official Journal of The Society for Biomaterials and The Japanese Society for Biomaterials* **2002**, 59, 63-72.
- [277] G. D. Nicodemus, S. J. Bryant, *Tissue Eng. Part B: Rev.* **2008**, 14, 149-165.
- [278] M. Guvendiren, H. D. Lu, J. A. Burdick, *Soft matter* **2012**, 8, 260-272.
- [279] L. Ouyang, C. B. Highley, C. B. Rodell, W. Sun, J. A. Burdick, *ACS Biomater. Sci. Eng.* **2016**, 2, 1743-1751.
- [280] C. W. Peak, J. Stein, K. A. Gold, A. K. Gaharwar, *Langmuir* **2018**, 34, 917-925.
- [281] T. Gao, G. J. Gillispie, J. S. Copus, A. K. Pr, Y.-J. Seol, A. Atala, J. J. Yoo, S. J. Lee, *Biofabrication* **2018**, 10, 034106.
- [282] C. B. Highley, K. H. Song, A. C. Daly, J. A. Burdick, *Adv. Sci.* **2019**, 6, 1801076.
- [283] A. Habib, V. Sathish, S. Mallik, B. Khoda, *Materials* **2018**, 11, 454.
- [284] C. O'Connell, J. Ren, L. Pope, Y. Li, A. Mohandas, R. Blanchard, S. Duchi, C. Onofrillo, *Methods Mol. Biol* **2020**, 2140, 111-133.
- [285] S. Naghieh, M. Sarker, N. Sharma, Z. Barhoumi, X. Chen, *Appl. Sci.* **2020**, 10, 292.
- [286] D. Chimene, R. Kaunas, A. K. Gaharwar, *Adv. Mater.* **2020**, 32, 1902026.
- [287] M. Sarker, X. Chen, *J. Manuf. Sci. Eng.* **2017**, 139, 081002.
- [288] L. Ouyang, R. Yao, Y. Zhao, W. Sun, *Biofabrication* **2016**, 8, 035020.
- [289] W. L. Ng, W. Y. Yeong, M. W. Naing, *Int. J. Bioprinting* **2016**, 2, 53-62.
- [290] D. Therriault, S. R. White, J. A. Lewis, *Appl. Rheol.* **2007**, 17, 10112-1-10112-8.
- [291] S. Wüst, M. E. Godla, R. Müller, S. Hofmann, *Acta Biomater.* **2014**, 10, 630-640.
- [292] N. C. Negrini, N. Celikkin, P. Tarsini, S. Farè, W. Świążzkowski, *Biofabrication* **2020**, 12, 025001.
- [293] M. K. Kim, W. Jeong, S. M. Lee, J. B. Kim, S. Jin, H.-W. Kang, *Biofabrication* **2020**, 12, 025003.
- [294] N. Soltan, L. Ning, F. Mohabatpour, P. Papagerakis, X. Chen, *ACS Biomater. Sci. Eng.* **2019**, 5, 2976-2987.
- [295] M. Müller, P. Fisch, M. Molnar, S. Eggert, M. Binelli, K. Maniura-Weber, M. Zenobi-Wong, *Mater. Sci. Eng.: C* **2020**, 108, 110510.
- [296] Y. Meng, J. Cao, Y. Chen, Y. Yu, L. Ye, *J. Mater. Chem. B* **2020**, 8, 677-690.
- [297] L. Wang, M.-e. Xu, L. Luo, Y. Zhou, P. Si, *Sci. Rep.* **2018**, 8, 1-13.
-

- 
- [298] A. Athirasala, A. Tahayeri, G. Thirvikraman, C. M. França, N. Monteiro, V. Tran, J. Ferracane, L. E. Bertassoni, *Biofabrication* **2018**, *10*, 024101.
- [299] S. A. Wilson, L. M. Cross, C. W. Peak, A. K. Gaharwar, *ACS Appl. Mater. Interfaces* **2017**, *9*, 43449-43458.
- [300] J. Göhl, K. Markstedt, A. Mark, K. Håkansson, P. Gatenholm, F. Edelvik, *Biofabrication* **2018**, *10*, 034105.
- [301] G. Ahn, K.-H. Min, C. Kim, J.-S. Lee, D. Kang, J.-Y. Won, D.-W. Cho, J.-Y. Kim, S. Jin, W.-S. Yun, *Sci. Rep.* **2017**, *7*, 1-11.
- [302] J. Y. Shin, Y. H. Yeo, J. E. Jeong, S. A. Park, W. H. Park, *Carbohydr. Polym.* **2020**, *238*, 116192.
- [303] S. V. Murphy, A. Skardal, A. Atala, *J. Biomed. Mater. Res. Part A* **2013**, *101*, 272-284.
- [304] B. Duan, E. Kapetanovic, L. A. Hockaday, J. T. Butcher, *Acta Biomater.* **2014**, *10*, 1836-1846.
- [305] L. E. Smith, R. Smallwood, S. Macneil, *Microsc. Res. Tech.* **2010**, *73*, 1123-1133.
- [306] R. K. Benninger, D. W. Piston, *Curr. Protoc. Cell Biol* **2013**, *59*, 4.11.1-4.11.24.
- [307] A. S. Gladman, E. A. Matsumoto, R. G. Nuzzo, L. Mahadevan, J. A. Lewis, *Nat. Mater.* **2016**, *15*, 413-418.
- [308] A. Kirillova, R. Maxson, G. Stoychev, C. T. Gomillion, L. Ionov, *Adv. Mater.* **2017**, *29*, 1703443.
- [309] Q. Yang, B. Gao, F. Xu, *Biotechnol. J.* **2020**, *15*, 1900086.
- [310] D. G. Tamay, T. Dursun Usal, A. S. Alagoz, D. Yucel, N. Hasirci, V. Hasirci, *Front. Bioeng. Biotechnol.* **2019**, *7*, 164.
- [311] D. Chimene, K. K. Lennox, R. R. Kaunas, A. K. Gaharwar, *Ann. Biomed. Eng.* **2016**, *44*, 2090-2102.
- [312] R. Levato, T. Jungst, R. G. Scheuring, T. Blunk, J. Groll, J. Malda, *Adv. Mater.* **2020**, *32*, 1906423.
- [313] E. A. Appel, M. W. Tibbitt, M. J. Webber, B. A. Mattix, O. Veiseh, R. Langer, *Nat. Commun.* **2015**, *6*, 1-9.
- [314] N. A. Jalili, M. K. Jaiswal, C. W. Peak, L. M. Cross, A. K. Gaharwar, *Nanoscale* **2017**, *9*, 15379-15389.
- [315] M. K. Hausmann, P. A. Ruhs, G. Siqueira, J. r. Läger, R. Libanori, T. Zimmermann, A. R. Studart, *ACS Nano* **2018**, *12*, 6926-6937.
- [316] W. Xu, B. Z. Molino, F. Cheng, P. J. Molino, Z. Yue, D. Su, X. Wang, S. Willför, C. Xu, G. G. Wallace, *ACS Appl. Mater. Interfaces* **2019**, *11*, 8838-8848.
-

- 
- [317] F. Yang, V. Tadepalli, B. J. Wiley, *ACS Biomater. Sci. Eng.* **2017**, *3*, 863-869.
- [318] Z. M. Jessop, A. Al-Sabah, N. Gao, S. Kyle, B. Thomas, N. Badiei, K. Hawkins, I. S. Whitaker, *Biofabrication* **2019**, *11*, 045006.
- [319] K. Schütz, A. M. Placht, B. Paul, S. Brüggemeier, M. Gelinsky, A. Lode, *J. Tissue Eng. Regen. M.* **2017**, *11*, 1574-1587.
- [320] J. Hazur, R. Detsch, E. Karakaya, J. Kaschta, J. Teßmar, D. Schneidereit, O. Friedrich, D. W. Schubert, A. R. Boccaccini, *Biofabrication* **2020**, *12*, 045004.
- [321] C. Loebel, C. B. Rodell, M. H. Chen, J. A. Burdick, *Nat. Protoc.* **2017**, *12*, 1521-1541.
- [322] Y. Jin, C. Liu, W. Chai, A. Compaan, Y. Huang, *ACS Appl. Mater. Interfaces* **2017**, *9*, 17456-17465.
- [323] T. Ahlfeld, G. Cidonio, D. Kilian, S. Duin, A. Akkineni, J. Dawson, S. Yang, A. Lode, R. Oreffo, M. Gelinsky, *Biofabrication* **2017**, *9*, 034103.
- [324] S. Murugesan, T. Scheibel, *Adv. Funct. Mater.* **2020**, *30*, 1908101.
- [325] A. Lee, A. Hudson, D. Shiwarski, J. Tashman, T. Hinton, S. Yerneni, J. Bliley, P. Campbell, A. Feinberg, *Science* **2019**, *365*, 482-487.
- [326] A. McCormack, C. B. Highley, N. R. Leslie, F. P. Melchels, *Trends Biotechnol.* **2020**, *38*, 584-593.
- [327] Z. Wang, S. J. Florczyk, *Materials* **2020**, *13*, 354.
- [328] W. Liu, Z. Zhong, N. Hu, Y. Zhou, L. Maggio, A. K. Miri, A. Fragasso, X. Jin, A. Khademhosseini, Y. S. Zhang, *Biofabrication* **2018**, *10*, 024102.
- [329] Q. Gao, Y. He, J.-z. Fu, A. Liu, L. Ma, *Biomaterials* **2015**, *61*, 203-215.
- [330] Q. Pi, S. Maharjan, X. Yan, X. Liu, B. Singh, A. M. van Genderen, F. Robledo-Padilla, R. Parra-Saldivar, N. Hu, W. Jia, *Adv. Mater.* **2018**, *30*, 1706913.
- [331] J. H. Galarraga, M. Y. Kwon, J. A. Burdick, *Sci. Rep.* **2019**, *9*, 1-12.
- [332] L. Ouyang, C. B. Highley, W. Sun, J. A. Burdick, *Adv. Mater.* **2017**, *29*, 1604983.
- [333] A. Panwar, L. P. Tan, *Molecules* **2016**, *21*, 685.
- [334] T. Bassiri, A. Levy, M. Litt, *J. Polym. Sci. Part B: Polym. Lett.* **1967**, *5*, 871-879.
- [335] D. Tomalia, D. Sheetz, *J. Polym. Sci. Part A: Polym. Chem.* **1966**, *4*, 2253-2265.
- [336] W. Seeliger, E. Aufderhaar, W. Diepers, R. Feinauer, R. Nehring, W. Thier, H. Hellmann, *Angew. Chem. Int. Ed.* **1966**, *5*, 875-888.
- [337] T. Kagiya, S. Narisawa, T. Maeda, K. Fukui, *J. Polym. Sci. B: Polym. Lett.* **1966**, *4*, 441-445.
- [338] T. X. Viegas, Z. Fang, K. Yoon, R. Weimer, B. Dizman, *Engineering of Biomaterials for Drug Delivery Systems*, **2018**, 173-198.
-

- 
- [339] T. R. Dargaville, J. R. Park, R. Hoogenboom, *Macromol. Biosci.* **2018**, *18*, 1800070.
- [340] F. Wiesbrock, R. Hoogenboom, C. H. Abeln, U. S. Schubert, *Macromol. Rapid Commun.* **2004**, *25*, 1895-1899.
- [341] K. Kempe, C. R. Becer, U. S. Schubert, *Macromolecules* **2011**, *44*, 5825-5842.
- [342] R. Hoogenboom, B. Monnery, *Method for the preparation of uniform, high molar mass cyclic imino ether polymers*, *U. S. Patents* 10118991 **2018**, 11.
- [343] B. D. Monnery, V. V. Jerca, O. Sedlacek, B. Verbraeken, R. Cavill, R. Hoogenboom, *Angew. Chem. Int. Ed.* **2018**, *57*, 15400-15404.
- [344] R. W. Moreadith, T. X. Viegas, M. D. Bentley, J. M. Harris, Z. Fang, K. Yoon, B. Dizman, R. Weimer, B. P. Rae, X. Li, *Eur. Polym. J.* **2017**, *88*, 524-552.
- [345] T. Lorson, M. M. Lubtow, E. Wegener, M. S. Haider, S. Borova, D. Nahm, R. Jordan, M. Sokolski-Papkov, A. V. Kabanov, R. Luxenhofer, *Biomaterials* **2018**, *178*, 204-280.
- [346] A. Zahoranová, R. Luxenhofer, *Advanced Healthcare Materials*, 2001382.
- [347] M. Glassner, M. Vergaelen, R. Hoogenboom, *Polym. Int.* **2018**, *67*, 32-45.
- [348] R. Luxenhofer, Y. Han, A. Schulz, J. Tong, Z. He, A. V. Kabanov, R. Jordan, *Macromol. Rapid Commun.* **2012**, *33*, 1613-31.
- [349] T. Saegusa, T. Hirao, Y. Ito, *Macromolecules* **1975**, *8*, 87-87.
- [350] M. M. Bloksma, U. S. Schubert, R. Hoogenboom, *Macromol. Rapid Commun.* **2011**, *32*, 1419-1441.
- [351] H. M. Lambermont-Thijs, M. W. Fijten, A. van der Linden, B. M. van Lankvelt, M. M. Bloksma, U. S. Schubert, R. Hoogenboom, *Macromolecules* **2011**, *44*, 4320-4325.
- [352] R. Luxenhofer, S. Huber, J. Hytry, J. Tong, A. V. Kabanov, R. Jordan, *J. Polym. Sci., Part A: Polym. Chem.* **2013**, *51*, 732-738.
- [353] K. Aoi, M. Okada, *Prog. Polym. Sci.* **1996**, *21*, 151-208.
- [354] R. Luxenhofer, R. Jordan, *Macromolecules* **2006**, *39*, 3509-3516.
- [355] R. Luxenhofer, M. Bezen, R. Jordan, *Macromol. Rapid Commun.* **2008**, *29*, 1509-1513.
- [356] A. Kowalczyk, J. Kronek, K. Bosowska, B. Trzebicka, A. Dworak, *Polym. Int.* **2011**, *60*, 1001-1009.
- [357] W. Seeliger, W. Thier, *Angew. Chem. Int. Ed.* **1966**, *5*, 612.
- [358] B. D. Monnery, S. Shaunak, M. Thanou, J. H. Steinke, *Macromolecules* **2015**, *48*, 3197-3206.
-

- 
- [359] M. Glassner, D. R. D'hooge, J. Y. Park, P. H. Van Steenberge, B. D. Monnery, M.-F. Reyniers, R. Hoogenboom, *Eur. Polym. J.* **2015**, *65*, 298-304.
- [360] N. Zhang, R. Luxenhofer, R. Jordan, *Macromol. Chem. Phys.* **2012**, *213*, 973-981.
- [361] N. Zhang, S. Huber, A. Schulz, R. Luxenhofer, R. Jordan, *Macromolecules* **2009**, *42*, 2215-2221.
- [362] M. W. Fijten, C. Haensch, B. M. van Lankvelt, R. Hoogenboom, U. S. Schubert, *Macromol. Chem. Phys.* **2008**, *209*, 1887-1895.
- [363] R. Obeid, C. Scholz, *Biomacromolecules* **2011**, *12*, 3797-3804.
- [364] M. Reif, R. Jordan, *Macromol. Chem. Phys.* **2011**, *212*, 1815-1824.
- [365] S. Zalipsky, C. B. Hansen, J. M. Oaks, T. M. Allen, *J. Pharm. Sci.* **1996**, *85*, 133-137.
- [366] R. Jordan, K. Martin, H. J. Räder, K. K. Unger, *Macromolecules* **2001**, *34*, 8858-8865.
- [367] M. Einzmann, W. H. Binder, *J. Polym. Sci., Part A: Polym. Chem.* **2001**, *39*, 2821-2831.
- [368] R.-H. Jin, *J. Mater. Chem.* **2004**, *14*, 320-327.
- [369] K. Aoi, H. Suzuki, M. Okada, *Macromolecules* **1992**, *25*, 7073-7075.
- [370] R. Hoogenboom, M. W. Fijten, G. Kickelbick, U. S. Schubert, *Beilstein J. Org. Chem.* **2010**, *6*, 773-783.
- [371] R. H. Cichewicz, S. A. Kouzi, *Med. Res. Rev.* **2004**, *24*, 90-114.
- [372] A. L. Demirel, S. Yurteri, I. Cianga, Y. Yagci, *J. Polym. Sci., Part A: Polym. Chem.* **2007**, *45*, 2091-2104.
- [373] S. Ates, P. Tatar-Guner, Y. Yagci, A. Levent Demirel, *Des. Monomers Polym.* **2013**, *16*, 137-144.
- [374] M. T. Zarka, O. Nuyken, R. Weberskirch, *Chem. Eur. J.* **2003**, *9*, 3228-3234.
- [375] K. Schwekendiek, F. Glorius, *Synthesis* **2006**, *2006*, 2996-3002.
- [376] P. Persigehl, R. Jordan, O. Nuyken, *Macromolecules* **2000**, *33*, 6977-6981.
- [377] C. Taubmann, R. Luxenhofer, S. Cesana, R. Jordan, *Macromol. Biosci.* **2005**, *5*, 603-612.
- [378] K. Kempe, R. Hoogenboom, U. S. Schubert, *Macromol. Rapid Commun.* **2011**, *32*, 1484-1489.
- [379] A. Gress, A. Völkel, H. Schlaad, *Macromolecules* **2007**, *40*, 7928-7933.
- [380] Y. Chujo, K. Sada, A. Naka, R. Nomura, T. Saegusa, *Macromolecules* **1993**, *26*, 883-887.



- 
- [381] S. Cesana, A. Kurek, M. A. Baur, J. Auernheimer, O. Nuyken, *Macromol. Rapid Commun.* **2007**, 28, 608-615.
- [382] S. Cesana, J. Auernheimer, R. Jordan, H. Kessler, O. Nuyken, *Macromol. Chem. Phys.* **2006**, 207, 183-192.
- [383] S. Kobayashi, E. Masuda, S. Shoda, Y. Shimano, *Macromolecules* **1989**, 22, 2878-2884.
- [384] T. B. Bonn , K. L dtke, R. Jordan, P.  t p nek, C. M. Papadakis, *Colloid. Polym. Sci.* **2004**, 282, 833-843.
- [385] R. Luxenhofer, M. L pez-Garc a, A. Frank, H. Kessler, R. Jordan, *PMSE Prepr.* **2006**, 95, 283-284.
- [386] L. Tauhardt, M. Frant, D. Pretzel, M. Hartlieb, C. B cher, G. Hildebrand, B. Schr ter, C. Weber, K. Kempe, M. Gottschaldt, *J. Mater. Chem. B* **2014**, 2, 4883-4893.
- [387] G. Volet, T. X. Lav, J. Babinot, C. Amiel, *Macromol. Chem. Phys.* **2011**, 212, 118-124.
- [388] K. Kempe, R. Hoogenboom, M. Jaeger, U. S. Schubert, *Macromolecules* **2011**, 44, 6424-6432.
- [389] M. Miyamoto, K. Naka, M. Tokumizu, T. Saegusa, *Macromolecules* **1989**, 22, 1604-1607.
- [390] G.-H. Hsiue, H.-Z. Chiang, C.-H. Wang, T.-M. Juang, *Bioconjugate Chem.* **2006**, 17, 781-786.
- [391] N. Adams, U. S. Schubert, *Adv. Drug Deliv. Rev.* **2007**, 59, 1504-1520.
- [392] B. Guillermin, S. Monge, V. Lapinte, J. J. Robin, *Macromol. Rapid Commun.* **2012**, 33, 1600-1612.
- [393] K. Lava, B. Verbraeken, R. Hoogenboom, *Eur. Polym. J.* **2015**, 65, 98-111.
- [394] E. Rossegger, V. Schenk, F. Wiesbrock, *Polymers* **2013**, 5, 956-1011.
- [395] M. Litt, A. Levy, J. Herz, *J. Macromol. Sci.: Part A-Chemistry* **1975**, 9, 703-727.
- [396] P. Lin, C. Clash, E. M. Pearce, T. Kwei, M. Aponte, *J. Polym. Sci., Part B: Polym. Phys.* **1988**, 26, 603-619.
- [397] D. Christova, R. Velichkova, W. Loos, E. J. Goethals, F. Du Prez, *Polymer* **2003**, 44, 2255-2261.
- [398] J.-S. Park, K. Kataoka, *Macromolecules* **2007**, 40, 3599-3609.
- [399] M. M. Bloksma, C. Weber, I. Y. Perevyazko, A. Kuse, A. Baumg rtel, A. Vollrath, R. Hoogenboom, U. S. Schubert, *Macromolecules* **2011**, 44, 4057-4064.
-

- 
- [400] S. Salzinger, S. Huber, S. Jaksch, P. Busch, R. Jordan, C. M. Papadakis, *Colloid. Polym. Sci.* **2012**, 290, 385-400.
- [401] S. Huber, N. Hutter, R. Jordan, *Colloid. Polym. Sci.* **2008**, 286, 1653-1661.
- [402] M. M. Bloksma, D. J. Bakker, C. Weber, R. Hoogenboom, U. S. Schubert, *Macromol. Rapid Commun.* **2010**, 31, 724-728.
- [403] P. Tatar Güner, A. L. Demirel, *J. Phys. Chem. B* **2012**, 116, 14510-14514.
- [404] M. M. Bloksma, R. M. Paulus, H. P. van Kuringen, F. van der Woerd, H. M. Lambermont-Thijs, U. S. Schubert, R. Hoogenboom, *Macromol. Rapid Commun.* **2012**, 33, 92-96.
- [405] C. Weber, R. Hoogenboom, U. S. Schubert, *Prog. Polym. Sci.* **2012**, 37, 686-714.
- [406] P. J. Bouten, K. Lava, J. Van Hest, R. Hoogenboom, *Polymers* **2015**, 7, 1998-2008.
- [407] K. Kempe, M. Lobert, R. Hoogenboom, U. S. Schubert, *J. Polym. Sci., Part A: Polym. Chem.* **2009**, 47, 3829-3838.
- [408] C. Wang, L. Feng, H. Yang, G. Xin, W. Li, J. Zheng, W. Tian, X. Li, *Phys. Chem. Chem. Phys.* **2012**, 14, 13233-13238.
- [409] R. Hoogenboom, M. W. Fijten, H. M. Thijs, B. M. van Lankvelt, U. S. Schubert, *Des. Monomers Polym.* **2005**, 8, 659-671.
- [410] E. F. J. Rettler, J. M. Kranenburg, H. M. Lambermont-Thijs, R. Hoogenboom, U. S. Schubert, *Macromol. Chem. Phys.* **2010**, 211, 2443-2448.
- [411] K. Kempe, S. Jacobs, H. M. Lambermont-Thijs, M. M. Fijten, R. Hoogenboom, U. S. Schubert, *Macromolecules* **2010**, 43, 4098-4104.
- [412] K. Kempe, E. F.-J. Rettler, R. M. Paulus, A. Kuse, R. Hoogenboom, U. S. Schubert, *Polymer* **2013**, 54, 2036-2042.
- [413] S. Nam, J. Seo, S. Woo, W. H. Kim, H. Kim, D. D. Bradley, Y. Kim, *Nat. Commun.* **2015**, 6, 1-9.
- [414] J. H. Kim, Y. Jung, D. Lee, W. D. Jang, *Adv. Mater.* **2016**, 28, 3499-3503.
- [415] T. Lorson, M. M. Lübtow, E. Wegener, M. S. Haider, S. Borova, D. Nahm, R. Jordan, M. Sokolski-Papkov, A. V. Kabanov, R. Luxenhofer, *Biomaterials* **2018**, 178, 204-280.
- [416] R. Luxenhofer, R. Jordan, *Mater. Matters* **2013**, 8, 70-73.
- [417] M. Hartlieb, K. Kempe, U. S. Schubert, *J. Mater. Chem. B* **2015**, 3, 526-538.
- [418] A. M. Kelly, F. Wiesbrock, *Macromol. Rapid Commun.* **2012**, 33, 1632-1647.
- [419] A. Zahoranová, J. Kronek, *Handbook of Polymers for Pharmaceutical Technologies* **2015**, 4, 231-258.
- [420] M. Hartlieb, K. Kempe, U. S. Schubert, *J. Mater. Chem. B* **2015**, 3, 526-538.
-

- 
- [421] Y. Chujo, Y. Yoshifuji, K. Sada, T. Saegusa, *Macromolecules* **1989**, *22*, 1074-1077.
- [422] Y. Chujo, K. Sada, T. Saegusa, *Macromolecules* **1990**, *23*, 2636-2641.
- [423] Y. Chujo, K. Sada, T. Saegusa, *Macromolecules* **1990**, *23*, 2693-2697.
- [424] Y. Chujo, K. Sada, K. Matsumoto, T. Saegusa, *Macromolecules* **1990**, *23*, 1234-1237.
- [425] T. R. Dargaville, R. Forster, B. L. Farrugia, K. Kempe, L. Voorhaar, U. S. Schubert, R. Hoogenboom, *Macromol. Rapid Commun.* **2012**, *33*, 1695-700.
- [426] M. A. Cortez, S. M. Grayson, *Macromolecules* **2010**, *43*, 4081-4090.
- [427] C. Diehl, H. Schlaad, *Chem. Eur. J.* **2009**, *15*, 11469-11472.
- [428] K. Kempe, C. Weber, K. Babiuch, M. Gottschaldt, R. Hoogenboom, U. S. Schubert, *Biomacromolecules* **2011**, *12*, 2591-2600.
- [429] D. Nahm, F. Weigl, N. Schaefer, A. Sancho, A. Frank, J. Groll, C. Villmann, H.-W. Schmidt, P. D. Dalton, R. Luxenhofer, *Mater. Horizons* **2020**, *7*, 928-933.
- [430] F. Lombardi, A. Lodi, J. Ma, J. Liu, M. Slota, A. Narita, W. K. Myers, K. Müllen, X. Feng, L. Bogani, *Science* **2019**, *366*, 1107-1110.
- [431] Y. Chujo, K. Sada, T. Saegusa, *Polym. J.* **1993**, *25*, 599-608.
- [432] Y. Chujo, K. Sada, T. Saegusa, *Macromolecules* **1993**, *26*, 6320-6323.
- [433] Y. Chujo, K. Sada, T. Saegusa, *Macromolecules* **1993**, *26*, 6315-6319.
- [434] I. C. Kwon, Y. H. Bae, S. W. Kim, *Nature* **1991**, *354*, 291-293.
- [435] V. Percec, T. K. Bera, R. J. Butera, *Biomacromolecules* **2002**, *3*, 272-279.
- [436] X. Wang, X. Li, Y. Li, Y. Zhou, C. Fan, W. Li, S. Ma, Y. Fan, Y. Huang, N. Li, *Acta Biomater.* **2011**, *7*, 4149-4159.
- [437] A. Zahoranová, M. Mrlík, K. Tomanová, J. Kronek, R. Luxenhofer, *Macromol. Chem. Phys.* **2017**, *218*, 1700031.
- [438] T. Lorson, S. Jaksch, M. M. Lübtow, T. Jüngst, J. r. Groll, T. Lühmann, R. Luxenhofer, *Biomacromolecules* **2017**, *18*, 2161-2171.
- [439] T. Lorson, PhD thesis, *Julius-Maximilians-Universität Würzburg*, **2019**.
- [440] B. D. Monnery, R. Hoogenboom, *Polym. Chem.* **2019**, *10*, 3480-3487.
- [441] M. M. Lübtow, M. Mrlík, L. Hahn, A. Altmann, M. Beudert, T. Lühmann, R. Luxenhofer, *J. Funct. Biomater.* **2019**, *10*, 36.
- [442] M. S. Haider, T. Ahmad, M. Yang, C. Hu, L. Hahn, P. Stahlhut, J. Groll, R. Luxenhofer, *Gels* **2021**, *7*, 78.
- [443] L. Hahn, M. Maier, P. Stahlhut, M. Beudert, V. Flegler, S. Forster, A. Altmann, F. Toppe, K. Fischer, S. Seiffert, B. Bottcher, T. Lühmann, R. Luxenhofer, *ACS Appl. Mater. Interfaces* **2020**, *12*, 12445-12456.
-

- 
- [444] L. Hahn, E. Karakaya, T. Zorn, B. Sochor, M. Maier, P. Stahlhut, S. Forster, K. Fischer, S. Seiffert, A.-C. Pöppler, R. Detsch, R. Luxenhofer, *Biomacromolecules* **2021**, *22*, 3017-3027.
- [445] L. Hahn, L. Keßler, L. Polzin, L. Fritze, S. Forster, H. Helten, R. Luxenhofer, *Macromol. Chem. Phys.* **2021**, *222*, 2100114.
- [446] L. Hahn, M. Beudert, M. Gutmann, L. Keßler, P. Stahlhut, L. Fischer, E. Karakaya, T. Lorson, I. Thievessen, R. Detsch, T. Lühmann, R. Luxenhofer, *Macromol. Biosci.* **2021**, *21*, 2100122.
- [447] T. Lorson, S. Jaksch, M. M. Lubtow, T. Jungst, J. Groll, T. Lühmann, R. Luxenhofer, *Biomacromolecules* **2017**, *18*, 2161-2171.
- [448] S. Sinnwell, H. Ritter, *Macromol. Rapid Commun.* **2006**, *27*, 1335-1340.
- [449] R. Luxenhofer, A. Schulz, C. Roques, S. Li, T. K. Bronich, E. V. Batrakova, R. Jordan, A. V. Kabanov, *Biomaterials* **2010**, *31*, 4972-4979.
- [450] C. Hu, L. Hahn, M. Yang, A. Altmann, P. Stahlhut, J. Groll, R. Luxenhofer, *J. Mater. Sci.* **2021**, *56*, 691-705.
- [451] Y. F. Jin, C. C. Liu, W. X. Chai, A. Compaan, Y. Huang, *ACS Appl. Mater. Interfaces* **2017**, *9*, 17457-17466.
- [452] I. Boucenna, L. Royon, P. Colinart, *J. Therm. Anal. Calorim.* **2009**, *98*, 119-123.
- [453] K. Haraguchi, T. Takehisa, *Adv. Mater.* **2002**, *14*, 1120-1124.
- [454] K. Haraguchi, K. Uyama, H. Tanimoto, *Macromol. Rapid Commun.* **2011**, *32*, 1253-1258.
- [455] S. M. Hong, D. Sycks, H. F. Chan, S. T. Lin, G. P. Lopez, F. Guilak, K. W. Leong, X. H. Zhao, *Adv. Mater.* **2015**, *27*, 4035-4040.
- [456] D. Chimene, C. W. Peak, J. L. Gentry, J. K. Carrow, L. M. Cross, E. Mondragon, G. B. Cardoso, R. Kaunas, A. K. Gaharwar, *ACS Appl. Mater. Interfaces* **2018**, *10*, 9957-9968.
- [457] J. L. Dávila, M. A. d'Ávila, *Int. J. Adv. Manuf. Technol.* **2018**, *101*, 675-686.
- [458] Y. F. Jin, Y. Y. Shen, J. Yin, J. Qian, Y. Huang, *ACS Appl. Mater. Interfaces* **2018**, *10*, 10461-10470.
- [459] C. Hu, M. S. Haider, L. Hahn, M. Yang, R. Luxenhofer, *J. Mater. Chem. B* **2021**, *9*, 4535-4545.
- [460] S. Bennour, F. Louzri, *Adv. Chem.* **2014**, *2014*, 1-10.
- [461] F. A. Jerca, A. M. Anghelache, E. Ghibu, S. Cecoltan, I.-C. Stancu, R. Trusca, E. Vasile, M. Teodorescu, D. M. Vuluga, R. Hoogenboom, *Chem. Mater.* **2018**, *30*, 7938-7949.
-

- [462] T. R. Dargaville, R. Forster, B. L. Farrugia, K. Kempe, L. Voorhaar, U. S. Schubert, R. Hoogenboom, *Macromol. Rapid Commun.* **2012**, *33*, 1695-1700.
- [463] A. Hrynevich, I. Liashenko, P. D. Dalton, *Adv. Mater. Technol.* **2020**, *5*, 2000772.
- [464] C. Hu, T. Ahmad, M. S. Haider, L. Hahn, P. Stahlhut, J. Groll, R. Luxenhofer, *Biofabrication* **2021**, DOI: <https://doi.org/10.1088/1758-5090/ac40ee>.



# |Affidavit

I hereby confirm that my thesis entitled “Novel Hybrid Hydrogels Based on Poly(2-oxazoline)” is the result of my own work. I did not receive any help or support from commercial consultants. All sources and / or materials applied are listed and specified in the thesis.

Furthermore, I confirm that this thesis has not yet been submitted as part of another examination process neither in identical nor in similar form.

Place, Date

Signature

Hiermit erkläre ich an Eides statt, die Dissertation „*Neuartige Hybrid Hydrogele auf Basis von Poly(2-oxazolin)*“ eigenständig, d.h. insbesondere selbstständig und ohne Hilfe eines kommerziellen Promotionsberaters, angefertigt und keine anderen als die von mir angegebenen Quellen und Hilfsmittel verwendet zu haben.

Ich erkläre außerdem, dass die Dissertation weder in gleicher noch in ähnlicher Form bereits in einem anderen Prüfungsverfahren vorgelegen hat.

Ort, Datum

Unterschrift





# |Curriculum Vitae

## PERSONAL INFORMATION:

Birth Date: Mar. 20th 1993

Citizenship: P. R. China

Gender: Female

## ACADEMIC EDUCATION:

Since 10/2018

### **Doctoral thesis**

Graduate School of Science and Technology (GSST), Julius-Maximilians-Universität Würzburg, Germany

Focus: Polymer chemistry

Supervisor: Prof. Dr. Robert Luxenhofer

Thesis topic: "Novel hybrid hydrogels based on poly(2-oxazoline)"

09/2015 - 06/2018

### **Master**

Department of Chemistry, Xi'an Jiaotong University, P. R. China

Focus: Polymer chemistry

Supervisor: Prof. Dr. Yong Mei Chen

Master thesis topic: "Preparation and study of a biocompatible dual-physical crosslinked photoluminescent hydrogel"

09/2011 - 07/2015

### **Bachelor**

Department of Applied Chemistry,  
Northwest Agriculture and Forestry University, P. R. China

Focus: Applied chemistry

Supervisor: Prof. Dr. Le Zhou & Prof. Dr. Yong Mei Chen

Bachelor thesis topic: "Study on the preparation and performance of a photoluminescent self-healing hydrogel based on carboxymethyl cellulose"

### SCIENTIFIC ACTIVITY & AWARDS:

- |                   |   |
|-------------------|---|
| 05/2021 - 05/2021 | The 48th World Polymer Congress IUPAC-MACRO2020+, Hybrid Event, in South Korea<br><i>Online Short Talk Sessions _ Outstanding Online Short Talk Award</i>       |
| 04/2021 - 04/2021 | 2st Virtual European Polymer Conference   |
| 09/2020 - 09/2020 | Additive Manufacturing Meeting Medicine (AMMM) 2020   |
| 09/2020 - 09/2020 | 1st Virtual European Polymer Conference   |
| 03/2020 - 03/2020 | 5th Bioinspired Materials 2020, Web conference Organized by DGM-Inventum GmbH<br><i>Poster and Online Short Talk</i>  |
| 02/2019 - 02/2019 | 9th Scientific Seminar of the North Bavarian Biomaterials Alliance (NBBA), at Department of Materials Science and Engineering, University of Erlangen-Nuremberg |

Signature